



The  
University  
Of  
Sheffield.

# Nano-reinforced Epoxy Resin Composites with Reduced Graphene Oxide

A thesis submitted to the University of Sheffield in partial fulfilment for the  
Degree of Doctor of Philosophy

By:

Ahmed Abdulmajeed Al-Zahrany

Department of Materials Science and Engineering  
University of Sheffield

September 2019



## **Declaration**

I declare that this thesis has not been submitted as an exercise for a degree at this or any other university and it is entirely my own work.

I agree to deposit this thesis in the University's open access institutional repository or allow the library to do so on my behalf, subject to British Copyright Legislation and The University of Sheffield Library conditions of use and acknowledgement.

Ahmed A Alzahrany

September 2019



# ABSTRACT

Graphene has attracted intense scientific interest over the last decade because of its outstanding properties. However, to recover the properties of graphene, graphene oxide (GO) must be reduced. Several reduction approaches have been used to synthesis of reduced GO (RGO), but most of these approaches require the use of chemicals such as hydrazine that seem have a negative effect on the environment, and this was a significant consideration in the current study. The objective of my thesis is to development of simple, low-cost, environmental friendly and controllable approaches for the high (tube-furnace) and low (vacuum-oven-assisted) temperature reduction of GO to RGO and its effects on the processing and properties of incorporating nano-scale reinforcements in the matrix of epoxy (EP) to produce multi-scale composites. Moreover, this thesis investigated the dielectric properties of the RGO–SiO<sub>2</sub>/EP nanocomposites fabricated by the sol–gel process.

The resulting RGO- based composites were characterised by a variety of different technique, including AFM, SEM, TEM, XPS, XRD, FTIR, Raman and TGA. The analysis revealed that these RGO-based composites have excellent properties and stability.

We successfully applied the uniform dispersion of RGO sheets in Epoxy matrix to obtain Epoxy–RGO nanocomposites by embracing a combination of different dispersion techniques with presence of a tetrahydrofuran solvent, high shear mixing and bath sonication, for two different processing times of 90 and 30 min, respectively.

The thermal conductivity of Epoxy was improved by up to 85%, reaching the maximum value of 0.36 W m<sup>-1</sup> K<sup>-1</sup> at 1.0 wt.% RGO as well as electrical conductivity improved by about seven orders of magnitude to 5.92×10<sup>-7</sup> S m<sup>-1</sup>. The resultant values indicated that the dielectric properties after a long time of dispersing presented a higher dielectric constant and dielectric loss than that of the RGO–SiO<sub>2</sub>/EP nanocomposites at a shorter time of dispersing. These results were fast and highly efficient compared with other report data.

## ACKNOWLEDGEMENTS

I wish to express my sincere thanks and gratitude to Dr Ihtesham ur Rehman and Dr Biqiong Chen who have supported me through this work with their patience and knowledge whilst allowing me the room to work in my own way. Without their supervision and guidance, this work would not have been completed.

I wish to thank all the staff of CSIC, including Dr Simon Hayes and Dr Joel Foreman. There have been moments throughout this work when I have needed their knowledge and expertise and they were always there to help. I also wish to thank Eng. Attiah Alzahrany from King Saud University for helping me to arrange the DMA tests, solve problems in the lab and for providing me with opportunities to gain experience. I wish to make special thanks to Dr Ihtesham ur Rehman who helped with my experiments but supported and stood behind me when I really struggled. I would like to thank Dawn Bussey for the last part of my AFM photography. We changed three AFMs to obtain the best images. Additional thanks to the Inha University's Department of Polymer Science and Engineering (Korea), who provided measured data of electrorheological ER fluid samples to help me complete the final part of my experiment.

I wish to thank all the students in the postgraduate office of the Sir Robert Hadfield Building for providing a fun and enjoyable place to study. I would like to thank Zaid Mohammadsalih, Xiangshuai Geng and Alaa Almansoori for their friendship and flexibility in arranging the experiment together. I would also like to express my thanks to my daughters. Without their encouragement and moral support, I would not have been able to come to the United Kingdom to pursue my PhD degree. Lastly, but not least, a big thank you to my wife, Fatimah Asiri, who is always curious about what I am doing with my PhD and volunteered to be my peer reviewer.

## List of Symbols

A	Area
Å	angstrom unit
a	lattice parameter: unit cell <i>x</i> -axial length
l	Length
F	Force
NPs	Nanoparticles
at %	atom percent
wt. %	weight fraction percent
vol.%	volume fraction percent
$\omega$	angular frequency
$\epsilon'$	dielectric permittivity
$\epsilon''$	dielectric constant or relative permittivity
$\theta$	Bragg diffraction angle
$\lambda$	wavelength of electromagnetic radiation
$\rho$	Density
k	thermal conductivity
$\rho$	electrical resistivity
$\sigma$	electrical conductivity
$P_c$	percolation threshold
$\sigma_y$	yield strength
TS	tensile strength
$\sigma$	Stress
$\epsilon$	Strain
$C_p$	heat capacity at constant pressure
$E_Y$	modulus of elasticity or Young's modulus
R	gas constant
T	Temperature
$T_g$	glass transition temperature
$T_d$	degradation temperature
v	Velocity
GO	graphene oxide
RGO	reduced graphene oxide
CRGO	chemically reduced graphene oxide
TRGO	thermally reduced graphene oxide

## Unit Abbreviations

A	Ampere
Å	Angstrom
Nm	Nanometre
$\mu$ m	Micrometre
mm	Millimetre
cm	Centimetre
m	Meter
S	Second
N	Newton
g	Gram
Kg	Kilogram
Pa	Pascal
MPa	Megapascal
GPa	Gigapascal
$T$	Temperature
°C	degrees Celsius
K	degrees Kelvin
W	Watt
eV	electron volt
mol	Mole
J	Joule



# Contents

<b>1</b>	<b>Chapter 1: General introduction</b>	<b>1</b>
1.1	Introduction	1
1.2	Aims and objectives of the thesis	5
<b>2</b>	<b>Chapter 2: Literature Review</b>	<b>9</b>
2.1	Introduction	9
2.2	Polymer matrix	10
2.2.1	Thermoplastic polymers	10
2.2.2	Thermosetting polymers	11
2.3	Epoxy resin systems	11
2.3.1	Epoxy resins and their curing agents	11
2.3.2	Properties of epoxy	16
2.4	Reinforcing agents	17
2.4.1	Fillers	17
2.4.2	Nanofillers	18
2.5	Graphene	20
2.5.1	The Discovery of Graphene	20
2.5.2	Properties of Graphene	21
2.5.3	Potential Applications of Graphene	22
2.6	Synthesis of graphene	22
2.6.1	Bottom-up approach	23
2.6.2	Top-down approach	24
2.7	GO reduction methods	26
2.7.1	Chemical reduction	26
2.7.2	Thermal reduction	27
2.8	Comparison properties of GO and RGO	29
2.9	The structure of GO and RGO	29
2.10	Epoxy composites	33
2.10.1	Preparation polymer–RGO nanocomposites	34
2.11	Processing conditions	36
2.12	Dispersion of RGO	38
2.12.1	Using solvent	38
2.12.2	Decoration of RGO sheets with metal/metal oxide nanoparticles	41
2.13	Theory	47
2.13.1	Dispersion State	47
2.13.2	Interfacial Interactions	48
2.13.3	Thermal Properties	49
2.13.4	Electrical Conductivity	50

2.13.5	Mechanical Theory .....	53
2.14	Properties of polymer–RGO nanocomposites .....	56
2.14.1	Mechanical properties .....	56
2.14.2	Conductive Properties .....	58
2.14.3	Thermal stability .....	61
2.14.4	Dielectric constant .....	62
2.15	Analytical techniques .....	65
2.16	Applications .....	78
<b>3</b>	<b>Chapter 3: Synthesis and characterise of RGO sheets reduction via a tube furnace at high temperature and vacuum oven at low-temperatures.....</b>	<b>82</b>
3.1	Introduction .....	83
3.2	Experimental section .....	85
3.2.1	Materials .....	85
3.2.2	The preparation of graphite oxide .....	85
3.2.3	The preparation of GO .....	86
3.3	Section One .....	87
3.3.1	Reduction by using a tube furnace .....	87
3.3.2	Characterisation .....	89
3.4	Results and Discussion .....	91
3.4.1	Criteria utilised in determining the effect of reduction .....	91
3.5	Section Two .....	104
3.5.1	Reduction by using vacuum oven .....	104
3.6	Results and discussion .....	108
3.6.1	Spectroscopic measurements .....	108
3.7	Comparison between two synthesis methods .....	124
3.8	Conclusion .....	127
<b>4</b>	<b>Chapter 4: Synthesis and properties study of EP–RGO nanocomposites .....</b>	<b>129</b>
4.1	Introduction .....	130
4.2	Experimental section .....	131
4.2.1	Materials .....	131
4.3	Section One-Tube furnace .....	132
4.3.1	Production of EP nanocomposites reinforced by RGO (produced at high-temperature) .....	132
4.3.2	Characterisation .....	133
4.4	Results and discussion .....	137
4.4.1	Spectroscopic measurements .....	137
4.4.2	Thermal and thermomechanical properties .....	140
4.4.3	Mechanical properties .....	148
4.4.4	Conductivities properties .....	155

4.5	Section Two- Vacuum oven.....	162
4.5.1	Production of EP nanocomposites reinforced by RGO (at low-temperature) .....	162
4.5.2	Characterisation .....	163
4.6	Results and discussion .....	163
4.6.1	Spectroscopic measurements .....	163
4.6.2	Thermal and thermomechanical properties.....	167
4.6.3	Mechanical properties.....	174
4.7	Conclusion .....	178
<b>5</b>	<b>Chapter 5 Effect of RGO–SiO<sub>2</sub> nano-hybrids on the mechanical and electrical properties of epoxy.....</b>	<b>181</b>
<b>5.1</b>	<b>Introduction.....</b>	<b>182</b>
5.2	Experimental section.....	182
5.2.1	Materials .....	182
5.2.1	Synthesis of GO, RGO–SiO <sub>2</sub> nano-hybrids and their nanocomposites .....	183
5.3	Characterisation .....	188
<b>5.4</b>	<b>Results and discussion .....</b>	<b>189</b>
5.5	Section One-GO and RGO–SiO <sub>2</sub> hybrid.....	189
5.6	Section Two-RGO–SiO <sub>2</sub> nanocomposites .....	203
5.7	Mechanical properties.....	215
5.8	Dielectric characteristics .....	219
<b>5.9</b>	<b>Conclusion .....</b>	<b>224</b>
<b>6</b>	<b>Chapter 6: General Discussion .....</b>	<b>226</b>
<b>7</b>	<b>Chapter 7 .....</b>	<b>248</b>
	<b>General conclusions and future work .....</b>	<b>248</b>
7.1	General conclusions .....	248
7.2	Future work.....	250
7.3	Conferences and papers .....	251
7.4	Papers in preparation.....	251
<b>8</b>	<b>References.....</b>	<b>252</b>
<b>9</b>	<b>Appendix.....</b>	<b>279</b>

# List of Tables

<b>Table 2-1.</b> Structures of commonly used epoxy resins .....	13
<b>Table 2-2.</b> Structures and properties of commonly used curing agents for epoxy resin (Mazumdar 2002) .....	14
<b>Table 2-3.</b> Some properties of epoxy based composite materials, using anhydride as a curing agent (Hull & Clyne 1996). .....	17
<b>Table 2-4.</b> A list of different approaches for producing graphene and the resultant characteristics.....	26
<b>Table 2-5.</b> Typical properties of mono-layer graphene, GO and RGO.....	29
<b>Table 2-6.</b> Comparison of some PNCs preparation methods (Wang et al. 2016) .....	35
<b>Table 2-7.</b> A summary of various approaches used to fabricate RGO-nanoparticles composites. ....	46
<b>Table 2-8.</b> The range of conductive values versus their CPC applications (Narkis et al. 1998). ....	78
<b>Table 3-1.</b> The characteristics, manufacturer and supplier of the materials used.....	84
<b>Table 3-2.</b> The C/O ratio and electrical conductivity of typical reports on the reduction of GO. ....	98
<b>Table 3-3.</b> Atomic concentrations of O1s, C1s and their ratios obtained by XPS survey spectra. ....	101
<b>Table 3-4.</b> Comparison of mass change for GO at different reduction temperatures under vacuum oven with different time periods .....	105
<b>Table 3-5.</b> Summary of XRD patterns of graphite, GO and RGOs samples.....	116
<b>Table 3-6.</b> Carbon and oxygen content (%) in the samples obtained from the XPS test. ....	118
<b>Table 3-7.</b> The XPS spectra for the B.E (eV) obtained in C1s analysis for both GO and RGOs samples compared with graphite sample. ....	119
<b>Table 3-8.</b> A summary comparison of the structure results of RGO sheets produced by the reduction techniques. ....	125
<b>Table 4-1.</b> The characteristics, manufacturer and supplier of the materials used.....	130
<b>Table 4-2.</b> Thermal decomposition T <sub>50%</sub> temperature for EP, EP/GO, and EP/RGOs samples. ....	142
<b>Table 4-3.</b> Dynamic mechanical properties of neat EP and its EP-nanocomposites used in different loading of RGO.....	147
<b>Table 4-4.</b> Average Tensile Properties Neat EP and its Nanocomposites. ....	150
<b>Table 4-5.</b> Different procedures for dispersing TRGO in EP resins and the thermal, electrical and mechanical properties of RGO/EP composites.....	160
<b>Table 4-6.</b> Different procedures for dispersing TRGO in EP resins and the thermal, electrical and mechanical properties of RGO/EP composites.....	161
<b>Table 4-7.</b> Summary of decomposition temperature (T <sub>d</sub> ) for EP and its nanocomposites.....	167
<b>Table 4-8.</b> DMA results for EP and its nanocomposites of GO and RGOs at 0.5wt % level...	172
<b>Table 4-9.</b> Illustrates the static mechanical properties of nanocomposites.....	176
<b>Table 5-1.</b> Lists the typical material characteristics that are desired to use during this work and their manufacturer and direct supplier.....	182
<b>Table 5-2.</b> Atomic ratio of RGO–SiO <sub>2</sub> corresponding to calculated weight %.....	197
<b>Table 5-3.</b> Thermal degradation temperatures (T <sub>5%</sub> ) for EP-RGO–SiO <sub>2</sub> nanocomposites under nitrogen and air atmospheres.....	208
<b>Table 5-4.</b> DMA results for EP and its nanocomposites at different loading of fillers.....	214
<b>Table 5-5.</b> Illustrate the mechanical properties of EP, EP–GO and its nanocomposites.....	216
<b>Table 6-1.</b> Comparison of increments in the modulus, tensile strength and T <sub>g</sub> , among various	

## List of Figures

<b>Figure 2-1.</b> The curing process of the anhydride–epoxy system with an accelerator, adopted from Gu et al. 2015. ....	16
<b>Figure 2-2.</b> The 2D structure of carbon materials is called graphene; 0D fullerene (on the left end); 1D nanotubes (CNTs) (on the middle) and 3D graphite (on the right end). Adopted from Geim and Novoselov (2007). ....	18
<b>Figure 2-3.</b> (a) The nonstoichiometric structural model of GO Lerf et al. 1998 and (b) Schematic illustration of GO reduction (Huang et al. 2018). ....	30-31
<b>Figure 2-4.</b> Atomic resolution, aberration-corrected TEM image of a single layer RGO membrane. (a) Original image and (b) with color added to highlight the different features. ...	32
<b>Figure 2-5.</b> RGO sheets dispersed in distilled H <sub>2</sub> O and other different organic solvents using an ultra-sonication bath for sixty minutes. Upper row: dispersion immediately after sonication. Lower row: dispersions three-weeks after sonication, (Paredes et al. 2008). ....	39
<b>Figure 2-6.</b> RGO–NPs composite formed from RGO nano-sheets covered by AuNPs: (A) AFM image of a mono-layer of RGO (B) A RGO nano-sheet covered by a layer of 3.5 nm AuNPs. (C and D) TEM images of the RGO sheet decorated with AuNPs at low and high resolutions (Zhuo et al. 2013). ....	43
<b>Figure 2-7.</b> Images of some significant CPCs materials. From left side to right: Capacitors related to charge storage application; aircraft tyre/ antistatic material; circuit board material for ESD application; mobile phone/ EMI shielding (Strumpler 1999; Dang et al. 2012; Arjmand 2014). ....	80
<b>Figure 3-1.</b> The procedure and technique to synthesise RGO sheets. ....	87
<b>Figure 3-2.</b> AFM images of monolayered of RGO deposited on mica substrate. ....	92
<b>Figure 3-3.</b> SEM images of RGO (A) and GO (B) and Graphite (C); TEM images of RGO (a) and GO (b) at different magnifications and TEM image of side-view of natural graphite (c)...	94
<b>Figure 3-4.</b> FT-IR spectra of GO before and after reduction by thermal treatment at 1400°C. The peaks corresponding to different functional groups are indicated. ....	95
<b>Figure 3-5.</b> XRD (A) and TGA (B) of GO and its reduction (RGO). ....	97
<b>Figure 3-6.</b> (A) C1s XPS survey and (B) XPS spectra of graphite, GO and RGO. ....	101-102
<b>Figure 3-7.</b> TEM image of RGO produced by vacuum oven at low temperature (180°C) ...	107
<b>Figure 3-8.</b> FTIR spectra of GO and RGOs. ....	109
<b>Figure 3-9.</b> The crystal structures of graphite, GO and RGOs samples by Raman spectroscopy. ....	111
<b>Figure 3-10.</b> XRD curves of graphite, GO and RGOs samples. ....	115
<b>Figure 3-11.</b> Survey scan spectra of pure graphite, GO, RGOs. ....	117
<b>Figure 3-12.</b> C 1s XPS spectra of graphite (A), GO (B), RGO at different temperature (C, D, and E) ....	120
<b>Figure 3-13:</b> The TGA plots for graphite, GO and RGOs. ....	122
<b>Figure 4-1.</b> SEM micrographs of (A) Neat EP and its nanocomposites with (B) 1.0 wt. % of GO, (C) 0.1 wt. % of RGO, (D) and (D') low and high-magnification of 0.5 wt. % of RGO and (E) 1.0 wt. % of RGO. ....	137
<b>Figure 4-2.</b> FT-IR spectra of (a) neat EP (b) EP- 0.1 wt.% RGO (c) EP- 0.5 wt.% RGO (d) EP- 1.0 wt. % RGO and (e) EP- 1.0 wt. % GO nanocomposites. ....	139

<b>Figure 4-3.</b> TGA and DTG curves of neat EP, EP- 0.1 wt. % RGO, EP- 0.5 wt. % RGO, EP- 1.0 wt. % RGO and EP- 1.0 wt. % GO nanocomposites.....	141
<b>Figure 4-4.</b> DSC thermograms of neat EP, EP- 0.1 wt. % RGO, EP- 0.5 wt. % RGO, EP- 1.0 wt. % RGO and EP- 1.0 wt. % GO nanocomposites.....	143
<b>Figure 4-5.</b> Dynamic mechanical properties of the EP nanocomposites, (A) storage modulus and (B) $\tan \delta$ .....	145
<b>Figure 4-6.</b> Typical tensile strength versus tensile strain curves for neat EP and its composites filled with different RGO concentrations.....	149
<b>Figure 4-7.</b> Plots of Tensile strength (A) and Young's modulus (B) of neat EP and its nanocomposites with different RGO loading and 1.0 wt. % GO nanocomposites.....	150-151
<b>Figure 4-8.</b> Modulus determined by nanoindentation for 1.0 wt. % RGO in EP.....	153
<b>Figure 4-9.</b> Tensile Modulus determined by nanoindentation for EP-RGO nanocomposites.....	153
<b>Figure 4-10.</b> Plots of thermal conductivities vs temperatures (25 –100°C) of neat EP and its nanocomposites.....	155
<b>Figure 4-11.</b> Electrical conductivity ( $\sigma_{dc}$ ) versus filler weight fraction ( $\phi$ ) for RGO/EP composites. Inset shows a log–log plot of $\sigma_c$ versus ( $\phi - \phi_c$ ).....	157
<b>Figure 4-12.</b> FTIR spectra of pure EP and RGOs reinforced EP nanocomposites.....	163
<b>Figure 4-13.</b> SEM images of cryo-fracture surfaces of (A) neat EP and its nanocomposites at 0.5 wt. % content of RGO at different reduction temperatures of (B) 120°C, (C) 160°C and (D) 180°C.....	164
<b>Figure 4-14.</b> TGA curves for pure EP and its nanocomposites.....	166
<b>Figure 4-15.</b> The $T_g$ values obtained by DSC for EP and its nanocomposites.....	169
<b>Figure 4-16.</b> The storage modulus $E'$ and loss factor $\tan \delta$ of EP and its nanocomposites at 0.5 wt. % of GO and RGOs obtained at different temperatures.....	171
<b>Figure 4-17 (A).</b> Plots of the Tensile modulus values for the pure EP and its nanocomposites at 0.5 wt.% of fillers.....	174
<b>Figure 4-17 (B):</b> Plots of the tensile strength for the pure EP and its nanocomposites at 0.5 wt. % of fillers.....	175
<b>Figure 5-1.</b> EP system mixing setup.....	185
<b>Figure 5-2.</b> TEM images of (A) GO, (B) RGO–SiO <sub>2</sub> nano-hybrids and (B') high magnification RGO-SiO <sub>2</sub> nano-hybrids.....	189
<b>Figure 5-3.</b> The SEM images of (A) GO and (B) RGO–SiO <sub>2</sub> (1:1) nano-hybrids.....	190
<b>Figure 5-4.</b> Representative AFM images of RGO-SiO <sub>2</sub> at high magnifications.....	191
<b>Figure 5-5.</b> The FT-IR spectra for GO, RGO, SiO <sub>2</sub> and RGO–SiO <sub>2</sub> powder.....	193
<b>Figure 5-6.</b> The XRD patterns for GO, RGO, SiO <sub>2</sub> and RGO–SiO <sub>2</sub> .....	194
<b>Figure 5-7.</b> Survey scan spectra of SiO <sub>2</sub> , GO, RGO and RGO–SiO <sub>2</sub> .....	197
<b>Figure 5-8.</b> C 1s XPS spectra of GO (A), RGO (B) and RGO–SiO <sub>2</sub> , and O 1s for SiO <sub>2</sub> (D) and RGO-SiO <sub>2</sub> (F), and Si2p for SiO <sub>2</sub> and RGO–SiO <sub>2</sub> (E, and G).....	198
<b>Figure 5-9.</b> The crystal structure of GO, RGO and RGO–SiO <sub>2</sub> by Raman technique.....	199
<b>Figure 5-10.</b> TGA curves of GO, RGO and RGO–SiO <sub>2</sub> nano-hybrid composite. The images are magnified 25kV.....	201
<b>Figure 5-11.</b> The SEM images of (A) a pure EP composite, and EP nanocomposites containing 5.0 wt. % of (B) silica, 1.0 wt. % of (C and D) RGO–SiO <sub>2</sub> nano-sheets using THF and distilled	

water for dispersion, and 3.0 wt. % of (E and F) RGO–SiO <sub>2</sub> nano-sheets at low and high times of dispersion respectively. The images are magnified 25 kV.....	203
<b>Figure 5-12.</b> FT-IR spectra for (a) neat EP and its nanocomposites of RGO–SiO <sub>2</sub> (b, c) at 1 wt. % (H <sub>2</sub> O, THF), (d, e) at 3 wt. % (30, 90 min), (f) at 5 wt. % and 5 wt. % of pure SiO <sub>2</sub> .....	204
<b>Figure 5-13.</b> TGA/DTG thermograms for nanocomposites examined under N <sub>2</sub> atmosphere.	207
<b>Figure 5-14.</b> TGA thermograms of nanocomposites examined in air.....	208
<b>Figure 5-15.</b> The DMA plots for EP and its nanocomposites: (a) E'; and (b) tan δ.....	211
<b>Figure 5-16.</b> Plots of the elastic modulus for the pure EP and its nanocomposites at different concentrations of SiO <sub>2</sub> and RGO–SiO <sub>2</sub> .....	215
<b>Figure 5-17.</b> Dielectric constant (ε'): (a) SiO <sub>2</sub> , GO and EP–RGO nanocomposite; (b) RGO-SiO <sub>2</sub> /EP nanocomposites.....	219
<b>Figure 5-18.</b> Dielectric loss (ε'') of RGO–SiO <sub>2</sub> /EP nanocomposites.....	221

# 1 Chapter 1: General introduction

## 1.1 Introduction

The term nanotechnology generally refers to the developments in science and engineering at nanometre scale, for the fabrication of novel materials, structures and devices. These devices have properties that have been designed to meet specific scientific and technological objectives. A new class of materials that emerged from these advances in nanotechnology are generally known as nanocomposites, and these are fabricated by incorporating nanoscale reinforcements inside a material matrix. When the matrix is a polymer, they are described as polymer nanocomposites (PNCs).

The development of techniques for producing a structure made from a single layer of graphite has greatly revolutionised nanotechnology since it was isolated in 2004 (Geim and Novoselov 2007). Since then, much effort has gone into the volume production of graphene to address the requirements of different industries, especially the composite industry. The incorporation of graphene into host polymer matrices has been a focus of research in many laboratories in both academia and industry to achieve further improved properties, and there has been a tremendous growth in ideas for potential applications of these materials in industries involved in energy production, aerospace and electronics.

The first challenge is in developing a high-production approach for pure graphene. Many techniques have been applied to meet this challenge, and one particularly promising approach is based on graphene reflux through repeated separation techniques adopted by Rountree et al. 2016. A second challenge with these materials is in obtaining the best polymer nanocomposites (PNCs) material for various industrial applications. The published research on PNCs has focused on developing methods of incorporating graphene and its alternative forms into different polymer matrices (i.e. polypropylene (PP), polyesters and epoxies) (Silvestre et al.



2016). However, as graphene material exhibits random dispersion in the host polymer matrices arising from the strong Van der Waals forces of attraction, alternative forms of modified graphene such as graphene oxide (GO) and reduced GO (RGO) have been studied extensively because these forms are easier to disperse.

Many studies have focused on endeavours to reduce the irregular dispersion of carbon fillers into various polymer matrices, by using specified manufacturing methods. The in-situ polymerisation method has received considerable attention in this regard in order to overcome the impact of processing conditions on dispersion which appears in the solution mixing method comprising ultra-sonication and high-shear mixing (See section 2.12, for a more detailed discussion). Using the sonication and high-shear mixing techniques together can be an effective process for dispersing the low contents of fillers in polymers such as in the reinforcement of expanded graphite/epoxy, as confirmed by Yasmin et al. 2006. Prior to this study, the main technique for providing a uniform dispersion was ultra-sonication, as reported in the study of Chen et al. 2015.

On the other hand, type of reduction techniques of GO can also help to obtain a uniform dispersion of RGO in polymer matrices. The strong oxidation of raw graphite flakes produces graphite acid with a high abundance of various oxygenated-containing functional groups (OCFGs) that are distributed on structural planes and edges, thereby offering an indirect path for producing GO.

In contrast, thus far, two different approaches have been extensively studied to produce RGO sheets in bulk quantities and at low cost. The first is based on a chemical reductant such as hydrazine hydrate ( $N_2H_4$ ) to obtain chemically reduced graphene oxide (CRGO). The defect of the  $sp^2$  structure in this chemical approach is larger compared to thermally reduced graphene oxide (TRGO), and this can be attributed to the remaining oxide functional groups and defects on the main structure of CRGO sheets. For example, reduction by strong chemical reducer  $N_2H_4$

resulted in the formation of  $sp^3$  hybridised C–N bonds on the main structure of the reduced sheets. Such disorders prevent the production of RGO sheets with high thermal and electrical conductivities. This method was employed by Park et al. 2014 to reduce GO in the preparation of nanocomposites of PS/CRGO *via* a solution mixing process. The resultant nanocomposites were slightly improved in terms of their electrical and thermal conductivities.

The second way of obtaining RGO in the previous studies is by using the thermal reduction approach of graphite oxide (in this work we have used GO rather than graphite oxide to prevent internal pressure build-up between RGO sheets and tear of  $sp^2$  form) at high temperatures using a tube furnace. This approach is widely used to form an effective structure and wrinkled nano-sheets with a 'fluffy' appearance and an electrical conductivity that is higher than that of CRGO. McAllister et al. 2007 employed a tube furnace for rapid heating ( $>2000^\circ\text{C min}^{-1}$ ) and high ultimate temperature of  $1050^\circ\text{C}$  for graphite oxide to produce TRGO. The drawbacks of this technique are the low-volume production and the requirement of high temperature requiring significant energy consumption and operational challenges. The researcher community has therefore sought a more efficient and green techniques such as laser irradiation, commercial microwave oven and hydrothermal technique for producing RGO with high properties.

However, a complete exclusion of oxygen-carrying groups does not occur during the reduction from GO to RGO. Instead, oxygen groups are still present with considerably lower density, while, oxygen functional groups exist in GO. The RGO is dispersed in a solvent during the preparation of composites of RGO with a polymer; as a result, better dispersion is displayed through RGO in comparison to graphene, as the oxygen groups are still present on the surface of RGO. Consequently, the RGO has improved properties conduction and mechanical properties. Harsh conditions result in a ruptured structure during fabrication. The strength is lost because of the ruptured structure, and as a result, the mechanical and conductive properties deteriorate, likely not through these broken structure channels.

The occurrence of the exfoliated morphology of graphene sheets having the tremendous surface area, yield several advantages in the polymer nanocomposites include a higher glass transition temperature, stiffness, and strength because of the polymer chain confinement effects. The distribution of graphene layers in the polymeric matrix and the interfacial bonding present amongst the graphene layers and the polymeric matrix enhance the physicochemical properties. Compatibility between pristine graphene and organic polymers was not displayed; thus, no homogeneous composites were created. A hurdle arising that affected the potential use as a mechanical reinforcing agent was the agglomeration of graphene. In contrast, the partially-oxygenated graphene makes up the RGO that comprises several functional groups, such as epoxy, carboxylic, and the presence of debris that can significantly change the van der Waals interactions, thus providing the organic polymers with better compatibility. However, as mentioned, the properties are not improved mainly because of the ruptured  $sp^2$  structure.

Several routes of mechanical exfoliation have been planned to eradicate the issues while saving the original  $sp^2$  structure and improving the dispersion of RGO in the polymer matrix. This work studies the interfacial cohesion, types of nano-additives, size, and the nano-additive/EP matrix. The results show that the thermal reduction of GO with non-rupture of  $sp^2$  structure improves the dispersion, electrical conductivity and mechanical characteristics of the nanocomposites.

In this work, we studied novel methods of thermally reducing of GO to produce RGO material with a superior electronic structure and low-percolation threshold. Nonetheless, the thermal reduction of GO at low temperatures through the use of a vacuum oven or high temperatures through a tube furnace has never been reported. In the case of the tube furnace method, the reduction process at high temperature with the fast heating rate involves significant energy consumption and operational challenges. Thus, the method for preparing RGO from dry GO powder at a low-exfoliation temperature is more favourable. The vacuum oven technique

exhibits several adequate characteristics such as low energy-consumption and low pollution. Moreover, the reduction process at low temperature has higher exfoliation efficiency compared with that at high temperature. Although oxygen reduction efficiency for the reduction process at low temperature is comparatively lower than the same at higher temperature, the resulted RGO sheets are easily chemically active for either functionalisation or covalent bonding with the polymer matrix. We believe that our work will give researchers further insight into the utilization of epoxy/RGO for more advanced applications. Better dispersion and improved mechanical performance have been observed when GO was inculcated into the EP systems, however, Young's modulus and the glass transition temperatures ( $T_g$ ) often decreased. The mechanical properties and electrical conductivity of the epoxies improved when the size of the Graphene sheets ranged from 1 to 25  $\mu\text{m}$ , while not compromising the basic properties; however, poor dispersion that yielded processing difficulties and high cost was observed because of re-aggregation in the polymer matrix.

## **1.2 Aims and objectives of the thesis**

The primary aims of this thesis are to develop new techniques to obtain RGO sheets with uniform dispersion and exfoliation without agglomerations in the polymer matrix and compare the RGO sheets obtained by the tube furnace and vacuum method to determine if the  $\text{sp}^2$  structure has been improved. We also investigated the performance of nanocomposites after incorporating the resultant RGO of both techniques into the epoxy matrix at very low contents. Easy and rapid manufacturability is also a key requirement to minimising the manufacturing cost.

The main objectives of this thesis are summarised as follows:

- (i) To use modified Hummer's Approach for the synthesis of GO with the assistance of the freeze-drying technique.

- (ii) To synthesis RGO nanosheets by two new techniques, the tube furnace (reduction process of GO at high temperatures) and the vacuum oven (at low temperatures).
- (iii) To characterise the formation mechanism and properties of RGO.
- (iv) To use the synergistic effect on the dispersion by combining the high shear-mixing and sonication together to achieve better dispersion of RGO in diglycidyl ether bisphenol-A (DGEBA; Epon 828).
- (v) To study a polymer nanocomposite material through improving the dispersion process of fillers into the matrix to achieve high thermal and electrical conductivities and good mechanical properties simultaneously. The achieved results of EP/RGO nanocomposites of both techniques were then compared.
- (vi) To fabricate nano-hybrid composites by combining the RGO and metal oxide nanoparticles (NPs) together as filler systems, followed by a study of the effect of the combined composite fillers on the properties and structure of epoxy nanocomposites.

The potential applications emerging from the knowledge developed in this study on low-loading conductive composites with a uniform dispersion of RGOs in a matrix is beneficial to the manufacturing of electrostatic discharge (ESD) protection (e.g. printed circuit board carriers or chips for the shipping of electronic and other sensitive equipment) and can have a positive impact on the development of sensors, electromagnetic shielding materials and conductive electrodes.

This thesis is arranged into seven chapters and one appendix to present all the work performed during this PhD.

Chapter 2 presents a detailed literature review of the various polymer systems that could be used in this research. The literature focuses on epoxy resin. After discussing the polymer systems, the filler materials, e.g. graphene, are described in detail with all their positives and

negatives. The synthesis methods of graphene and its derivatives GO and RGO, and their potential applications are discussed. Lastly, the synthesis of nanocomposites is described with a particular emphasis on the dispersion of RGO in polymers and epoxies. The characterization methods are also discussed in detail.

In Chapter 3, the exfoliation and reduction of GO at low temperatures using the vacuum oven as a novel method is discussed and is compared with the RGO obtained by using the tube furnace. Three different degrees of reduction of RGO were investigated at temperatures of 120, 160 and 180°C for 24 h. This vacuum approach process can be considered a simple and efficient production method compared to the rapid heating and chemical approaches. Moreover, these temperatures for the reduction process of GO material have been determined based on the optimal time required to ensure the complete exfoliation of GO. This was done to obtain optimal conditions for the production of RGO sheets with the main aim of identifying the lowest possible temperature that could be utilised with GO material to produce RGO under vacuum. Cost effectiveness in relation to energy utilization is a major requirement in composite research; hence, an attempt was made to obtain optimal (lowest) conditions for RGO production. A full description of the experiment conditions, RGOs and GO morphology and distribution is reported.

Chapter 4 details the fabrication of epoxy nanocomposites cured with methyl nadic anhydride. Aspects such as the RGO percolation threshold, the effect of the RGOs on the matrix, the thermal and electrical conductivities and mechanical properties of the fully cured material are described in this chapter. This chapter reports the effect of high-dispersion RGOs on the microstructure, mechanical, electrical and thermal behaviour of EP nanocomposites with low variation of the RGO weight fraction. A dispersion method that deploys a high-ultrasonic mixer frequency of 120 kHz at a power of 240 W at 60°C and high shear mixer setting of 1600 rpm is used to disperse RGO nano-sheets in EP matrix, and this method results in RGO with a

homogeneous dispersion. The results show that the elastic modulus, tensile strength, thermal and electrical conductance were all simultaneously improved. The results also show that RGO nano-sheets have a significant influence on the epoxy–anhydride curing system, thereby increasing the glass transition temperature of the cured EP matrix.

Chapter 5 reports a novel and simple process for synthesising well-dispersed silica/reduced graphene oxide (RGO–SiO<sub>2</sub>) composites. The RGO–SiO<sub>2</sub> nano-hybrid was fabricated by a sol–gel process through a chemical reaction of the hydrolysis of TEOS with the existence of hydrophilic GO produced from Hummer’s approach, followed by the reduction of GO into RGO with the help of the vacuum oven method at 120°C. The synthesis and characterization of RGO–SiO<sub>2</sub> nano-hybrids is also reported. In this study, the RGO–SiO<sub>2</sub> nano-hybrid was incorporated with matrices with different mixing times by using the high-shear mixer technique. EP–nanocomposites were synthesised using organic solvent and then their mechanical, thermal and electrical properties at different loading concentrations were investigated. SiO<sub>2</sub> nanoparticles embedded ultrathin RGO to improve the dispersion in matrix, acting as a stabiliser against the aggregation of individual sheets of RGO.

Chapter 6 presents the general discussion of this research.

Chapter 7 presents the general conclusions and suggestions for continuation of this research.

## 2 Chapter 2: Literature Review

### 2.1 Introduction

Polymers are materials composed of large-sized molecules with high molar mass that consist of repeated structural subunits. These materials can be linear or branched in structure, i.e. thermoplastic polymers or cross-linked, i.e. thermosetting polymers. Thermoplastic polymers can be found in either an amorphous or semi-crystalline state and may be brittle or ductile materials. Thermoset polymers have an amorphous structure arising from the 3D network that is formed by crosslinking, and this structure inhibits the movement of polymer chains to crystallization or packing. Polymers offer a host of applications including electronic devices, structural adhesives and coatings. It has been shown in previous studies that the incorporation of micro-size fillers (e.g. glass fibre and talc) results in traditional microcomposites, which may show improved properties that are normally absent in pure polymers. In recent years, the incorporation of low-volume fractions of nano-size fillers has become the widely applied strategy for diversifying and improving polymer composites. Polymer-based nanocomposites are described as a new sort of multiphase material in which the nanoscale particles are uniformly dispersed within a polymeric matrix at low-filler loadings (Huang et al. 2007).

These polymer nanocomposites materials can provide enhancements in electrical, thermal and mechanical properties compared with the traditional composites or pure polymers. Depending on the nature and type of nano-filler used, the nanodomains can strongly restrict the polymer chains or improve the toughening efficiency of the polymer. Most changes observed in the properties of polymer nanocomposites with inorganic nanoparticles fillers are caused by the binding or mixing of two different phases. The inorganic phase contributes to the high-performance thermal and mechanical properties, whereas the organic phase provides the processing and adhesive properties (Ke 2005).



## **2.2 Polymer matrix**

Polymer molecules consist of a large number of similar repeating units, called a homopolymer, or different types of monomers, called a copolymer. These large molecules are typically linear, branched, or cross-linked in topology, and in a highly interconnected case, the structure develops into a large 3D network. Polymers, which are linear or branched but not cross-linked are generally also known as thermoplastic and can be reprocessed by exposure to heat or even by dissolution in a suitable solvent. A cross-linked polymer, also referred to as a thermosetting polymer, involves a three-dimensional network and, unlike thermoplastics, cannot be re-melted or reshaped without permanent degradation of the chemical bonds. There are both naturally occurring (i.e. silk, cellulose, DNA and proteins) and synthetic polymers such as nylon, polyethylene and epoxy.

These matrices have attracted significant attention from the graphene research community because of their potential applications. The purview of the current study is on thermosetting polymers because of their excellent electrical and mechanical properties and the potential for employing them in an extensive range of industrial applications. When choosing a host material for particular applications, the polymer materials first need to have modest mechanical performance (the tensile strength  $> 40$  MPa and Young's modulus  $> 2$  GPa) when compared with that of matrices made from metal or ceramics. For the previously mentioned reasons, the matrices are filled with different types of reinforcing fillers to improve both the mechanical performance and other thermal and electrical properties (Hu et al. 2014).

### **2.2.1 Thermoplastic polymers**

The types of polymers that are established from linear and branched chains can be repeatedly reheated and also recycled via specific processing techniques, for instance extrusion and injection moulding. Depending on the applied strain rate and temperature, thermoplastic polymers can possess high mechanical properties (Hull & Clyne 1996) and can be very resistant

to chemical substances (Biron 2007). Thermoplastic materials are classified into semi-crystalline and amorphous polymers. These polymers are characterised by their transformation from the glassy state to the rubbery state. Examples of semi-crystalline polymers are linear polyethylene (PE), polyethylene terephthalate (PET) and isotactic polypropylene (PP). Whereas, amorphous thermoplastics comprise a large group of materials, including glassy, brittle polymers (such as polystyrene (PS), poly(methyl methacrylate) (PMMA) and styrene acrylonitrile resin (SAN)) and ductile polymers (such as poly (vinyl chloride) (PVC) and polycarbonate (PC)) (Moore 1963; Gay 2014).

## **2.2.2 Thermosetting polymers**

The thermosetting plastics are produced by crosslinking a resin with a curing agent as an organic reactive intermediate material. This reaction can occur at room temperature but is often performed at elevated temperature and leads to the formation of a 3D-network with a high molecular weight through an irreversible chemical reaction, which is referred to as polymerization or cure. Examples of these types of materials include unsaturated polyesters, phenolic and epoxy polymers (Young & Lovell 1990; Gay 2014). Thermosetting polymers are typically amorphous because of the three-dimensional network that restricts the motion of polymer chains and inhibits crystallization.

## **2.3 Epoxy resin systems**

### **2.3.1 Epoxy resins and their curing agents**

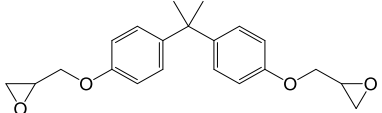
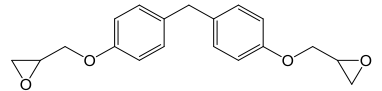
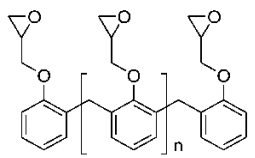
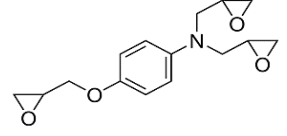
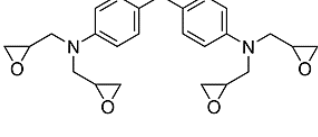
In 1936, Castan and Greenlee discovered the first epoxy resin resulting from the direct reaction of epichlorohydrin which is a highly reactive electrophilic compound with a 2,2-Bis(4-hydroxyphenyl) propane known as bisphenol A. Epoxy resin oligomers are thermosetting polymers in which one molecule contains two or more epoxide groups. Epoxies are one of the most adaptable high-performance materials and have been utilized in different applications

because of their high mechanical performance, thermal stability and ease of processing. The applications of epoxy and its nanocomposites include surface coatings, structural adhesives, electrical and electronic systems (e.g. in sensors) and engineering composites (Ellis 1993).

Among polymer-based nanocomposites, the diglycidyl ether of bisphenol A (DGEBA) is the epoxy resin commonly used by most researchers. When cured, this epoxy resin forms a highly cross-linked 3D structures. This is ideal for chemical resistance, thermal and mechanical properties which most widely used in electronic products and composite applications (Tschoppe et al. 2014). However, this epoxy, like most thermosetting polymers, have some limiting factors, which include inherent brittleness, low fracture toughness and high electrical resistivity, limiting the widespread use of the epoxy (EP) in various high-performance applications. In addition, a number of researchers (Garg & Mai 1988; Chang & Brittain 1982) have concluded that high cross-link density will decrease the fracture toughness of pristine epoxies due to internal stresses induced during curing of the EP, where resistance to crack initiation is very low and the void growth because of the plastic deformation is constrained. To solve this issue, several researchers have used nano-sized organic and inorganic particles such as carbon nanofibres (CNFs), carbon nanotubes (CNTs) and nanoparticles of metal oxides as fillers to reinforce the EP matrix and to make advanced polymer composites with improved properties (Al-Saleh & Sundararaj 2009; Kim et al. 2008). However, the incorporation of inorganic nanomaterials in the EP matrix increases its viscosity, causes poor dispersion of the nano-filler and makes processing difficult (Qi et al. 2014).

Table 2-1 lists the chemical structures of most frequently used epoxy resins with various epoxide functional groups. For high-performance applications (i.e. aerospace and defence), tri- and tetra-functional EP matrix composites can attain the required properties, but the bi-functional EP is preferred in most civil applications.

**Table 2-1. Structures of commonly used epoxy resins**

Epoxy resins	Functionality eq./ mol	Structures
Diglycidyl ether of bisphenol A (DGEBA)	2	
Diglycidyl ether of bisphenol F (DGEBF)	2	
Epoxy novolac	3	
Triglycidyl <i>para</i> -amino phenol (TGPAP)	3	
Tetraglycidyl-4,4'-diaminodiphenylmethane (TGDDM)	4	

Epoxy resins can be cured with a range of curing agents (hardeners) to form highly cross-linked 3-D network structures. Based on the chemical formulation of the curing agent, epoxy resins can be cured at temperatures ranging from 25° to 180°C. These crosslinking agents (i.e. amines and anhydrides) can either act as a catalyst to move the curing reaction or join the curing reaction, which then becomes part of the cross-linked network structure. Thus, a  $T_g$  of a cured epoxy system can depend on the chemistry of the epoxy resins, hardeners and curing temperatures.

**Table 2-2.** Structures and properties of commonly used curing agents for epoxy resin (Mazumdar 2002).

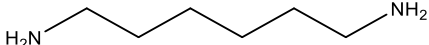
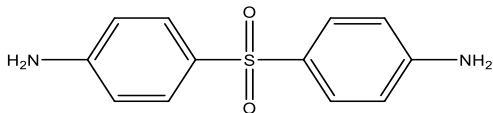
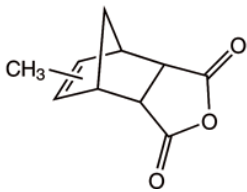
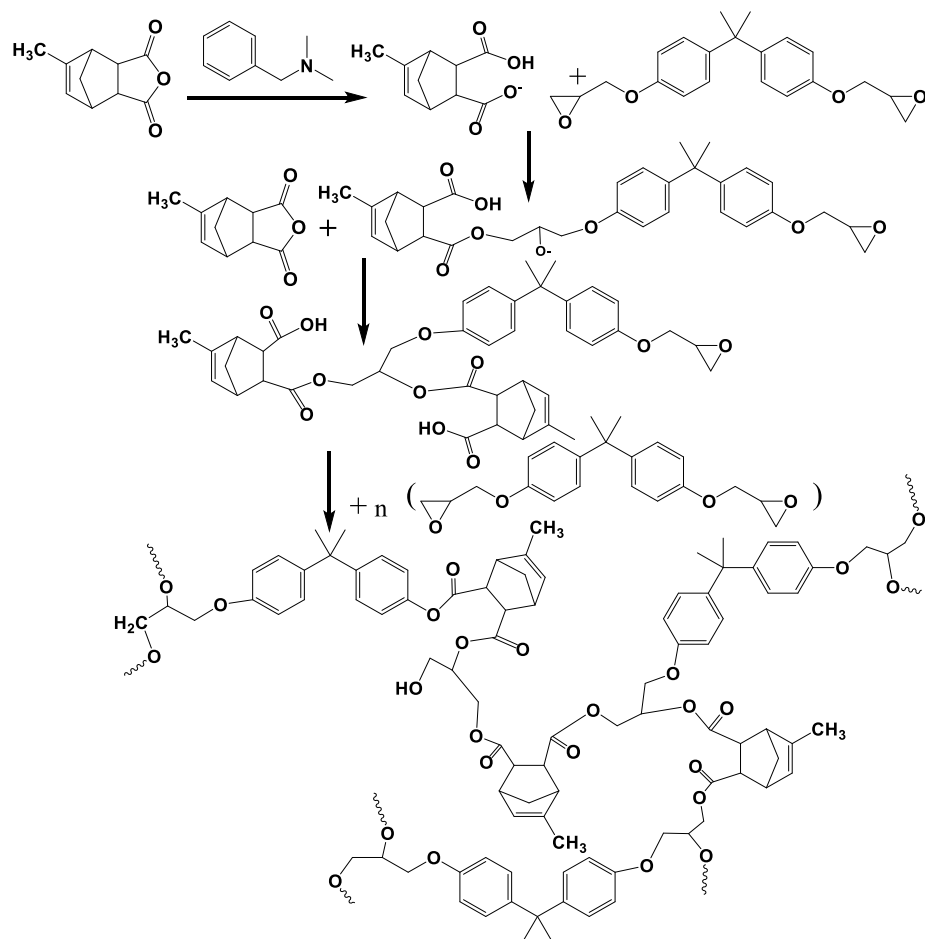
Curing agent	Representative Product	Properties
Aliphatic amine	<p style="text-align: center;">1,6-Hexanediamine</p> 	<p>Curing occurs at room temperature but frequently requires a slightly elevated temperature. It has excellent bonding properties and is very reactive. It can be resistant to some inorganic acids, water and solvents, but it has poor resistance to many organic solvents.</p>
Aromatic amine	<p style="text-align: center;">4,4'-DDS</p> 	<p>Curing requires high temperatures. It has excellent chemical resistance and better mechanical properties than the Aliphatic amine. It also shows an excellent heat resistance at 160°C. It is widely used in high-temperature adhesives and notably in curing matrix resins.</p>
Anhydrides	<p style="text-align: center;">Methyl-5-norbornene-2,3dicarboxylic anhydride (MNA)</p> 	<p>Requires stricter curing conditions than amine curing agents. Form cured systems have comparatively good chemical, mechanical and electrical properties, whilst a small amount of heat is emitted during the curing process. This curing agent has a long pot-life.</p>

Table 2-2 lists the most frequently used curing agents, their chemical formulation and some typical properties. The mechanical properties of cured epoxy resins depend on the chemical structure of the curing agent (Grillet et al. 1991). In comparison with aliphatic amine cured systems, the pot life of epoxy resins cured by anhydride (such as the MNA used in this study) is often long and the exothermic reaction is low. In comparison with epoxy cured aromatic amines, resins cured by anhydride offer the best chemical resistance to aqueous acids, but these resins have poorer chemical resistance to some other reagents. However, most epoxy systems cured by anhydride exhibit less reactivity and require relatively high reaction temperature (>

120°C) to initiate and propagate the curing reaction.

Fig. 2-1 shows the curing mechanism of bisphenol-A-diglycidyl ether with a hardener methyl nadic anhydride (anhydride, MNA) with the existence of a catalyst, resulting in cross-linked molecular chains. This mechanism involves the following two main steps:

The initiation step includes the anhydride ring opening with a catalyst which must contain a pair of electrons in order to give the anion form. This in turn attacks the oxirane ring resulting in the monoester form. With this step, the chain propagation reaction occurs through the formed compound that contains cyclic ether at its terminal end. This terminal end is then attacked by another anhydride anion forming the diester form. The diester compound has a negative charge on the carboxylic group on the terminal end of the structure. This negative charge in turn attacks a number (n) of the repeat units of the bisphenol-A, transforming the chain into a cross-linked structure (Gu et al. 2015).



**Figure 2-1.** The curing process of the anhydride–epoxy system with an accelerator, adopted from Gu et al. 2015.

### 2.3.2 Properties of epoxy

The most important considerations to take into account when selecting a composite process are the resultant mechanical, electrical, thermal and physical properties of the material. Epoxy resin is the most important organic matrix for many applications, particularly in the composite industry because of its high tensile strength, high modulus, high adhesion and dimensional stability, low shrinkage, good chemical and corrosion resistance (Zhang et al. 2015) (see Table 2-3). Moreover, it has resistance against moisture, solvents and chemical attacks. However, it is relatively more brittle than polyester and has poor resistance to wear and crack propagation (Boyle et al. 2001; Brent 2008).

**Table 2-3.** Some properties of epoxy based composite materials, using anhydride as a curing agent (Hull & Clyne 1996).

Property	Units	Epoxy
Elastic modulus	GN m <sup>-2</sup>	3–6
UTS	MN m <sup>-2</sup>	35–100
Elongation at break	%	1–6
Curing shrinkage	%	1–2
Thermal conductivity	W m <sup>-1</sup> K <sup>-1</sup>	0.1
Epoxy density	Mg m <sup>-3</sup>	1.1–1.4

## 2.4 Reinforcing agents

Reinforcing solid materials are often used as part of composite polymers and act to modify the mechanical and physical properties of the end product and also reduce the costs of the composites (Rehab & Salahuddin 2005). Some of the specific properties that can be improved by adding the reinforcing agents to the matrix include dimensional stability, heat resistance, hardness, tensile strength, stiffness and electrical conductivity (in cases where the insulating properties of the polymer matrix are not desired).

### 2.4.1 Fillers

Inorganic fillers, with dimensions in the micrometre range, usually extend from 0.5 to 50 µm. For example, glass fibres, silica and carbon black, have been applied extensively to improve the mechanical behaviours of polymers (Móczó & Pukánszky 2008). Typically, the content of the reinforcing agent in a conventional composite is in the range of 20 to 30 wt. % of micro-sized fillers, limiting the interfacial interaction between these particles and the host polymer matrix (Bhattacharya 2016).



## 2.4.2 Nanofillers

A nanocomposite is a multiple-phase component formed from solid material in which at least one of the components have 1D, 2D or 3D shapes of less than  $< 100$  nanometre (nm) (Ajayan et al. 2003). Nano-fillers can be classified according to the dimensions described by Bhattacharya (2016). Geim and Novoselov (2007) have highlighted the types of nano-fillers derived from a 2D of graphene structure, as shown in Fig. 2-2:

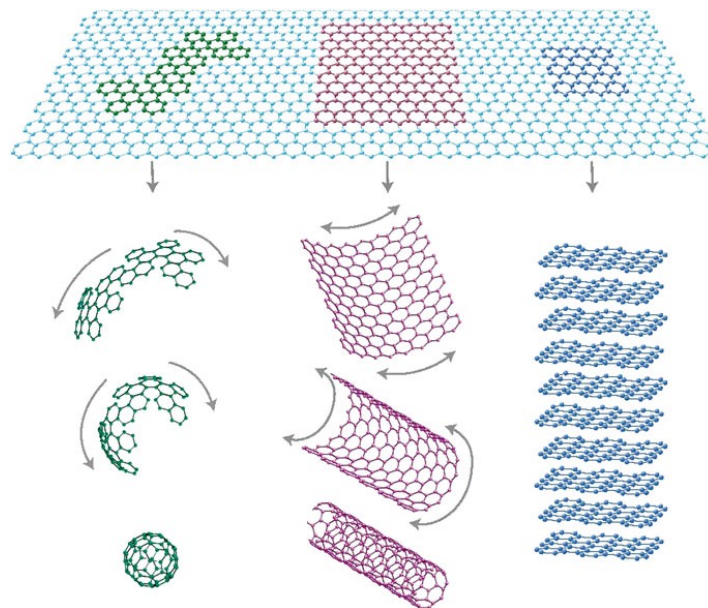


**Figure 2-2.** The 2D structure of carbon materials is called graphene; 0D fullerene (on the left end); 1D nanotubes (CNTs) (on the middle) and 3D graphite (on the right end). Adopted from Geim and Novoselov (2007).

One-dimensional nano-fillers include nanotubes (CNTs) and nanowires with a diameter smaller than  $0.1 \mu\text{m}$ . Two-dimensional nano-fillers are found in the form of nanoplates such as pristine graphene and nanoclay, and three-dimensional nano-fillers comprise cubical or spherical nanoparticles such as graphite and nanometric silica beads. Improvements in the nanocomposites performance are highly affected by the following characteristics of the nano-fillers (Bhattacharya 2016). These include:

- High mechanical properties such as ultimate tensile strength and elastic tensile modulus

- A high specific surface area to achieve a successful interaction with the polymer matrix
- A uniform distribution within the matrix and avoid agglomeration

Typically, the content of a nano-filler in the polymer matrix is lower than 10 wt. %, which may be ascribed by their large aspect ratio (A.R) (Lepoittevin et al. 2003) exhibited by the nano-reinforcing agent.

Cho et al. (2006) studied the extent of the effect of particle size on the performance of polymeric composites for micro and nanospherical alumina particles. They observed that the nanocomposites showed a large increase in the elastic modulus ( $E_Y$ ) for decreasing particle sizes at the nanoscale, whereas, the  $E_Y$  in a conventional composite was not significantly influenced when the particles had a diameter of 1  $\mu\text{m}$  or larger. The ultimate tensile strength (UTS) for the conventional composites improved for decreasing particles size of the order of a  $\mu\text{m}$  size. However, composites having 3.0 vol. % of nanoparticles showed lower tensile strength compared with microparticles. This reduction is associated with the likelihood of randomly dispersed nanoparticles for higher filler loading.

## 2.5 Graphene

### 2.5.1 The Discovery of Graphene

Carbon (from Latin; carbo ‘coal’) is a non-metallic chemical element that has an atomic number of 6. It is tetravalent-making with four electrons available to form covalent chemical bonds. Carbon is capable of forming many allotropes due to its valency. Well-Known forms of carbon include diamond and graphite. In recent decades many more allotropes and forms of carbon have been discovered and researched including sheets such as graphene and ball shapes such as Buckminsterfullerene (Buckyballs) which was discovered in 1985 with the formula C<sub>60</sub>. It is composed of 60 carbon atoms that link together to form a hollow ball. This molecule is highly stable, being able to withstand high pressures and temperatures. Further discoveries of other fullerenes from C<sub>20</sub> to C<sub>80</sub> followed in the ensuing years. In 1991, another breakthrough by Sumio Iijima led to the discovery of carbon nanotubes (Bhattacharya 2016).

The original name of graphite, which is an allotrope of carbon, can be traced to the Greek word “graphein”. It is identified by its lamellar (layered) construction of many monolayers of carbon that are associated with each other by weak van der Waals forces. The distance between planes in the graphite structure is 0.335 nm, and the separation between carbon atoms is 0.142 nm in the lattice (Wallace 1947). It was realised in the early 1940s that such monolayers, if isolated, can be utilised with unique mechanical and electrical features (Wallace 1947).

This monolayer which is composed of sp<sup>2</sup> hybridized carbon atoms is called “graphene” when isolated from graphite. This name was coined by Boehm in the mid-1980s (Boehm et al. 1994). However, graphene-like-materials were obtained from graphite oxide through chemical techniques in the 1960s (Boehm et al. 1962). Despite the fact that the exfoliation of graphene has been known for many decades, it was A. Geim and Novoselov who isolated a graphene monolayer at room temperature in 2004 (Novoselov et al. 2004).

## 2.5.2 Properties of Graphene

Graphene is composed of monolayer sheets of  $sp^2$  hybridized carbon atoms arranged in a 2D hexagonal lattice structure. This graphene sheet is a zero-band-gap material where the conduction and valence bands, known technically as  $\pi$  and  $\pi^*$  bands, touch each other at a point called the Dirac point. Therefore, the charge carriers in graphene have a very small effective mass. As a result, the carrier mobility can reach  $200,000 \text{ cm}^2 \text{ V}^{-1} \text{ s}^{-1}$  at a carrier density of  $10^{12} \text{ cm}^{-2}$  (Chen et al. 2008; Kumar et al. 2013). It has been reported that electrons can travel through graphene sheets more easily than even through copper (Lemme 2010; Tse et al. 2011).

The mechanical properties of a graphene sheet have been investigated with numerical simulations (theoretically) and in experimental measurements using atomic force microscopy (AFM) (Van Lier et al. 2000). Olevsky et al. (2013) states that “Graphene is found to be one of the strongest natural materials with a mechanical strength higher than diamond and over 300 times greater than a steel film of the same thickness”. It was reported that defect-free graphene has a Young’s modulus of 1.02 TPa and a fracture strength of 130 GPa in the zig-zag direction, as measured by nanoindentation using an AFM, exceeding the corresponding values of carbon nanotubes (CNTs) (Van Lier et al. 2000; Galusek & Galusková 2015).

In addition to its high strength, graphene is flexible and can stretch up to 20% (elastically) of its initial length (Chen, J et al. 2013). Apart from those outstanding properties, graphene has a thermal conductance ( $>5000 \text{ W m}^{-1} \text{ K}^{-1}$ ) (Chen, J et al. 2013) that is higher than all the other carbon structures. Graphene also has a theoretical surface area of  $2600 \text{ m}^2 \text{ g}^{-1}$ . Despite being the thinnest material, it can absorb as much as 2.3% of light that passes through it because of its unique electronic band structure (Kumar et al. 2013).

### **2.5.3 Potential Applications of Graphene**

The high thermal conductivity of graphene offers potential for the development of thermal interface materials (TIMs). This potential is due to a more efficient heat dissipation that keeps the electronic devices cool by more efficiently dissipating the heat generated by current flow. Moreover, because of the significant carrier mobility, (~ 40 times higher than the typical electron mobility for Si) and its high current carrying capability, graphene is a very attractive candidate for electronic devices applications. However, one of the challenges to exploiting these applications is finding manufacturing methods for the volume production of graphene-based devices (Chung 2012; Li et al. 2016).

## **2.6 Synthesis of graphene**

Since the discovery of graphene, scientists have been trying to find effective and efficient ways for producing highly pure graphene at larger scales for commercial use and at low cost (Chandrasekaran 2014). The two main approaches for synthesizing graphene are known as top down and bottom up, and these approaches are described in the next sections.

## **2.6.1 Bottom-up approach**

This approach consists of growth of graphene sheets using small organic molecules (i.e. hydrocarbon gas precursors) on a substrate. Examples of the bottom-up approach are chemical vapour deposition (CVD) (Lee et al. 2017) and epitaxial growth on SiC (Hass et al. 2008), and they are described separately below and summarised in Table 2-4.

### **2.6.1.1 Epitaxial Growth from SiC**

This technique involves thermal desorption of silicon from silicon carbide at low pressures (approximately 0.133 mPa) and high temperatures ( $>1250^{\circ}\text{C}$ ) and results in a formation of carbon-rich layers on the surface that is subsequently graphitized as carbon islands. Therefore, this technique has been recently optimized to provide a single-layer of graphene (Hass et al. 2008). This process is expensive because of the necessity for high processing temperatures and the high cost of the silicon carbide SiC substrate, but it is more scalable and controllable than the exfoliation technique. Moreover, compared with the exfoliation technique, the epitaxial method tends to form more fragile and defective graphene because of the large lattice mismatch between SiC and graphene that occurs.

### **2.6.1.2 Chemical vapour deposition CVD**

Transition metal catalysts (copper or nickel) are used in the CVD process with the assistance of hydrocarbon gas precursors such as  $\text{CH}_4$  (reaction at  $1000^{\circ}\text{C}$ ) (Lee et al. 2017), which is the most common carbon gas source used for synthesizing graphene layers. For instance, (Li et al. 2010) reported that the fastest CVD graphene synthesis process uses  $\text{CH}_4$  as the carbon source, in which they successfully achieved continuous single-layer graphene films in 2.0 min at a reaction temperature of  $1035^{\circ}\text{C}$ . Other gases have also been used; for example, Chen et al (2012) successfully showed the synthesis of high quality and excellent-crystallinity single-layer graphene sheets using  $\text{CH}_4$  gas.

A low quantity of large-sized, defect-free graphene sheets has been obtained using epitaxial and CVD growth. However, the limited quantity of graphene sheets is not adequate for the preparation of polymer nanocomposites require a high content of nano-fillers that can be easily dispersed within the polymer matrix.

## **2.6.2 Top-down approach**

This production begins with the use of graphite derivatives and finishes with graphene. The techniques utilised in the top-down approach are typically by exfoliation that separates the individual layers of graphite in order to obtain graphene, as illustrated in Table 2-4.

### **2.6.2.1 Mechanical Exfoliation for Graphene**

Mechanical exfoliation of graphite was the first method used to isolated monolayer graphene. In this case, a longitudinal or transverse force is generated on the surface of a layered material by means of any mechanical energy (Chandrasekaran 2014).

The external force that is needed to mechanically cleave a monolayer is  $\sim 300 \text{ nN l}^{-1} \text{ m}^{-2}$  (Zhang et al. 2004). Novoselov and Geim succeeded in producing a monolayer of graphene by using mechanical cleaving of 1 mm thick highly ordered pyrolytic graphite (HOPG) in 2004 (Novoselov et al. 2004). HOPG which is stuck onto the adhesive tape is repeatedly peeled several times, and the last transfer is done on a Si wafer which is cleaned with solvents (e.g. ethanol). As soon as the scotch tape with a few graphene layers is stuck to the Si wafer, then the adhesive tape is gently peeled in order to obtain a good cleavage. The final peeling is performed with fresh scotch tape and a rapid peel. The silicon wafer involves graphene flakes composed of single-layer to few-layer graphene and is washed again with solvents (Chandrasekaran 2014). Because of the few defects in the graphene obtained from mechanical exfoliation, it has potential use in the fabrication of electronic devices. However, such use is currently only conducted in the laboratory because several other issues need to be addressed

such as the low production yield and intensive labour requirements.

### **2.6.2.2 Synthesis of graphene oxide (GO)**

The synthesis of graphene oxide from graphene flakes by using a strong chemical oxidising agent was developed 150 years ago (Hayes et al. 2014). A technique called Hummer's method is a reliable chemical process of producing quantities of graphene oxide that is susceptible to the incorporation of aqueous solutions (Buchsteiner et al. 2006). This process leads to the expansion of the carbon lattice layers and a change in the hybridization state because of the formation of OCFGs (i.e., hydroxyl, carboxyl and carbonyl groups) between the layers of graphene during the exfoliation process. The carbon atoms attached to an epoxy or a hydroxyl group are the main sites of defective  $sp^3$  carbon atoms formed after the oxidation process (Schniepp et al. 2006), indicating an interruption of the carbon lattice from a planar  $sp^2$  to a distorted  $sp^3$  hybridized structure (Szabó et al. 2006). The sheets which are attached to the functional groups are called GO sheets. GO can be characterized as an electronic hybrid material composed of a large band gap between sigma ( $\sigma$ ) states of  $sp^3$ -hybridized carbon atoms with conducting  $\pi$ -states from  $sp^2$ -bonded carbons. Because of the attached functional groups, GO sheets are electrically insulating. Hence, the thermal and chemical approaches are required for reduction process in order to obtain graphene (Szabó et al. 2006). The reduction process has been employed to change the carbon hybridised from  $sp^3$  to  $sp^2$ , which is considered an effective path for adjusting the carrier transport gap and thereby converting GO sheets from being non-conductive material with a sheet resistance ( $R_s$ ) value of  $\sim 1012 \Omega \cdot m$  to a graphene-like semimetal. Thus, controlling the reduction process is an effective way of adjusting the band gap (Eda et al. 2009).



**Table 2-4.** A list of different approaches for producing graphene and the resultant characteristics.

Approach	The precursor	Layer stacking	layers size	Electronic properties	Throughput/Cost
<b>CVD growth</b>	Hydrocarbons	mono- to multi	$\geq 50 \mu\text{m}$	high-quality	Low/High
<b>Mechanical exfoliating</b>	Raw graphite	mono- to multi	$10 \mu\text{m}$	high-quality	Low/Low
<b>Reduction of GO material</b>	Raw graphite	Monolayer	Tens of nm- $100 \mu\text{m}$	low-quality	High/Low
<b>“Unzipping” of CNTs</b>	CNTs	mono- to multi	a few $\mu\text{m}$	inferior-quality	Low/Low
<b>SiC epitaxial growth</b>	SiC- wafer	mono- to multi	$\geq 50 \mu\text{m}$	high-quality	Low/High

*Modified with permission from Guo & Dong 2011.*

## 2.7 GO reduction methods

The major processes used for reducing GO involve chemical or thermal treatment, and these are described separately in the following sections.

### 2.7.1 Chemical reduction

Chemical processing provides a low-cost and scalable technique to yield bulk quantities of RGO. However, this approach does not enable the level of GO reduction to be readily adjusted because the physical properties of CRGO material are dependent on reaction conditions. For example, it is known that the C/O ratio and electrical conductivity of RGO vary based on the chemical identity of the reductants (such as hydrazine) (Stankovich et al. 2007). To date, many reducing agents, such as sodium hydride (Mohanty et al. 2010), vitamin C (Ding et al. 2015), hydrazine (Gao et al. 2010),  $\text{NaBH}_4$  (Chua & Pumera 2012) and dimethylhydrazine (Stankovich et al. 2006) have been used to reduce GO in order to produce RGO sheets in the solution phase. For instance, Park et al (2011) prepared chemical RGO sheets by add GO powder to a flask containing purified water (3mg/ml). Immediately after addition, hydrazine

monohydrate (1  $\mu$ l for 3 mg of GO) was added to the mixture and the flask was immersed into an oil bath at 80°C. After additional stirring for 12 h, the resulting black powder was filtered and dried under house-vacuum for 12 h. The reduction of GO by using pure hydrazine in the solution phase is especially interesting because it can yield RGO sheets with high quality (C/O ratio of  $\sim$ 10). Hydrazine is a strong antioxidant which effectively scrubs the many oxygen functional groups that exist at the surface of carbon lattices (Malucelli 2017). However, this approach often comprises highly toxic chemicals and requires a long time for reduction, which results in a high removal cost during the industrial delivery of RGO sheets (Park et al. 2011). A number of effective methods have been explored to yield RGO or even pristine graphene through GO exfoliation and later chemical reduction in solution (Park et al. 2011; Zhang et al. 2011), however the issues concerning the solvents used should be considered. The solvents include reducing agents such as sodium borohydride or hydrazine, which are dangerously unstable and toxic. Thus, this method often involves highly toxic chemicals, and it also requires high-temperature treatment, or requires long reduction time, and produces RGO materials with a relatively high oxygen content that produces high sheet resistance (Rommoz et al. 2018), Furthermore, because the final resultant of material should be free from residual solvents, it is desirable to find a green route for the reduction of graphene.

### **2.7.2 Thermal reduction**

The thermal reduction process of GO sheets has been applied through using high-temperature treatment (Zhang et al. 2011) that changes the surrounding condition of GO material (i.e., argon, hydrogen, nitrogen, ultra-high vacuum) to produce RGO sheets. The degree of GO reduction is determined by the changes of the heating temperature and the duration of the processing (McAllister et al. 2007; Zhang et al. 2011; Malucelli 2017).

The steps of exfoliating GO begin by a thermal shock procedure of the sample, and the effectiveness of this procedure is based on the decomposition rate of the OCFGs. As reported

by (McAllister et al. 2007), a rapid heating rate ( $>2000^{\circ}\text{C min}^{-1}$ ) and high ultimate temperature ( $1050^{\circ}\text{C}$ ) are required to secure the perfect exfoliation of GO. When the decomposition rate of the hydroxyl  $[-\text{OH}]$  and epoxy  $[\text{C}-\text{O}-\text{C}]$  site override the rate of diffusion of the evolved gases ( $\text{CO}$ ,  $\text{CO}_2$ ) released from the reduction process, they cause a build-up of pressure between the carbon lattice layers. This pressure becomes large enough to overcome the van der Waals forces (2.5 MPa, theoretically) binding the RGO sheets together. Exfoliation then occurs, which provides about 80% of the RGO sheets consisting of single layers with a thickness between 1.0 to 3.0 nm and an average size between 0.3 and 2.0 microns (McAllister et al. 2007). The exfoliation process is accompanied by thermal expansion of 100–300 times the volume to produce very low-bulk density RGO nano-sheets, but these are highly wrinkled because of the loss of  $\text{CO}_2$ . Huh (2011) has placed graphite oxide powder into a quartz tube and inserted it into a horizontal tube furnace under a flow of laminar  $\text{N}_2$  gas, and thermal treatment was applied from 24 to  $2000^{\circ}\text{C}$  for an hour.

The RGO sheets were found to be electrically conducting, meaning they were not GO, which is an insulator. The main drawback for employing this method is the massive energy consumption required to attain elevated temperatures as well as the operational difficulties which make the GO reduction process unattractive for an industrial environment.

The hydrothermal de-oxygenation process is another technique in which the thermal reduction of GO is performed at elevated pressure inside a closed vessel such as an autoclave. This method has several advantages over the chemical reduction method such as simplicity, and the high temperature and pressure promotes the recovery of  $\pi$ -conjugation after dehydration, which is convenient for minimizing defects and controlling the degree of reduction of the GO (Ghorbani et al. 2015). However, high temperature and the pH value of a GO suspension impacts the structure and behaviour of the ultimate RGO obtained (McAllister et al. 2007; Hayes et al. 2014). However, it must be noted that thermal and chemical reduction do not completely reduce

the GO or remove the lattice defects (Chandrasekaran 2014).

## 2.8 Comparison properties of GO and RGO

GO is a promising candidate material that may be used in different polymer matrices for improving the physical and mechanical properties of the resultant nanocomposites. The large A.R of GO and its derivatives with the high dispersion in host polymer matrices represents an important step in improving the final properties of composites compared to the other carbonous nano-fillers such as CNTs. However, the largest increase in the properties is achieved with a uniform dispersion of a nano-filler in the host polymer matrices.

*Table 2-5 . Typical properties of mono-layer GO and RGO*

Properties	GO	RGO
Elastic modulus/ $E_Y$	0.22 TPa	N/A
Tensile strength/ UTS	120 MPa	N/A
Optical transparency	N/A (Because of defects in the functional groups and, the value is expected to be lower)	between 60 and 90%, rely on the reduction agent and the production process
Carrier density	N/A (due to defects in the functional groups and the value is expected to be lower)	N/A
Electron mobility at room temperature	N/A (because of the disruption in mobility and the value is anticipated to be lower)	N/A (expected to be an intermediate value owing to fewer defects)
Electrical conductivity	$1 \times 10^{-1} \text{ S m}^{-1}$	200 to $2.98 \times 10^4 \text{ S m}^{-1}$
Thermal conductivity	$0.5-1 \text{ Wm}^{-1}\text{K}^{-1}$	$3-61 \text{ Wm}^{-1}\text{K}^{-1}$

*Reproduced with authorization from Elsevier Publishers Ref. Mittal et al. 2015 & Renteria et al. 2015.*

## 2.9 The structure of GO and RGO

The structural models for GO material have been suggested in many previous studies (Szabó et al. 2006) and are composed of an orderly lattice consisting of separated repeat units because the structure of GO material is a partially amorphous character, although previous studies have

not determined or clarified the case. The nonstoichiometric structure reported by Lerf and Klinowski is the generally accepted model of GO (Fig. 2-3a). It describes the main structure of GO as being decorated by OCFGs with hydroxyl ( $-OH$ ) and epoxy groups on the carbon basal plane, whereas the carboxylic acids ( $-COOH$ ) groups are found at the edges of the GO sheet (Lerf et al. 1998).

By using the AFM technique, both esters and tertiary alcohols were revealed on the GO structure. Moreover, AFM can be utilised to determine the thickness and the number of layers of GO. It has been reported (Eda & Chhowalla 2010) that the thickness of a single layer of a GO sheet is around 1.0–1.4 nm, which is thicker than a single-layered graphene sheet. This extra thickness has been attributed to the presence of OCFGs in the plane and edges of the GO sheet and the presence of  $H_2O$ -confined molecules because of the hydrophilic nature of the GO material (Eda & Chhowalla 2010).

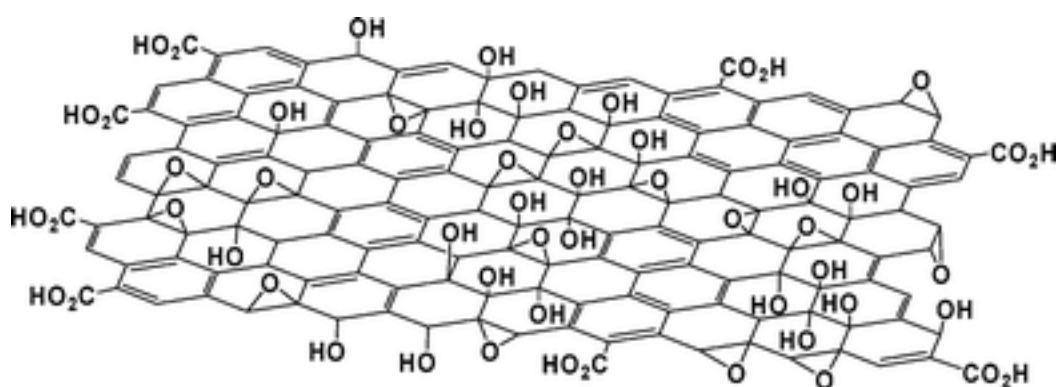


**Figure 2-3(a).** *The nonstoichiometric structural model of GO Lerf et al. 1998.*

Mkhoyan et al. (2009) combined the annular dark field (ADF) technique with SEM microscopy to explore the existence of oxygen atoms distributed on the GO structure. An analysis of the surface showed that the average roughness of the GO is about 0.6 nm and that its in-plane distortions from  $sp^3$  hybridized bonds led to the amorphous structure.

RGO not quite resemble either GO or graphene but is something in between these materials. It is moderately hydrophobic but can be dispersed in water to some extent, as well as in several organic solvents. It is a rather good electrical conductor but not as good as graphene. Its mechanical properties are closer to GO than pristine graphene. RGO is not as easy to use as GO but it is significantly easier to produce than pristine graphene by reduction from graphite oxide or GO, which can be achieved with a multitude of methods. Moreover, RGO has generally bears few OCFGs residual in the structure, declaring it hardly soluble in polar solvents as evident in fig. 2-3(b). Absence of repulsion notably between the RGO pieces further enhances their aggregation. Amidst the reduction reaction, the aromatic structure undergoes partial restoration as RGO outstands to recover electrical conductivity. Several determinants dominating the preparation process' phases influence the formed RGO's characteristics. Invariably, the source, quality, and size of the graphite as well as oxidation process deployed are key factors in the determination of GO's properties and hence identically affect the resultant RGO. Different reductants - like hydrazine can reduce GO even though the reduction can be achieved by using several nonchemical approaches, inclusive of plasma treatment and intense UV radiation. The variations accruing to RGO, which typically are very minute, may, however, bear a profound affection dependent upon the planned utilization of the RGO. For instance, the residual impurities following the reduction process may encompass a few atoms of nitrogen or substantial contamination of heavy metal. According to Edwards & Coleman (2013), the reduction may as well get rid of certain unique functional groups.

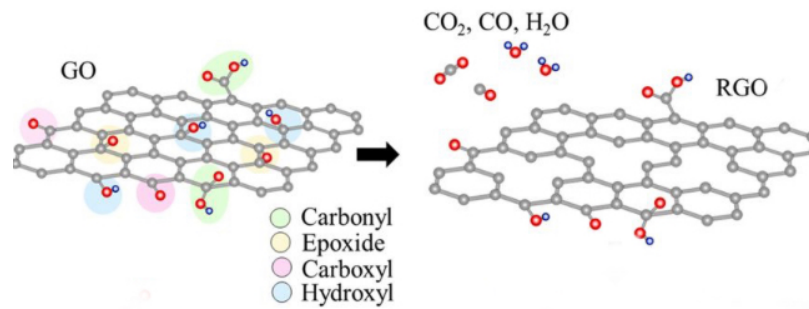


**Figure 2-3(b).** Schematic illustration of GO reduction (Huang et al. 2018).

Furthermore, the simplest reduction approach for GO entails thermal annealing since dry GO outstands to be thermally unstable notably at a temperature range of 150-200oC compared to graphene’s honeycomb structure. Additionally, Gomez-Navarro et al. (2010) depicted high-resolution imaging regarding single layers, hence offered insight about the atomic structure accruing to the RGO layers as illustrated in fig. 2-4 (a, b).

Nonetheless, various sections of the image have color markings (fig. 2-4b). There is evidence that the largest region of the layers consists of clean well-crystallized graphene sections wherein there is vivid observation of the hexagonal lattice (the light gray color connoted in fig. 2-4(b)). Moreover, they further noted a substantial amount of areas for carbonaceous adsorption prevails and trapped heavier atoms (as portrayed by the dark gray color in fig. 2-4 (b)). The mean magnitude of the observable super-crystallized regions dominates the range 3-6 nm yet statistics connote that they occupy nearly 60% of the underlying surface. Formation of larger holes was noted under electron irradiation, hence the high density accruing to the present images’ topological defects can be vividly linked to exfoliation of RGO by reduction and oxidation processes.

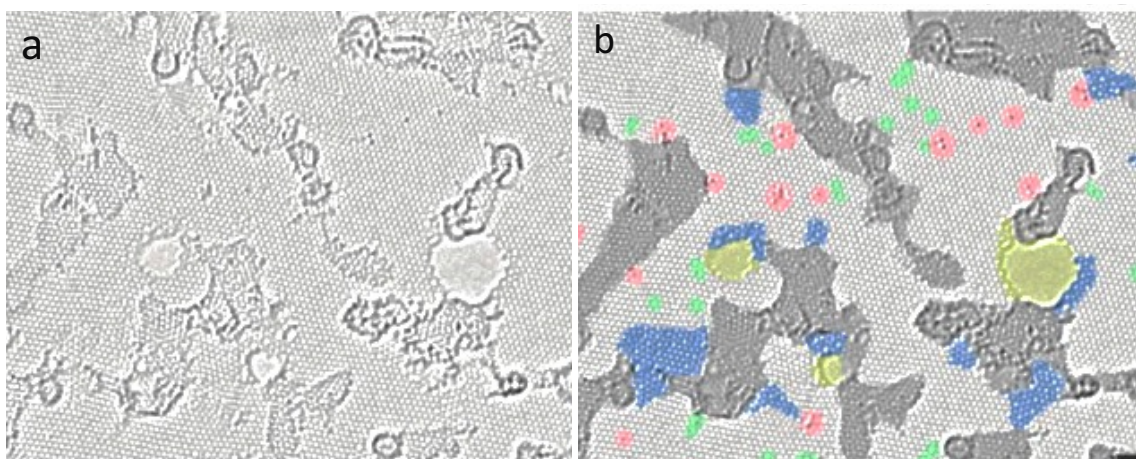


**Figure 2-4.** Atomic resolution, aberration-corrected TEM image of a single layer RGO membrane. (a) Original image and (b) with color added to highlight the different features. The crystalline graphene area that is free from defect is portrayed in the native light-gray color. Moreover, the blue areas denote the disordered single-stratum carbon networks, or rather the extended topological defects that assert prevalence of the reduction-oxidation reaction. Holes accompanied by their reconstructions at the edges are depicted in yellow color while the dark-gray color shows the contaminated areas. The green regions show the remote topological defects – dislocation cores or single-bond rotations while the red regions pinpoint unit adatoms or rather substitutions at a scale bar of 1 nm as asserted by Gomez-Navarro et al. (2010).

## 2.10 Epoxy composites

Epoxy, like most thermosetting polymers, have some limiting factors, including inherent brittleness and fracture toughness. These limiting factors constrain their widespread use in high-performance applications. Because of these limitations, several researchers have used nano-sized organic and inorganic particles such as RGO, carbon nanotubes (CNTs), carbon nanofibres (CNFs) and nanoparticles of metal oxide to reinforce the epoxy matrix and make new polymer composites with enhanced properties (Zhang et al. 2011; Al-Saleh & Sundararaj 2009; Kim et al. 2008). The key feature of PNCs is the size and shape of the dispersed nano-fillers and the interfacial bond between the nano-fillers and the polymer matrix (Galpaya 2012; Dabrowska et al. 2014).



Inorganic additives such as aluminium oxide and silica have been used to improve the toughness of epoxy without sacrificing their properties, but the viscosity is increased, leading to a poorer dispersion of the nano-filler making processing difficult (Tang et al. 2012; Lu et al 2009; Qi et al. 2014). However, adding a small amount of RGO in the polymer matrix can significantly improve the electrical, thermal, and mechanical properties ( Zhang et al. 2011; Kim et al. 2010). The properties of PNCs can be affected by the type and content of RGO used, the polymer matrix, the interfacial interaction, and wrinkling in the RGO and RGO dispersion in the matrix (Galpaya 2012). For example, an epoxy resin is a very poor thermal conductor, and its properties can be significantly improved by adding RGO nano-sheets that can be measured via the preparation and testing of EP-RGO nanocomposites. Pu et al. (2014) reported the thermal conductivity of the EP nanocomposite with 2 wt.% RGO is improved by 21% in comparison with that of neat EP ( $0.173 \text{ W mK}^{-1}$ ). The study reported also by Tang et al. (2013) revealed that the fracture toughness, tensile strength and elastic modulus of the epoxy improve by 30%, 21% and 7%, respectively, on reinforcing it with 0.1 vol. % of RGO, and its electrical conductivity improved by two orders of magnitude ( $4.57 \pm 1.13 \times 10^{-9}$ ). Consequently, RGO nanocomposites can be used as thermal interface materials (TIM) for heat dissipation.

## **2.10.1 Preparation polymer–RGO nanocomposites**

The polarity, hydrophobicity, molecular weight, functional groups and many other factors present in the RGO, polymer and the solvent vary according to the preparation method chosen. (Das & Prusty 2013). Three different preparation methods of incorporating the matrix polymer with the RGO layers are described in the following sections:

### **2.10.1.1 Solution mixing**

Solution-based mixing methods generally involve mixing the colloidal suspensions of RGO fillers into the polymer matrix. The polymer itself is usually already in a solution or is dissolved with the polymer in the suspension of the RGO by simple stirring or shear mixing. After this

step, the suspensions need to be heated and other steps (such as vacuum oven) must be used to remove the solvents (Potts et al. 2011). This mixing method has been widely used to incorporate RGO sheets into a range of polymers matrices, including polystyrene (Stankovich et al. 2006) and poly(vinyl alcohol) (PVA) (Zhao et al. 2010a).

### **2.10.1.2 Melt blending**

A more practical and versatile approach known as melt blending has been used to fabricate RGO PNCs, especially for thermoplastic polymers. In this technique, in the melt state, RGO fillers are dispersed mechanically into the polymer matrix under a shear force and at high temperature. The polymer chains are intercalated to form nanocomposites. The advantage of this processing is its relatively low cost and avoidance of the use of toxic solvents (Galpaya 2012). However, its major drawback is the reduced A.R of the RGO sheets because of the strong shear forces used during processing. Also the degree of dispersion of the sheets in the composite is not particularly good compared with that of the solution mixing method (Galpaya 2012; Greco et al. 2012).

### **2.10.1.3 In-situ polymerization**

In this method, initially the nano-fillers are made to swell in a liquid monomer or multi-monomer. This process is followed by polymerisation using an external source in the presence of a dispersed initiator. The monomers are intercalated between the layered structure of GO or RGO, which subsequently increases the inter-layer spacing and separates the RGO sheets. Nanocomposites prepared via in-situ processing led to a well-dispersed morphology and better mechanical properties compared with other techniques. Some reports have described the successful fabrication of PNCs with epoxy (Monti et al. 2013), PMMA, poly(urethane) and PVA polymers with this method (Galpaya 2012). The major drawback of this technique is the increasing viscosity with time which leads to limits in the filler content added in the matrix (Galpaya 2012).

Polystyrene-expanded GO composites prepared with this method at a lower percolation threshold of 3 wt. % loading resulted in an electrically conducting material with a conductivity of  $10^{-2} \text{ S cm}^{-1}$  (Chen et al. 2001). In-situ polymerization of PMMA in the presence of GO exhibited increased storage modulus by 14% at a filler loading of 0.5 wt. % (Feng et al. 2013; Aldosari et al. 2013).

**Table 2-6.** Comparison of some PNCs preparation methods (Wang et al. 2016).

Fabricating method	Throughput	Pros	Cons
<i>In-situ</i> polymerization	Bulk	Extremely efficient, low cost, quality-dispersion	At a later stage, polymerization rate loss
Solution mixing	Bulk	Good dispersion, versatile	Extensive use of organic solvents
Melt blending	Mass-production	Cost efficient, eco-friendly	Inferior dispersion

## 2.11 Processing conditions

To address the issue of the RGO dispersion, several methods have been previously tried that can be categorized into ultrasonication, chemical and mechanical dispersion methods (Lin et al. 2017). The ultrasonication method uses the energy created by high-intensity ultrasonic waves to disperse the nano-sheets. This energy is applied to separate the RGOs from the bundles and can be readily dispersed within the liquid medium (Soltani & Kyu 2017). It is regarded as a suitable method for dispersing the RGOs in solvents (e.g. water, THF) and low-viscosity resins. However, this method does not work efficiently in systems with high viscosity. Moreover, this method results in the destruction of the structure of the RGOs because of the intensive and long use of the ultrasound (Shelimov et al. 1998).

The mechanical mixing method is an alternative process for dispersing RGO material in the host matrix. This method involves three-roll milling, magnetic and the high-shear mixing techniques. These techniques apply local shear stresses to separate the bundles into single nano-

sheets. Determined by the size of the mechanical mixing apparatus, a large content of fillers can be produced with this process (Lin et al. 2017). Moreover, the shear mixing technique is widely cited in the published literature as a promising method for obtaining a regular-distribution of nano-fillers in a matrix. The main reason for researching this area is to develop the most effective way of processing both nanostructure polymer and nanoparticles so perfect matrix-particles interactions can be obtained (Lin et al. 2017). The dispersion quality in shear mixing is determined by macroscopic factors such as the speed of mixing, the equipment design and the time to achieve optimal processing.

Recently, many researchers have focused on developing and enhancing the most appropriate processing method for nanocomposite materials, which can enhance the interactions in the nanoparticle matrix. Sonication, combined with high-speed shear mixing, has been considered an alternative processing strategy for the dispersion of RGO or GO in epoxy systems and for obtaining better mechanical and electrical properties (Peponi et al. 2014). For example, (Yasmin et al. 2006) used several processing methods for the fabrication of EP nanocomposites that incorporated expanded GO at low concentrations of 1–2 wt. %. These methods included sonication, shear mixing, direct mixing and combinations of these first two methods. In those studies, the mechanical performance of the nanocomposites was examined as a function of processing technique and the level nanoparticle loadings in the matrix. The results demonstrated that samples fabricated by a combination of sonication and shear mixing techniques recorded a better value of elastic modulus and ultimate strength, whilst the direct mixing showed the lowest properties results amongst all the processing techniques. Furthermore, the duration of sonication is another key factor that can influence the mechanical behaviour of the resultant nanocomposites. Although a longer sonication time can lead to a higher yield of GO nano-sheets from expanded GO, the prolonged sonication time of GO nano-sheets and epoxy resin can result in a degradation of the mechanical features of the resultant nanocomposite by premature polymerization of the polymer chains.

In addition, the effect of the rotation speed of a shear mixer has been studied by (Cosmoiu et al. 2016). In these investigations, the homogeneous dispersion of carbon nanotubes (MWCNTs) in an EP resin at low concentrations of 0.1, 0.3 and 0.5 wt. % were studied using shear mixing and high-energy sonication, with temperature control during the process. High-speed shear mixing at 1500 rpm led to an acceptable dispersion, and the results indicated that the tensile stiffness and strength can be dramatically improved with sufficient dispersion of nano-fillers in the polymer matrix. In addition, the authors observed that some of researchers in the field used a shear mixer for about 60 to 120 min. However, the dispersion process (mechanical mixing and sonication) cannot be achieved successfully if the volume fraction of nano-fillers is increased above 3 wt. %. The selected rotation speed of shear mixing in the current study was 1600 rpm, and the total time of shear mixing and bath sonication was around 120 min. This study provided the best balance for selecting an optimal manufacturing process.

In addition, Pullicino et al. (2016) studied the impact on nanostructures and the mechanical performance of GNP/epoxy composites at diverse GNP (0.1 to 5 wt. %) loadings of shear mixing at different speeds and with different durations. They found that the size of agglomerates was affected by the shear mixing speed and the duration. At 3000 rpm and 2 h of mixing, the EP nanocomposites exhibited a 12% increase in Young's modulus when the mixing time was increased from 1 h to 2 h. They also noticed there was a 30% reduction in the average size of the agglomerate (i.e. 26.3  $\mu\text{m}$ ) under these conditions compared to that at 1000 rpm and 1 h duration.

## **2.12 Dispersion of RGO**

### **2.12.1 Using solvent**

RGO sheets are wrinkled 2D carbon materials that are strongly attached to OCFGs at its edges and basal plane. The existence of OCFGs on the surface of the GO sheet can have a strong

impact on its mechanical, electrochemical and electronic properties. The OCFGs can also result in property differences between these nano-sheets and RGO nano-sheets (Gómez-Navarro et al. 2010). The structural defects in RGO obtained by applying a strong oxidation procedure can limit its potential applications for example in electronics. This occurs because the presence of OCFGs can reduce the RGO sheets' electrical conductivity. Nonetheless, the presence of the functional groups makes the RGO sheets strongly hydrophilic, potentially leading to the RGO sheets having a greater dispersibility in several solvents, such as THF, DMF, NMP, ethylene glycol and particularly in water, as shown in Fig. 2-5 (Paredes et al. 2008). The greater dispersibility is attractive for applications such as detecting low levels of cancer cells and cleaning polluted water.

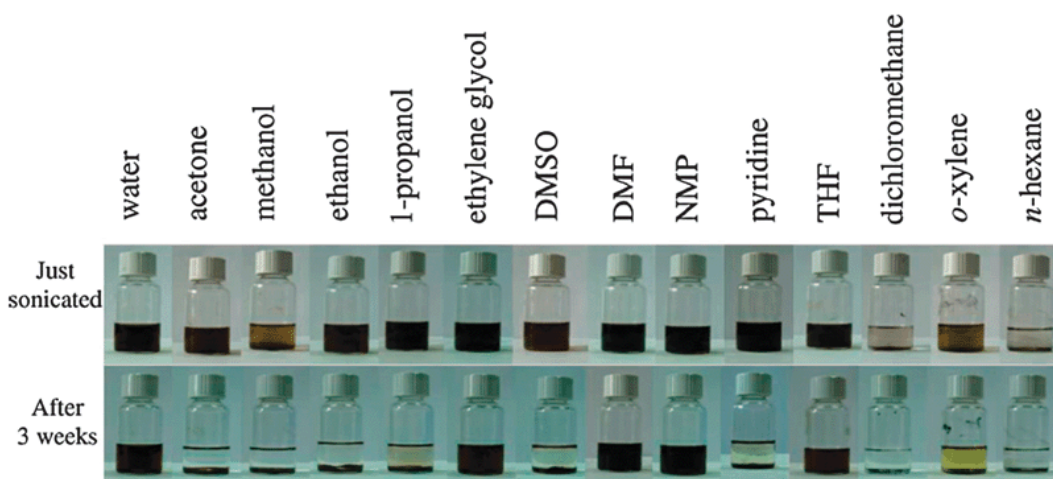


**Figure 2-5.** RGO sheets dispersed in distilled H<sub>2</sub>O and other different organic solvents using an ultrasonication bath for sixty minutes. Upper row: dispersion immediately after sonication. Lower row: dispersions three-weeks after sonication, (Paredes et al. 2008).

However, other solvents displayed short-term stability and precipitated into the bottom of the glass bottle in a span of anything from hours to a couple of months depending on the Hansen parameters of RGO materials. Furthermore, (Konios et al. 2014), examined the long-term stability of RGO sheets dispersed in different types of solvents by leaving the suspensions undisturbed for 3 weeks. In common with RGO was found to have an excellent dispersibility in glycol, NMP, ethylene and water, meaning that OCFGs exist at defect locations. As a

consequence, the comparative stability of RGO within aqueous solutions might be attributed to the electrostatic repulsion arising from the negative charge of RGO sheets as they are dispersed in distilled H<sub>2</sub>O.

In contrast, the pristine graphene nano-sheets are likely to aggregate because of the van der Waals interactions, which were identified by (Bhattacharya 2016). Hence, this result presents a major challenge for incorporating these sheets in polymer matrices with a homogeneous dispersion. (Park et al. 2009) confirmed that homogeneous colloidal suspensions of chemically reduced GO (CRGO) may be easily made in THF and DMF and other types of organic solvent systems, but this was not possible for other types of solvent systems such as diethyl ether and toluene.

It is important to understand the solubility parameters of a wide range of organic solvents to achieve a stable suspension in these materials. To explore the dispersion mechanism for RGO nano-sheets within a large group of organic solvents, the solubility parameters developed by Hansen were employed. This theory involved three parameters: the dispersion cohesion ( $\delta_D^2$ ), the polarity cohesion ( $\delta_P^2$ ) and the hydrogen bonding cohesion ( $\delta_H^2$ ) (Konios et al. 2014). These parameters are related in the following manner:

$$\delta_T^2 = \delta_D^2 + \delta_P^2 + \delta_H^2$$

which gives the Hildebrand solubility parameter ( $\delta_T^2$ ). The following equation was utilized to evaluate the Hansen parameters of the RGO samples:

$$(\delta_i) = \frac{\sum_{solv} C \delta_{i,solv}}{\sum_{solv} C}$$

where  $i = D, P, H$  or  $T$ ;  $C$  is the RGO solubility and  $\delta_{i,solv}$  is the  $i_{th}$  Hansen parameter in a given organic solvent (Konios et al. 2014). It has been estimated that the Hansen parameters for RGO are  $\delta_T \sim 25.4 \text{ MPa}^{1/2}$  and  $\sim 22 \text{ MPa}^{1/2}$ , respectively. Solvents that have  $\delta_T$  close to that estimated

values are expected to be a long-term stable suspensions. For example, the  $\delta_T$  values for DMF and THF are about 24.9 and 19.5 MPa<sup>1/2</sup>, respectively, which are quite similar to  $\delta_T$  values for RGO samples, and these are commonly used to obtain long-term stable suspensions (Konios et al. 2014).

### **2.12.2 Decoration of RGO sheets with metal/metal oxide nanoparticles**

Nanocomposites are nano-size hybrid materials which combine the individual properties of the component materials (fillers and matrix) to lead to synergistic and novel properties. RGOs are capable of being homogeneously distributed easily with both H<sub>2</sub>O and other organic solvents to yield stable dispersions by using ultrasonication. RGO can be used as the substrate for the dispersion of metal oxide because of the presence of abundant OCFGs including carbonyl, epoxy and hydroxyl moieties on the RGO structure (Buchsteiner et al. 2006). Additionally, these functional groups can act as anchoring centres or nucleation locations for the attachment of NPs (Xu et al. 2008).

RGO offer advantageous characteristics when used as a substrate for the dispersion of NPs. These advantages are the following: (i) Limited growth of metal/metal oxide NPs, which improves the dispersion and stability of RGO (Hsu & Chen 2014); (ii) A high surface area that can obstruct the aggregation of NPs (Dutta et al. 2013); (iii) The attached nanoparticles might be also used as a stabilizer against the re-aggregation of RGO nano-sheets into graphitic structure, and for broadening the displacing of RGO in the solid state (Huang et al. 2010); (iv) Excellent properties of individual RGO such as high tensile strength and thermal conductivity with an excellent thermal stability (Zhou et al. 2009; Huang et al. 2010; Ji et al. 2012). These abovementioned advantages have stimulated extensive polymer/RGO-NPs nanocomposites research with a view of developing a variety of applications such as the storage of energy, optoelectronic devices and solar cell technology. (Ojha et al. 2014; Zahed & Hosseini-Monfared



2015). These nanocomposites can be synthesized by attaching different types of nano-size particles to the RGO sheets' surface via in-situ (growing the NPs on the RGO surface structure) and ex-situ (attaching premade metal/metal oxide NPs onto the RGO surface structure) methods. These methods are described separately in the next sections and summarised in Table 2-7.

### **2.12.2.1 *In situ* decoration of nanoparticles onto RGO**

Techniques for the fabrication of RGO-based metal/metal oxide nanocomposites via the in-situ chemical reduction of metal precursors utilising reducing agents such as  $\text{NH}_4\text{OH}$ , hydrazine hydrate and ascorbic acid are the most common and widely applied methods for growing metal on 2D materials (Khan et al. 2015).

The functional groups that hold negative charges onto the structure of RGO (depending on the degree of reduction) can lead to the nucleation of positively-charged metallic salts, resulting in the growth of metal nanoparticles on the surface of RGO. Furthermore, controlling the density of oxygenated functional groups on the RGO nanostructure can readily tune the NPs density in the resulting nanocomposites. Fig. 2-6 illustrates a RGO–Au nanoparticles composite produced by this technique which was then investigated using AFM and TEM tools.

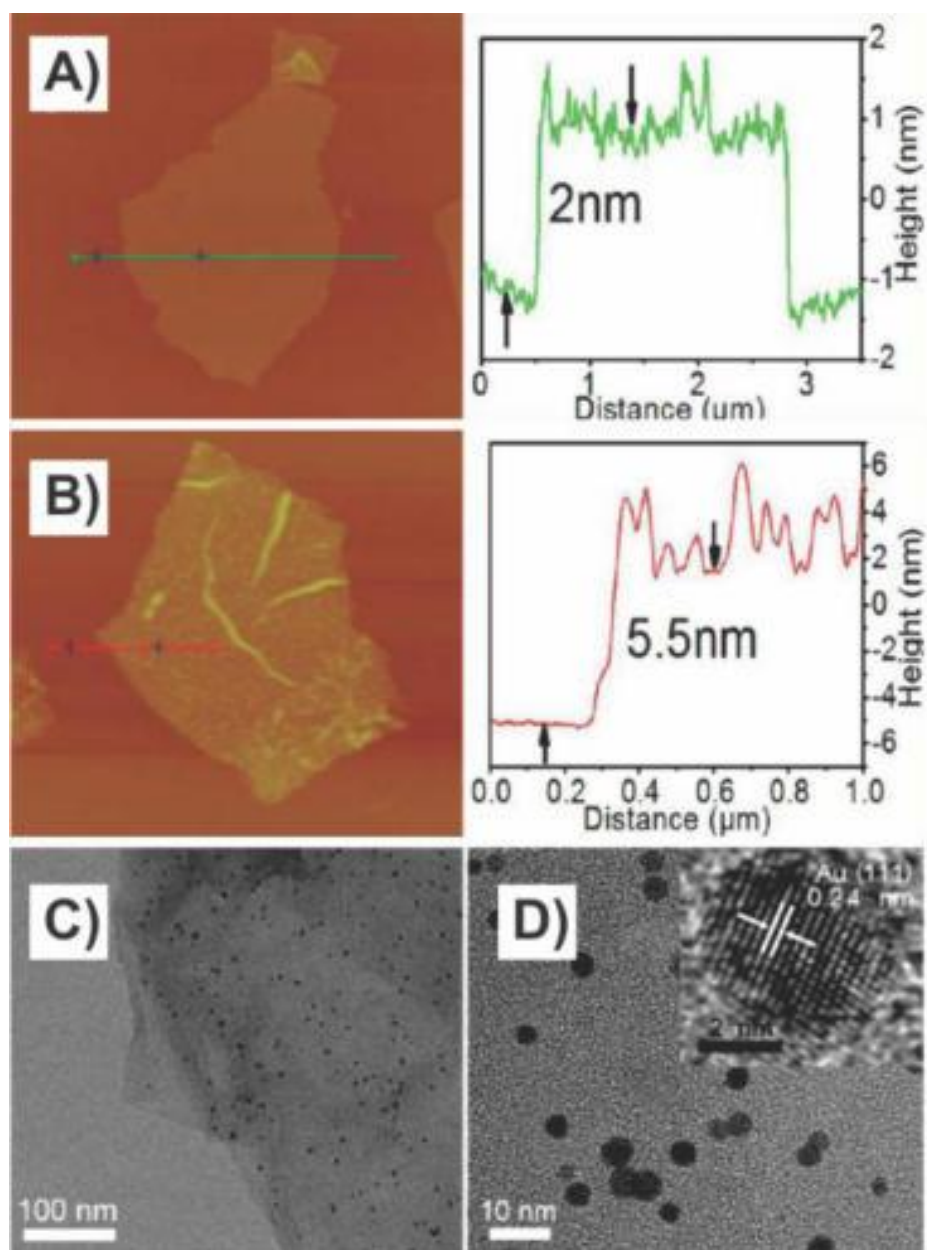


**Figure 2-6.** RGO–NPs composite formed from RGO nano-sheets covered by AuNPs: (A) AFM image of a mono-layer of RGO (B) A RGO nano-sheet covered with a layer of 3.5 nm AuNPs. (C and D) TEM images of the RGO sheet decorated with AuNPs at low and high resolutions (Zhuo et al. 2013).

Kim et al. (2011) synthesized hydrothermally reduced graphene/Co<sub>3</sub>O<sub>4</sub> composites as anode materials for use in lithium-ion batteries (LIBs) by the reduction of cobalt acetate ((C<sub>2</sub>H<sub>3</sub>O<sub>2</sub>)<sub>2</sub>Co.4H<sub>2</sub>O) and RGO sheets in deionized water (DI) with hydrazine and NH<sub>4</sub>OH as reducing agents. The uniform surface coverage of hydrothermally reduced graphene (HRG)

provides nucleation sites for  $\text{Co}_3\text{O}_4$  nanoparticles on the conductive surface of HRG nano-sheets.

Other methods of deposition of metal/metal oxide nanoparticles on 2D materials are performed with the assistance of the following techniques: pulsed laser deposition (PLD) (Bajpai et al. 2011), thermal evaporation (Zhou 2010b), sputtering methods (Son et al. 2010) and a hydrothermal method (Zhou et al. 2009). These are some of the most popular approaches for preparing nanoparticles with high crystallinity on a single layer of carbon.

### **2.12.2.2 Ex-situ decoration of nanoparticles on RGO**

Ex-situ techniques include methods of mixing separate solutions of pre-synthesised nanoparticles and RGO sheets. Before the mixing process, the RGO sheets and/or nanoparticles can readily be functionalized through linking agents which can use either covalent C–C coupling reactions, or non-covalent,  $\pi$ – $\pi$  stacking and electrostatic interactions. Nanoparticle functionalisation of RGO sheets enhances their solubility and thereby expands the potential for preparing nano-hybrid composites. The main advantage of an ex-situ technique is that it provides perfect control over the shape, size, and nanoparticle functionality. Despite this advantage, this technique may suffer from a non-uniform coverage of nanocrystals by RGO and low density (Georgakilas et al. 2012; Yin et al. 2015).

Various inorganic NPs have been anchored to RGO sheets utilising this technique. The non-covalent bonding and  $\pi$ – $\pi$  stacking interactions between RGO sheet and the nanoparticles are the major driving forces for anchoring inorganic nanoparticles onto the 2D materials (Yin et al. 2015). For instance, CdSe quantum dots (QDs) were encapsulated within a thin layer of conductive polymer polyaniline and were covered on the surface of the RGO by  $\pi$ – $\pi$  stacking interactions between the conductive shell and the RGO conjugated system to yield the QD@PANI–G hybrid (Nguyen et al. 2013; Al-nafiey 2016).

### 2.12.2.3 RGO-encapsulated metal oxide nanoparticles

Because RGO is a two-dimensional flexible sheet, it may easily be used for covering and encapsulating NPs. RGO sheets are the most widely used with this encapsulated approach because of their relatively hydrophilic state. In particular, the most frequently used technique to wrap NPs with RGO is providing the nanoparticle surface with a positive surface charge. This is achieved by covering it with 3-Triethoxysilylpropylamine using the sol-gel process, leading to a strong linking with the RGO through non-covalent bonded-electrostatic interaction (Khan et al. 2015). However, GO sheets carry a net negative charge as a consequence of ionization of the  $-COOH$  and  $-OH$  moieties over its structure. Thus, the sheets may be covered directly with positively charged NPs via electrostatic self-assembly interactions. For example, RGO-NPs nano-hybrids such as  $GO-SiO_2$  NPs which subsequently convert to  $RGO-SiO_2$  via the thermal treatment process (Georgakilas et al. 2012),  $RGO-Fe_3O_4$  NPs (Zhu et al. 2010) and  $GO-MnO_2$  NPs (Zhai et al. 2012) have been prepared through blending negatively charged GO or RGO nano-sheets with positively charged metal oxide nanoparticles.

Numerous studies have elucidated the wrapping-up of metal oxide NPs with RGO sheets. For instance, (Yin et al. 2015) recently presented RGO-encapsulated silicon oxide NPs via an electrostatic interaction method. More specifically, silicon oxide NPs were being first functionalized with APTES, which changed the negative surface charge into a positive one. As a result of encapsulation, the  $SiO_2$  nanoparticles are capable of preventing the agglomeration of individual graphene sheets whilst preserving a high electrical conductivity.

In similar studies Yang et al. (2009) also reported the functionalization of a RGO surface with APTES. The APTES was grafted onto the RGO structure with the epoxy groups via covalent bonds. The silicon-functionalized RGO ( $Si-RGO$ ) was merged with a silica matrix through hydrolytic condensation of an excess of APTES in the existence of  $RGO-Si$ .

**Table 2-7.** A summary of various approaches used to fabricate RGO–nanoparticles composites.

<b>Method</b>	<b>Typical NPs</b>	<b>Key characteristic</b>	<b>Key refs</b>
<b>In-situ</b>	Metal-nanoparticle, particularly metal oxide NPs, QDs and noble metals	(i) It can readily tune the NPs density used to form the composite; (ii) highly effective and simple to perform; (iii) one-pot synthesis; (iv) can produce NPs with narrow size distribution and high crystallinity; (v) can be difficult to control the morphology and size of the NPs (in the hydrothermal approach).	(Guo et al. 2011; Georgakilas et al. 2012)
<b>Ex-situ</b>	Inorganic -nanoparticle, particularly noble metals	(i) nanoparticles are prepared in advance which allows accurate control of the size and shape of the NPs that are used to form a composite; (ii) ex situ techniques comprise covalent or noncovalent interactions such as electrostatic interactions, hydrogen bonding, van der Waals interactions and $\pi$ - $\pi$ stacking.	(Georgakilas et al. 2012; Yin et al. 2015)
<b>Encapsulation</b>	Metal NPs, and metal oxide	(i) highly stable, which limits the level of exfoliation of the NPs from RGO or conversely; (ii) high quality of contact that occurs between RGO and the encapsulated NPs (iii) electrostatic interactions between the filler and NPs.	(Zhou et al. 2013; Yin et al. 2015)

## 2.13 Theory

### 2.13.1 Dispersion State

There is general agreement amongst material scientists that graphene sheets almost always remain entangled, and if somehow these are dispersed, the force of attraction because of the van der Waals force does not let them remain dispersed (Pettes et al. 2011). However, it is also considered that size, shape, synthesis methods and surface chemistry are the main factors that impact the agglomeration of graphene. The dispersion state of the graphene usually determines the application of graphene to boost to the properties of the targeted system (Pettes et al. 2011). Considering the polymer matrix, the uniform dispersion of graphene is highly unlikely because commercially available graphene has a large surface area ( $\sim 2500 \text{ m}^2 \text{ g}^{-1}$ ) and hence remains severely entangled. Therefore, the application of such graphene commercially and in lab research is adversely affected. Here, the non-agglomerated RGO achieves the required properties of the composite, and the composite strength declines because of the behaviour of aggregates as stress concentrators and inter-layer sliding. The dispersion of RGO in a polymer matrix, particularly concerning the proportion of RGO over some wt. %, has not been optimized (Atif & Inam 2016).

RGO dispersion is performed with the help of two diverse approaches. The first approach allows the separation of RGO through an external force e.g. mechanical mixing and sonication. In this method, the separated RGO are dispersed in a polymer or surfactant complex to become stabilized (Atif & Inam 2016). Thus, the RGO is not further re-aggregated, and metastable dispersion can be achieved through this approach. The second approach mixes the RGO in a solvent to be peeled off at each layering from the bundle, then acquiring a solution by dissolving it in the solvent (Atif & Inam 2016). Therefore, it can be assumed that the dispersion of RGO in a polymer matrix can be controlled at two points. Also, the use of chemical functionalization, mechanical mixing, or surfactants can initially modify the dispersion state in the uncured state.

Furthermore, at the curing stage, alterations are obvious at the dispersion state (Atif & Inam 2016), and curing at greater temperature, may result in RGO agglomeration. The temperature at curing, along with time, chemical composition of the matrix, and the method of applying heat determine the effect of curing on the dispersion state of RGO.

The natural abilities of the RGO structure and the increased properties of RGO-based PNCs by RGO content show similarities (Pettes et al. 2011). The results obtained from molecular dynamics (MD) simulations indicate that the firmness of polymers can be increased more efficiently through the uniform dispersion of RGO in the polymer matrix rather than poorly dispersed RGO (Rahman 2013). The modelling for the three distinct dispersion states of RGO, which are single layer RGO, uniformly dispersed RGO, and agglomerated RGO was analysed by Rahman (Rahman 2013). Around 3 wt. % RGO with P3m space group symmetry of RGO sheet was found to exist in every unit cell (Dubois et al. 2009). Large-scale atomic/molecular massively parallel simulator (LAMMPS), which is an open source MD code created in the Sandia National Laboratory, was the source for conducting the calculations (Plimpton 1995). The exposure of engineering strain of  $1 \times 10^{-4}$  was applied on unit cells at every 300 steps up till 1500 steps to obtain stress-strain response through the MD method based on the NVT (canonical) ensemble, number of molecules (N), box size ( $V=L^3$ ) and a constant temperature (T) of 0.1 K. The results obtained showed that uniformly dispersed RGO–epoxy is more firm than the agglomerated RGO–epoxy nanocomposites (Rahman 2013).

### **2.13.2 Interfacial Interactions**

The mechanical properties of RGO-based PNCs improved based on interfacial interactions, because an efficient transfer of load from the matrix to the reinforcement is required for easing the stress concentration when a weaker matrix phase is observed. The interfacial area has a great impact on the interfacial interactions. Thus, an increased interfacial area results in increased interfacial interactions. Smaller reinforcement size and greater altered topography

also result in increased interfacial area. A considerable increase in surface area can be obtained by texturing the topography, even if an unchanged sized sheet is used. The mechanical properties of PNCs also increased, as an increase in interfacial area with the polymer matrix is observed with greater surface area. The mechanical properties of PNCs further increase because of the occurrence of mechanical interlocking amongst polymers and reinforcement. The filler and matrix may have poor physical bonding in the case of a smooth surfaced reinforcement. Conversely, polymer chains are locked within the spongy structure of support in the case of a corrugated surface. Furthermore, increased interfacial interactions and associated growth in mechanical properties are observed because of mechanical interlocking. The level of mechanical interlocking can be increased if the surface is made porous or rough (Atif & Inam 2016). Mechanical interlocking with the polymers is obtained as a result of the textured fillers causing local reinforcement of the fibre-matrix interphase (Atif & Inam 2016). Thus, it can be assumed that the mechanical properties of RGO based PNCs can be considerably increased because of the mechanical interlocking.

### **2.13.3 Thermal Properties**

RGO-based PNCs, because of RGO's greater thermal conductivity, have greater prospects of being high-performance TIMs. The dissipation of heat from electronic devices may also be barricaded when the high thermal conductivity of RGO is efficiently utilized. However, the thermal conductivity of polymers can be more effectively increased with the graphene instead of CNTs (Atif & Inam 2016). Experimentally, a non-linear dependence of the effective thermal conductivity ( $K_{\text{eff}}$ ) of RGO-based PNCs onto RGO weight has been reported (Atif & Inam 2016). Xie et al. (2008) gave an idea of the analytical model for understanding the effective thermal conductivity of RGO-based nanocomposites. However, the model did not consider the interfacial thermal resistance; hence, high thermal conductivity values were presented in the model. Lin et al. proposed a model to identify effective thermal conductivity of graphene-based



nanocomposites using the Maxwell-Garnett effective medium approximation theory (Lin et al. 2010).

The thermal conductivity values obtained from the theoretical calculations of PNCs were higher than its experimental values (Atif & Inam 2016). Thermal boundary resistance (TBR, also known as Kapitza resistance) existing amongst RGO and polymer chains can further explain this result (Atif & Inam 2016). Interfacial thermal resistance restricts the heat transfer in the composite system that emerges by weak phonon-phonon coupling and then leads to the backscattering of phonons at the borderline area. As the interfacial area increases, an increase in interfacial thermal resistance is also observed. The high surface area thus makes this resistance quite significant when graphene is used.

### **2.13.4 Electrical Conductivity**

Graphene/RGO displays outstanding electrical conductivity because of the graphitic composition. At room temperature, the charge carrier mobility of graphene can reach 15,000  $\text{cm}^2/\text{V s}$  (Bolotin et al. 2008). Effective paths for conduction can be provided through graphene when uniform dispersion of graphene or RGO in the polymer matrix occurs. As a result, an increase in electrical conductivity of nanocomposites is obtained. A large increase in the electrical conductivity of RGO-based PNCs at a certain RGO loading is experienced, where they change from being insulators to being conductors. The percolation threshold is the term used for this RGO loading (Atif & Inam 2016). The utilization of RGO can be minimized by lowering the percolation threshold to the lowest possible. The percolation threshold and electrical conductivity of RGO-based PNCs can be strongly impacted by the dispersion state or degree of agglomeration of RGO (Atif & Inam 2016).

The dispersion state, physicochemical interactions amongst the matrix and the reinforcement, shape of the reinforcement, and technique used to produce PNCs has a strong influence on the percolation threshold. The conductivity models are categorized into structure-oriented

(McCullough 1985), thermodynamic (Syurik et al. 2014), and statistical (Zallen 1983). Prior to and after the processing, the structure-oriented models consider the microstructure of nanocomposites. Its high dependency on microstructure leads to the realization that the prediction made for the conductivity behaviour of PNCs is more realistic because of the structure-oriented models. The structure-oriented models are used in place of the microstructure with fitting parameters where the microstructure attainment is an issue. The microstructure cannot be wholly replaced by these fitting parameters particularly at nano-scale.

The microstructure is the factor that determines the electrical conductivity of PNCs. The alignment of the nano-fillers determines the conduction of the produced PNCs, after a conducting nano-filler is filled within a polymer (Atif & Inam 2016). An uninterrupted network by the nano-fillers is required to form a smooth path for the electrons (Atif & Inam 2016). The percolation threshold for PNCs can be approximated using several proposed models using nano-fillers such as graphite, CNTs, and graphene. Fitting parameters are utilized in several proposed models, thus making it difficult to reach the actual values. The properties of nanocomposites are determined through the microstructure, and its effective incorporation into the proposed models provide values that are close to the actual values. Syurik et al. (2014) slightly modified McCullough's model with current maps obtained by conductive AFM (CA-AFM).

McCullough's model can be categorized as a structure-oriented model with factors such as microstructure depending upon the matter of support (McCullough 1985). The chain-like network of support can be credited for the increased electrical conductivity. The factors affecting the chain length are size, shape and volume fraction of reinforcement. The chain-like network under the percolation threshold is irregular, and the whole of the chain is not conjoined. The conduction has blockages as the chain continuity breaks; thus, the PNCs start acting as insulators. The chains adhere together once the percolation threshold is reached, and a

continuous network is built to serve as the path for electrons and PNCs, which by then are working as conductors. The isotropic distribution of reinforcement in the matrix is depicted in the following equation (Syurik et al. 2014).

$$\frac{\sigma_m}{\sigma} = \frac{v_m^2(1 - \langle\lambda\rangle)}{V_m}$$

Here,  $\sigma_m$  is the electrical conductivity of matrix,  $\sigma$  is the electrical conductivity of the composite, and  $v_m$  is volume fraction of matrix. The chain parameter  $\langle\lambda\rangle$  to reach perfect shapes of reinforcement such as spheres, sheets and ropes can be replaced as shown in the following equation (Syurik et al. 2014),

$$\langle\lambda\rangle \cong \lambda (\langle a^2 \rangle)$$

here,  $\langle a^2 \rangle$  depicts the mean-square value of the aspect area of the conductive chains (a). While producing PNCs, the factors such as the air entrapment, evaporation of volatiles, and the comparative movement of reinforcement and polymer chains make porosity unavoidable. The conductivity is affected because of the porosity, and an apparent density ( $\rho_{ap}$ ) based on the specific density through the pore coefficient is considered as depicted in the following equation (Syurik et al. 2014).

$$k_p = \frac{\rho_f}{\rho_{ap}}$$

The latex technology that is a reproducible technology is utilized for the production of PNCs. In this technology, the reproduced samples formed with similar parameters show no change in the tendency of conductivity (Atif & Inam 2016). Here,  $k_p$  is a constant to be calculated only once. The conductivity performance based on the reinforcement loading is presented in the following equation.

$$\frac{\sigma_m}{\sigma} = \frac{G^2(1 - w_f)^2(1 - \langle\lambda\rangle)}{V_m}$$

$$G = \frac{v_f}{w_f}$$

The  $\lambda$  has a value between  $0 < \lambda < 1$  for all composites, which lays in the limitations applied by McCullough's model (McCullough 1985). The latex technology is responsible for the preparation of GNPs/PS PNCs that permits the reproducible percolation threshold (Berger & McCullough 1985). The average thickness of 2–3 atomic layers and average surface area 1–3  $\mu\text{m}^2$  were considered for GNPs. The GNPs had proportions of weight of 0, 0.6, 0.9, 1.5, and 2.0 wt. %. Direct current (DC) mode was used to calculate the electrical conductivity, and the direction taken was parallel to the sample top surface using a 2-probe configuration and a Keithley 2602 system source meter. The  $I/V$  characteristics acquired were used for calculating the conductivity with the following equation (Syurik et al. 2014),

$$\sigma = \frac{b \cdot I}{V \cdot A}$$

Here,  $V$  denotes applied voltage and  $I$  denotes the current flowing through a cross-section ( $A$ ) and between the distance ( $b$ ). The conductivities shown by CA-AFM and 2-point DC measurements concur. At low GNP, the conductivity of the polymer is close to the dielectric matrix. This is attributed to the absence of a continuous pathway of GNPs conduction. DC measurements recommend the percolation threshold of 0.9 wt. %, which is corroborated by SEM and CA-AFM. The increase in conductivity is five orders of the percolation threshold distinguished by DC measurements.

### 2.13.5 Mechanical Theory

Broad theory for the strengthening of polymers by nanoplatelets is applied to understand the effect of ways to control strengthening through matrix modulus, particle geometry and the strength of the filler–matrix interface. The individual nanoplatelets have no interactions with each other and are oriented in the polymer matrix. If particles such as RGO sheets are present in the PNCs, then the following equation could be used.

$$E_c = E_{eff} \eta_o \eta_1 V_p + E_m (1 - V_p)$$

Here,  $\eta_o$  denotes the Krenchel orientation factor (Li et al. 2016a) and  $\eta_l$  denotes the length factor (Hull & Clyne 1996). The parameter  $E_{eff}$  is the effective Young's modulus of the filler dependent only on its structure. For instance, for monolayer graphene,  $E_{eff}$  is 1 TPa and for few-layer graphene, it is even lower (Gong et al. 2012). Li et al. (2016) recently showed that for randomly-oriented nanosheets,  $\eta_o = 8/15$ , whereas the orientation factor  $\eta_o$  is 1 for aligned nanosheets. The effectiveness of the movement of stress from the matrix to the filler is given by the length factor  $\eta_l$  ( $0 \leq \eta_l \leq 1$ ). Moreover, the shape of the filler and the strength of the filler–matrix interface allows for the stress transfer.

It is assumed that shear stress at the nanosheets/matrix interface is responsible for the stress transfer from the matrix to the individual aligned nanosheets (Gong et al. 2010). When axial stress,  $\sigma_1$  lying parallel to the plane of the nanosheets, is placed upon the system, Young's modulus of the matrix becomes lower than that of the nanosheets, causing deformation of the lines. Shear stress at the nanosheets/matrix interface is thus created. The uniform strain assumption conveys that the strain in the middle of the nanoplatelet equals that of the matrix if the nanoplatelet is of sufficient length. The load is mainly carried in the composite by the nanosheets, as the nanosheets have a greater Young's modulus compared to the matrix.

Shear lag theory (Hull & Clyne 1996) is responsible for the representation of the performance of a single discrete nanoplatelet in a matrix, where the nanosheets assumed are of length  $l$  and a cover of resin with an overall thickness of  $T$  covers the thickness  $t$  (Gong et al. 2010). Another assumption states that there is an elastic deformity of the nanosheets and matrix, and the edge of the nanosheets–matrix remains in its position. The distribution of the stress in the nanosheets related to distance,  $x$ , along the nanosheets at a given level of matrix strain,  $e_m$ , is given in the following equation,

$$\sigma_f(x) = E_{eff} e_m \left[ 1 - \frac{\cosh(ns \frac{x}{T})}{\cosh(ns/2)} \right]$$

$$\text{where } n = \sqrt{\frac{2G_m}{E_{eff}}} \left(\frac{t}{T}\right)$$

If the axial stress of the nanosheets is considered  $E_{eff}$  indicates the effective Young's modulus of the nanosheets,  $G_m$  indicates the shear modulus of the matrix and  $s = l/t$  is the aspect ratio (A.R) of the nanosheets.

For an aligned individual RGO sheet in the PNCs, Young's modulus is given as the following

$$E_f = E_{eff} \left[ 1 - \frac{\tanh(ns/2)}{(ns/2)} \right]$$

The Krenchel orientation factor ( $\eta_o$ ) is used if the RGO sheets do not show alignment (Li et al. 2016), and the equation then obtained is the following,

$$E_f \approx E_{eff} \eta_o \frac{(ns)^2}{3}, \text{ where } ns \text{ is small.}$$

In PNCs formed from an arrangement of RGO nanosheets, the closeness of neighbouring particles is associated with the ratio  $t/T$  and consequently to the volume fraction of filler,  $V_f$ . The geometry of the arrangement of the nanosheets determines the accurate connection here. Additionally, considering a stack of nanosheets squeezed between layers of the polymer matrix, the assumption indicates that  $t/T \sim V_f$ .

$$E_c \approx E_m \left[ 1 - V_f + \frac{s^2}{12} \frac{\eta_o}{(1+v)} V_f^2 \right]$$

Although this equation can then be used to predict the Young's modulus of the composite,  $E_c$ , the rule of mixtures often breaks down, typically through the agglomeration of the nanofiller particles, especially at high loadings. The agglomeration often occurs in thermosetting systems such as epoxy resins where a significant increase in  $E_c$  can be obtained for low loadings of RGO, but no further increase is found above a certain loading of the nanofiller.

The Young's modulus of the composite,  $E_c$  can also be predicted through this equation, but the rule of mixtures is inaccurate at high loadings, usually caused by the agglomeration of the nanofiller particles. A substantial increase in  $E_m$  is achieved for low loadings of RGO as the agglomeration occurs in thermosetting systems such as epoxy resins (Young et al. 2017).

This theory does have its constraints, however. It is only concerned with the elastic deformation of the polymer-based nanocomposites at relatively low wt. % of loading before any agglomeration effects occur. Notwithstanding, the ability of nanofillers such as RGO to increase the stiffness of a polymer is of major technological importance towards a full understanding of the mechanical properties of polymer-based nanocomposites reinforced with nanosheets.

## **2.14 Properties of polymer–RGO nanocomposites**

### **2.14.1 Mechanical properties**

RGO-based PNCs exhibit superior mechanical properties compared with graphite-based composites or neat polymers. Because RGO has high levels of tensile strength and stiffness, its use as a nano-reinforcement in polymer matrices exhibits the large possibility of further improving the mechanical performance of composites. Moreover, RGO sheets can provide high thermal and electrical conductivity and improved thermal stability in a host polymer matrix, even at low loadings. In contrast, the strong adhesion between the polymer and RGO is an important property for better reinforcement because the incompatibility between two phases lowers the stress transfer, resulting in the lower strength of PNCs. Hydrogen-bond interactions and weak van der Waals forces are responsible for improved mechanical properties (Tang et al. 2013; Galpaya 2012).

Rafiee et al. (2009) measured the mechanical properties of EP nanocomposites with graphene and CNTs additives at  $0.1 \pm 0.002$  wt. % loading. The results demonstrate that the EP reinforced by graphene sheets exhibit higher Young's modulus, tensile strength and resistance of crack

propagation compared to the CNTs nanocomposites. These significantly improved mechanical properties of graphene PNCs over carbon nanotubes were associated with their wrinkled structure (rough) and high specific surface area as well as the 2D geometry. Olowojoba et al. (2016) reported an increase in the modulus from  $2900 \pm 70$  MPa for the neat EP to  $3290 \pm 60$  MPa for the 1.0 wt. % EP/RGO composite (i.e. an increase of 13.4%). Liu et al. (2014) reported that the tensile strength and Young's modulus of EP nanocomposites reinforced by 0.1 wt. % of graphene were increased by 160% and 65%, respectively, compared with the same of neat EP.

Bora et al. (2013) manufactured unsaturated polyester/RGO nanocomposites, and their results showed significant increases in the mechanical properties at a low RGO loading. The values of the modulus and tensile strength of the composites increased by 87% and 123%, respectively, at 3 wt. % of filler loading.

In recent years, the advancement of nanomaterials based on RGO nano-sheets in a polymer matrix has enabled further research in materials science. These nanocomposites exhibit large increases in their properties compared with their polymer counterparts (Galpaya 2012). Such properties can be achieved at a very low nano-filler loading level in the matrix. The excellent properties of high electrical conductivity (200 to  $3.5 \times 10^4$  S  $\text{cm}^{-1}$ ) (Renteria et al. 2015) and thermal conductivity (3 to 61  $\text{Wm}^{-1}\text{K}^{-1}$ ) (Mittal et al. 2015) make RGO very useful in various applications, including energy storage (Tran & Jeong 2015), fuel cells (Bashyam & Zelenay 2006) and electronics (Hass et al. 2008). Moreover, dispersing RGO nano-sheets and its derivatives such as graphene and GO in polymers yield nanocomposites with better properties than those of polymers based on other nanocomposites (Wei et al. 2015). Nevertheless, to take full advantage of beneficial properties of RGO material, many practical obstacles need to be overcome. These include attaining excellent interfacial bonding properties and good dispersion of the RGO sheets in the polymeric matrix (Olowojoba et al. 2017).



Rafiee et al. (2009) compared the impact of integrating 0.1 vol% of different conductive carbon nano-fillers such as single and multi-walled CNTs and graphene platelets in EP system. They prepared the carbon–EP composites from a dispersion of various carbon fillers in acetone. They reported on the mechanical properties and showed that graphene platelet –EP composites were superior to CNT–EP nanocomposites, as demonstrated by an increase in UTS (+40%) and elastic modulus (+31%) than the same of neat EP compared with an increase of 14% and 3% for the same for CNTs, respectively. Additionally, the fracture toughness of graphene platelet–EP composites increased (+53%) over the neat epoxy compared to an enhancement of 20% for CNTs. They assigned this excellent performance to the strong interfacial adhesion of graphene platelets because of the wrinkled surface and the existence of oxygenated functional groups. However, Olowojoba et al. (2016) reported a slight reduction in the tensile strength, thermal stability and  $T_g$  for in-situ TRGO filled in EP resins at different loadings, using a three-roll mill method. They attributed this decline in performance to defects and the slight change in the molecular weight between cross-links for the EP matrices. However, Pullicino et al. (2016) studied the effect of using the shear mixer based on the speed and time on the nanostructures and static mechanical properties of GNP/EP nanocomposites. Its EP nanocomposites had an increase in Young’s modulus by 12 % as the mixing time increased from 1.5 h to 2 h. They also noticed a reduced in the average agglomerate size by 30 % (26.3  $\mu\text{m}$ ) compared to that obtained at 1000 rpm and 1 h duration.

## **2.14.2 Conductive Properties**

### **2.14.2.1 Electrical conductivity**

RGO materials have high surface conductivity that greatly improves the electrical conductivity of polymer-based composites with very low RGO loading. These composites exhibit a nonlinear relationship of the electrical conductivity versus the filler contents in the matrix. At a concentration known as the percolation threshold ( $P_c$ ), a sudden rise in the electrical conductivity occurs in polymer composites because of the configuration of a conductive

network by fillers. It is worth mentioning that there are many factors that can influence the percolation threshold, as follows:

(a) the dispersion state or degree of agglomeration of RGO has a significant influence on the percolation threshold and electrical conductivity of RGO-based polymer nanocomposites, (b) the loading fraction, c) the fabrication process, d) the lateral size of the RGO sheet, e) the degree of reduction, expressed as the C/O ratio, f) the inter-sheet junction and (g) the characteristics of the wrinkles. (Galpaya 2012). The electron tunnelling resistance between the RGO junctions plays a more dominant role in the electrical conductivity of RGO polymer nanocomposites in which the RGO loadings is low and the nanocomposites are well dispersed in the insulating matrix. This type of resistance forms the resistor network for electron conductance (Potts et al. 2011). For nanocomposites with good dispersion, individual RGO sheets are separated by polymer layers, and the resultant electron tunnelling resistance can be several orders of magnitude greater than the resistance of individual RGO sheets (Potts et al. 2011).

Pristine graphene sheet has the highest conductivity, but the difficulty in fabricating a large amount of graphene by the mechanical exfoliation method limits its use as a filler. This limitation has led to the use of a thermal and chemical approach, which obtains graphene by the reduction of an insulating GO material via removing the OCFGs and thereby partially restoring the conductivity and obtaining RGO as an appropriate conductive filler for improving the polymer composite. It is reported that the reduction of GO by a thermal treatment process results in a higher electrical conductivity than that obtained through a chemical reduction process, and this is attributed to the successful absence of OCFGs in the thermal process (Galpaya 2012).

Shen et al. (2012) have reported that the electrical conductivity of RGO sheet after chemical reduction with glucose (RGO-g) shows a large increase that was ( $2.5 \times 10^2 \text{ S cm}^{-1}$ ) greater by four orders of magnitude that obtained by thermal reduction at low temperature, and suggests that thermal reduction at 210 °C is not enough. This is possibly due to (a) the presence of

oxygenated species; and (b) the smaller sp<sup>2</sup> domains created by thermal reduction process of GO (that can be verified by  $I_D/I_G$  ratio), which makes it difficult to restore the electrical conductivity network in RGO. For this reason, in current study it was used tube furnace technique at high temperature and also vacuum oven at low temperatures to obtain RGO sheets. In the current study, the electrical conductivity of RGO-120 obtained by vacuum oven method was comparable to the previous result of Shen et al. (2012), whereas RGO-160 and RGO-180 showed increases that were  $2.67 \times 10^2 \pm 6.0 \text{ S cm}^{-1}$ ,  $2.93 \times 10^2 \pm 4.0 \text{ S cm}^{-1}$ , respectively.

However, Kim et al. (2010) have investigated the impact of chemical and thermal reduction in GO sheets on the conductivity of RGO/polyurethane nanocomposites. The lower Pc value of <0.5% by volume was observed for a TRGO sample compared with that of CRGO which was >2.7 vol%. However, the CRGO sample did not exhibit any decline of surface resistance, which is similar to that observed in a GO sample. This result can be attributed to the loss of conductivity after graphite oxidation.

### **2.14.2.2 Thermal conductivity**

RGO sheets have high thermal conductivity ( $\sim 3\text{-}61 \text{ Wm}^{-1}\cdot\text{K}^{-1}$ ) governed by the lattice vibrations (phonons) (Renteria et al. 2015). This high thermal conductivity has resulted in it being employed as a filler in different applications to improve the thermal stability and thermal conductivity of polymer composites. It is important to mention that there are several factors that influence the thermal properties of the composites, such as the orientation and dispersion of the sheets and their A.R. In addition, the 2D structure of graphene sheets may have lower interfacial thermal resistance than that of CNTs, leading to a larger conductivity enhancement in polymer composites (Singh et al. 2011). A strong nano-filler/polymer interface is essential to obtaining good thermal conductivity. RGO is similar to graphene, but the thermal conductivity based on RGO composites with various polymer matrices, such as EP and PP, has been studied earlier, but not extensively (Galpaya 2012).

Shahil & Balandin (2012) have prepared TIMs based on EP and a multilayer of RGO nano-sheets. The thermal conductivity has been obtained up to values of  $\sim 5.1 \text{ Wm}^{-1} \cdot \text{K}^{-1}$  at 10 vol% concentration for TIMs, which is consistent with a thermal conductivity increase of about 2400% compared with pure EP. This large enhancement has been attributed to good dispersion of the RGO flakes and very low thermal resistance at the RGO/polymer interface.

### **2.14.3 Thermal stability**

Various researchers have studied the effect of RGO nano-sheets on the thermal properties (e.g.  $T_g$  and  $T_d$  values) of different polymer matrices. The glass transition  $T_g$  and thermal degradation  $T_d$  parameters are considered to be the most useful properties for characterizing the thermal stability of EP nanocomposites (Wei et al. 2015).

It has been observed that graphene, RGO and GO materials can increase the  $T_g$  value of EP matrix because of the strong adhesion force that occurs between the EP matrix and the nano-fillers which limits the mobility of EP chains on the nano-filler surface. In contrast, a decrease in  $T_g$  value is anticipated because of weakly adhering nano-fillers which instigate segmental motion of the polymer chains, lowering the  $T_g$  value. Chen et al. (2012) observed an increase in the  $T_g$  value of EP/RGO nanocomposite at 0.5 wt.% by 54% compared with neat EP composite (105°C), which caused by an impediment in the mobility of polymer chains arising from the hydrogen bonding with surface oxygen functionalities and strong mechanical interlocking with RGO. However, these nano-fillers are stiffer materials than the EP matrix, which could lead to considerable confinement on the polymer chains (Galpaya et al. 2014).

For thermal degradation temperatures, the  $T_d$  (defined by the maximum mass loss rate in thermal gravimetric analysis (TGA)) changed up to 30°C for EP nanocomposites by merging them with 0.5 wt. % functionalized graphene were reported (Wei et al. 2015). Prolongo et al. (2014) demonstrated that 0.5 wt. % RGO sheets can increase the  $T_d$  of EP from about 377°C to

397°C. Similarly, Yousefi et al. (2014) affirmed that both GO and RGO sheets enhanced the  $T_d$  of the EP matrix at 1.5 wt. % loading, providing higher thermal stability because of the merged nano-fillers. The decomposition of RGO-based nanocomposites is slower than pure EP, and the slower decomposition can be ascribed to a restriction in the chain mobility of polymers close to the RGO surface. In contrast, (Wang et al. 2014) merged functionalised graphene sheets into an EP matrix and reported a decrease in  $T_d$ . This decrease was due to the existence of thermally unstable chemicals, which on decomposition decreased  $T_d$  than that observed with EP.

## 2.14.4 Dielectric constant

The dielectric constant is a measure of the polarizability of a material under the influence of an electric field (Maphundu et al. 2017). Using dielectric spectroscopy, the characterisation of bulk materials and the dynamics of molecular motion of a complex material can be determined (Kochetov et al. 2012). In this research, the RGO–SiO<sub>2</sub>/EP nanocomposite samples were investigated over a frequency range of 1 KHz – 6 MHz, to study dipolar polarization mechanisms. These mechanisms provide insights into how permanent and induced electric dipoles orient themselves in the direction of the external electric field. However, most of the commercially available polymers have a low-dielectric-constant (where  $k < 10$ ). The critical value corresponding to the volume fraction of loading (vol.%) at which this transition occurs is called the percolation threshold,  $P_c$ , (Maphundu et al. 2017; Peng et al. 2013). Above the  $P_c$  value, the electrical conductivity of the nanodielectric improves because of the occurrence of a continuous build-up of conductive networks within the matrix (Maphundu et al. 2017).

In the literature review, lower dielectric constant values for the polymer nanocomposites at very low-filler contents have been reported. The lower dielectric constant values are substantially attributed to the effect of the region of the interphase. The matrix/filler interaction causes the interphase region to be more articulated at low-filler loadings. Therefore, the interphase is strongly dependent on the inter-nanoparticle distance and hence the filler concentration in the

matrix. The incorporation of nano-fillers in the matrix obstructs polymer chain movement and to a lesser extent the polarization. The low value of the dielectric constant at a low-filler loading may be that the hydroxyl groups (–OH groups) exhibit the main structure of RGO sheets (see fig. 2-3b), which can configure strong bonding with the polymer chains (Tanaka et al. 2005). Another study by Singha & Thomas (2008) suggests that the oxirane groups may lead to strong H bonds with the free –OH in the nanoparticles.

Polymer-based nanocomposites incorporating conductive carbon-fillers have been widely employed as potential dielectric materials for applications such as flexible lithium-ion battery and embedded capacitor materials (Dang et al. 2012). The large RGO sheets and their good dispersion in EP matrix play a significant role in achieving a dielectric constant well over 14,000 with 3 wt. % of RGO at 1 kHz, which has been one of the best results reported thus far. The RGO/epoxy nanocomposites present a typical percolation threshold of 0.26 wt. % because of the uniform dispersion of monolayer RGO sheets and their ultra-large size (Yousefi et al. 2014). The key requirement for fabricating nanocomposites with a high dielectric constant is to obtain a uniform dispersion of nanofillers loading into the matrix. In related work Shevchenko et al. (2012) reported a high dielectric constant of  $10^3$  using RGO/polypropylene (PP) nanocomposites prepared through an in-situ polymerization approach, and only 0.25 vol.% of RGO sheets need to have a much higher dielectric constant because of the homogeneous dispersion of RGO sheets in polymers.

In contrast, RGO material is commonly co-loaded with various inorganic parts, i.e. metal oxide nanoparticles, to enhance a specific physical property or to improve the polymer composites with multiple functions to acquire multifunctional polymer nanocomposites, which can be attained through adding small quantities of RGO concentration. For example, (Zhang et al. 2014) prepared a core–shell CuS/RGO nano-hybrid to obtain PVDF composites via an in situ growth method with the existence of Cetrimonium bromide (CTAB) powder at an elevated

temperature of 140°C, and the resultant composites showed excellent dielectric properties. Qian et al. (2013) successfully synthesised a unique structural design of Al<sub>2</sub>O<sub>3</sub> coated with a thin layer of graphene via an electrostatic self-assembly route, resulting in PVDF composites which not only exhibited high thermal conductivity and retained electrical insulation (i.e. volume resistivity recorded over  $4 \times 10^{14} \Omega \text{ cm}$ ). However, (Huang et al. 2014) fabricated RGO–SiO<sub>2</sub> hybrids by the sol–gel method, and the resultant composite was subsequently incorporated into the EP matrix. They confirmed that the filler–matrix interfacial interaction had improved mainly because of its uniform dispersion, which led to better mechanical properties. Likewise, the filler had enhanced thermal stability and the electrical properties of the EP nanocomposites, where the dielectric constant reached 77.23 at 1 kHz for with 20 wt. % of filler, 22 times that of the pure EP resin, whereas a typical percolation transition was found near 0.174 vol%. Moreover, this increase in properties can be ascribed to perfect flexibility, where the ultra-thin layers of the RGO material can cover over the surfaces of inorganic particles. Moreover, the inner silica layers' act as a stabilizer against the aggregation that provides good dispersion of RGO in the EP matrix. Thus, only small concentrations of RGO material can contribute to increasing the electrical properties. Thus, the dielectric constant is highly dependent on RGO concentration and AC frequency.

Therefore, metal or nano-metal oxide/RGO nano-hybrid 2D nanostructures, for instance, TiO<sub>2</sub>–RGO (Chen et al. 2013), Fe<sub>3</sub>O<sub>4</sub>/graphene (Wang et al. 2012) and SiO<sub>2</sub>/RGO (Kou & Gao 2011) have lately been obtained to afford higher performance in different potential applications than RGO or a non-metal/metal oxide alone. These applications include Li-ion batteries (LIBs), CO<sub>2</sub> converters and photo- catalysts (Hsiao et al. 2013).

Lastly, it is important to note that the conductivity mismatch between the EP matrix and the RGO. This conductivity mismatch led to very high charge storage capacities that are not normally associated with materials having high dielectric constants.

## 2.15 Analytical techniques

There is the essence of ensuring that RGO single sheets are products of the aforementioned synthesis approaches. Additionally, the size of these sheets, as well as the linked functional groups, are substantial in polymer dispersion. This section presents a brief and concise review of the approaches that best match the characterization accruing to GO and RGO sheets.

There is significant reluctance in characterizing RGO following its containment of few OCFGs and aromatic carbons. Consequently, only a few bands can be observed with the majority of the existing spectroscopic approaches. Nonetheless, Raman Spectroscopy is the most outstanding spectral characterization technique regarding RGO. It can be applied in the estimation of the RGO sheets' thickness and also the edges' ratio besides additional defect sites accruing to sites of pristine graphene. Considering RGO sheets, two sharp spectral characteristics prevail – the G' and G bands. Moreover, the excitation wavelength that is independent on G band is a product of the RGO's pristine aromatic system besides prevailing as ca.  $1585\text{ cm}^{-1}$ . According to Beams et al. (2015), the wavelength depicts sensitivity to alterations in the structure of RGO besides being deployed in monitoring the changes. The structural defects that accrue to the RGO structure – inclusive of the sheet edges – yield the D band, which is a new Raman active vibration. This band bears correspondence to the breathing modes accruing to the carbon rings adjacent to the prevailing defect sites. The D band can be intensive regarding damn minute graphene particles especially for scenarios involving GO particles that are highly oxidized. According to Vidano et al. (1981), the position of this band is dependent upon the underlying excitation wavelength and takes a falling trend notably from  $1360\text{ cm}^{-1}$  (wherein the excitation at  $\lambda_{ex} = 514\text{ nm}$ ) up to  $1325\text{ cm}^{-1}$  (wherein the excitation at  $\lambda = 647.1\text{ nm}$ ). Additionally, Ni et al. (2008) assert that the strength accruing to D band relative to that of G band robustly relies upon the magnitude of the disorder dominating the graphitic materials.



RGO research often entails two primary X-ray approaches - XRD (X-ray diffraction) and XPS (X-ray photoelectron spectroscopy). Guo et al. (2009) reveal that the XRD measurement amounts to informative equipment in probing the structure, local symmetry, and oxidation state, a condition that is productive for experimenting crystalline structure – a key parameter regarding operations with polymer nanocomposites. Nonetheless, there is a constrained utility of the XRD with the plain RGO even though it avails extra information regarding the thicker structures. XRD finds its application in demonstrating the intercalation linked to graphite. Bragg's equation proved key in determining the d-spacing accruing to RGO, graphite, and GO

$$n\lambda = 2d\sin\theta$$

where  $n$  is the order of diffraction (an integer),  $\lambda$  refers to the wavelength,  $d$  denotes the prevailing interlayer spacing while  $\theta$  refers to the scattering angle.

For instance, the sharp reflection prevalent at  $2\theta = 26.3^\circ$  (Cu  $K\alpha$  radiation, X-ray  $\lambda = 0.154$  nm) in graphite notably undergoes a shift  $14.1^\circ$ - $14.9^\circ$  in graphite oxide and shifts to  $9^\circ$ - $12^\circ$  in GO. Nonetheless, XRD vanishes as exfoliation of the GO sheets occurs to yield single sheets. According to Guo et al. (2009), an outstanding function accruing to XRD regarding the characterization of the graphene sheet entails confirmation of the process of reducing GO into RGO.

Application of the XPS facilitates acquisition of information regarding the elemental constitution of materials as well as the chemical domain of the underlying atoms. Considering graphene, only the aromatic carbons ought to be monitored, apart from other minor  $sp^3$  carbons prevalent at the edges. Invariably, the XPS provides much information linked to the chemically manipulated graphene, like RGO and GO since it can encounter application in computing the C/O ratio besides the identification of the specific form of oxygen functionalities.

The aggregate extent of oxidation can further encounter quantification from standard elemental analysis. Moreover, the XPS can measure the oxygen quantity dominating the surface besides

detecting the types of bonds between carbon and oxygen. The existence of chemical shifts accruing to XPS Cas spectra affirms prevalence of C=O, O-C=O, or C-O on RGO and GO even though they are constrained to the quantification of their comparative amounts. Identically, Infrared absorption bears similar constraints. XPS further paves room for characterization of the defects dominating GO/RGO besides offering a piece of qualitative information regarding the defects. Considering XPS, the peak ratio of C1s: O1s can be correlated to the approximation of the RGO sheets' defect density. According to Matteyi et al. (2009), a higher ratio figure depicts better reduction as well as lower defects.

IR (Infrared spectroscopy) has little application in pure graphene as it practically has no active IR vibrations. Nonetheless, a weak band following a C=C bond linked to vibration may encounter detection. On the other hand, the scenario is different for the IR spectrum accruing to RGO and GO. It is dominated with various oxygen correlated vibration bands that are challenging to detect following the overlapping of the prevalent broad bands as well as the multiple vibrations that are closely related. According to Sing et al. (2012), this massive distinction between the RGO spectra and graphene declares IR a fairly productive tool regarding monitoring of the oxidation accruing to the RGO or graphene.

Regarding FTIR, the common peaks that bear correspondence to functional systems in GO entail O-H stretching at 3400cm<sup>-1</sup>, C=O stretching at 1687-1710 cm<sup>-1</sup>, C-H stretching at 2910 cm<sup>-1</sup>, C-O stretching at 1208 cm<sup>-1</sup>, C-H stretching at 2875 cm<sup>-1</sup>, C=C stretching at 1542-1568 cm<sup>-1</sup>, C-O-H bending at 1409 cm<sup>-1</sup>, and C-OH stretching at 1113 cm<sup>-1</sup> (Yang et al. 2012). These elementary signals get much weaker as some of them even vanished over RGO, a condition indicating the substantial reduction of GO into RGO. Additionally, the authors deployed Raman to depict extra confirmation of the effective omission of functional groups from GO besides indicating the yield of RGO. Following the distinction in the preparation analogy as well as the interaction between RGO supports and polymer, the ranks of the

elementary peaks emanating from the functional groups may encounter a slight shift (Karimzadeh et al.2015). The usage of FTIR notably for examining the structural integrity accruing to RGO-dependent polymer nanocomposites was broadly adopted. The FTIR outcome is substantially a partial assertion regarding the residual detection following the identification constraint of the tool. Sing et al. (2012) assert that an outstanding recommendation entails combining this approach with other methods like XPS, XRD, and Raman to achieve further confirmation of the underlying information.

Krishnamoorthy et al. (2012) reveal that TGA amounts to an analytical approach deployed in determining the thermal stability of a material as well as its fraction regarding volatile elements by evaluating the weight change that prevails amidst heating of a specimen. Nonetheless, the measurement can typically take place in the air, an inactive atmosphere (like argon, or helium), and recording of the weight as a function of as a function of increasing temperature (Stankovich et al. 2007). Invariably, the TGA tool is applied in quantifying and analyzing organic species prevalent between the RGO layers besides probing the efficiency of reactions involving reduction and oxidation (Some et al. 2013). Practical TGA analysis was done to examine the GO sheet's thermal stability besides comparing it to that of the precursor graphite and the RGO. The TGA examination regarding graphite depicts its high thermal stability despite the temperature escalating to 1000°C. Following the fact that GO is not thermally stable, it commences losing mass as from 100°C as a result of the vaporizing volatiles and the previously absorbed water particles in the layers of the GO sheet. According to Durmus et al. (2014), the primary loss in mass prevails in the range 180-200°C following removal of the prevalent OCFGs like -OH, COOH, and epoxide. Moon et al. (2010) connotes regarding RGO that the OCFGs were already gotten rid of amidst the reduction reaction, hence the aggregate loss in weight is evident in the 300-900°C temperature range – it can be linked to the existence of some remnants of organic species notably on the sheets, asserting the better thermal stability for RGO than for GO.

Correlations between the characteristics and structure of nano-composite materials can be revealed via linkage of structural examinations (like XRD and Raman spectroscopy) as well as mechanical tests to yield a superior interpretation of the underlying nanocomposites. Invariably, the repercussions of amplifying the content of filler in the mechanical properties linked to polymer nano-composites can be experimented via flexural, impact, or tensile tests. Some former outcomes for mechanical properties of EP reinforced with carbon nano-structures like graphene and RGO are evident from the literature of Botta et al. (2018). According to Kuan et al. (2008), incorporating carbon fillers notably into a polymer matrix bears high expectations of enhancing the mechanical characteristics, more precisely once graphene, carbon, and RGO nanotubes are deployed as the reinforcing materials. Nevertheless, the dispersion accruing to nanoparticles in polymer materials as well as the interfacial adhesion binding the matrix and the nanoparticles have a substantial effect on the underlying mechanical properties. Invariably, in such a scenario of homogeneous dispersion regarding nanofillers, the prevalent failure approach is pull-out besides yielding higher strength notably in the polymer nanocomposite materials. The nanocomposite preparation approaches are crucial besides the fact that the heterogeneous dispersion can yield earlier failure for the matrix and hence the desired properties cannot be attained. According to Altan et al. (2016), some agglomerates can prevail and consequently reduce the nano-composites' strength.

Several imaging approaches are frequently deployed in measuring the number of RGO layers in structures besides studying the arrangement accruing to the RGO-dependent polymer in existing composites. Such methods entail scanning electron microscopy (SEM), transmission electron microscopy (TEM), and atomic force microscopy (AFM).

AFM is tool in the identification of distinct sheets on plane surfaces as well as in estimating the thickness and size of the sheet. This approach yields information regarding small domains only even though it can meet deployment in several forms of evaluation set-ups, inclusive of nanoindentation and conductivity on a unit sheet of graphene or RGO. The reliability and

convenience accruing to AFM declare it the top-most technique linked to layer number counting and thickness measurement. Considering a typical measurement, this approach uses a cantilever in conjunction with a sharpened tip (approximately 5-10 nm), which scans across the RGO-based substrate's surface. Nevertheless, the sensitive alterations in the vibration amplitude, as well as the tip's frequency, are gathered following the subtle transformations regarding the surface's heterogeneity, a condition favoring analysis of the sample's topography. The attained 3-D images facilitate the evaluation of the graphene films' thickness. Since perfect graphene bears a unit atom thickness of approximately 0.35 nm, counting the number of the underlying layer could occur. The primary issue regarding imaging of a single atom thick graphene entails that rarely an absolute contact prevails between the sample and the tip. Moreover, according to Thomas (2013), surface chemistry and image feedback settings further, influence the results. Even though AFM was broadly utilized in counting layers and determining thickness, a broad range of the measured values (notably 0.3-0.5 nm) was revealed from the literature linked to the thickness of a unit layer graphene, asserting an element of inaccuracy. This analogy asserts the necessity of high experimental competency once deploying AFM since the aforementioned scenario will frequently prevail. Considering a tapping mode AFM image regarding RGO notably on a mica material, the mean thickness is approximately 0.8 nm. This value is very similar to the reported thickness of GO mono-layer. Having pristine graphene whose thickness is nearly 0.4 nm, the relatively higher thickness accruing to as-made RGO is attributed to the prevalence of the covalent bonds (C-O) at both the top and underneath surfaces, absorbed contamination, and distorted sp<sup>3</sup> carbon lattices. Whereas the mean thickness of GO sheet is approximately 1.2 nm.

Furthermore, TEM and SEM are typically used in the visualization of structure and morphology accruing to RGO sheets as well as its polymer nano-composites that offer pieces of information to the visualization of dispersion notably in the polymer matrix. SEM facilitates the study of larger structures or rather areas. The electron beam facilitates scanning of samples prevalent in

the SEM microscope. Once the electron beam meets movement across the sample's surface, the underlying charge accumulates on it hence affecting the imaging process if the subject sample is non-conductor. Nevertheless, TEM can similarly detect an RGO sheet's thickness accurately. This approach calls for thin samples even though the measurements meet a downfall from the sheets' transparency. Regarding the SAED (selected area diffraction mode), TEM bears the potential of mapping the atoms accruing to RGO substrates besides connoting the sheets' number of strata or the dominant RGO defects.

In addition to that, DMA (dynamic mechanical analysis) is an approach for characterizing the viscoelastic behavior of a material. It entails evaluating the material's response towards an oscillating force as a key function of the underlying temperature. Invariably, the oscillating vigor exerts sinusoidal stress given by:  $(\sigma = \sigma_0 \sin \omega t)$  on the sample hence yielding a substantial sinusoidal strain. The deformation amplitude accruing to the sine wave's peak and the lag between strain and stress sine waves undergo effective measurement to facilitate computation of a complex modulus as shown:  $(E^* = E' + iE'')$ . Wherein  $(E')$  is the storage modulus which implies the stress that's in phase with the underlying strain over the strain experiencing sinusoidal deformation. It measures the energy-storage potential of a material. Additionally,  $(E'')$  is the loss modulus, which refers to the stress off phase with the prevalent strain overstrain and it is a key measure of the energy dissipation potential of a material. The loss tangent refers to the ratio storage modulus: loss modulus as shown:  $(\tan \delta = E''/E')$ . According to ASTM Standards (2006),  $T_g$  can be attained by executing a DMA experimentation while the temperature increase at a fixed heating rate as per ASTM D4065-06. Testing of samples can be tested under varying configurations like torsion, single cantilever, or dual cantilever. Menard (2008) asserts that the configuration alternatives are relying upon the material type, a form of stress on the material, and the material's modulus. Furthermore, the storage modulus accruing to EP nanocomposites (1.9 GPa and exceeding 13%) were tracked following the addition of 0.1 and 2 wt. % of RGO at 40°C, respectively. Olowojoba (2017) depicts that the influential factors

that increasing the ( $E'_g$ ), as reported in the literature, may encompass the RGO's wavy topology as well as the RGO lattice's imperfections emanating from the  $sp^3$ -hybridized fields that pave way for better mechanical interlocking notably between the EP matrix and the RGO. Additionally, the OCFGs undergo a reaction with the EP resulting in covalent bonds formation and hence an improved filler-matrix interface besides achieving increased load transfer properties. According to Olowojoba (2007), the reduction of the underlying storage modulus amidst glassy state domain emanates from the rising molecular mobility.

Nonetheless, the RGO bears the potential to improve the EP matrix's  $T_g$  following the adhesion force acting between the RGO and EP to decrease the EP chains' mobility on the underlying RGO surface. On the other hand, a reduction in  $T_g$  is probable for unstable interfaces and weak-adhering fillers allowing mobility of the chain polymer hence reducing the  $T_g$ . According to Li et al. (2012), an increase in the EP's  $T_g$  prevails after constraining segmental movement of the polymer chains through hydrogen bonding and mechanical interlocking with the functionalities of the surface oxygen. Moreover, Park et al. (2014) have measured a  $T_g$  amplification of 14°C in the EP/RGO nanocomposites at 1phr (parts-per-hundred-resin) of RGO notably in an EP matrix. Invariably, this analogy depicts an expected result accruing to the robust adhesion between the matrix and the filler following the conformational alterations of the matrix at the dominating interface (EP/RGO). Nonetheless, there has been vast reporting that RGO lowers the thermal degradation temperature or rather the glass transition of the EP matrix even though hardly there is unanimous accord regarding this adverse trend. According to Galpaya et al. (2014) suggested a theory, nanocomposites'  $T_g$  is dependent upon the equilibrium between two effects -molecular confinement and impact on reaction conversion. The EP matrix is less stiff than the RGO sheets, a condition that can result in substantial confinement notably on the material polymer chains. Invariably the RGO sheets may further impede the curing reaction of the EP following a reaction of the curing agent or EP resin and the functional groups dominating the RGO surface. The condition may further emanate from the RGO sheets' covering of the

resin's reactive sites following its extensive surface area. Chief prevalence of this analogy would yield a reduction of the cross-link density of the polymer besides increasing the mobility of the polymer chain.

Furthermore, the various reduction approaches yielded exfoliated RGO sheets bearing varying amounts and forms of the remaining operational groups – as asserted by characterization of XRD, FT-IR, TGA, and Raman. In addition to that, their electrical conductivity dominated the range 200 to  $2.98 \times 10^4$  S m<sup>-1</sup> notably at 24°C. The four-probe method can be effective in measuring the underlying electrical resistance. The Keithley paradigm 8009 test connected with 6517B Electrometer was deployed to attain a 0.5 pA (pico-ampere) accuracy. This approach bears merit of high precision as a result of eradicating the impedance contribution emanating from the contact resistance and wiring. The conduction of electricity in nanocomposites results from the establishment of a progressive conductive network set up by the fillers. Consequently, the spherical nanofillers are less probable of percolating at reduced volumetric concentrations compared to the aligned nanosheets. An ideal material to attain such a percolated network at reduced loading fractions is graphene following its property of 2-D structure as well as intrinsically high conductivity. Wajid et al. (2013) presented that the ultra-low electrical percolation threshold was at 0.088 vol. % for EP/Graphene nanocomposites. This result was attained by dispersing the graphene with the aid of tip sonication, shear mixing, and mechanical mixing. Identically, Liang et al. (2009) further reported substantial amplification in the underlying electrical conductivity by adding RGO into EP nanocomposites matrix notably by mechanical mixing and bath sonication. The conductivity's improvement was  $0.8 \times 10^{-10}$  –  $0.8 \times 10^{-2}$  S/cm after addition of 8 vol. % of RGO into the underlying EP. Such enhancements are only valid once the RGO undergo thorough de-bundling and homogeneous dispersion in an epoxy matrix. Moreover, Monti et al. (2013) reported dispersing RGO into EP matrix to examine the prevalent electrical conductivities. Targeting at enhancing the dispersion, they applied mechanical mixing and tip sonication on the mixture processing besides deploying



various solvents like THF or chloroform. The superior electrical conductivity manifested for the sample having 3 wt. % RGO besides noting that an amplification of the RGO concentration increased the corresponding thermal conductivity.

LCR meter is a piece of equipment for performing an electronic test and it computes the capacitance (C), inductance (L), as well as the resistance (R) accruing to a conductor. This machine proves to be ideal transfer equipment amidst comparison of nominally identical values of impedance. The linearity properties are much better for the narrower evaluation ranges. LCR functioning above a frequency range of 20-10<sup>6</sup> Hz and high precision as well as accuracy have invaded in the commercial industry and have only facilitated measurement uncertainties regarding the metrological level. Insulation characteristics fluctuate reasonably with the underlying frequency, hence an instrument for measuring a broad programmable range of frequency should be available. Improving the results' accuracy can initiate the achievement of enhanced process control, grander products, and increased efficiency. According to Suzuki et al. (2001), this analogy can be facilitated by taking an average of several measurements besides using computer programs to simplify the computation results.

The dielectric constant accruing to GO papers (nearly 70@ 10 kHz) was much inferior to that of the RGO counterparts following the electrical insulation property of GO sheets that hindered the relevant interfacial polarization. The ultra-large RGO sheets yielded outstanding dielectric constants exceeding 24,000 @ 1 Hz and nearly 22,000 at 1 kHz, the highest values ever evident from the open sources. The outstanding dielectric constant in the papers compared to the one in the polymer-based nanocomposites emanates from the comparatively higher volume of fraction in the RGO sheets than in the nanocomposites. Invariably, the RGO papers prove to be unsuitable for use as dielectric capacitors following their certainly high dielectric losses ranging from 100,000 and 70 at a frequency range of 1Hz – 1MHz besides having a standard value exceeding 3000 at 1 kHz for the GO papers. According to Yousefi et al. (2013), the

accountability to this analogy accrues to the damn weak interfacial bonds prevalent between the sample's RGO sheets.

Considering the conductive fillers, graphene, and RGO sheets have nurtured the researchers' attention. Invariably, Nan et al. (2010) reveal that graphene depicts a large aspect ratio besides amalgamating with special thermal, electrical, and mechanical stability that has been deployed in enhancing the EP's dielectric constant successfully as per the micro-capacitor model. Nonetheless, the dielectric loss accruing to the composite was typically amplified once the formation of the conductive paths occurred. More precisely, the composites transformed into conductors and not dielectric materials following the establishment of the conductive network, an analogy that hindered further usage as dielectric substrates. Consequently, Zhu et al. (2017) assert that a significant challenge entails enhancing the conductive fillers' dispersion in the underlying polymer matrix as well as restraining the composite's dielectric loss. As a result, applying surface modification on graphene is relevant.

Nevertheless, altering the surface characteristics further improves the compatibility accruing to polymers and graphene. Lately, Wei et al (2015) reported that a dielectric constant of 600 at a frequency of 1 kHz was revealed after the addition of 3 wt. % of graphene into an epoxy resin. On the other hand, as asserted by Wang et al. (2015), GO typically underwent adoption to achieve epoxy-based composites that have high dielectric constants following its versatile modification and good compatibility. For instance, the self-arranged RGO/epoxy nanocomposites (3 wt.% RGO) having highly anisotropic electrical characteristics are evident to bear exceptionally sound dielectric constant – 32 at a 1 kHz frequency, a value that is amongst the highest values ever spotted for operational epoxy-based nanocomposites (Wan et al. 2016). Moreover, several materials and structural properties of the composites and fillers yield are obligatory for this outcome, like the ultra-large magnitude of the RGO sheets, splendid dispersion of the RGO in an epoxy resin, as well as the RGO sheets' self-alignment into a

structure of layers. The composites further bear extremely high dielectric constants reliable upon the content of the RGO following the alteration of the accumulation at the superiorly conductive insulating/filler polymer interface as per the principle of polarization.

In addition to that, the ultrathin sheet of RGO applied on silica surfaces encountered the perception of being the key account for the improvement. Being on the interface of silica and epoxy, RGO operated as an eccentric coupling agent regarding the silica filler, a condition that reasonably improved the interfacial interaction between the composites of EP/SiO<sub>2</sub>-RGO and hence substantially enhanced the EP resin's mechanical characteristics. This approach can practically improve the dielectric properties accruing to polymer composites as the composite fillers hardly link directly to the polymer matrix, hence reduction of the dielectric loss and leakage currents is possible. Nonetheless, the treatment procedure of carbon nanotubes is chiefly complex besides being challenging to meet applications in the electronics sector. Consequently, there is a necessity and urgency of preparing the splendid dielectric substances by an effective and simple approach to satisfy extra industrial demands.

The tensile test machine meets intensive application in the determination of the tensile properties of the neat epoxy and RGO sheets reinforced EP composites as per the ISO 527.2 test process. The excellent reinforcement is attributed to the good dispersion of RGO sheets in the composites and also the robust physical/chemical interactions between the them. Furthermore, high modulus regarding RGO paves way for favorable load transfer notably from the matrix into the RGO sheets, resulting in high tensile strength as well as stress at key break values. The defects accruing to the sheet structure as a result of pyrolysis and oxidation potentially lower the effective in-plane stiffness of RGO, a reason for the comparatively small increase in the tensile properties evident for the glassy polymers. In conjunction with an increase in stiffness, the tensile strength also realized an improvement. Elongation for breaking normally falls severally after addition of substantially rigid fillers. However, elongation

accruing to most polymers fell with the incorporation of graphene or RGO even though the extent of the decrease is inferior to expectations. The defect-free graphene proves to be the stiffest substance (nearly 1 TPa) ever evident naturally and also has superior intrinsic strength of approximately 130 GPa. Acknowledging the prevalence of minor structural distortions, the examined elastic modulus accruing to RGO sheets is further outstanding at 0.25 TPa. While modulus increase with RGO dispersion is evident for all polymers, the analogy is sounder for the elastomeric matrices following the greater stiffness contrast that prevails between matrix and reinforcement. Regarding the glassy polymers, the quite surprising outcomes manifested from PMMA (33% enhancement at 0.01 wt. %) as well as epoxy (31% growth at 0.1 wt. %) with RGO reinforcement. This analogy has been linked to the robust hydrogen-bonding interaction regarding RGO's OCFGs as well as the mechanical interlocking dominant at the crumpled surface that may bar segmental mobility notably for the polymer chains close to the RGO surfaces (Ramanathan et al. 2008 & Rafiee et al. 2009).

The approach of nanoindentation has been intensively used to characterize of local mechanical properties accruing to various materials like nanocomposites and polymers. It can further be deployed in the collection of comparative elastic modulus as well as hardness data notably for RGO-based epoxy nano-composites. The fundamental concept regarding indentation experimenting entails touching a material whose mechanical properties are of interest with a material whose properties are known. Invariably, nanoindentation outstands as a unique indentation examination wherein measurement of the penetration distance occurs in nanometers (nm). Following the surface area of the sample and the small depth requirements, thin-film samples are effective for this testing approach. A key determinant in evaluating indentation data entails the area of contact notably between the specimen and the indenter. In typical indentation testing the area of contact is simply calculated from measurements of the residual impression left on the specimen. However, Al-Haik (2004) reveals that the contact area is in microns for nanoindentation and it hence proves to be too small for accurate measurement. Instead, the

penetration depth into the underlying specimen surface can be measured for combination with the acknowledged geometry accruing to the indenter for computation of the contact area. Additionally, the data collected amidst the indentation test, regarding load displacement, offers the basics for computing the hardness and modulus. Al-Haik (2004) reveals that the maximum indenter depth realized for a certain load as well as the gradient of the unloading graph (curve) computed tangential to the data instance at maximum weight is deployed in determining the modulus and hardness as per the approach presented by Pharr and Oliver.

Considering indentation loading, creep in a specimen can prevail to yield an alteration in indentation depth after application of a fixed test force. There is a slight distinction from thermal drift hence effective result interpretation is key. According to Al-Haik (2004), many studies executing nanoindentation notably on polymers, inclusive of EP, PMMA, and PS, have depicted large values of modulus relative to the evident tensile examination or rather DMA on the identical substances.

## **2.16 Applications**

Static electricity is a phenomenon arising from an imbalance of electric charges on the surface of materials (Vinson & Liou 2000). The most common way to generate this type of charge is through the contact and separation of materials, which is known as triboelectric charging (Ott 2009). When there is contact between two dissimilar materials, some materials tend to absorb/gain free charges, whilst others are prone to give up charges easily. Materials that tend to absorb electrons have a higher affinity for negative charge appearing on the two materials, and that surface is negatively charged after the dissimilar materials are separated. There are several factors that influence the magnitude of charge transfer, such as the dissimilarity in the attraction between two dissimilar materials to absorb electrons, the speed of separation and the pressure of contact.

The polymeric materials utilized in electronic devices are often insulating components, as the free electric charges build up on their surfaces and hence result in likely destruction because of catastrophic discharge. A large number of studies have been performed to advance conductive polymer compounds (CPCs) (Meng et al. 2017; Chun et al. 2010; Park et al. 2014; Jia et al. 2005). To overcome this problem, adding conducting fillers within polymeric matrices through developed preparation approaches improves the conductivity of the insulating matrix and may also enhance the mechanical properties such as the elastic modulus and the thermal properties.

CPCs are synthesised by adding conductive fillers (e.g. RGO, graphene, CNTs and metal NPs) in the host polymer. The traditional polymers materials such as PS, PC and EP are insulative; whereas, incorporating these matrices with conductive fillers can confer them with a broad range of conductivities via building up the conductive paths in a matrix and a configuration of a 2D or 3D conductive network.

While many challenges still exist for improving nanocomposites, some applications have already been made in different fields such as electrostatic discharge (ESD) protection (e.g. components of fuel injection systems for the automotive industry), electromagnetic interference (EMI) shielding (e.g. for protecting electronic devices) and electronic industrial applications. In contrast, the type and the amount of nano-filler introduced into the polymer matrix depends on the required mechanical and electrical properties and are determined by the intended applications. EMI shielding, ESD protection and charge storage are the main industrial applications for CPCs, and they demand high, average and low conductivity, respectively. Table 2-8 summarizes the utilized domain of conductivity for each of these CPC applications.

**Table 2.16.** The range of conductive values versus their CPC applications (Narkis et al. 1998).

Range of CPCs applications	Electrical Conductivity (S.m <sup>-1</sup> )
<b>Electromagnetic-interference/ EMI shielding</b>	$> 10^{+1}$
<b>Electrostatic discharge/ ESD Production</b>	$10^{-3}$ to $10^{-6}$
<b>Antistatic Dissipation</b>	$10^{-7}$ to $10^{-10}$
<b>Charge-Storage</b>	$< 10^{-11}$

Fig. 2-7 illustrates several uses of CPCs requiring specific domains of electrical conductivity. CPCs can offer advantageous dielectric properties within the low conductivity range for use in a charge-storage application, where the nanocapacitor structures involving the nano-fillers represent nanoelectrodes while the polymer matrix represents a nano-dielectric (Dang et al. 2007; Dang et al. 2012).

The CPCs used in ESD protection and antistatic dissipation applications typically have a medium electrical conductivity between  $10^{-3}$  and  $10^{-6}$  and  $10^{-7}$  and  $10^{-10}$ , respectively. In contrast, antistatic applications are characterized by materials that have the slowest way for charge to be dissipated, making it important to consider relative motion that occurs between the non-identical materials, such as airplane tyres and belts. ESD protection is also important in materials that can enable leaking accumulated surface charge to obviate damaging arcing discharges. These ESD applications are found in printed circuit board or electronic chips and other sensitive equipment (Strumpler 1999).



**Figure 2-4.** Images of some significant CPCs materials. From left side to right: Capacitors related to charge storage application; aircraft tyre/ antistatic material; circuit board material

*for ESD application; mobile phone/ EMI shielding (Strumpler 1999; Dang et al. 2012; Arjmand 2012).*

CPCs with high electrical conductivity can be employed for EMI shielding applications (Yang et al. 2005). Highly conductive CPCs, i.e. CPCs holding many interacting mobile charge carriers might also shield the EMI effectively.

The high conductivity with high A.R morphology for RGO or graphene sheets can enable Pc thresholds at lower content compared with that of MWCNTs and carbon black. This electrical conductivity offers applications of the conducting polymer (CP) to EMI shielding and ESD protection. The surface resistivity for ESD materials was found to be between  $10^{12}$  to  $10^5$   $\Omega$ /square, whereas EMI shielding material is reported to be less than  $10^5$   $\Omega$ /square. The EMI shielding efficiency in a chemical reduction of GO reinforced epoxy (CMG/EP) nanocomposite for 15 wt. % concentration from hydrazine reduced GO (Liang et al. 2009; Das & Prusty 2013) meets the industrial specification of about 20 dB in the X-band.



### **3 Chapter 3: Synthesis and characterise of RGO sheets reduction via a tube furnace at high temperature and vacuum oven at low-temperatures**

### 3.1 Introduction

A variety of reduction processes have been applied to GO to recover its lost electrical conductivity and mechanical properties (due to defects of structure) with different properties, such as the chemical and thermal reduction processes (Huh 2011; Chua & Pumera 2014).

Graphite oxide has been used as a starting material of thermal reduction at high temperature in previous studies, which reported a large rupture of the original  $sp^2$  structure because of the presence of OCFGs that converted to non-distribution gases along the surfaces and build up a large pressure between the layers to split into individual RGO layers. In this work, with the aid of sonication, graphite oxide splits into mono-few layers of GO that are then used directly through a thermal reduction process rather than graphite oxide in order to minimise the tear of the original  $sp^2$  structure. In contrast, the thermal reduction at high temperature is the main influence in the RGO structure, where many defects are formed because of in-plane C=C cracking during the removal of the residual partial epoxide group and hydroxyl group.

However, energy consumption is large, and hitches are everywhere in the operation when thermal treatment at very high temperatures occurs with fast heating rates. Thermal exfoliation of GO at a very low temperature is now essential. GO exfoliation and subsequent chemical reduction in solution were used to investigate several techniques to obtain RGO, but extra consideration should be given to the removal of residual solvents from the products and the safety of the solvents that were utilized. Therefore, it can be assumed that the techniques that are more promising are those that prepare RGO directly from dry GO powder at a low-exfoliation temperature.

There are a number of ways reduction can be achieved, though they are all methods based on chemical, thermal or electrochemical means. Some of these techniques are able to produce very high quality RGO, similar to pristine graphene, but can be complex or time consuming to carry

out. These methods, however, have many disadvantages and limitations including high energy requirement, low yield in terms of surface area, and limitation of instrument.

In recent years, the most commonly used chemical treatment can eliminate functional groups on GO to produce RGO with using highly toxic and harmful reducing agents. There is a possibility of creating significant environmental and health risk. Thermally reducing GO at higher temperatures such as 1000°C that has been shown the damages the morphology, electrical properties of the graphene platelets as pressure between builds up and carbon dioxide or carbon monoxide gases are released. The fast evolution of these gases has also been shown to exfoliate individual RGO sheets. This also causes a substantial reduction in the mass of the GO, creating imperfections and vacancies, and potentially also having an effect on the mechanical strength of the RGO produced.

Up to now, the vacuum oven-assisted method has become a promising route to produce very high quality RGO sheets. The RGO derived by this method could contain a significant amount of functional groups, as well as maintaining or improving the desired physical and chemical properties (morphology, mechanical strength, conductivity, optical properties, solubility/dispersibility nanosheets, etc.). This is because it is simple, inexpensive, and suitable for large-scale or mass production. Other primary benefits of this techniques are that there are no hazardous chemicals used, meaning no toxic waste to dispose of.

Inspired by the above facts, we herein, for the first time, propose a facile method for the reduction of GO.

Herein, we report a vacuum oven-assisted approach for in situ reduction of GO in large quantity at temperatures as low as 120, 160 and 180°C, and also thermal reduction of GO powder at high temperature via tube furnace technique at 1400°C. The novelty of this study is to synthesize an environmentally friendly, low-cost, highly efficient and simple methodology for the preparation

of RGO nanosheets.

By using AFM, FT-IR, XRD, Raman, XPS, TGA, SEM, TEM and four-point probe technique results, a thermal reduction process of GO within a temperature range of 120 to 180°C was investigated in detail and compared to thermal reduction at high temperature (1400°C) via a tube furnace.

## 3.2 Experimental section

### 3.2.1 Materials

The materials employed in the work are described in Table 3-1.

*Table 3-1. Displaying the characteristics, manufacturer and supplier of the materials used.*

<i>Material</i>	<i>Characteristics</i>	<i>Manufacture/ UK</i>	<i>Supplier/UK</i>
Synthetic graphite	Powder with grain size $\leq 20$ $\mu\text{m}$	Sigma-Aldrich	Sigma-Aldrich
Potassium permanganate	Powder of 97% purity		
Sodium nitrate ( $\text{NaNO}_3$ )	Powder of $\geq 99\%$ purity		
Hydrochloric acid (HCl)	Solution of 37 % purity in $\text{H}_2\text{O}$		
Sulphuric acid ( $\text{H}_2\text{SO}_4$ )	Solution of (95–98) %		
Hydrogen peroxide ( $\text{H}_2\text{O}_2$ )	Solution of (29–32) % purity in $\text{H}_2\text{O}$		

All the materials were used as received, without additional purifications.

### 3.2.2 The preparation of graphite oxide

A modified Hummers' method according to (Marcano et al. 2010) is employed to generate a graphite oxide solution. Briefly, 6 g of graphite powder (flake, 20  $\mu\text{m}$ ) and 3 g of  $\text{NaNO}_3$  were mixed together in an ice bath to control the sudden increase in temperature. A strong oxidant  $\text{H}_2\text{SO}_4$  solution (138 ml) was added slowly into the mixture and stirred vigorously for 30 min.

Then, 50 wt. % of  $\text{KMnO}_4$  (18 g) was added gradually to the mixture under constant stirring and heated up to  $35^\circ\text{C}$  for 24 h. Another 50 wt. % of  $\text{KMnO}_4$  was added progressively to the reaction mixture and stirred for 24 h. The yielded graphite oxide was treated further with added distilled water (400 mL) and  $\text{H}_2\text{O}_2$  solution (15 ml) until the colour turned a brilliant brown, indicating fully oxidized graphite. The mixture was separated by centrifugation and washed abundantly with distilled water and 5% HCl for 30 min at 10500 rpm till the pH of the solution reached approximately 4.5. Then, dialysis bags with a 14000 molecular weight cut off (manufacture by Fisher Scientific) were used to increase the value of pH, where the graphite oxide solution was placed inside the dialysis bags (30.5 cm – 21.3 mm wet diameter -  $3.57 \text{ ml.cm}^{-1}$ ) and totally immersed in a container filled with distilled water which was changed every 72 h. To ensure successful purification of graphite oxide solution, a water pump was employed to facilitate the water movement. After 124 h of processing via this method, the graphite oxide solution reached a pH between 6.5 and 7.0. Therefore, the repulsion force between individual GO sheets (basic medium) would be higher and hence react in a more stable manner.

### **3.2.3 The preparation of GO**

GO was prepared according to the method of (Ming et al. 2013) using the ultrasonication technique. The resultant graphite oxide suspension obtained from Hummers' method was exfoliated to generate GO nano-sheets by sonication at room temperature for 1 h using an ultrasonic generator (37 kHz, 280 W, Fisher brand Elma, Germany), centrifuged for 30 min at 8000 rpm and then poured in metallic dishes and frozen in a freezer at  $-40^\circ\text{C}$  for 48 h. Then, the frozen GO was dried in a freeze dryer (300 W, Bradley refrigeration. Edwards, UK) under a pressure around  $10^{-1}$  bar at  $-54^\circ\text{C}$  for 96 h. A fluffy powder of GO was obtained from this process (7.0 g), as shown in Fig. 3-1 (in the left side of the image).

## 3.3 Section One

### 3.3.1 Reduction by using a tube furnace

The procedure for preparing RGO powder was mainly based on the work of Mukhopadhyay (2013), but this approach is applied in this current study to the reduce GO instead of graphite oxide to obtain RGO sheets, as seen in Scheme 3-1. RGO was obtained by placing GO (5 g) into a quartz tube of an inner diameter of 40 mm and a length of 60 cm, sealed with one end. The other end of the tube (small vent) was closed with a rubber stopper and an argon (Ar) inlet was passed through the rubber stopper. The GO sample was flushed with Ar for 10 min and the quartz tube was then rapidly inserted into a pre-heated tube furnace (Elite Thermal Systems Limited) at 1400°C for about 30 s. This procedure acts as a thermal shock for the GO sample which is dependent on the decomposition rate of the OCFGs to complete the exfoliation process.

The rapid temperature increase makes the OCFGs attached on the carbon plane decompose into gases such as CO and CO<sub>2</sub> that build up a large pressure between the stacked layers, overcoming the van der Waals forces and providing of about 80% of the RGO sheets, which consist of single layers. This reduction process is accompanied by a volume expansion of 100–300 times: consequently, very low-bulk density RGO nano-sheets, highly wrinkled because of the loss of CO<sub>2</sub>, are obtained. Heating of the brown GO yields a black powder of RGO with a weight that is lower by about 62%, as shown in Fig. 3-1. The resultant sheets were shown to be electrically conducting, indicating they were not GO, which is insulating.

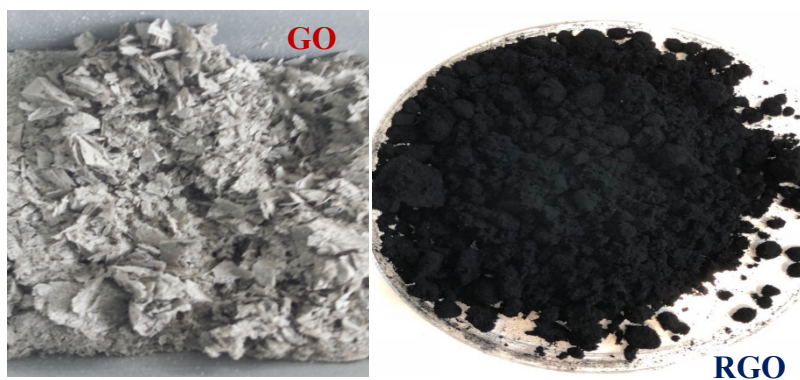
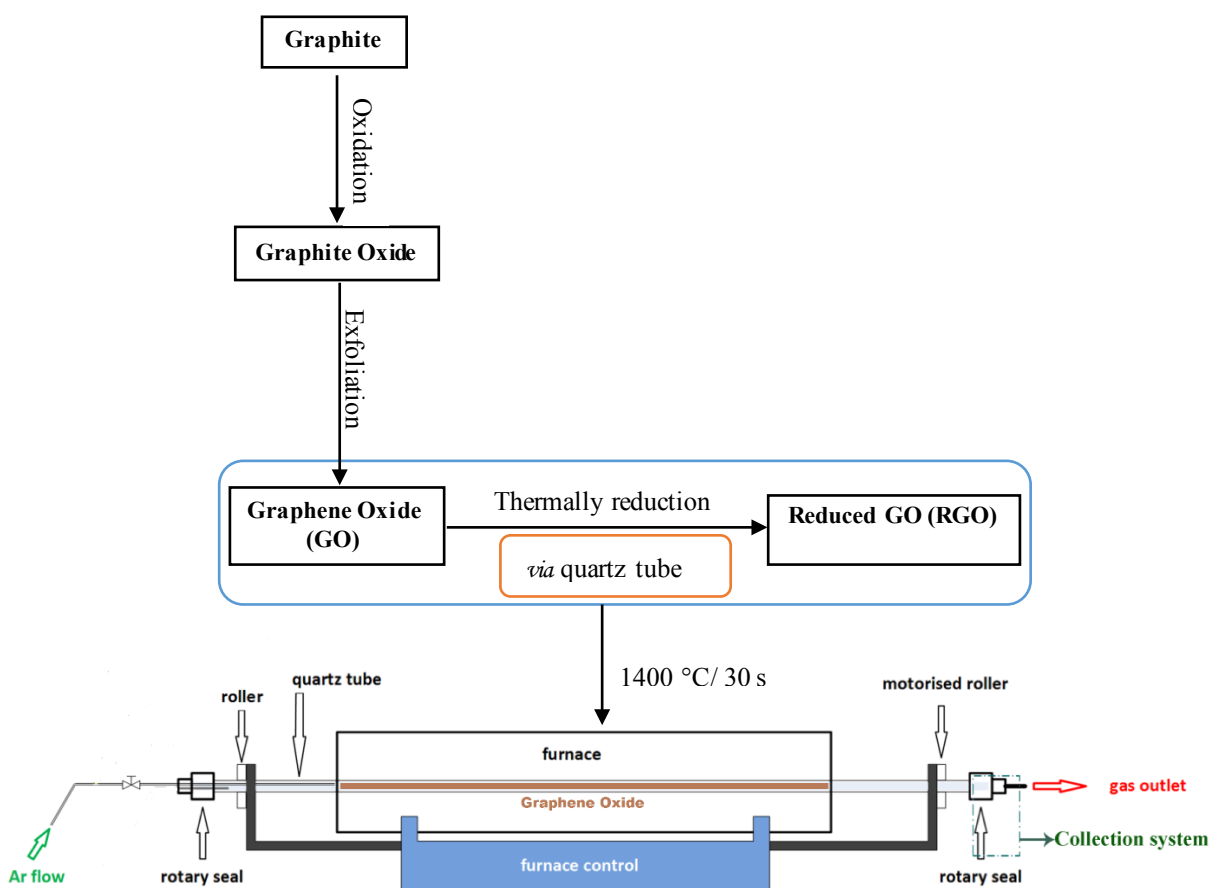


*Figure 3-1. Photographs showing (in the left side) GO powder and (in the right side) graphite dry reduction of GO (RGO).*



*Scheme 3-1. The procedure and technique to synthesise RGO sheets.*

### **3.3.2 Characterisation**

Some of the significant characterisation techniques are described in detail in the following paragraphs:

#### **1. Atomic Force Microscopy (AFM)**

The AFM measurements were performed using Dimension 3100 by CLI Digital Instruments, USA, for determining the lateral size and thickness of the RGO sheets. A very dilute suspension of RGO (0.02 mg/ml) in deionized water was sonicated for 30 min. Small drops were taken from the solution and spin coated on mica substrate uniformly and then left overnight to dry. The probe utilised for imaging was made from Si by Nanosensors<sup>TM</sup>, Switzerland, and it had a rectangular diving-board shape with a resonant frequency of (210–490) KHz. Images were recorded using Nanoscope software, and real-time scanning was performed at ambient temperature.

#### **2. Fourier Transform Infrared Spectroscopy (FT-IR)**

FT-IR Spectra of the GO and RGOs were recorded on a Perkin Elmer 100 Series FT-IR spectrometer using the attenuated total reflectance (ATR) technique. FT-IR was employed to characterise the functional groups present on the surface of samples. All spectra were obtained in transmittance mode, ranging from 400 to 4000  $\text{cm}^{-1}$  at 4  $\text{cm}^{-1}$  resolution by accumulating 16 scans with a scan speed of 0.2 cm/sec.

#### **3. X-ray diffraction analyser (XRD)**

The crystal structure of GO and RGOs were characterised by XRD analyser Bruker D2 Phaser using copper K-alpha radiation at a generator current of 10 mA and a generator voltage of 30 kV over the scanning range  $2\theta$  from 5 to  $10^\circ$ . The detector was a LynxEye micro-strip, and the wavelength ( $\lambda$ ) was 0.154051 nm. The total scan time was recorded as 20 min for each sample.

#### **4. Raman Spectroscopy**

Raman spectra were recorded using a Renishaw inVia Reflex spectrometer (England) for



characterising GO and RGOs. This system was integrated with an excitation wavelength of 532 nm argon-ion laser at a power of 25 mW and a spectral resolution of  $1 \text{ cm}^{-1}$ .

### **5. X-ray photoelectron spectroscopy (XPS)**

XPS is a powerful analytical technique that is used for analysing the surface composition of the GO and RGOs samples based on the measurement of the kinetic energies of photoelectrons that are emitted from atoms' orbitals when they are excited by soft X-ray photons (1–2 KeV). The samples were prepared for XPS analysis by pressing a small amount of powder onto high purity indium foil. The analyses were performed with a Kratos Ultra instrument working with a monochromatic Al  $K\alpha$  radiation (1486.6 eV) to emphasise the existence of functional groups and evaluate the change in oxygen/carbon atomic ratios for the samples. Survey scans were acquired from a binding energy of 0 to 1200 eV and at 160 eV pass energy and a step size of 1 eV. Also, high-resolution C 1s, N 1s, and O 1s spectra were collected, as identified, over a proper energy range at 20 eV and a resolution of 0.1 eV. The analysis area was around 700  $\mu\text{m}$  by 300  $\mu\text{m}$ . The data for each sample was corrected according to the calibrated binding energy for the main carbon peak C 1s at 285.0 eV.

### **6. Transmission Electron Microscopy (TEM)**

TEM equipment was utilised for studying the quality of dispersion of the RGO and GO materials in the solvent. The specimens were prepared by dispersing powders in ethanol ( $1 \text{ mg } 10 \text{ ml}^{-1}$ ) to form a suspension, followed by ultrasonication for 1 h, and a drop of colloidal liquid was placed onto Formvar carbon-coated copper mesh grids (400 mesh Agar Scientific). The thickness ranges from 1–30 nm carbon and 5–50 nm Formvar. This chosen coating is superlative for ultrathin specimen support. The samples were imaged by utilising an FEI Tecnai Biotwin Spirit TEM at an operating voltage of 80 KV. Gatan Orius digital camera equipped with Gatan digital micrograph software (Gatan Inc. USA) was used to recording the electron micrographs.

## **7. Scanning Electron Microscopy (SEM)**

SEM, Inspect F, Poland is a powerful magnification apparatus that is utilized to characterise the the powder samples of GO and RGO at different magnification powers. The powder samples of GO and RGO were distributed over the high purity pin stub holder and then taken for SEM imaging after coating. The samples were coated by using a gold sputter coater (Emscope SC, UK) to improve the image quality through minimising the electric charge built up in a non-conducting sample. The sample was placed in a vacuum chamber for coating under argon gas purge and vacuum pump. When the pressure inside the chamber reached 0.06 Tor (8.0 Pa), the coating process started at 15 mA for 3 min, which is the time required to complete the coating process for a gold sputter rate of  $10 \text{ nm min}^{-1}$ .

## **8. Thermal Gravimetric Analysis (TGA)**

TGA was performed on a Perkin Elmer Pyris 1 TGA instrument (USA) to study the thermal behaviour for graphite, GO and RGOs. The sample (5 mg) was placed in an aluminium crucible and ramped from 24 up to  $650^\circ\text{C}$  under flow of nitrogen at  $50 \text{ mL min}^{-1}$  with a heating rate of  $10^\circ\text{C min}^{-1}$ .

# **3.4 Results and Discussion**

## **3.4.1 Criteria utilised in determining the effect of reduction**

Because the reduction process can create a great alteration in the microstructure and properties of GO, some clear changes can be measured or detected to judge the reducing effect of different reduction processes.

### **3.4.1.1 Visual characteristics**

The optical observation technique was used to visualize the structure changes of GO after the reduction process. Because the reduction degree of RGO can significantly improve the

electrical conductivity of GO material, the increased charge carrier density and their mobility will enhance the reflection to incident light upon the surface, which produces an RGO film with a metallic shine compared to its GO film (Pei & Cheng 2012). The reduction of GO material in a colloid state through using chemical reduction method, as an example, hydrazine hydrate reduction, typically results in a black precipitation from the yellowish suspension, which is possibly a result of a decrease in polar functionality on the surface of the RGO sheets and therefore an increase in the hydrophobicity of the material (Pei & Cheng 2012). The thermal reduction technique produced RGO sheets in a black powder, as shown in Fig. 3-1.

### **3.4.1.2 AFM**

The morphologies of RGO powder were elucidated using AFM, SEM and high-magnification TEM measurements. A dilute distilled water suspension of RGO was sonicated for 40 min and dropped onto a newly exfoliated surface of mica substrate and then analysed via AFM at a force constant of  $40 \text{ N m}^{-1}$  and tip curvature less than 10 nm. AFM section analysis shows that RGO had a height of about 0.76 nm, as illustrated in Fig. 3-2; therefore, the exfoliation of graphite oxide by sonication successfully produced a few-layers of GO with abundant of OCFGs present on its structure, and then obtained RGO sheet with highly reduced of OCFGs, after exposes GO sheets to thermally reduction process. Because ideal single-layer graphene has a height of 0.35 nm, two nano-sheets could not exist. Several previous studies have identified the thickness of RGO layers between 0.8 and 1.3 nm (Geim & Kim 2008). Consequently, the presence of covalently attached OCFGs that still remain at the edges of RGO nano-sheets might be responsible for the increased thickness of the RGO (Kotchey et al. 2011). In RGO nano-sheets, some adsorbed molecules, functional groups, trapped molecules and structural defects are present, resulting in increased thickness (Jung et al. 2008).

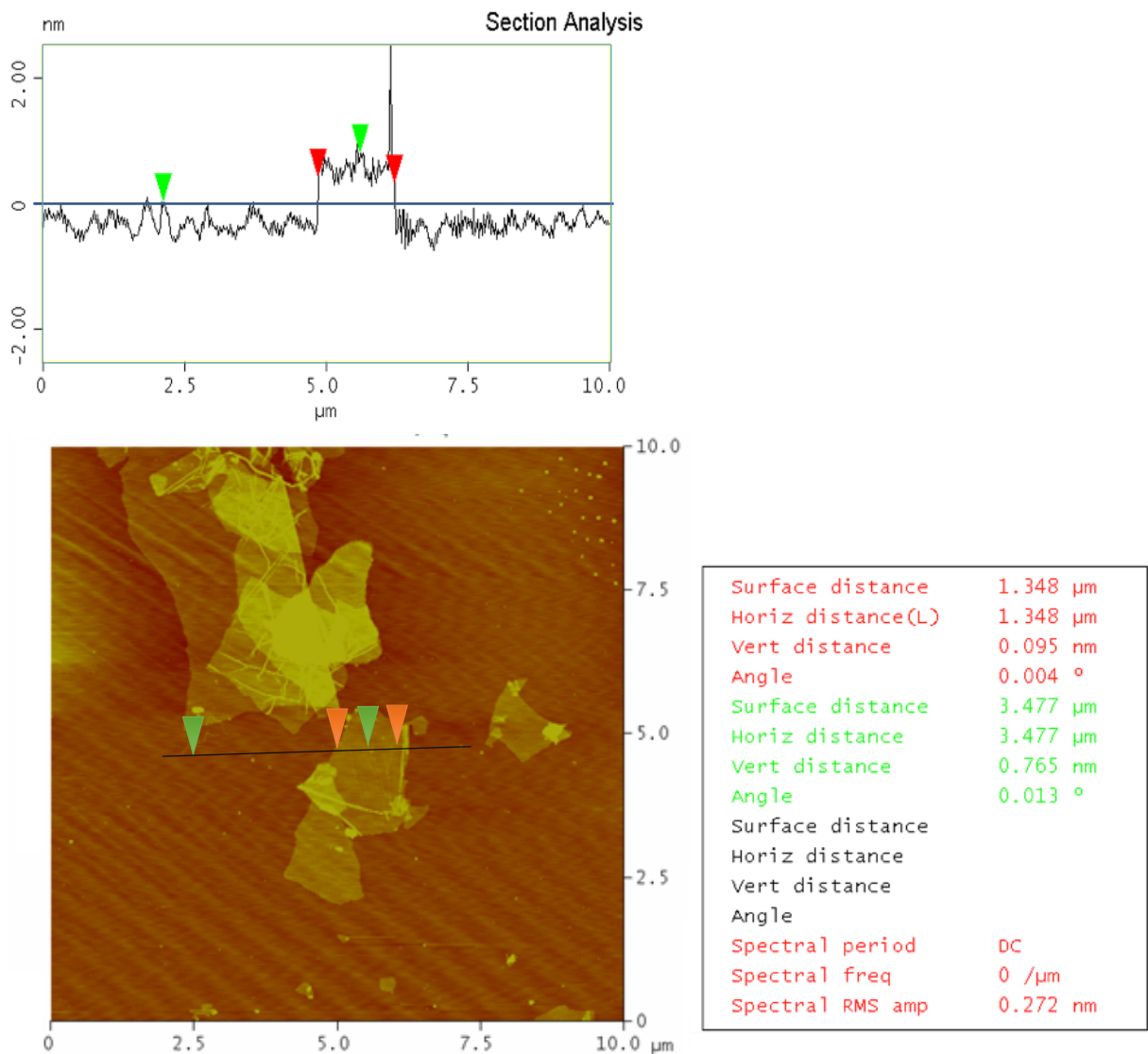


**Figure 3-2.** AFM images of monolayered of RGO deposited on mica substrate.

### 3.4.1.3 SEM and TEM

SEM images of the RGO, GO and graphite samples are shown in Fig. 3-3. These results show the formation of RGO and GO sheets from graphite layers with good uniformity, extending to several micrometres. The SEM image of Fig. 3-3 (A) shows layered sheets of RGO randomly aggregated with wrinkled and folded surfaces. The GO of Fig. 3-3 (B) shows that mono and

few-layered sheets stack tightly to create bulky conglomerates with distinctly smooth surfaces and layered structures at the edges (Kou & Gao 2011). The defects in the carbon structure provide an explanation for the observed wrinkles. These defects are because of the remnants of the oxygenated-functional groups with a C/O ratio of 2.27 on the GO structure that was confirmed by XPS, as shown in Table 3.2.

The TEM image of the RGO sheets (Fig. 3-3 (a)) shows a number of thin layers of sheets stacked together, and the average length is found to be  $1.2 \pm 0.9 \mu\text{m}$  (Kee et al. 2017), measured the length of RGO sheet using TEM where the average length reached about  $738.5 \pm 141.1 \text{ nm}$ . The TEM images of RGO and GO sheets show they are transparent compared with graphite with a lamellar structure. In contrast, the stacking graphite flake was observed to be very dark and opaque (Fig. 3-3 (b) and (c)). However, RGO obtained after thermal reduction at high temperature has surface wrinkles and a shrunken thickness.

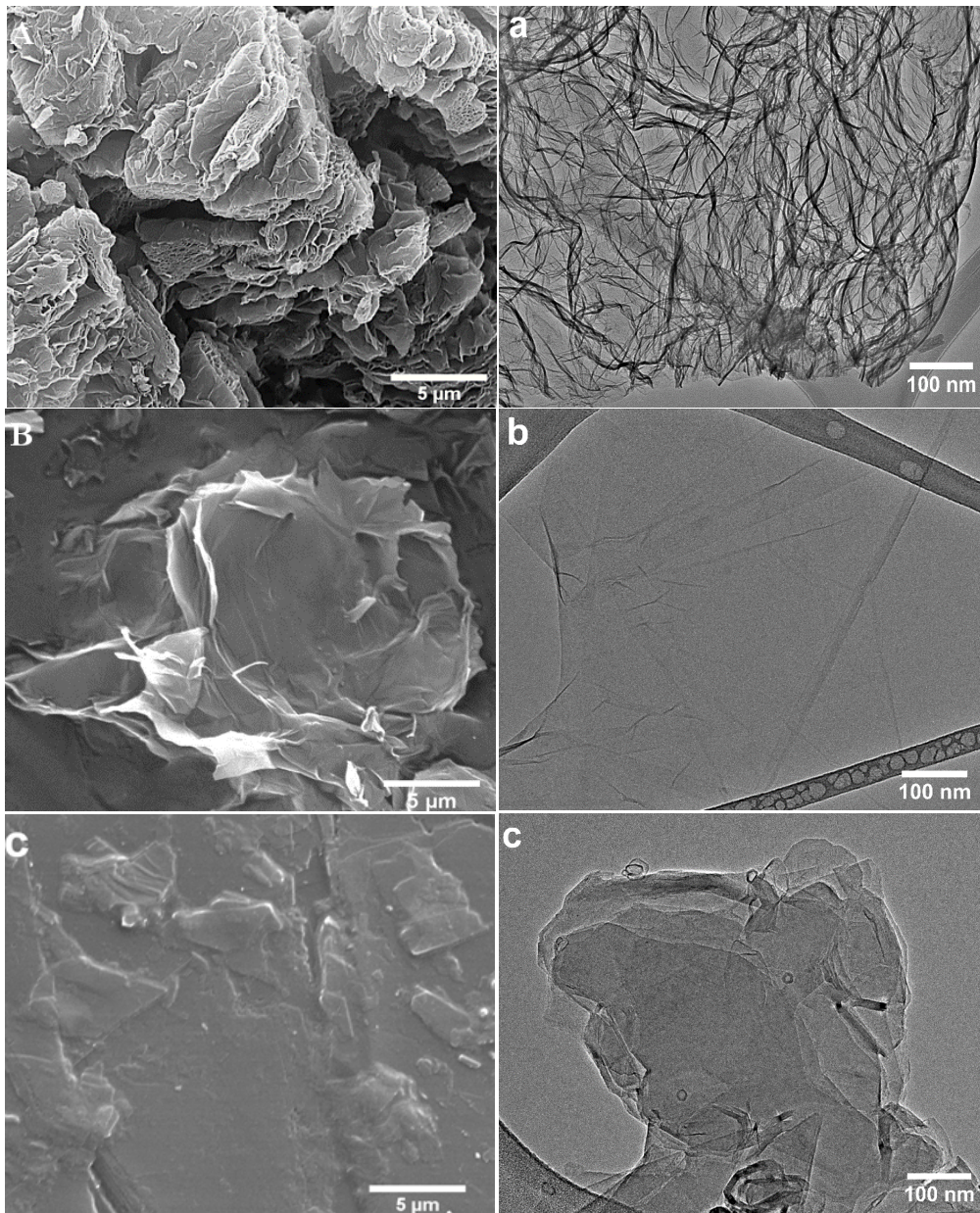


**Figure 3-3.** SEM images of RGO (A) and GO (B) and Graphite (C); TEM images of RGO (a) and GO (b) at different magnifications and TEM image of side-view of natural graphite (c).

In addition, the GO material indicates a very smooth surface with low levels of ripple and folding which can be identified in its bent edges. In contrast, the TEM images of GO and RGO, consistent with AFM images, indicate that the sheets exhibit homogeneity with an average lateral size of  $1.348 \pm 0.6 \mu\text{m}$  after scan in five random place on the surface of nanomaterials.

### 3.4.1.4 FT-IR

The GO and RGO powders were investigated by FT-IR spectroscopy. In Fig. 3-4, the characteristic absorption peaks centred at  $3400\text{ cm}^{-1}$  and  $1224\text{ cm}^{-1}$  were attributed to the deformation of the  $\text{-OH}$  bond of the GOs and  $\text{C-OH}$  groups, respectively, which are much stronger in GO than in RGO. The band at  $1721\text{ cm}^{-1}$  was associated with the stretching vibration of the carbonyl or carboxyl groups  $\text{C=O}$  bond (Li et al. 2008), and the sharp peak detected at  $977\text{ cm}^{-1}$  may be assigned to the presence of  $\text{C-O}$  deformation in the oxirane group (Nikolic et al. 2010). Thus, the peaks obtained in the FT-IR spectra provided evidence of the introduction of OCFGs to the nano-sheets, and the presence of these functional groups reveals that the samples oxidized.

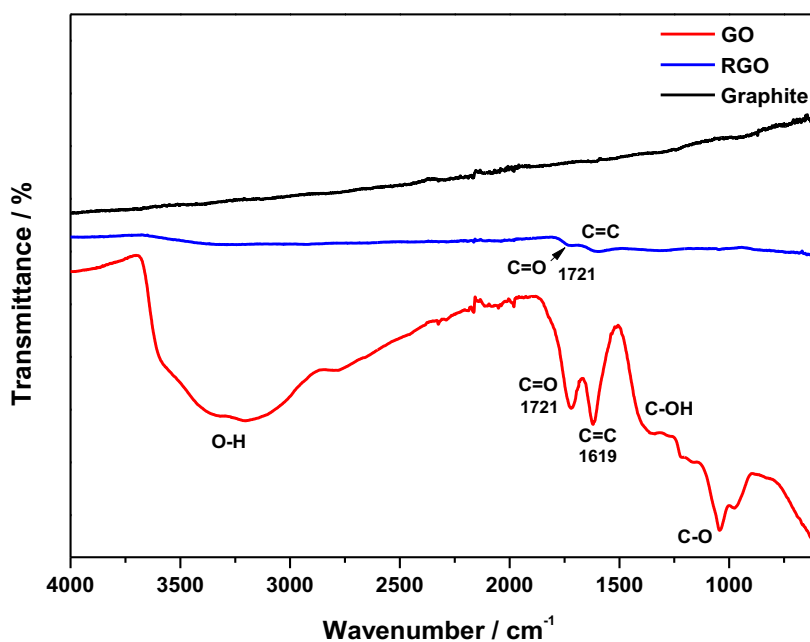


**Figure 3-4.** FT-IR spectra of GO before and after reduction by thermal treatment at  $1400^{\circ}\text{C}$ . The peaks corresponding to different functional groups are indicated.

Because of the rise in temperature, the OCFGs present in the aromatic plane structure of GO are converted to  $\text{CO}$  and  $\text{CO}_2$  gases (Bhattacharya 2016). This conversion generated a large pressure in the GO main structure, which overcame the van der Waals interactions that are responsible for binding the graphene nano-sheets. The large reduction of GO can be seen on

the RGO curve. When the two curves are compared, any functional groups containing oxygen are either removed or reduced. The C=O double bonds appear to be reduced at  $1721\text{ cm}^{-1}$  but are still prominent and can be seen clearly on the RGO curve.

### 3.4.1.5 XRD and TGA

To understand the effect of the oxidising agent in the Hummer's method, for preparing mono- or few-layered GO sheets and its subsequent with reduction process, XRD was performed to trace the exfoliation process. Fig. 3-5 (A) depicts the XRD diffractogram of graphite, GO and RGO. The flake graphite showed a sharp peak at approximately  $26^\circ$ ; after successfully oxidising into graphite oxide and being exfoliated via sonication, the GO reports a greatly reduced peak at  $2\theta = 11.6^\circ$  (this corresponds with the (002) reflection plane and a d-spacing of  $\sim 0.83\text{ nm}$ ). A noticeable reduction in  $2\theta$  may be seen in the diffractogram which concurs with the work by (Stobinski et al. 2014). A very weak and broad peak centred at  $2\theta = 22.2^\circ$  is attributed to the reduction of GO to RGO (corresponding d-spacing of  $\sim 0.4\text{ nm}$ ), which is theoretically considered as mono or few layered. Consequently, the diffraction peaks of GO and RGO may be very weak or even completely absent because of the destruction of regular stacks of graphite which are destroyed by exfoliation (Kou & Gao 2011). Furthermore, no diffraction pattern would be observed by XRD of both GO or RGO for single layers or amorphous samples.

Fig. 3-5 (B) shows the TGA curves of dried GO and RGO powder, and two main weight loss stages are observed for the GO powder. The initial weight loss below  $174^\circ\text{C}$  is attributed to the removal of adsorbed water molecules because of the hydrophilicity of GO nano-sheets. The second stage showed a significant weight loss ( $\sim 45.6\text{ wt. \%}$ ) at  $240^\circ\text{C}$  that is assigned to the decomposition of the labile oxygenated functional groups of GO, generating CO and CO<sub>2</sub> gases (Abdolhosseinzadeh et al. 2015; Lerf et al. 1998). These results suggest that GO material is thermally unstable. The residual weight of GO was reported to be less than 44% at above  $550^\circ\text{C}$ .



As expected, the RGO curve was highly stable up to 600°C compared with GO because of the removal of OCFGs by the thermal reduction process.

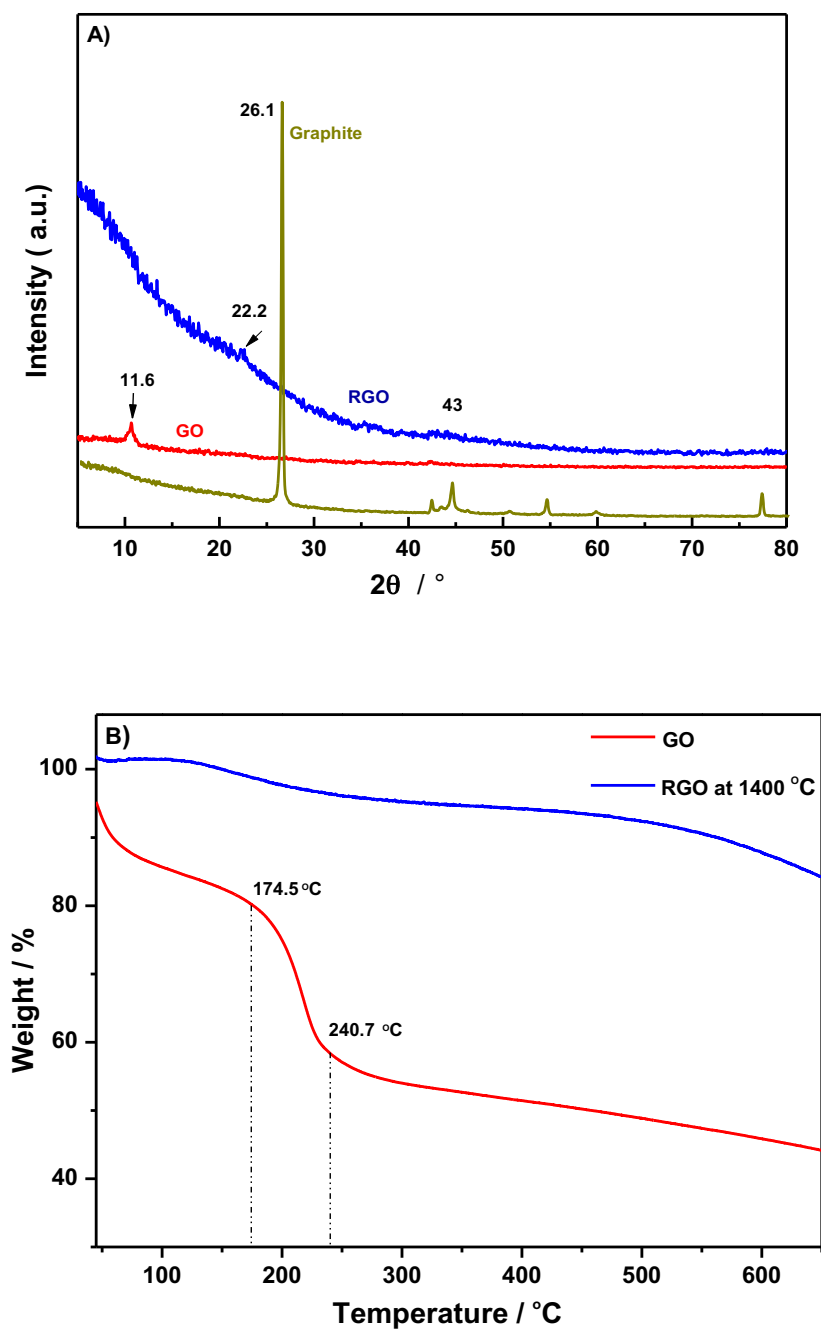


Figure 3-5. XRD (A) and TGA (B) of GO and its reduction (RGO).

### 3.4.1.6 XPS

Depending on the synthesis approach, GO with chemical compositions corresponding to a C/O ratio of 4:1 to 2:1 are typically produced. After the reduction process, the C/O ratio can be increased to approximately 12:1 in most cases (Pei & Cheng 2012; Bao et al. 2011).

The carbon to oxygen atomic ratio is usually obtained by XPS analysis and can give more detailed information on the chemical structure of RGO. Because the  $\pi$ -electrons from the  $sp^2$  carbon mostly determine the electrical and optical properties of carbon-based materials (Zhu et al. 2011), the fraction of  $sp^2$  bonding can provide a significant degree of insight into the electronic structure and the relationships between the structure and its properties. Table 3-2 shows a comparison of the reducing effect of GO by different methods.

**Table 3-2.** The C/O ratio and electrical conductivity of typical reports on the reduction of GO.

Sample	Treatment	C/O ratio	$\sigma$ (S cm <sup>-1</sup> )	Ref.
GO	Chemical Oxidation of graphite	1.9–2.8	Insulator	Bao C et al. 2011; Shen et al. 2018
CRGO	Reduced via chemical methods	4.0–10.3	2~72	Bao C et al. 2011; Pei & Cheng 2012
TRGO	Thermal reduction of graphite oxide	5.6~10.0	103~727	Zhu Y et al. 2011; Shen et al. 2018

XPS was conducted to determine the degree of reduction of GO under high temperature and characterise the chemical composition of the surface for quantitative analysis. Fig. 3-6 show the C1s XPS spectra of graphite, GO and RGO samples which were used to identify the OCFGs attached to the C atoms.

The survey scan spectrum indicates the existence of both carbon and oxygen atoms at the surface of all samples. Because of the high oxygen content associated with the GO sample that arises from the oxidative treatment, the scan XPS spectra showed an intense peak of O 1s, whilst

a tiny peak of O 1s was observed for the graphite sample, which can be clarified by slight atmospheric oxidation. However, the sharp peak of C 1s for the bare graphite spectrum displays only one asymmetric peak, centred at 284.1 eV, because of the  $\pi$ -bond shake up satellite. The C/O ratio for the reference sample (graphite) was observed to be 61.2 in the current study. This result was confirmed by (Wu et al. 2012) where they indicated the rich C and small trace of O in similar regions for graphite, which their observed ratio was 64.79.

In contrast, GO has a significant degree of oxidation which leads to the formation of OCFGs on the surface, and thereby the content of oxygen O1s considerably increased while this peak of O1s for the RGO sample considerably decreased. The wide scan spectra of the GO sample showed a sharp peak of both C 1s and O 1s at the positions 285 eV and 532.7 eV, respectively, Fig. 3.6 (A). The binding energy for SP<sup>2</sup>-bonded carbon (shown in graphite at 284.1 eV) of RGO is greater than that of the GO sample. (T.K et al. 2014) also reported the identical consequences of the spectrum XPS survey for GO, affirming the centres of C 1s and O 1s at 286 eV and 531 eV, respectively.

As listed in Table 3-3, the samples were highly influenced by the oxidation process, where the C/O ratio decreased as the concentration of OCFGs increased, but this ratio was significantly recovered with the reduction process for GO.

In the GO sample, the C/O atomic ratio is about 2.28, suggesting that it is associated with many OCFGs in the main structure of graphitic carbon through the oxidation process, and C1s/O1s can be calculated by dividing the area under C1s peak by that of O1s peak area. Whereas, after applying the thermal reduction method, the C/O ratio for RGO increased considerably from 2.28 to 6.61 for GO. It is still possible to clearly see the intensity peak of O1s for the RGO sample in survey spectra, indicating that there is some residual OCFGs remaining on the surface. Therefore, the results regarding the atomic ratio of C/O for RGO proves a successful reduction.

Fig. 3-6 (B) shows the C 1s XPS analysis for graphite, GO and RGO samples. For pure graphite, the C=C/C–C characteristic peak is related to  $SP^2$  and  $SP^3$  hybridized carbon at (284 eV). The characteristic peak of C–C stretching for graphite appeared at 284.5 eV, as reported by (Krishnamoorthy et al. 2013).

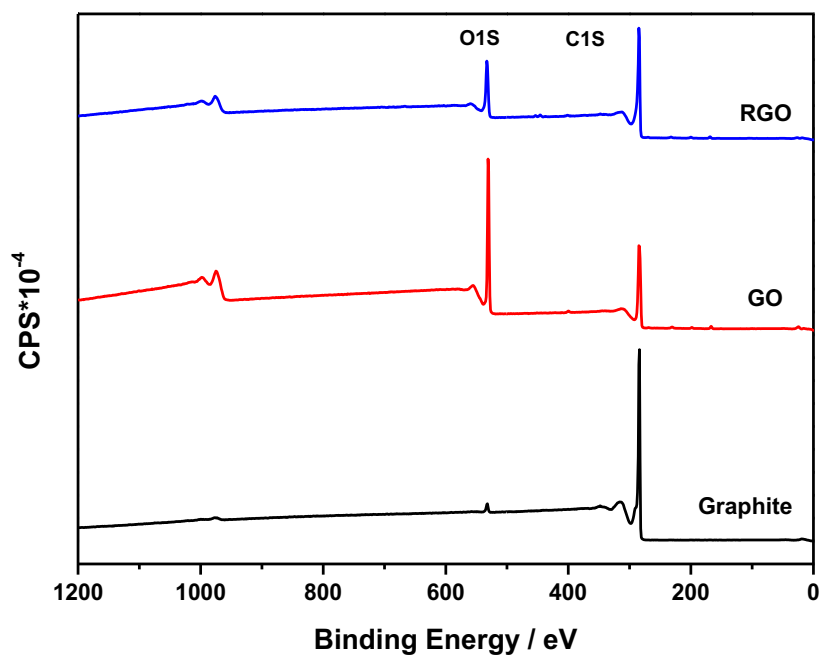
The GO sample can be specified by three intensity peaks, which are attached with C atoms in different functional groups because the GO sample has a higher oxidation degree compared with that of RGO samples. The peaks are the C=C/C–C (non-oxygenated ring) characteristic peak related to  $sp^2$  and  $sp^3$  hybridised at 285 eV, the phenol and ether C in C–O bonds at 287 eV and the carbonyl C–C=O peak at 289.1 eV. These results were confirmed by (Rathnayake et al. 2017). The intensity of the O1s peak of GO was observed to be very high, while it was low in the C1s peak. (Pei & Cheng 2012) have assigned the reason for this result to be significant oxidation.

The C 1s peaks of RGO sample also indicates that they have the same OCFGs as the GO sample. However, the peaks of these components for the RGO sample were significantly weakened in their intensity compared with that of GO sample, suggesting a significant de-oxygenation through applying the vacuum-assisted technique.

Moreover, those peaks show a slight shift in their locations compared with GO. In addition, The RGO spectrum shows an additional peak which is assigned to a carboxylic group at a higher binding energy appearing approximately at 291–292 eV. (Tang et al. 2012) found the peak of a carboxylic functional group for the RGO corresponding to 289 eV, which is somewhat lower than the binding energy (eV) for RGO in this current study. (Wu et al. 2012) also obtained the main components similar to RGO by using a chemical reduction method using hydrazine as the reducing agent.

**Table 3-3.** Atomic concentrations of O1s, C1s and their ratios obtained by XPS survey spectra.

Sample ID	Elements (%)		C/O ratio
	C1s	O1s	
Graphite	98.39	1.61	61.2
GO	68.08	29.94	2.28
RGO	84.68	<b>12.84</b>	6.61



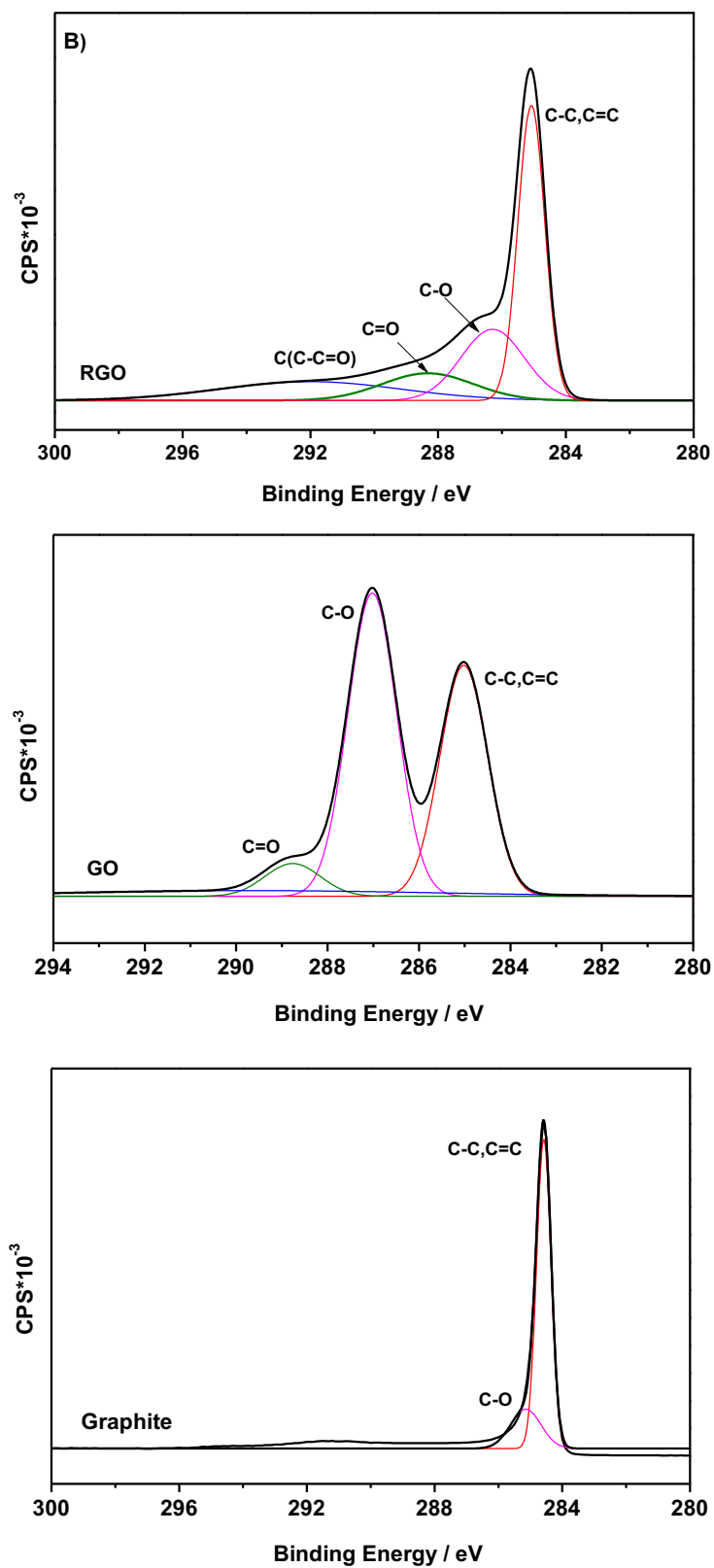


**Figure 3-6.** (A) C1s XPS survey and (B) XPS spectra of RGO, GO and graphite.

## 3.5 Section Two

### 3.5.1 Reduction by using vacuum oven

Tube furnace technique is complicated and many problems are encountered during thermal treatment under a fast heating rate and such a high temperature. There is a requirement of developing a strategy for the thermal exfoliation of GO under a very low temperature. With this approach, it is easier to access RGO sheets, and the required time for researching and developing RGO-based nanocomposites is reduced. Henceforth, it is better to go with approaches dealing with direct preparation of RGO out of dry GO powder under low temperatures.

To obtain RGO material, typically, 500 mg of the GO sample (powder with lighter-coloured grey) was placed inside a vacuum oven under the desired temperature and atmospheric pressure (0.1 MPa). Next, the GO sample was maintained inside the vacuum chamber for 24 h in order to obtain RGO sheets. Afterwards, the GO powder was placed in a narrow-neck flask and the narrow orifice was locked with a loosely tightened glass stopper to impede the fluffy nanoparticles of RGO from volatilisation into the oven atmosphere while allowing the generated gases during the reduction process to be expelled. Here, 120, 160 and 180°C were chosen as the reduction temperatures, and the obtained graphene nano-sheets were designated as RGO-120, RGO-160 and RGO-180, respectively.

The procedure for selecting the reduction temperatures of GO is the following:

Reduction of the GO was performed in situ with the assistance of the vacuum-oven method; however, to establish proper reduction conditions, it was essential to perform initial tests on GO. TGA was performed on this GO material under a nitrogen atmosphere. The result of such a process can be seen in detail in next section, in which the significant mass reduction of 30% was between 160 and 200°C is due to the pyrolysis of the most of the OCFGs attached to the

basal aromatic plane of a GO sheet, which involves (epoxide and hydroxyl groups), and this mass reduction largely recovers the optical, mechanical, thermal and electrical properties to those of pristine graphene. Although it would be helpful to reduce the GO sheets at temperatures higher than 180°C, defects in the backbone structure of RGO would increase.

Thus, this study demonstrates that GO reduction in the vacuum oven is an effective process for the RGO synthesis with less disrupted  $sp^2$  bonding networks in comparison with those obtained by chemical or thermal reduction of GO at high temperatures. In particular, this study shows that a process of thermal reduction in vacuum for 24 h at 180°C can considerably reduce the number of defects in RGO nano-sheets, as consistently proven by Raman measurements, XPS, XRD and TGA, where the intensity ratio of defect ( $I_D$ ) and graphene ( $I_G$ ) decreases, implying a decreased number of defects with respect to the increased heating temperature from 120 to 180°C via a vacuum oven. Whereas, in previous studies, extensive levels of disorder ( $I_D$ ) were reported through using tube furnace for GO reduction at elevated temperatures (Kudin et al. 2008; Reina et al. 2009; Wang et al. 2009) because of increased pressure between graphene layers of graphite oxide that led to the tearing of graphene sheets; and therefore, the intensity ratio ( $I_D/I_G$ ) recorded was greater than 1.2. This sensitive reduction of GO with the help of vacuum oven enabled the production of RGO with better structural, and mechanical and electrical properties.

The resultant samples were in the form of black powder with an evident expansion in volume. For comparison, a gradual decrease in the mass of the samples (RGO-120, RGO-160 and RGO-180) with increased temperatures was noted, which record approximately 17, 34 and 39 %, respectively. This decline in mass can be ascribed to the partial removal of OGFGs of GO under the influence of thermal treatment via the vacuum oven.

Table 3-4 illustrates the percentages change of mass of dry GO powder at different reduction temperatures at varying temperatures under vacuum. Dry GO (500 mg) was placed in a vacuum



oven at different reduction temperatures of 120, 160 and 180°C, at four different intervals (6, 24, 48 and 72 h). This procedure was performed to identify the optimal time that is required to ensure the complete exfoliation of GO and to obtain optimal conditions for the production of RGO sheets with the main aim of identifying the lowest possible temperature that could be utilised with GO material to produce RGO under vacuum. Although, tube furnace technique produced RGO with lower energy consumption near about 1.1kWh compared with vacuum oven which is higher than tube furnace by 1.3 kWh, the vacuum oven technique is relatively straightforward method, in relation to produce RGO in large quantities and less defects on RGO structure under using low temperatures which is a major requirement in composite research; hence, an attempt was made to obtain the optimal (lowest) conditions for RGO production with lower nanostructure defects, which was verified through this current study by reporting a good improvement of electrical conductivity for RGO-180 by about 32% compared with that of thermal tube furnace, RGO-1400 ( $223 \pm 3.5 \text{ S cm}^{-1}$ ).

**Table 3-4.** Comparison of mass change for GO at different reduction temperatures under vacuum oven with different time periods.

Time Period	Initial mass /mg	Mass (mg) after heating at	%	Mass (mg) after heating at	%	Mass (mg) after heating at	%
		120°C		160°C		180°C	
6 hours	500	484	3	465	7	456	9
24 hours	500	414	17	332	34	308	39
48 hours	500	393	21	316	37	293	41
72 hours	500	378	24	299	40	283	43

The results (as tabulated in Table 3-4) indicated that there is a slight decrease in the mass of GO materials in vacuum conditions, which has not exceeded 2 to 7% for each reduction temperature after 24 h. However, there was a significant change in mass loss with a percentage of 14 % at 120°C, and at 160 and 180°C, were nearly 30% at 24 h. Therefore, after 24 h from the time of the reduction process, there was no significant change in mass loss. Hence, the optimal time to remove most oxygenated functional groups that are associated with GO surfaces

can be determined at 24 h. Thermally RGO could be successfully produced by facile and low consumption approach, and obtaining RGO sheets at different reduction temperatures make it possible to utilise these materials as fillers for EP matrix.

Thermal processing functions call for solutions potent of performing accurate temperature measurement, combustion regulation, and precise gas as well as smooth transitions. Additionally, they require the optimization of energy utilization besides attaining environmental and economic savings. The low-temperature vacuum heat approach provides special merits to several industrial uses wherein the treatments entailing vacuum purges at the underlying cycle's onset are increasingly popular. Execution of these operations occurred in vacuum furnaces as well as the furnaces that use vacuum purges before the heating process commences. Such processing is advantageous following a highly regulated environment tailored to reduce surface interactions. Notably, the vacuum processing prevails in void space with no gases, vapors, or particles in absentia of any pressure hence it amounts to a thermal process that is economically reductive.

Furthermore, the valid reductive thermal functioning surrounding offers better, faster, more environmentally friendly, safer, and less costly outcome than all other solutions hence yielding high commercial added value output commodities. The low-temperature functionality can prevail as continuous or batch, as 'modules' or stand-alone units factored into a progressive vacuum system, thus providing several options for operation. This analogy regulates the production of gasses and vapors to initiate environmental friendliness wherein these gases and vapors encounter trapping into industrial chambers for productive uses. Moreover, low-temperature vacuum functioning amplifies quality and productivity, since the outstanding regulation of equipment and process variability prove more soundness than other substitute approaches. The operational and initial expenses often undergo an offset via a reduction in scenes of lower consumption of energy thus posing zero impact on the surrounding. Nevertheless, vacuum systems outstand as self-contained besides posing minimal safety risks

to plant personnel, inclusive of the operators. Mozetic et al. (2014) reveal that occasional concerns emerge regarding pinch points, heat discharged into the rooms, noise levels, and electrical dangers besides the absence of “burn-off” or rather flames as evident from the operational non-vacuum devices.

## 3.6 Results and discussion

### 3.6.1 Spectroscopic measurements

#### 3.6.1.1 TEM

The morphology and structure of RGO nanosheets were investigated through TEM observation. A monolayer or a few-layer RGO ( $n < 6$ ) stacked on each other with less folding and wrinkles as observed in Fig. 3-7. These layer RGO nanosheets were less than  $< 2 \mu\text{m}$  in width and flat because the vacuum oven exfoliation in the process of preparing RGO samples destroyed the van der Waals forces between the RGO layers.

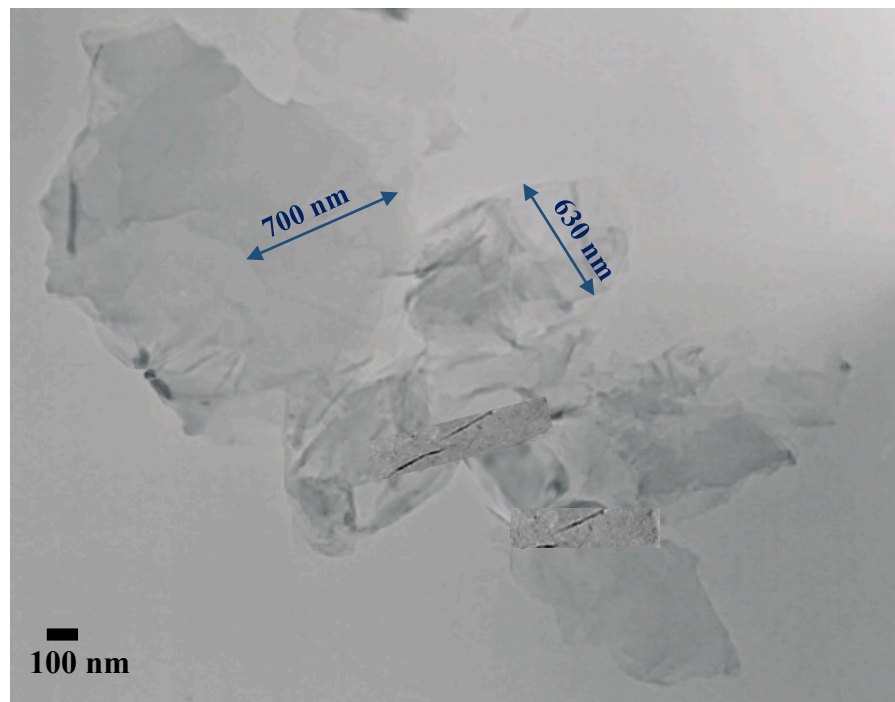


*Figure 3-7. TEM image of RGO produced by vacuum oven at low temperature (180°C)*

### 3.6.1.2 FT-IR

Typical FT-IR spectra for both GO and RGOs powders are shown in Fig. 3-8. The GO spectrum reveals a strong and very broad peak located between 3000 and 3500  $\text{cm}^{-1}$ . This peak can be related to the adsorbed  $\text{H}_2\text{O}$  or the existence of O–H groups, and a strong stretching band of carboxyl acid and carbonyl groups (C=O) appears at a wavenumber of 1723  $\text{cm}^{-1}$ . The strong band observed at 1624  $\text{cm}^{-1}$  can be assigned to the aromatic (C=C) skeletal vibrations of unoxidised graphitic domains (Khanam & Ponnamma 2015). This domain can cover anywhere between 1450 and 1680  $\text{cm}^{-1}$  and originates from the remaining C=C in the GO. However, some authors attributed this peak to the OCFGs, such as adsorbed water (Wu et al. 2012). The sharp peak at 1062  $\text{cm}^{-1}$  refers to the C–O stretching vibration in C–O–C in epoxide groups.

In-plane (O–H) hydroxyl group deformation vibrations in the C–OH group can be seen with a wavenumber of 1378  $\text{cm}^{-1}$ . The weak peak at 1224  $\text{cm}^{-1}$  is related to C–OH stretching vibration. Xu et al. (2013) confirmed the presence of OH, C–O, C=O and C=C groups in the edges and basal plane of the GO. The high hydrophilicity of GO arises from the abundance of these OCFGs (Ming et al. 2013; Yin et al. 2013).

After the reduction process of GO, a significant diminution in the intensity peaks of GO is generally observed because of the elimination of OCFGs associated with GO on both aromatic basal planes and edges. Moreover, it can be observed that there are gradual decreases in the intensity peaks of graphene with a rise of temperature from 120 to 180°C. Hydroxyl groups and O–H groups are reduced at 120°C and completely disappear for RGO nano-sheets at 160 and 180°C. Other peaks that appear in GO have become tiny after the reduction of GO at different temperatures. Therefore, the FTIR data indicates a successful thermal reduction.

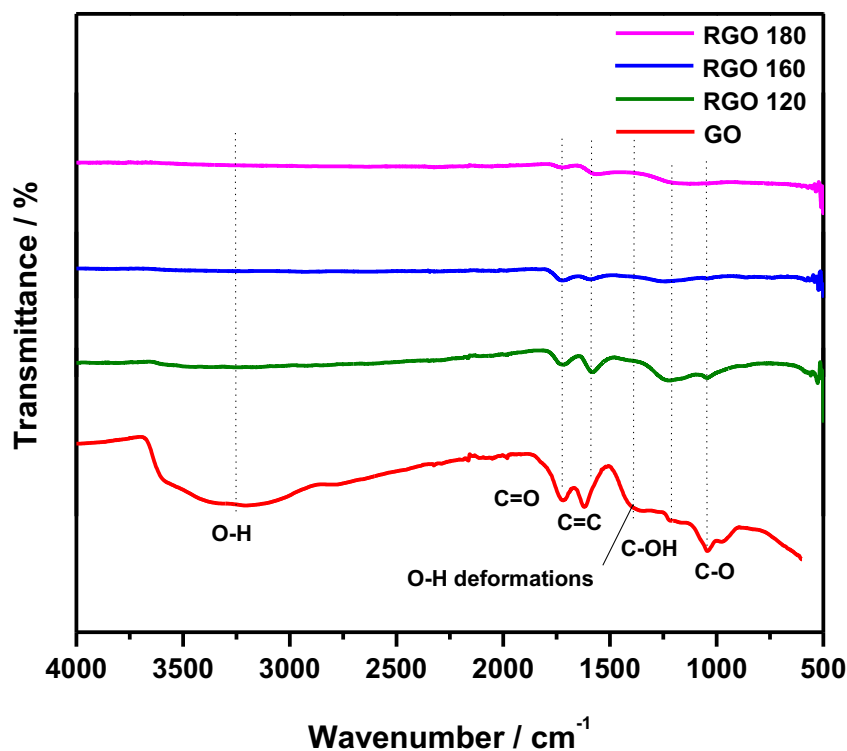


*Figure 3-8. FTIR spectra of GO and RGOs.*

Aside from the successful removal of the OCFGs through the thermal reduction process, the figure shows that the peak originating from the C=C band shifted from 1606 to 1581  $\text{cm}^{-1}$ . This is evidential of significant growth in the recapture of the basal structure of  $\text{sp}^2$ -hybridised graphitic domains, which arises because of the employment of the thermal reduction process on the GO sheets (Olowojoba et al. 2016). (Ju et al. 2010) reported that the vast majority of OCFGs were removed after exposing dried GO powder to 800°C in  $\text{N}_2$  for 1 h with a heating rate of 5°C  $\text{min}^{-1}$ . Therefore, a small number of the hydroxyl groups and epoxide groups remain on the structure after reduction.

### 3.6.1.3 Raman spectroscopy

Raman spectroscopy is a sensitive vibrational spectroscopic technique that is utilised to provide important details on nanostructure and quantify the density of defects and the structural disorder of graphitic materials. Fig. 3-9 illustrates the structure of graphite, GO and RGO using Raman

spectroscopy. Each sample was analysed 3 times to minimise the static error and average values were shown in study results.

Three prominent bands have been determined for graphite on the Raman spectrum, which are D-band, G-band and 2D-band (Ferrari 2007). The G band, centred on  $1580\text{ cm}^{-1}$ , arises from the first-order scattering of the  $E_{2g}$  phonons mode of  $C\text{ sp}^2$  atoms. In addition, both the D-band and the 2D band are the second-order scattering to a breathing mode of the k-point photons of  $A_{1g}$  symmetry and can be seen at  $1300\text{--}1400\text{ cm}^{-1}$  and  $1620\text{ cm}^{-1}$ , respectively (Krishnamoorthy et al. 2013).

The Raman spectrum of graphite contained a strong G band centred at  $1574\text{ cm}^{-1}$  and a small D-band at  $1347\text{ cm}^{-1}$  attributed to in-phase vibrations of the graphitic lattice and graphite material defects (i.e., bond length/angle disorder, vacancies and graphite edges defects), respectively. These peaks were confirmed by (Krishnamoorthy et al. 2013; Mohan et al. 2015), with a slight upward shift in the G band.

The second most prominent peak of graphite after the G-band is a 2D-band at  $2680\text{ cm}^{-1}$  (it is centred at  $\sim 2700\text{ cm}^{-1}$  in this work), and this is the overtone peak of the D-band. This band is very sensitive to the number of graphene sheets stacked together and their order in the graphite along the c-axis. (Muzyka et al. 2008) reported the D and G bands of graphite material centred at  $1358\text{ cm}^{-1}$  and  $1594\text{ cm}^{-1}$ , respectively, in addition to the observed clear peak of the 2D-band at  $\sim 2700\text{ cm}^{-1}$ . This peak occurs because of the double resonance effects that produced two photons with opposite momentum. The decreased intensity of the 2D band in the GO and RGOs can be associated with the breaking of the layer-stacking order because of the oxidation process. Meanwhile, this band is important also because it has a clear peak even with the absence of defects in the RGO layer (Eda & Chhowalla 2010).

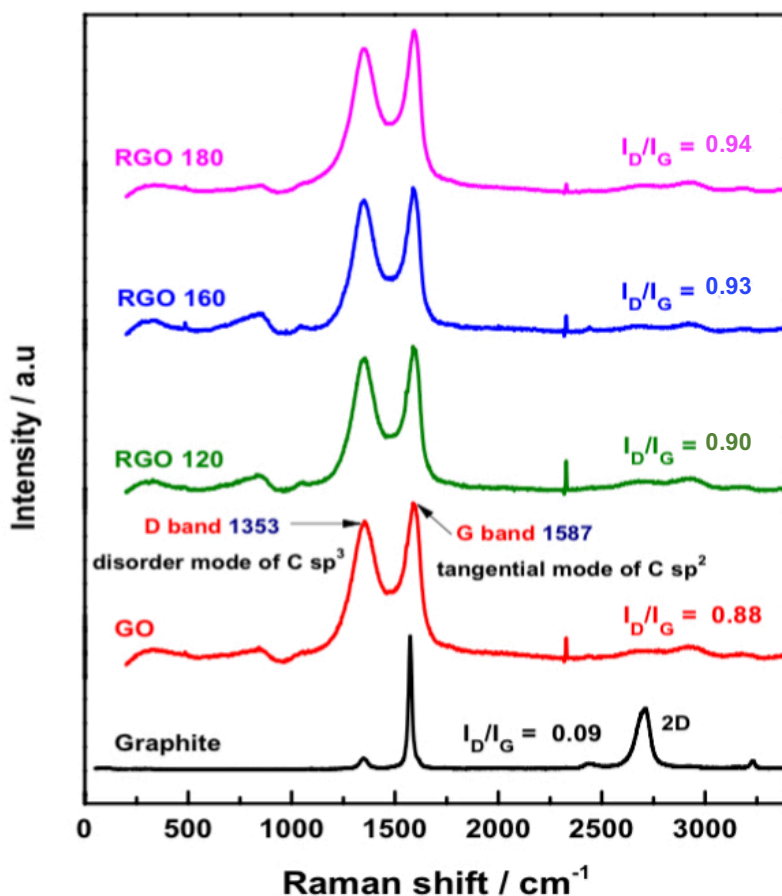


**Figure 3-9.** The crystal structures of graphite, GO and RGOs samples by Raman spectroscopy.

The spectrum of GO peaks shows a very slight difference to that of RGOs. However, the strong oxidising agent breaks the  $sp^2$  C bonding network and grafts many oxygenated functional groups at the edges and basal plane. This reaction leads to the destruction of the original idealistic symmetry of the graphene lattice and causes a broadening in the G-band and D-band peaks. In addition, the GO sample recorded an intensity ratio ( $I_D/I_G$ ) of 0.88 with the absence of the 2D-band.

The figure shows that the G-band peak in the GO sample is shifted towards a greater wavenumber of  $1587\text{ cm}^{-1}$ , compared with graphite ( $1574\text{ cm}^{-1}$ ). This shifting in G-band peak can be attributed to the formation of new  $sp^3$ -hybridised C atoms in the graphitic lattice.

Moreover, the D-band peak also shifted to a greater wavenumber of  $1353\text{ cm}^{-1}$ , and the  $I_D$  of GO also showed a higher value when compared with its  $I_D$  in the graphite spectrum. Thus, the oxidation process results in the 2D band vanish or weaken where the stacking-order for layers is destroyed (Krishnamoorthy et al. 2013).

The Raman peaks related to RGO samples are identified as follows:

- 1- Both the G and D-bands of the RGOs were prominent in specific position peaks.
- 2- The RGO samples show slight differences relating to the position of the D-band peaks compared to GO material, whereas the G-band exhibits a similarly prominent position for both GO and RGO at  $1587\text{ cm}^{-1}$ . The D-band peaks can be observed at  $1350 \pm 1.5\text{ cm}^{-1}$  ( $1353\text{ cm}^{-1}$  for GO), and this tiny shift of peaks towards a lower wavenumber can be ascribed to the generation of structural defects in the samples and the decrease in size of the in-plane  $sp^2$  domains (Chen et al. 2010).
- 3- The intensity ratio ( $I_D/I_G$ ) between the G band and D band can be employed to estimate the graphitisation quality or defective disorders of the crystalline graphite. After the thermal reduction process, the calculation of the intensity based on the ratio of D and G-bands ( $I_D/I_G$ ) increased from 0.88 for GO to 0.90, 0.93 and 0.94 for RGO-120, RGO-160 and RGO-180, respectively. The G-band in Raman spectra corresponds to the C-C chains of carbon atoms. The D-band is correlated with structural defects, such as holes, rotated carbon bonds, or deformed rings, and with chemical defects corresponding to oxy-functional groups (carbonyl and hydroxyl) attached to the planar carbon lattice and edges. When the oxygen content is decreased, which results from the more efficient reduction of GO, the intensity ratio  $I_D/I_G$  increases. This can correspond to the appearance of numerous (but small) restored  $sp^2$  regions. The size of defect-free  $sp^2$  regions is inversely related to the ratio of D band intensity to G band intensity ( $I_D/I_G$ ). This slight shift towards a higher value may be attributed to the formation of small graphitic domains as a result of the reduction process on the GO sample (Park et al. 2014),



inferring that more defects form when some oxygen atoms are removed. This result is also consistent with the explanation of (Chen et al. 2011) that newly created graphitic domains are smaller in size and more numerous. Chen et al. (2010) also reported that  $I_D/I_G$  increased from about 0.95 in the case of GO to 0.96 for RGO, confirming this current study.

However, these formed graphitic domains present in RGO samples have smaller sizes than those existing in GO before the reduction process. Moreover, the presence of these new domains was confirmed in large numbers in the RGO sample by (Stankovich et al. 2007). These results led those authors to select alternative methods for reducing GO, such as the chemical approach.

After baseline corrections, the  $I_D/I_G$  intensity ratio can be utilised to estimate the distance between disorders in graphene sheet which is roughly 1.0 for natural graphene and increases with the decline in average size of the  $sp^2$ -hybridized domain and average crystalline size ( $L_a$ ) (Pimenta et al. 2007):

$$L_a = (2.4 \times 10^{-10}) \lambda_{\text{laser}}^4 \left[ \frac{I_D}{I_G} \right]^{-1}$$

where  $L_a$  is the average crystalline size and  $\lambda$  is the laser wavelength which is about 512 nm. The studied average crystalline sizes of GO, RGO-120, RGO-160 and RGO-180 are 20.0, 19.5, 19.1 and 20.3 nm, respectively, indicating the decline in average crystalline size of RGO-120, and RGO-160 compared with GO, while the  $sp^2$  domain was increased in the case of RGO-180.

In conclusion, a result of applying the Raman technique is that after proceeding the reduction process on a GO sample with the help of the vacuum exfoliated/reduction process technique at atmospheric pressure (0.1 MPa), changes in the structure under the influence of different temperatures were observed. In fig 3-9, the D/G peak height ratio ( $I_D/I_G$ ) of RGO-180 was about 0.94 which confirming a high defect in RGO structure. Whereas, in unoxidized, single-layer graphene, the D disorder band is barely detectable ( $I_D/I_G \leq 0.01$ ) (Liu et al. 2008), the intrinsic defect concentration is very low which confirming high crystallinity.

The expansion force that arises from thermal decomposition for the GO sample under the effect of atmospheric pressure must overcome the van der Waals interactions that are responsible for binding pristine graphene sheets to each other and thereby yield the required RGOs in this current study. Meanwhile, the maximum required pressure to overcome the van der Waals forces was determined theoretically to be about 7.2 MPa. Moreover, using the vacuum method contributed to the reduction in the temperature required to achieve the GO exfoliation, where the critical temperature was identified to be 500°C under atmospheric pressure. However, this exfoliated temperature decreased to only around 120°C, which is the lowest temperature used in this current study. In addition, GO could be more unstable under vacuum because the temperature employed is lower than the onset decomposition temperature  $T_d$  of 200°C (by TGA analyser) (Zhang et al. 2011).

#### **3.6.1.4 XRD**

Fig. 3-10. a shows XRD patterns for pristine graphite, GO and RGOs. The raw graphite sample shows an intensity peak centred at  $2\theta = 26.3^\circ$ , corresponding to the inter-planar spacing between graphitic layers of 0.35 nm, which based on the regular crystalline pattern of graphite. However, after the successful oxidation process, the GO sample showed a significant decline at  $2\theta = 11.6^\circ$ , which is confirmed by (Chen et al. 2010; Tortello et al. 2016). Bragg's law has been used to determine the d-spacing of the samples and displayed an increase from 0.35 nm in the case of raw graphite to approximately 0.78 nm for the GO sample, implying that the GO was enlarged when the graphite was oxidised. In other words, the GO sample was successfully separated. This high expansion in the GO sample can be ascribed to the presence of OCFGs that were formed as a consequence of the oxidation process. Therefore, the abundance of these OCFGs that were intercalated between the GO layers led to the enlarged d-spacing.

In addition, the XRD pattern showed many peaks for RGO samples after the thermal reduction process. Fig. 3-10, and Table 3-5 show that the RGO samples (RGO-120, RGO-160 and RGO-180) had a lower d-spacing of 0.62, 0.49 and 0.46 nm, respectively.

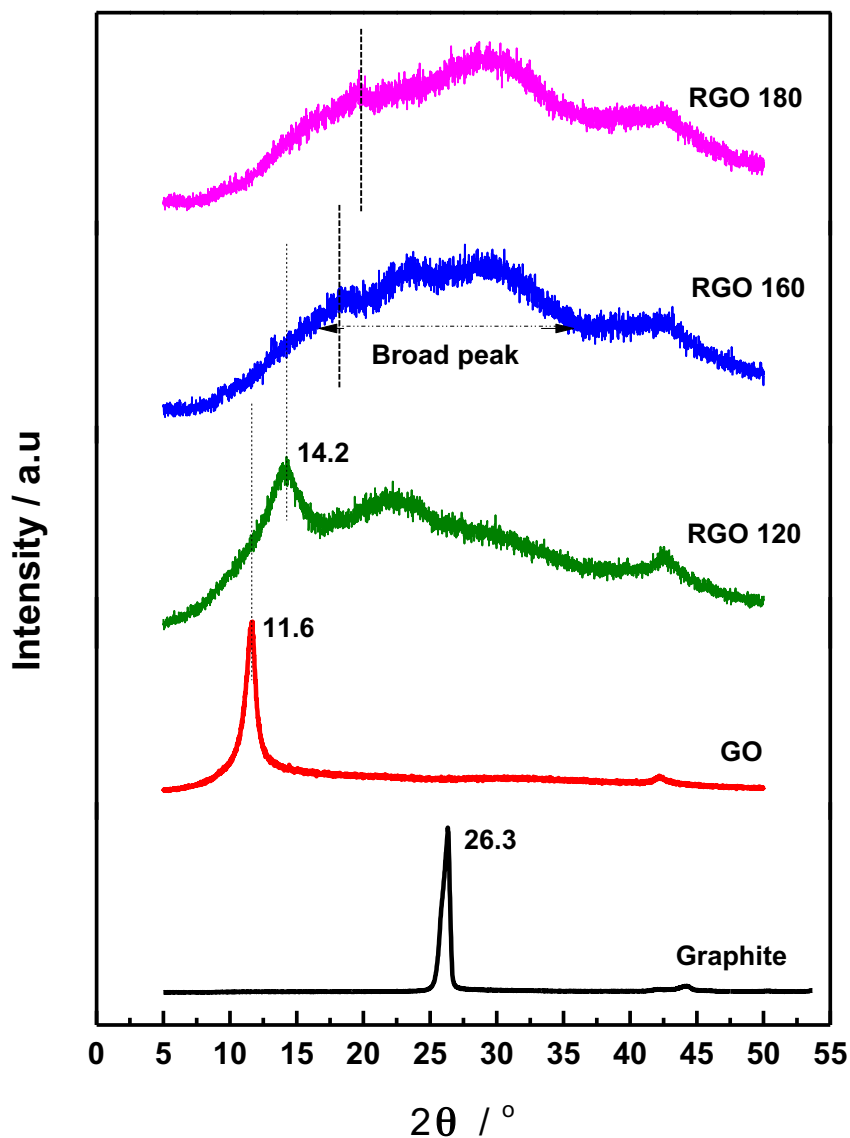


**Figure 3-10.** XRD curves of graphite, GO and RGOs samples.

This variation of the interlayer spacing between RGOs can be attributed to two main reasons:

1. The level of the oxidation process for graphite, which leads to the functionalisation of the individual GO sheets. As a result, it hinders the nano-sheets from stacking and thereby leads to a large increase in the interlayer spacing of GO.

2. The level of the reduction process of GO by applying any approach (e.g. thermal, green, chemical), resulting in the removal of many of the OCFGs that attach onto the main structure of GO. As a result, the individual sheets will stack again because of the  $\pi$ - $\pi$  stacking interaction.
3. The d-spacing of RGO-160 and RGO-180 were identified at 0.49 and 0.46, respectively, and the similarity may be because of the convergence of temperatures employed in the reduction process, which did not exceed 20°C.

*Table 3-5. Summary of XRD patterns of graphite, GO and RGOs samples.*

<b>Sample</b>	<b>Peak position / °</b>	<b>d-spacing / nm</b>
<b>Graphite</b>	26.3	0.35
<b>GO</b>	11.6	0.78
<b>RGO 120</b>	14.2	0.62
<b>RGO 160</b>	18.3	0.49
<b>RGO 180</b>	19.5	0.46

### 3.6.1.5 XPS

XPS was conducted to determine the degree of reduction of GO under different temperatures and to characterise the chemical composition of the surface for quantitative analysis.

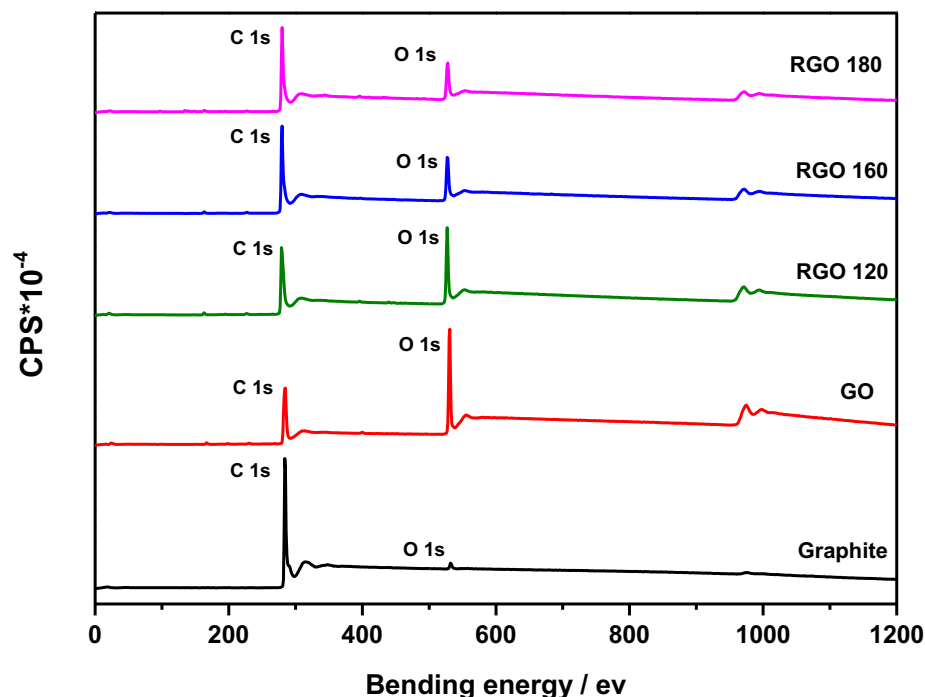


*Figure 3-11. Survey scan spectra of pure graphite, GO, RGOs.*

Figure 3-11 shows a representative of an XPS survey scan of graphite, GO and the RGO samples, obtained at different temperatures. The survey scan spectrum indicates the existence of both carbon and oxygen atoms at the surface of all samples. Because of the high oxygen content associated with the GO sample arising from the oxidative treatment, the XPS scan spectra shows an intensity peak of O 1s, as well as a tiny peak of O 1s for the graphite sample, which can be because of slight atmospheric oxidation.

However, the sharp peak of C 1s for the bare graphite spectrum displays only one asymmetric peak, centered at 284.1 eV because of the  $\pi$ -bond shake-up satellite. The C/O ratio for the reference sample (graphite) was observed to be 61.2 in the current study.

In contrast, GO has a significant degree of oxidation leading to the formation of OCFGs on the

surface (i.e. carboxyl, hydroxyl and epoxide groups) and therefore increasing the content of oxygen O1s. This peak of O1s for RGO considerably decreased because the degree of reduction increased. The wide scan spectra of the GO sample show a sharp peak of both C 1s and O 1s at the positions of 285 eV and 532.7 eV respectively, (Fig. 3-11).

As shown in Table 3-6, the samples were highly influenced by the oxidation process, as the C/O ratio decreased with the presence of abundant OCFGs. However, this ratio significantly recovered with the degree of reduction of GO. Thus, the atomic ratio of C/O is directly proportional to the increase in temperature.

**Table 3-6.** Carbon and oxygen content (%) in the samples obtained from the XPS test.

Sample	C %	O %	C/O ratio
Graphite	98.40	1.60	61.51
GO	68.12	29.93	2.28
RGO-120	76.16	22.21	3.43
RGO-160	83.40	15.36	5.42
RGO-180	83.67	14.11	5.93

In the GO sample, the C/O atomic ratio is about 2.28, suggesting that the GO has associated with many OCFGs in the main structure of the graphitic carbon through the oxidation process. After applying the thermal reduction method, the C/O ratio for RGO-120, RGO-160 and RGO-180 increased gradually, depending on the degree of temperatures used from 2.28 for GO to 3.43, 5.42, 5.93, respectively. It is still possible to clearly see the intensity peak of O1s for all RGO samples in the survey spectra, indicating that there are some residual OCFGs that remain on the surface. Therefore, this result of the atomic ratio of C/O, for RGO is evidence of a successful reduction.

Fig. 3-12 shows the C 1s XPS analysis for graphite, GO and RGO samples at different temperatures. For pure graphite (Fig. 3-12 (A)), the C=C/C-C characteristic peak is related to  $SP^2$  and  $SP^3$  hybridised carbon at 284 eV. The characteristic peak of C-C stretching for graphite

appeared at 284.5 eV, as reported by (Krishnamoorthy et al. 2013).

The GO sample can be specified by three intensity peaks that are linked to the C atoms in different functional groups. This connection is because of the high degree of oxidation of the GO compared to the degree of oxidation of the RGO samples. The four characteristic peaks are; C=C/C–C (non-oxygenated ring) characteristic peak related to  $sp^2$  and  $sp^3$  hybridised at (285 eV), the phenol and ether C in C–O bonds 287 eV, the carbonyl C (C=O, 289.1 eV) and the carboxyl C (O–C=O, 289.1 eV), as shown in Fig. 3-12 (B) and summarized in Table 3-7.

**Table 3-7.** The XPS spectra for the B.E (eV) obtained in C1s analysis for both GO and RGOs samples compared with the graphite sample.

Sample	Assigned C1s peak in this work with corresponding binding energy (eV)			
	C–C, C=C	C–O	C=O	O–C=O
<b>Graphite</b>	284.0	-	-	-
<b>GO</b>	285.0	287.0	288.9	-
<b>RGO-120</b>	285.0	287.3	289.1	291.1
<b>RGO-160</b>	285.0	286.2	289.2	292.1
<b>RGO-180</b>	285.0	286.0	289.0	291.5

The C 1s peaks of RGO-120, RGO-160 and RGO-180 also indicate that they afford the same OCFGs as the GO sample. However, the peaks of these four components for all RGO samples showed a very weakened intensity compared with those of the GO sample, suggesting a significant de-oxygenation when applying the vacuum-assisted technique (Fig. 3-12. C, D, E). Moreover, these peaks show a slight shift in their locations compared with GO. Additionally, additional peaks can also be clearly observed in the RGO spectrum, which can be assigned to carboxylic groups at higher binding energies appearing around 291–292 eV. Wu et al. (2012) also obtained the main components similar to RGO by using a chemical reduction method with the existence of hydrazine as a reducing agent. The RGO distributed into four components, and of which, three are comparable to the GO sample but with lower intensity values, and the fourth component is a carboxyl group at 291.5 eV that is entirely similar to all RGO reported in this

research. In contrast, RGO-1400 shows a higher degree of reduction compared to RGO sheet those produced at low temperatures by 10.2% for RGO-180. However, the reduction of GO is not mostly concerns with the elimination of all oxygenated-functional groups, rather it directly associated with the electrical conductivity (semiconducting to be precise) and effective graphitisation ( $sp^2$  form).



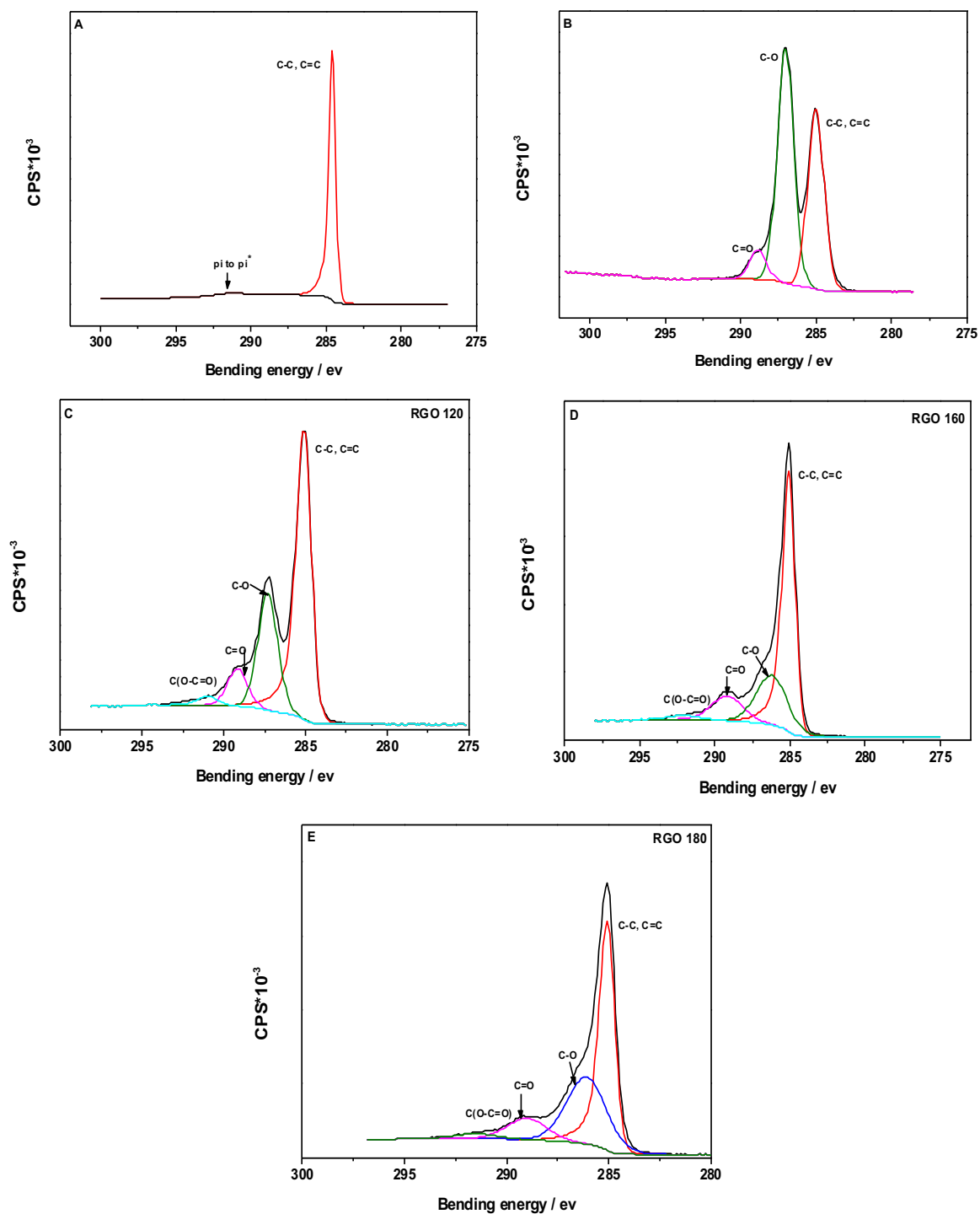


**Figure 3-12.** C 1s XPS spectra of graphite (A), GO (B), RGO at different temperature (C, D, and E).

### 3.6.1.6 TGA

TGA was used to determine the thermal stability of graphite, GO and RGO samples obtained at different temperatures, as shown in Fig. 3-13. It was taken the average of three specimens of each type.

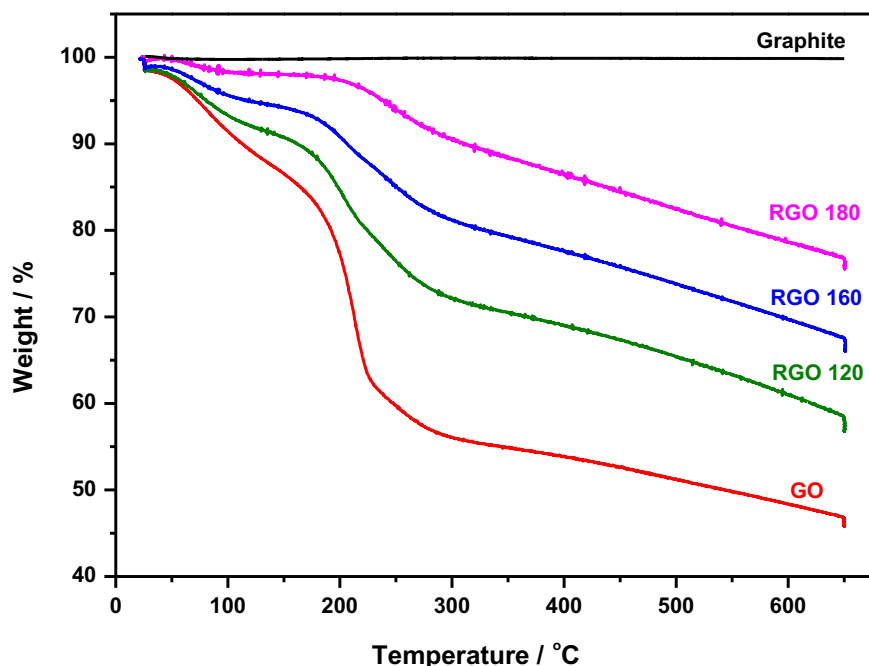


*Figure 3-13. The TGA plots for graphite, GO and RGOs*

The TGA curve for the raw graphite sample shows the best thermal stability over 650°C, as well as high thermal stability upon heating up to 900°C (Tang et al. 2014). Therefore, no obvious weight loss is observed, even at a high temperature. This retention of mass is explained by its highly graphitised structure (T.K et al. 2014; El-Khodary et al. 2014), whilst the GO sample is thermally unstable and begins to lose weight (approximately 15%), while heating below 100°C. This loss in mass can be ascribed to the evaporation of adsorbed H<sub>2</sub>O molecules.

Significant mass reduction of 30% between 160 and 200°C is due to the pyrolysis of the labile OCFGs on the surface of GO, accompanied by a release of massive gases such as CO, CO<sub>2</sub> and steam. However, most oxygen contents associated with the basal planes of GO material such as epoxy and hydroxyl groups may be eliminated at 180°C, resulting in a partial recovery of some

important optical, thermal and electrical properties. Conversely, other OCFGs associated tightly with the edges of GO only undergo pyrolysis at temperatures higher than 180°C because of their high stability (Pei & Cheng 2012).

In contrast with the GO sample, which has intense weight lowering at about 200°C, the RGO curves show slight reduction in weight below 200°C. In the case of the RGO-180 sample, the curve shows good thermal stability, as the main OCFGs are almost totally removed via the vacuum reduction technique. In contrast, RGO-160 and RGO-120 showed slight reductions in weight of 6 and 11%, respectively, demonstrating that OCFGs still exist on the RGO-160 and RGO-120 samples (it can be described as a partial reduction) to a lesser extent, after vacuum-assisted reduction. The results also, show that the residual masses around 600°C for RGO-120, RGO-160 and RGO-180 were 58.2, 69 and 80.3%, respectively. Therefore, these results indicate that the residual mass gradually increases as the temperature employed for the reduction process increases. In contrast, the thermal stability of RGO was confirmed when using a vacuum-assisted thermal treatment process at low temperatures, which is consistent with TGA result of RGO obtained by a tube furnace.

### **3.7 Comparison between two synthesis methods**

The RGO sheets obtained via a tube furnace show disordered structures, wrinkling and randomly aggregated features, impacting the unique properties of a single sheet. The thermal reduction degree of these RGO sheets is slightly higher than that of RGO produced by the vacuum-assisted method because of the removal of most OCFGs. The tube furnace at high temperatures is most effective at reducing C–O–C groups but has low to moderate efficiency in reducing carboxylic acid groups, according to the XPS results.

The electrical conductivity can be used as a direct indicator of the defect recovery degree and the reduction degree. GO and RGO films were fabricated by the vacuum filtration method. The electrical conductivity of both GO and RGOs is calculated by

$$\sigma t = \frac{1}{R_s}$$

where  $R_s$  ( $\Omega \text{ S}^{-1}$ ) is the electrical resistance of a sheet,  $\sigma$  ( $\text{S cm}^{-1}$ ) is the bulk conductivity and  $t$  is the sample thickness. The electrical resistance can be measured by the four-probe method. It was taken the average value of three specimens of each type.

The electrical conductivity of RGO nanosheets obtained by the tube furnace (at  $1400^\circ\text{C}$ ) and vacuum routes (at  $120$ ,  $160$  and  $180^\circ\text{C}$ ) were calculated to be  $223 \pm 3.5$ ,  $202 \pm 7.5$ ,  $267 \pm 6.0$ ,  $293 \pm 4.0 \text{ S cm}^{-1}$ , respectively. After performing the reduction by both approaches, all the electrical conductivity has been improved compared with GO, referring to the reduction of GO and the restoration of the  $\text{sp}^2$  carbon re-constructed conductive pathways. The electrical conductivity of RGO obtained via the vacuum method (at  $180^\circ\text{C}$ ) is the highest; combining with the results of XPS indicates that substantial de-oxygenation, principally the removal of carbonyl species, can help improve the electrical conductivity. Therefore, the reduction of GO is not mostly concerned with the elimination of all oxygenated-functional groups; rather, it is directly associated with the electrical conductivity (semiconducting, to be precise) and effective graphitization. Some products can recover their higher electrical conductivity more than the original graphene by the determining the time and optimal temperature of reduction. Table 3.8 illustrates the results of applying the synthesis methods to the structure of GO. The table shows that the GO reduction via the vacuum-assisted method has the lowest number of defects generated because of in-plane  $\text{C}=\text{C}$  cracking during the removal of the residual hydroxyl and partial epoxide groups. In addition, the table shows that the GO reduction at low and high temperatures via vacuum oven and tube furnace are environmentally friendly, low-cost, large quantity and gives the minimal electrical resistivity. However, vacuum oven is a relatively

straightforward methodology. Although, the C/O ratio of RGO-1400 is higher than that of RGO-180, the electrical conductivity of RGO obtained via the vacuum method (at 180°C) is  $293 \pm 4.0 \text{ S cm}^{-1}$  which is higher than that obtained via a tube furnace by 32%, which indicates a restoration of  $sp^2$  structure. It can be claimed that reducing of GO is not mostly concerned with the elimination of all oxygenated-functional groups; rather, it directly associated with the electrical conductivity (semiconducting to be precise) and effective graphitisation. Both synthesis methods (tube furnace and vacuum oven techniques) are efficient for producing RGO from dry GO powder.

**Table 3-8.** A summary comparison of the structure results of RGO sheets produced by the reduction techniques.

<b>Vacuum-assisted method</b> <i>at low temperatures/24 h</i>	<b>Tube-furnace method</b> <i>At high temperature/30 s</i>
Relatively straightforward method	This technique involves significant operational challenges.
Within low-temperature zones, a lattice relaxation of RGO occurs because of out-gassing generated from the residual carboxyl and partial hydroxyl groups.	Within 1400°C, a large number of defects are generated because of in-plane C=C cracking during the removal of the residual hydroxyl and partial epoxide groups.
Large quantity	Low quantity
The electrical conductivity of RGO-180 sheets ( $293 \pm 4 \text{ S cm}^{-1}$ ) is higher than that of RGO obtained at high temperature via a tube furnace by about 32%.	RGO sheets display an amorphous structure.
contain single to few-layered sheets with an average thickness of $\sim 0.46 \text{ nm}$ (at 180°C), and their lateral size of $< 2 \mu \text{ m}$ is comparable to that of conventional RGO generated at 1400°C at atmospheric pressure. These sheets stacked each other with less folding and wrinkles.	contain single to few-layered sheets with an average thickness of $\sim 0.4 \text{ nm}$ , and their average size of $> 2 \mu \text{ m}$ . One of the reasons for this difference is because of RGO wrinkling at large deformation.
Reduction process at a low temperature of 180°C has exfoliation efficiency compared to an elevated temperature of 1400°C. Raman spectra illustrate that the vacuum method can produce RGO sheets with less defect as compared to other approaches, such as reduction by hydrazine agent or conventional thermal processes.	The thermal reduction process was affirmed by the significant increase in the C/O ratio when compared with the GO, which also confirms a notably increased thermal stability.

## 3.8 Conclusion

1. RGO nano-sheets was successfully produced by using new and straightforward methods, which are the tube furnace method and the vacuum assistance method. These efficient methods utilised in this study were more ecologically-friendly ways of producing RGO in contrast to other approaches that comprise serious chemical reactions and involve reactive conditions with high toxicity.
2. Although reaction times under vacuum are relatively longer than those under thermal treatment at high temperature, this new technique is still simpler and more efficient than the other methods reported in previous studies. Thus, other techniques, such as using a microwave hydrothermal reactor (Majcher et al. 2013), may be used at different temperature and time intervals to obtain RGO sheets. Using XPS analysis, the O/C ratio of the GO sheets reduced from 44 to 16% after vacuum oven at 180°C. Because, hydrazine and microwave hydrothermal reactor at 180°C are reduced the O/C ratio down to 15% and 17% respectively, vacuum oven reduction method can be considered as a serious potential competitor for hydrazine and MHR methods (Kimiagar et al 2015). Kimiagar et al. (2015) reported that there was high increase in defects' density after reduction and the ratio of  $I_D/I_G$  was 1.5, whilst there was slight improvement in  $I_D/I_G$  of RGO-180 structure (0.94) in current study. It is envisaged that the method developed in this study could be a more efficient and cost-effective reduction process to produce RGO sheets.
3. The thermal reduction process was affirmed by the significant increase in the C/O ratio in both methods when compared with the GO, which also confirms notably increased thermal stability.
4. The reduction process at a low temperature of 180°C has exfoliation efficiency compared to an elevated temperature of 1400°C. Although the reduction efficiency of

oxygenated functional groups was comparatively lower, the obtained RGO sheets were readily chemically active for covalent bonding with the matrix. At lower temperatures of 120°C, 160°C and 180°C, a vacuum-assisted method for thermal exfoliation and large quantity in situ reduction of GO was reported. Just a few layered sheets with an average thickness of 0.62, 0.49 and 0.46 nm of RGO sheets were obtained; additionally, their lateral size ( $< 2 \mu\text{m}$ ) is comparable to that of conventional RGO generated at 1400°C, at atmospheric pressure ( $> 2 \mu\text{m}$ ). The increased C/O atomic ratio in comparison to that of graphite oxide confirmed the in situ thermal reduction occurring during the exfoliation process.

5. Raman spectra illustrate that the vacuum-oven method can produce RGO sheets with fewer defects than to other approaches, such as reduction by hydrazine or thermal reduction by a tube furnace at high temperatures.

6. The electrical conductivity of RGO obtained via the vacuum method (at 180°C) is the highest; combining with the results of XPS indicates that substantial de-oxygenation, principally the remove of carbonyl species, can help improve the electrical conductivity.

## **4 Chapter 4: Synthesis and properties study of EP–RGO nanocomposites**



## 4.1 Introduction

In recent years, the advancement of nanomaterials based on RGO in a polymer matrix has opened a new horizon in materials science. These polymer nanocomposites exhibit large increases in their properties compared with their polymer counterparts that were reinforced by GO sheets. Such properties can be achieved at a very low nano-filler loading level in the matrix. The excellent properties of high electrical conductivity, thermal conductivity, mechanical strength and surface area make RGO very useful in various applications. But, RGO sheets is very hard to disperse it homogeneously in polymer matrix compared to GO. This is due to its insolubility in the matrix, van der Waals forces, and  $\pi$ - $\pi$  stacking between the individual sheet. Typically, RGO is prone to aggregate in a variety of polymer matrices. These obstacles include attaining excellent interfacial bonding properties and good dispersion of the nano-sheets in the polymeric matrix. However, to date, a relatively limited number of studies have attempted to characterise and evaluate the thermal and electrical conductance and mechanical performance of EP composite incorporated with low-level contents of RGO nano-sheets and good dispersion. In the present study, we report the effect of high-dispersion RGOs on the microstructure, mechanical, electrical and thermal behaviour of EP nanocomposites with a low variation of the RGO weight fraction. Herein, we report an efficient method for the dispersion of RGO nano-sheets in the matrix by a combination of two techniques for improving the dispersing of RGO in the matrix. A dispersion method that deploys a high-ultrasonic mixer frequency of 120 kHz and power of 240 W under the influence of temperature at 60°C and high shear mixer at 1600 rpm was used to disperse RGO nano-sheets in the EP matrix, resulting in homogeneous dispersion of RGO. The results showed that the elastic modulus, tensile strength, thermal and electrical conductance were all simultaneously improved. In addition, the results show that using RGO nano-sheets had a significant influence on the epoxy-anhydride curing system by increasing the  $T_g$  of the cured EP matrix.

## 4.2 Experimental section

### 4.2.1 Materials

The materials employed in the work are described in Table 4-1.

**Table 4-1.** *The characteristics, manufacturers and suppliers of the materials used.*

<i>Material</i>	<i>Characteristics</i>	<i>Manufacture/ UK</i>	<i>Supplier/UK</i>
EPON 828	DGEBA with 185–192 g/eq, Medium viscosity: 100–160 poise at 25°C.	Delta Resins Ltd	Delta Resins Ltd
Epoxy embedding medium, hardener MNA	Oily liquid of $\geq 99\%$ purity	Sigma-Aldrich	Sigma-Aldrich
N,N-Dimethyl-benzylamine	Catalyst of $\geq 99\%$ purity		
Tetrahydrofuran (THF)	Liquid, purity $> 99.9\%$	Sigma-Aldrich	Sigma-Aldrich
Distilled water	Liquid	Sheffield Univ. Lab	Sheffield Univ. Lab
RGO sheets (1)	Produced by using a tube furnace at high temperature		
RGO sheets (2)	Produced by using a vacuum oven at low temperatures		

All the materials were used as received without additional purifications.

## **4.3 Section One-Tube furnace**

### **4.3.1 Production of EP nanocomposites reinforced by RGO (produced at high-temperature)**

For the synthesis of EP–RGO nanocomposites, the desired amount of RGO was dispersed in THF (4 mg ml<sup>-1</sup>) using an ultrasonic treatment for 1 h at room temperature and was then continuously stirred for 4 h. A simple method was employed to disperse the RGO/THF mixture at different loadings into the EP resin. After magnetic stirring the mixture for 4 h, the mixture underwent ultrasonication at a frequency of 120 kHz at a power of 240 W at 60°C for 30 min (the glass beaker was covered during the process). Lastly, the specimen was subjected to high-shear mixing (Silverson, UK) at 1600 rpm for 90 min. Next, the mixture was transferred to a magnetic stirrer hot-plate to remove the solvent through evaporation by heating at 70°C for 2 h and was then further de-gassed overnight in a vacuum oven at 70°C.

A stoichiometric amount of anhydride curing agent and catalyst was added to the mixture (the ratio of DGEBA to anhydride and catalyst was kept at 100:90:1) at 60°C and the mixture was stirred for 20 min to obtain good homogeneity. The mixture was immediately poured into a release-agent coated silicone mould as the viscosity of the mixture reduced after the addition of hardener and catalyst. The residual THF was removed by degassing in a vacuum oven at 75°C for 2 h and, then pre-cured at 120°C for 3 h and then at 150°C for 3 h with a ramp up at 0.3°C/ min. A post-cure step of 180°C for 2 h was performed and then ramp down at 0.5°C/ min to 24°C. The neat EP was also prepared by the same procedure. The prepared samples of EP reinforced by RGO material were then tested for their morphological, electrical conductivity, mechanical performance and thermal behaviour.

### 4.3.2 Characterisation

Some of the significant characterisation techniques are described in detail below:

#### 1. Fourier Transform Infrared Spectroscopy (FT-IR)

FT-IR Spectra of the EP with its nanocomposites were recorded on a Perkin Elmer 100 Series. It was employed to characterise functional groups present on the surface of samples. All spectra were obtained in transmittance mode, ranging from 400 to 4000  $\text{cm}^{-1}$  at 4  $\text{cm}^{-1}$  resolution by accumulating 16 scans with a scan speed of 0.2  $\text{cm}/\text{sec}$ .

#### 2. Scanning Electron Microscopy (SEM)

SEM, Inspect F, Poland is a powerful magnification apparatus that is utilized to characterise the cryogenic fracture surface for the EP and EP/RGO at different magnification powers. To obtain a clean fracture surface, the samples were snapped inside the container filling with liquid nitrogen; after being soaked for about 5 min, the samples were broken at the required place, and they were mounted to the aluminium sample holder (Agar Scientific, Germany) of 25 mm diameter, 16 mm height with a doubled angle of 90°. Then, the fracture surfaces of the samples were coated by using a gold sputter coater (Emscope SC, UK). The reason behind this coating is that the most of polymers are non-conductive materials and thus need to have their conductivity improved, and the image quality is improved through minimising the electric charge build up in a non-conducting sample. The sample was placed in a vacuum chamber for coating under argon gas purge and vacuum pump. When the pressure inside the chamber reached 0.06 Tor (8.0 Pa), the coating process started at 15 mA for 3 min, which is the time required to complete the coating process at a gold sputter rate of 10  $\text{nm min}^{-1}$ .

#### 3. Thermal Gravimetric Analysis (TGA)

TGA was performed on a Perkin Elmer Pyris 1 TGA instrument (USA) to study the thermal behaviour for EP with its nanocomposites. The sample (5 mg) was placed in an aluminium

crucible and ramped from 24 up to 650°C under flow of nitrogen at 50 mL min<sup>-1</sup> with a heating rate of 10°C min<sup>-1</sup>.

#### **4. Differential Scanning Calorimetry (DSC)**

The Perkin Elmer, Pyris 6 DSC was used to measure the value of  $T_g$  for EP with its nanocomposites. The sample (10 mg) was precisely weighed in an aluminium pan and sealed tightly. The reference pan was left empty. Both the aluminium pans (sample/reference) were placed inside the DSC machine and ramped from 24 up to 240°C under the flow of N<sub>2</sub> gas purge at 50 mL min<sup>-1</sup> with a heating rate of 10°C min<sup>-1</sup>. Two cycles were performed for each sample, and the  $T_g$  values were taken from the 2<sup>nd</sup> heating cycle to remove any effects from the remaining traces of solvent into the sample as well as any thermal history.

#### **5. Dynamic Mechanical Analysis (DMA)**

DMA apparatus was performed on a Perkin Elmer, DMA 8000, USA, under a dual cantilever mode to measure the storage modulus for the EP with its nanocomposites where the strain was 0.5% (0.005 mm). The experiments were run in a temperature range from 20 to 200°C at a ramp rate of 3°C min<sup>-1</sup>. The test was performed on a rectangular cross-section of the samples 40 × 10 × 2 mm at the oscillatory frequency of 1 Hz.

#### **6. Mechanical test**

The Hounsfield universal testing machine (Hounsfield, UK) equipped with a 5 kN load cell was used to measure the tensile properties under a crosshead speed of 1 mm min<sup>-1</sup>. The dog-bone specimens were made using a preheated silicone mould, with dimensions of 80.0 × 10.0 × 2.0 mm in accordance with ISO 527-1/2. The Appendix shows the specification of this standard. Five specimens were used for each measurement, and the reported results represent an average result.

#### **7. Electrical resistivity**

The volumetric electrical resistivity test of the rectangular sample was conducted with a two-

probe method according to ASTM D4496 at 23°C. This method is appropriate for the sample that possesses an electrical resistivity  $> 10^{10} \Omega \text{ cm}$ . At least three samples were measured for each formulation. In the two-probe method, the sample was scratched with the sharp scalpel blade, dipped manually in liquid-nitrogen and then broken at the required place (6 cm long). The fracture surface ends were coated with silver conductive paint and left to dry for 1 h. One probe was placed on each end surface and applied an electric field across the specimen (100 V) using a Keithley 2400 Source Meter. The electrical resistivity is calculated from the following equation:

$$\rho = \frac{(\Delta V)(w)(t)}{(i)(L)}$$

where  $\rho$  is the volume electrical-resistivity ( $\Omega \text{ cm}$ ),  $\Delta V$  is the voltage drops over length of sample (volts),  $i$  is the current (amps),  $w$  the sample width (1 cm),  $t$  is the sample thickness (0.22 cm) and  $L$  is the length over which the voltage drop is measured.

The electrical resistivity of EP/RGO nanocomposites was measured with a Keithley Model 8009 test linked with 6517B Electrometer (ASTM D257) at 23°C by applying an electric field across opposite sides of specimen (100 V) and the resistance  $R$  measured after applying the specified voltage against sample for 60 s, which was the electrification time. Four specimens were measured for each formulation. The electrical resistivity  $\rho_t$  is calculated from the following equation:

$$\rho_t = \frac{R A_C}{h} \quad (\Omega \cdot \text{cm})$$

where  $h$  is the thickness of the specimen (m),  $A_C$  is the effective area for the electrode ( $\text{m}^2$ ) and  $R$  is the resistance,  $\Omega$ . The sample test was 10 cm square with a thickness of 0.22 cm, and the diameter of the electrode was 5.4 cm.

## 8. Thermal conductivity

A thermal properties analyser (Flashline-3000, ANTER, USA) was used to measure the thermal diffusivity for EP with its nanocomposites according to the ASTM E1461-13 standard. The specimens were coated with graphite paint to improve their absorption properties. The front surface (not reflect light) of a sample is heated by a flash pulse source (a xenon discharge lamp), and the temperature increase on the rear surface is recorded via an infrared detector. The test specimen was 10 × 10 mm and about 1 mm thick. A temperature ranges of 30–100°C was used, with a laser voltage of 450 V and a pulse width of 600 s. Once thermal diffusivity was measured the thermal conductivity can be calculated from the following equation:

$$k = \rho\alpha C_p \quad (\text{W m}^{-1} \text{K}^{-1})$$

where  $\rho$  is the density of samples ( $\text{Kg m}^{-3}$ ),  $\alpha$  is the diffusivity ( $\text{m}^2 \text{s}^{-1}$ ) and  $C_p$  is the specific heat ( $\text{J kg}^{-1} \text{K}^{-1}$ ).

## 9. Nanoindentation test

The samples cut from untested tensile specimens were subjected to a nanoindentation testing using a quantitative nanomechanical test instrument (TriboScope TS70; Hysitron, Inc., MN, USA). The typical test was run to a maximum force of 10 mN and a depth of 1500 nm. The load was applied using a partial unloading load function using multiple load-unload cycles. For each sample, 9 indents were made in a 3×3 array with 15  $\mu\text{m}$  indent spacing. A diamond Berkovich indenter probe (Hysitron) was used for the tests, and the elastic moduli (E) of the specimen was calculated using the contact stiffness per the Oliver–Pharr method. The elastic moduli were obtained from the slope of load-displacement curves through the TS-70 proprietary software (Hysitron) in the standard unloading analysis. At least four samples were measured for each formulation.

## 4.4 Results and discussion

### 4.4.1 Spectroscopic measurements

#### 4.4.1.1 SEM

The morphologies of the neat EP and its nanocomposites from the cross-sectional fracture surface were determined by SEM images at low and high magnification in order to study the effect of dispersion and the interfacial interactions between RGO nano-sheets and the EP composite.

As shown in Fig. 4-1 (A), the regions of the fracture surface of the neat EP is relatively smooth with no specific microstructure. Generally, the comparison between the fracture surface of the pure EP and the fracture surface of EP incorporated with GO or RGO sheets shows that the latter have coarse surfaces compared with the smoother surface of the former. Also, Fig. 4-1 (B) shows that the EP incorporated with GO appears GO sheets with micrometre size exfoliated into irregular flakes. These flakes are evenly dispersed in the polymer with some random restacks. In contrast, the RGO sheets at different loadings (0.1, 0.5 and 1.0) (images C, D and E) are tightly adhered to the EP, with some aggregates in some positions. The fractured cross-sections in Fig. 4-1 (C) were fairly rough with river lines when a small content of RGO nano-sheets was introduced into the matrix. With increasing RGO concentration, the cross-sections of the surfaces were very rough and complicated in the EP matrix, as shown by the wrinkled and crumpled structures seen in Fig. 4-1 (D and E). For example, at higher magnification, Fig. 4-1 (D') exhibits a much coarser fracture surface at 0.5 wt. % of RGO loading. As the loading of RGO was increased, more aggregations can be seen.



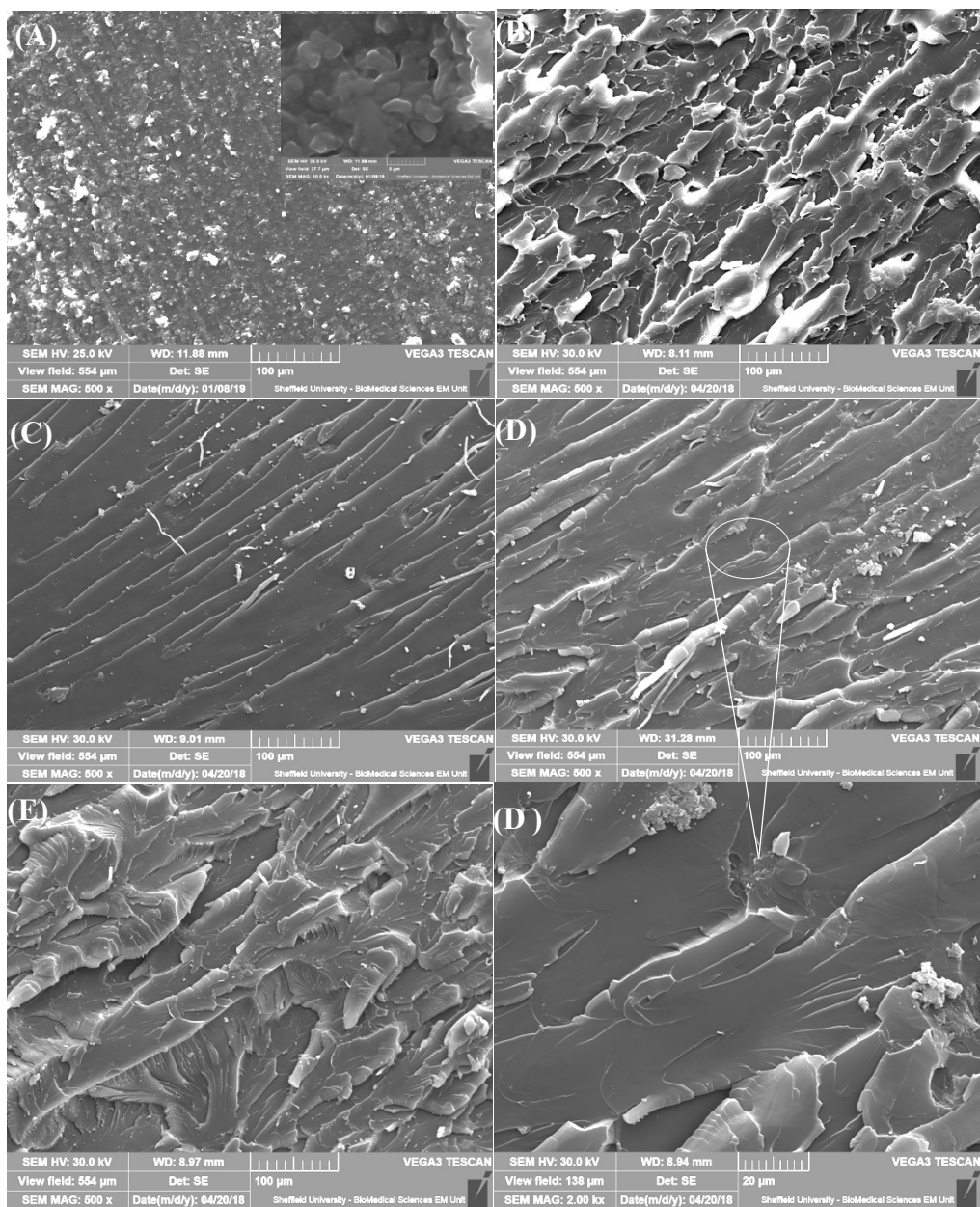


**Figure 4-1.** SEM micrographs of (A) Neat EP and its nanocomposites with (B) 1.0 wt. % of GO, (C) 0.1 wt. % of RGO, (D) and (D') low and high-magnification of 0.5 w.t % of RGO and (E) 1.0 wt. % of RGO.

#### 4.4.1.2 FT-IR

Fig. 4-2 shows the FT-IR spectra of EP, EP/GO and EP/RGO at different loading. A chain of peaks at 514 and 668  $\text{cm}^{-1}$  correspond to C–H out of plane-bending vibrations of the aromatic ring. The absorption peaks related to epoxy are located at 1606  $\text{cm}^{-1}$  which is ascribed to the stretching vibration of the benzene ring C=C, 1508  $\text{cm}^{-1}$  (C–C aromatic stretching vibration),

1044  $\text{cm}^{-1}$  corresponds to aromatic  $\text{C}-\text{O}-\text{C}$  bond, and 791 stretching  $\text{C}-\text{O}-\text{C}$  of ether group. The absorption peaks related to epoxy are located at 1606  $\text{cm}^{-1}$ , which is ascribed to the stretching vibration of the benzene ring  $\text{C}=\text{C}$ ; 1508  $\text{cm}^{-1}$ , which is ascribed to the  $\text{C}-\text{C}$  aromatic stretching vibration; 1044  $\text{cm}^{-1}$ , which corresponds to the aromatic  $\text{C}-\text{O}-\text{C}$  bond; and 791  $\text{cm}^{-1}$ , which corresponds to the stretching of  $\text{C}-\text{O}-\text{C}$  of the ether group. The absorptions peaks at 1260 and 1108  $\text{cm}^{-1}$  are related to the stretching vibrations of the  $\text{Ar}-\text{O}-\text{C}$  bond. Moreover, 2851 and 2967  $\text{cm}^{-1}$  are associated with symmetric and asymmetric vibrations of  $\text{CH}_2$ , respectively. In contrast, the high-intensity peaks at 970 and 914  $\text{cm}^{-1}$  associated with the oxirane ring in the uncured EP resin that is referenced by (Romão et al. 2006; Pizzutto et al. 2011) fully disappeared after the curing process of EP and its nanocomposites, as shown in Fig. S1 in the Appendix. Therefore, the absence of these peaks supports the notion that there is a high degree of cross-linking in the neat EP and its nanocomposites.

All previous FT-IR peaks refer to the main spectrum peaks of the absorption peaks of epoxy and confirm the attachment of RGO aromatic planes with EP (Nikolic et al. 2010). The majority of EP peaks obtained in the current study were confirmed by (Hsu et al. 2014). Moreover, in the current study, the peak at 1737  $\text{cm}^{-1}$  corresponding to  $\text{C}=\text{O}$  of  $-\text{COOH}$  on RGO shifted to 1723  $\text{cm}^{-1}$  owing to the formation of  $\text{C}-\text{O}$  bond in EP-RGO composites. In addition, the peak at 915  $\text{cm}^{-1}$  of EP nanocomposites disappeared, which also indicated the forming reaction between EP and RGO (Ding et al. 2017).

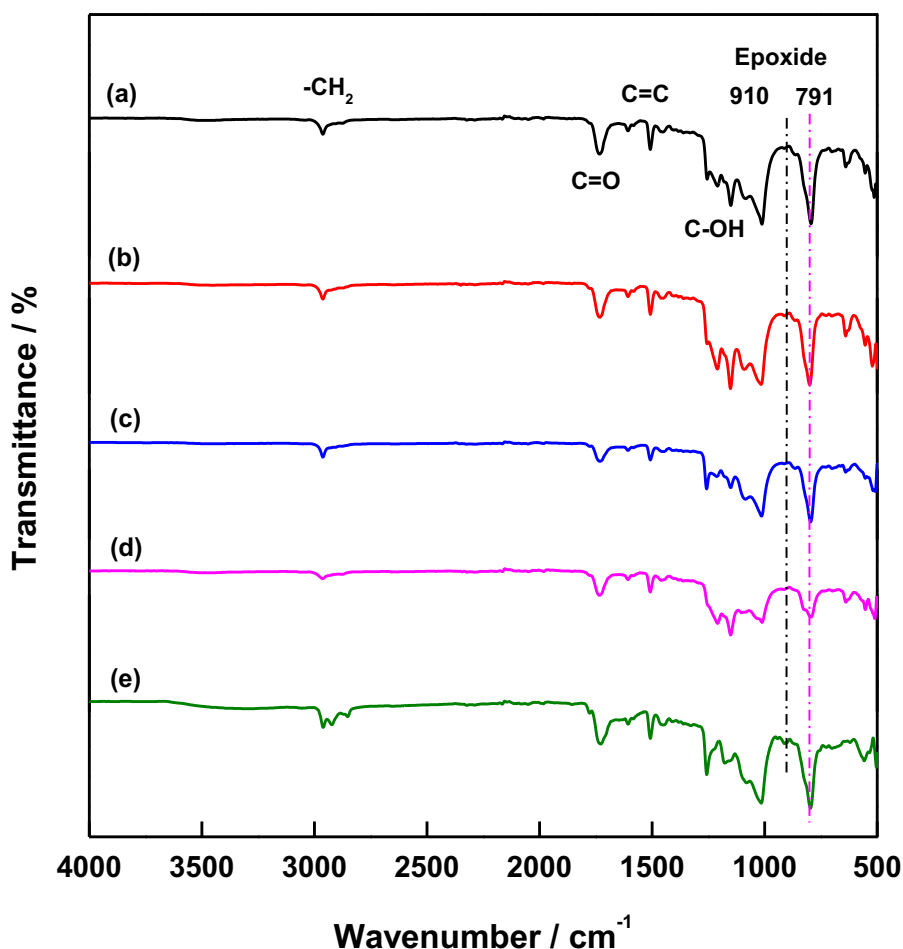


**Figure 4-2.** FT-IR spectra of (a) neat EP (b) EP- 0.1 wt. % RGO (c) EP- 0.5 wt. % RGO (d) EP- 1.0 wt. % RGO and (e) EP- 1.0 wt. % GO nanocomposites.

Moreover, by comparing the five curves of the cured EP and its nanocomposites, the FT-IR spectra show similar peaks to that of the neat EP but with an attenuated intensity because of the incorporation of RGO sheets, which do not exceed 1.0 wt. %.

## 4.4.2 Thermal and thermomechanical properties

### 4.4.2.1 TGA

In order to evaluate the effect of RGO sheet addition in the EP matrix, thermogravimetric analyses were performed. Fig. 4-3 shows the TGA curves of EP, EP/GO, EP/RGO at various weight fraction loadings and their  $T_d$  temperature peaks obtained by DTG curves under the influence of nitrogen at a heating rate of  $10^\circ\text{C min}^{-1}$ . Every samples repeated two times to

produce reproducibility of analysis and  $T_{50\%}$  is typically determined by using DTG curves at the maximum peak., as shown in Table 4-2.

For comparison purposes, the TGA thermograms of EP nanocomposites containing of GO sheets was tested too. It can be seen that the main weight degradation behavior took place at around 300-500°C, which was attributed to the degradation of EP network.

From the Fig. 4-3, the decomposition temperature  $T_d$  value of RGO/EP composites showed an increased trend with the increase of RGO content, and 0.5 and 1.0 wt.% of RGO resulted in a significant increase of ~15 and 18°C, respectively, compared to blank epoxy sample (330°C). In addition, the  $T_{50\%}$  (50% weight loss) of RGO/EP composites also showed an increased trend with the increase of RGO content, and 1.0 wt.% of RGO sheets resulted in a significant increase of 10°C, while the incensement of  $T_{50\%}$  for the GO loading did not appreciably affect the  $T_d$  value of EP composites. Similarly, Yousefi et al. (2014) reported that RGO sheets enhanced the  $T_d$  of the EP matrix at 1.5 wt. % loading by 8°C, meaning a higher thermal stability because of the merged RGO nano-sheets. These results showed a better thermal stability of RGO at low concentration than the other previous studies (Yousefi et al. 2014).

The slight increase of thermal stabilities may be attributed to the highly cross-linked structure and RGO surface area which restrict thermal motion of the EP molecular chain. Moreover, the layered structure of the nanocomposite, which makes a zigzag pathway for the volatile degradation products, also hinders the thermal degradation rate of the materials. Furthermore, this result can be attributed to the good interaction that occurs between EP and the nano-sheets, as well as the uniform dispersion of these sheets along the matrix.

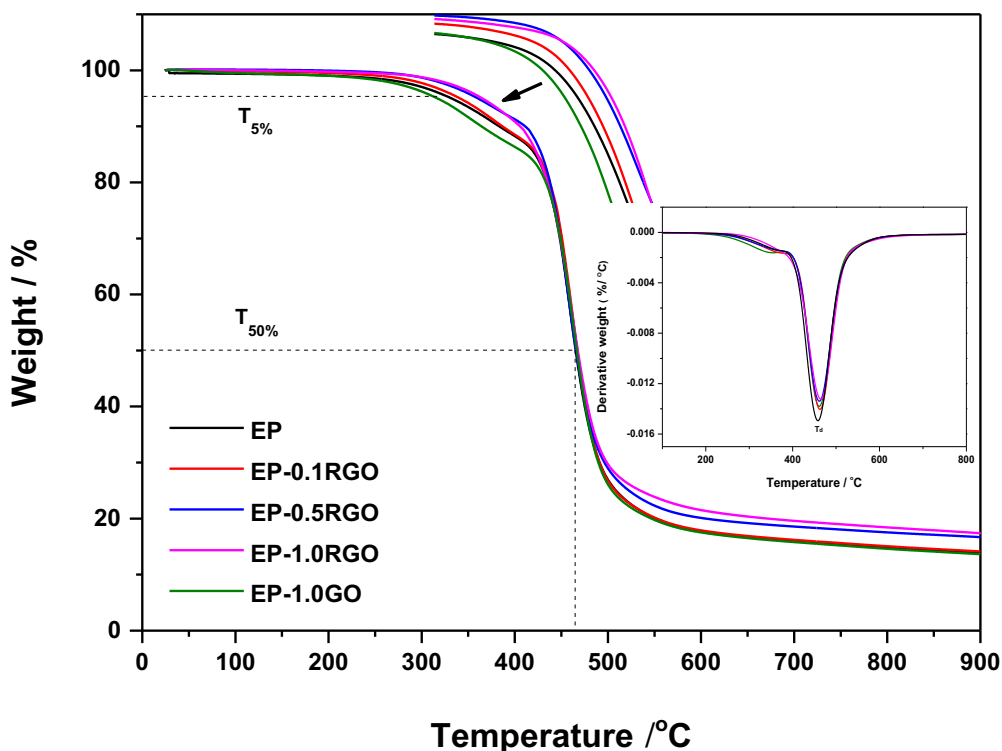


**Figure 4-3.** TGA and DTG curves of neat EP, EP- 0.1 wt. % RGO, EP- 0.5 wt. % RGO, EP- 1.0 wt. % RGO and EP- 1.0 wt. % GO nanocomposites.

However, Wang et al (2014) reported a decrease in  $T_d$  for the EP matrix merged with functionalised graphene, because of the existence of thermally unstable chemical, as compared with monolithic EP. The decomposition of RGO nanocomposites is ultimately slower than that of neat EP because of its restricted polymer chain mobility near the RGO surface (Xie et al. 2016). They also found that the weight loss at 800°C of all EP–RGO–based nanocomposites is dramatically reduced with increased RGO loading, as compared to neat EP. In addition, the good interfacial affinity between RGO nano-sheets and the EP matrix could limit the volatilisation of small molecules at high temperature, thus increasing the thermal stability of the nanocomposites (Xie et al. 2016). Table 4-2 shows the  $T_d$  temperature peaks of all samples and confers an indication of the increased thermal performance with the integration of GO and RGO at different loadings in the EP matrix at  $T_{50\%}$ .

**Table 4-2.** Thermal decomposition  $T_{50\%}$  temperature for EP, EP/GO, and EP/RGOs samples.

<b>Sample</b>	<b>Wt. %</b>	<b><math>T_d / ^\circ\text{C}</math></b>	<b>Derv. Wt. (% / <math>^\circ\text{C}</math>)</b>
<b>EP</b>	0.0	458±0.5	0.0149
<b>EP/RGO</b>	0.1	463±0.2	0.0140
<b>EP/RGO</b>	0.5	465±0.2	0.0134
<b>EP/RGO</b>	1.0	468±0.1	0.0132
<b>EP/GO</b>	1.0	461±0.3	0.0138

#### 4.4.2.2 DSC

The  $T_g$  values of EP composites filled with RGO nano-sheets can be obtained from DSC heating scans, as shown in Fig. 4-4. The average of  $T_g$  value was taken from three specimens test of each type.  $T_g$  is typically calculated by using half-height technique in the transition region. The result showed that, the  $T_g$  value of neat EP was lower than that of EP nanocomposites samples, and the difference between the samples is about 14.3 $^\circ\text{C}$  when compared with the 1.0 wt. % RGO (155. 8 $^\circ\text{C}$ ) sample.

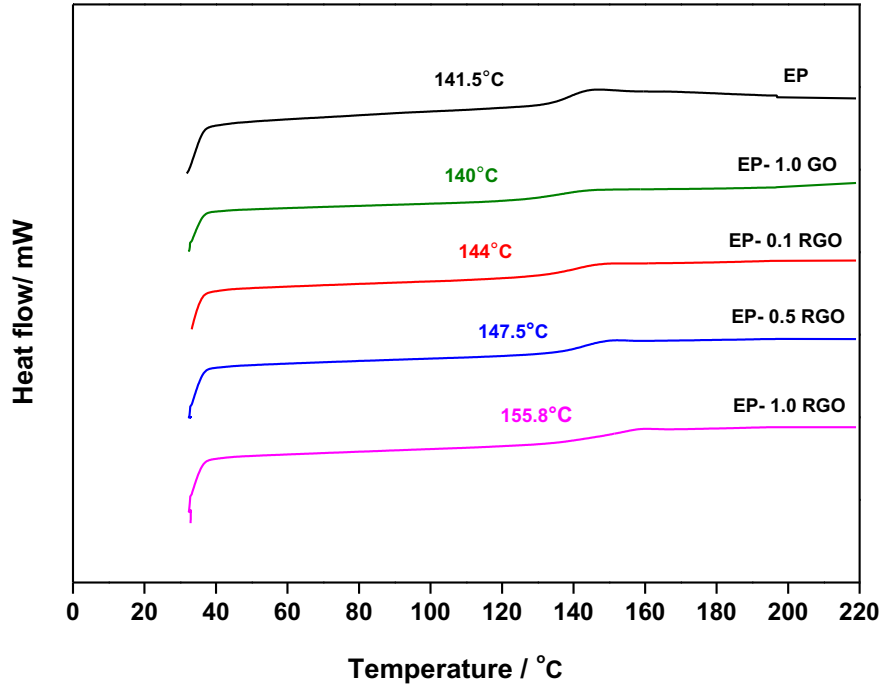


**Figure 4-4.** DSC thermograms of neat EP, EP- 0.1 wt. % RGO, EP- 0.5 wt. % RGO, EP- 1.0 wt. % RGO and EP- 1.0 wt. % GO nanocomposites.

Fig. 4-4 shows the DSC thermograms of neat EP and its nanocomposites with the obtained results for  $T_g$  observed on the curve. The neat EP exhibits a high  $T_g$  of more than  $141.5 \pm 0.5^\circ\text{C}$ , which is regarded as an excellent thermal resistance for EP composites fabricated by the solution blending method. However, EP nanocomposites showed that gradually increased  $T_g$  values can be obtained with the incorporation of the RGO nano-sheets in the matrix and that a higher weight content (0.1, 0.5, 1.0) of RGO in the matrix corresponds to a higher  $T_g$  value of EP-RGO nanocomposites ( $144 \pm 0.4$ ,  $147.5 \pm 0.6$ ,  $155.8 \pm 0.4^\circ\text{C}$ , respectively). This increase in  $T_g$  value is likely because of the well-dispersed RGO that has a wrinkled structure and large surface area in contact with the thermoset EP matrix and that this restricts the polymeric chain mobility (Feng et al. 2012). Moreover, the uniform-dispersion of nano-sheets along the matrix leads to the configuration of an interphase around each nano-sheet in which the mobility of polymer chains could be restricted (Pan et al. 2015). In contrast, the  $T_g$  of the EP-1.0 wt. % GO nanocomposite shows a decrease to about  $140 \pm 0.7^\circ\text{C}$ .

In experiment studies, Feng et al. (2013) have reported a dramatic decline in  $T_g$  (below 150°C) when the RGO concentration exceeds 1.25 wt. % in an EP matrix. The higher loading of RGO (> 1 wt. %) leads to a decrease in the cross-linking in the EP matrix and thereby decreases the packing density of polymeric cross-linking networks, leading to a lower  $T_g$ . In contrast, the heat of cure was undetectable for all samples, indicating that the materials become completely cured. In addition, the shifting in the  $T_g$  means a high degree of cure.

#### **4.4.2.3 DMA**

DMA is an efficient technique used to determine the viscoelastic properties of materials and displays the energy stored in the elastic structure (Menard et al. 2015). Fig. 4-5 (A) and (B) exhibit the variation of  $E'$  and  $\tan \delta$  as a function of the temperature of pure EP. The average of  $T_g$  and modulus value were taken from three specimens test of each type. The result showed that, the values of  $E'$  for pure EP and its nanocomposites decrease gradually as the temperature increases. The interpretation for this behaviour is based on the relation of the chain motion of polymer with increased in temperature. The inclusion of GO (1.0 wt. %) into the matrix leads to significant increases in  $E'$  values in the glassy state region, from  $2.1 \pm 0.04$  GPa of pure EP to about  $2.3 \pm 0.02$  GPa for EP/GO. Moreover, nanocomposites showed highly increased  $E'$  values with an addition of 0.1, 0.5 and 1.0 wt. % RGO loading level onto the matrix and reached nearly  $2.24 \pm 0.02$ ,  $2.85 \pm 0.03$  and  $2.3 \pm 0.02$  GPa, respectively, as shown in Table 4-3.



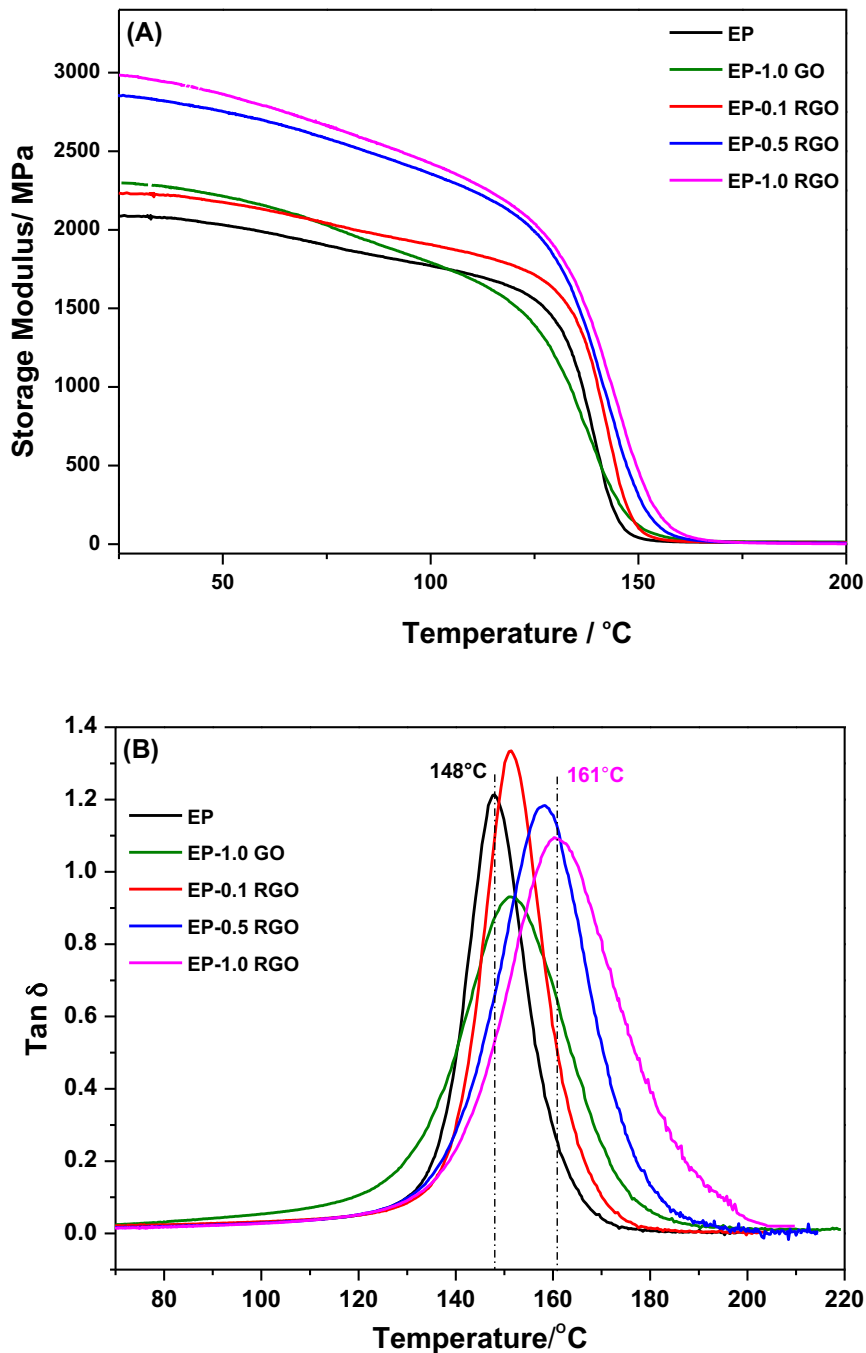


**Figure 4-5.** Dynamic mechanical properties of the EP nanocomposites, (A) storage modulus and (B)  $\tan \delta$ .

The RGO (at 0.1 wt. %) sample which has the lowest loading content reported a slightly similar result with the (1 wt. %) EP-GO sample, indicating that RGO sheets are higher in stiffness than GO materials. The higher storage modulus in the glassy state may be because of the influence of cure (cross-link density). In addition, the  $T_g$  of pure EP is  $148 \pm 0.5^\circ\text{C}$ , while this value

increased to about  $152 \pm 0.4^\circ\text{C}$  for EP-GO at 1.0 wt. %. When compared with EP/GO, the  $T_g$  values of RGO showed large increases by adding 0.5 and 1.0 wt. % which measured  $158 \pm 0.3$  and  $161 \pm 0.2^\circ\text{C}$ , respectively. These large increases are because of the high surface area and good dispersion of nano-sheets onto the polymeric matrix, which could lead to strong interfacial interactions between the matrix and nano-fillers. As a result, the strong interfacial interactions hinder the polymer chains' mobility and shift the chains towards high- $T_g$  values. Moreover, the  $\tan \delta$  peaks are wide and broad for nanocomposites with increasing  $T_g$  values, reflecting confinement in segmental relaxation transition.

Generally, there are also other factors that could affect the  $T_g$  values such as intermolecular forces, crosslinking and molecular weight. It is significant that there is a slight difference in  $T_g$  values obtained by the DMA and DSC technique; the  $T_g$  value obtained via the DMA technique is approximately 10 to  $15^\circ\text{C}$ , higher than that obtained via the DSC technique. The reason behind this difference is that, the DMA tool is a mechanical deformation measurement, while DSC is a thermal measurement.

The number average molecular weights,  $M_{nc}$ , between cross-links are listed in Table 4-3 and calculated from the rubbery region by the using following equation:

$$M_{nc} = \frac{q\rho RT}{E_r}$$

where  $R$  is the universal gas constant, which is equals  $8.314 \text{ cm}^3 \text{ MPa K}^{-1} \text{ mol}^{-1}$ ;  $q$  is the front factor value for density of the epoxy, which was determined at  $20^\circ\text{C}$  to be 0.725 (Pearson & Yee 1989);  $\rho$  is the density of the EP measured at room temperature, which is equal to  $1.3 \text{ g cm}^{-3}$  using a Mettler Toledo density balance with a resolution of 0.1 mg; and  $E_r$  is the storage modulus in the rubbery region and determined at a temperature of 443 K ( $170^\circ\text{C}$ ).

**Table 4-3.** Dynamic mechanical properties of neat EP and its EP-nanocomposites used in different loading of RGO.

Specimen	Storage moduli, $E_g$ , at 25°C (MPa)	Storage moduli, $E_r$ , at 180°C (MPa)	Average molecular weight between cross-links, $M_{nc}$ (g mol <sup>-1</sup> )	$T_g$ (°C)
Neat EP	2099±43	12.3	282	148±0.5
0.1 RGO/EP	2243±20	12.8	271	151±0.3
0.5 RGO/EP	2858±26	13.5	257	158±0.3
1.0 RGO/EP	2985±19	16.5	210	161±0.2
1.0 GO/EP	2296±23	15.0	231	152±0.4

It is noteworthy that the  $M_{nc}$  decreased from 282 g mol<sup>-1</sup> in the neat EP to 210 g mol<sup>-1</sup> in the EP-composite specimen filled with 1.0 wt. % RGO nano-sheets. In contrast, (Olowojoba et al. 2016; Chen J et al. 2013) reported that the value of  $M_{nc}$  for EP-nanocomposites filled with different RGO loading were greater than that of pure EP, meaning that the cross-linked network was destroyed. The chemical interaction between the residual functional groups on the RGO surface and EP may result in increased in the  $M_{nc}$  between the cross-links of the cured EP matrix as the RGO loading increased.

### 4.4.3 Mechanical properties

#### 4.4.3.1 Tensile test

The mechanical testers have slack in their joints and movement in the grips. Consequently, any movement of the frame and grips was measured, as well as the movement in the samples. As a result, tested a sample which we knew will not deform in the tested load range and then measured the movement in the frame and not movement in the sample. Thus, by doing this, we determined the compliance of the machine (how much it deforms for every newton of load which is applied to the sample). We then plotted a graph of mm/N (mm on the y-axis and N on

the x-axis) and took the gradient of the line. This was our machine compliance, and we use it to correct our data.

The true sample extension was calculated by multiplying the machine compliance (a single constant value) for each load reading and then subtracting the compliance extension from the measured extension. The modulus was measured as the slope (tangent line) of the initial linear portion of the stress-strain curve,  $E = \frac{\Delta\sigma}{\Delta\varepsilon}$ . The first point utilized in calculating the Young's modulus was determined at approximately 5 MPa of stress, and the other point was taken at the end stress value on the gradient of the linear region. The values were visually identified from the stress vs. strain curve and dragged directly from the Excel data for calculation.

The stress-strain curves of neat EP and its nanocomposites with 0.1, 0.5, 1.0 wt. % RGO and 1.0 wt. % GO are shown in Fig 4-6. The EP nanocomposite curves exhibited the tendency for a linear increase up to the breaking point and displayed brittle deformation. The tensile properties were averaged values from the results obtained from five dog-bone shaped specimens (gauge length of 25 mm) and calculated in accordance with ISO 527-1/2 at a speed of 1 mm min<sup>-1</sup>. The UTS increased from 44.7 ± 3.4 MPa to 51.6 ± 2.5 MPa of 0.1 wt. % RGO and 58.6 ± 2.8 MPa of 0.5 wt. % RGO nanocomposites (as shown in Fig. 4-7 (A)), corresponding to 15.4 % and 31%, respectively, increases in tensile strength compared with that of the neat EP, as calculated in Table 4.4. This test was performed under room temperature and the averaged value of each type were taken from 5-7 specimens.

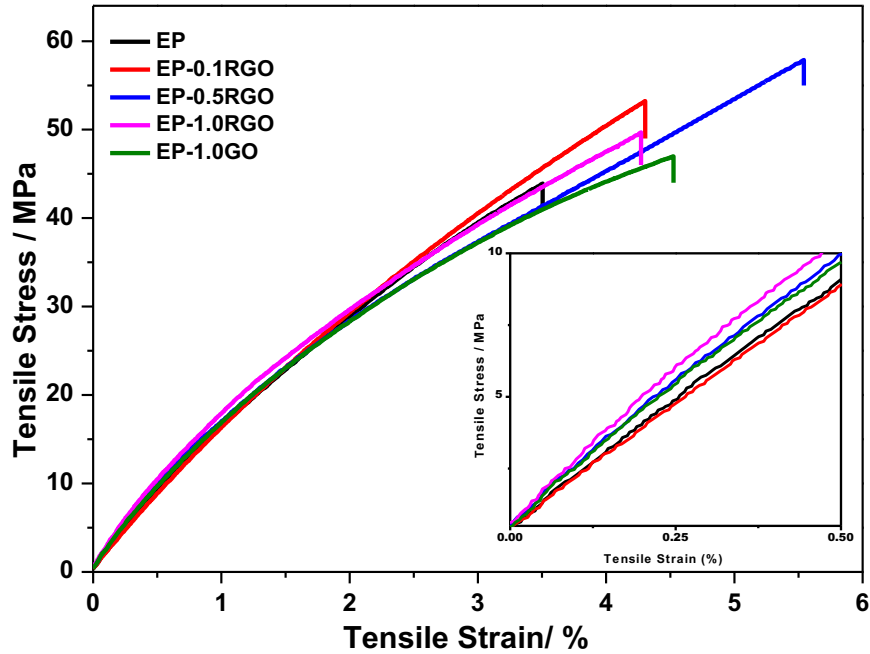


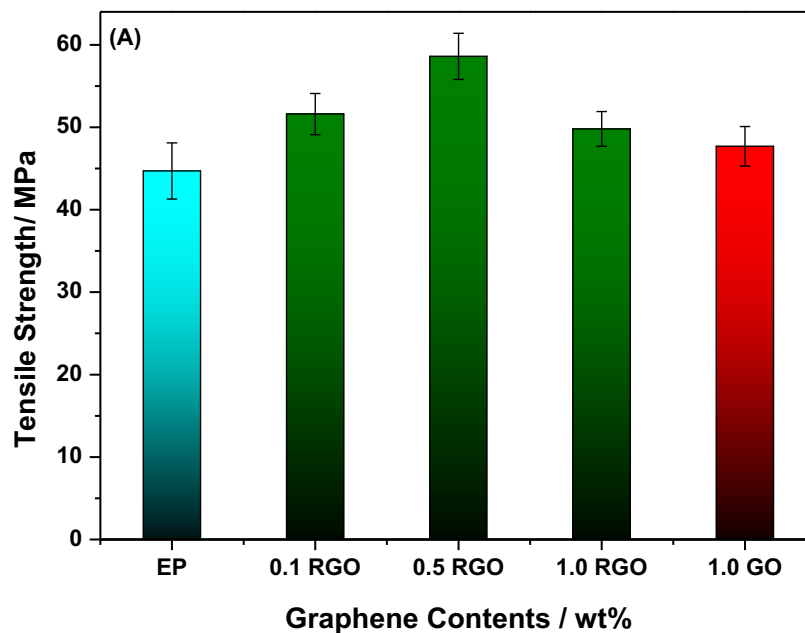
**Figure 4-6.** Typical tensile strength versus tensile strain curves for neat EP and its composites filled with different RGO concentrations.

The reason for these increased results might be attributed to the cross-linking interaction that occurs between the epoxy groups and hydroxyl groups on the surface of RGO and matrix. However, the tensile strength decayed marginally when the content loading of GO or RGO nano-sheets exceeded 0.5 wt. %. This evidence strongly supports the notion that the excessive nano-sheets loading in the matrix caused uneven dispersion, thereby inducing defects in the EP matrix and resulting in phase separation. Another reason was that the tensile loading caused a localised stress field surrounding the filler nano-sheets until the energy is dispersed by specimen deformation occurs (Pan et al. 2015).

**Table 4-4.** Average Tensile Properties Neat EP and its Nanocomposites.

Material	Young's Modulus/ GPa	UTS/ MPa	Elongation at Break/ %	Energy at break /MJ m <sup>-3</sup>
Neat EP	2.71± 0.23	44.7 ± 3.4	3.5 ± 0.55	87 ± 0.9
0.1 RGO	2.82± 0.18	51.6 ± 2.5	4.3 ± 0.44	128 ± 0.7
0.5 RGO	3.23± 0.16	58.6 ± 2.8	5.5 ± 0.22	186 ± 0.5
1.0 RGO	3.56± 0.19	49.8 ± 2.4	4.5 ± 0.36	125 ± 0.7
1.0 GO	2.99± 0.17	47.7 ± 2.4	4.5 ± 0.23	130 ± 0.8

The results also showed an increase in tensile strain and energy at the break, as shown in Table 4-4. The increase in elongation upon the break indicates a slight increase in ductile behaviour of EP-nanocomposites because of the increment of the high elastic modulus of RGO nano-sheets when compared with the control specimen (neat EP).



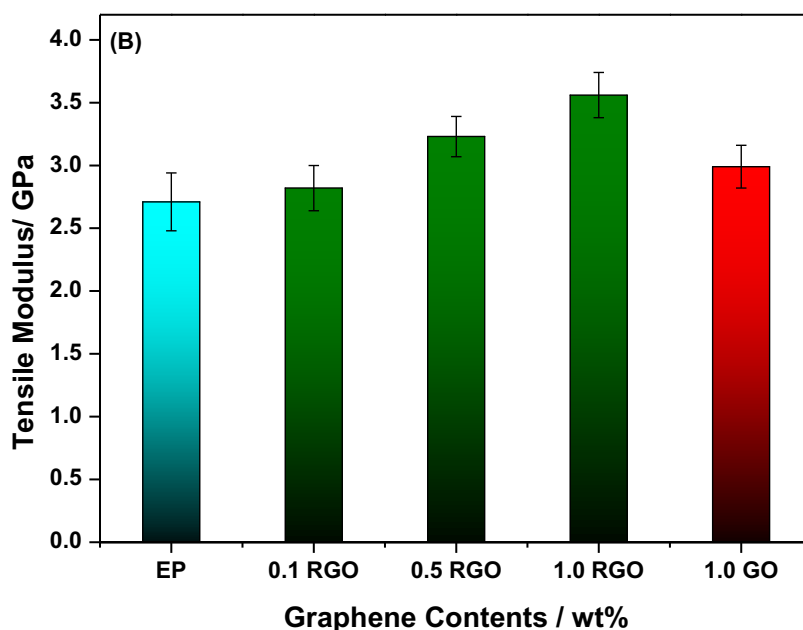


**Figure 4-7.** Plots of Tensile strength (A) and Young's modulus (B) of neat EP and its nanocomposites with different RGO loading and 1.0 wt. % GO nanocomposites.

Fig. 4-7 (B) and Table 4-4 displays the Young's moduli of the EP-composites with different wt. % RGO concentrations. The tensile modulus of neat EP was  $2.71 \pm 0.23$  GPa and up to  $3.56 \pm 0.18$  GPa for the nanocomposites at 1.0 wt. % RGO loading, corresponding to an increase of 19.7%. Tschoppe et al. (2014) observed a modest 8.5 % increase in tensile modulus after adding 1.0 wt. % of thermally RGO.

The increase in tensile modulus observed in the EP-nanocomposite specimens' maybe attributed to the relatively high elastic modulus of the RGO filler. In addition, the RGO nano-sheets bond efficiently (strongly) with the polymer chains because of the interfacial adhesion force between RGO sheets and EP matrix. This adhesive force restricts the mobility of EP chains on the RGO surface and causes mechanical interlocking of wavy RGO sheets with the EP matrix. The results show that the additive of RGO sheets improved the mechanical properties of EP-nanocomposites specimens.

### 4.4.3.2 Nanoindentation test

The elastic modulus was measured from a 16-cycle indentation test at 10 mN with a resolution of 50 nN. The nanoindenter of TriboScope TS70 produced reliable results in the displacement range because of its design. The test specimen was  $10 \times 10$  mm and about 1 mm thick. Experimental TS-70 proprietary software (Hysteron) was applied to analyse the massive values of curve data that rapid and reproducible. However, this software program was designed to calculate the elastic modulus based on the Oliver-Pharr method. The partial unloading-load function curve data was utilized for the nonlinear numerical power law fit. The elastic modulus of nanocomposites was obtained from the unload curve by applying the following equation (Tranchida et al. 2006; Tranchida et al. 2007).

$$E = \frac{(1 - \nu_s^2)}{\frac{2 \sqrt{C_0 \cdot h_c^2 + C_1 \cdot h_c}}{a \cdot m (h_{max} - h_f)^{m-1} \cdot \sqrt{\pi}} - \frac{(1 - \nu_i^2)}{E_i}}$$

where  $E_i$  is the elastic modulus of the indenter, and  $\nu_s$  and  $\nu_i$  are the Poisson's ratio of the sample material and indenter. The  $a$  and  $m$  are constants, and  $h_c$  is the contact depth during indentation full load which is not equal to the full displacement  $h_{max}$  of the indenter into the specimen, and  $h_f$  is the final residual indent depth.  $C_0$  and  $C_1$  terms were adjusted to account for the probe rounding. A diamond Berkovich indenter has a Poisson's ratio of 0.07 and an elastic modulus of 1141 GPa. To provide accurate results of modulus at all displacement, the nanoindentation system applies a load to the indenter tip while simultaneously superimposing an oscillating force much smaller than that of the nominal load.

A typical curve for modulus  $E$  as a function of penetration depth is shown in Fig. 4-8 for 1.0 wt. % RGO in the EP matrix. The  $E$  value found is the mean of modulus measurements by nanoindentation over the range of Berkovich indenter penetration from 500 to 1500 nm.



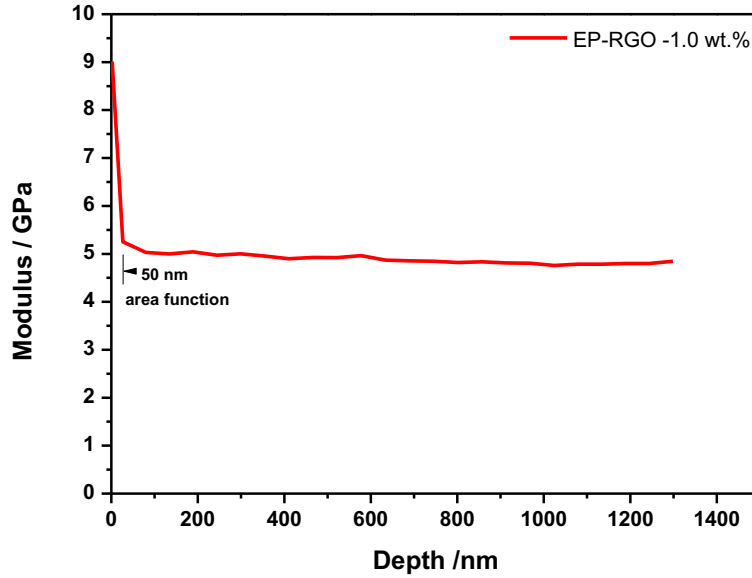


**Figure 4-8.** Modulus determined by nanoindentation for 1.0 wt. % RGO in EP.

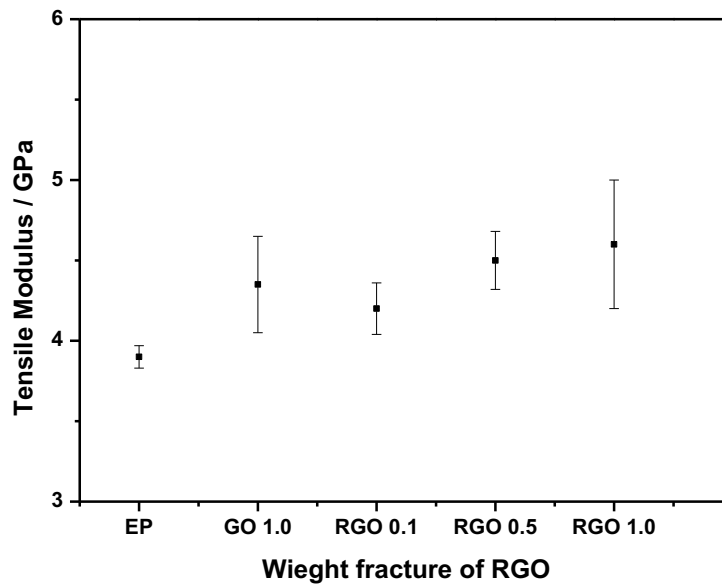


**Figure 4-9.** Tensile Modulus determined by nanoindentation for RGO/EP nanocomposites.

Fig. 4-9 shows the average modulus as determined by the nanoindentation test. The Y-error bars shown represent  $\pm 1$  standard deviation (SD) of the data. When the indenter (Berkovich probe) encounters a polymer–matrix–rich area or an RGO–rich area on the specimen, an error can be introduced into the data via this test approach. Therefore, as the RGO concentration increases, the error bars become larger because a larger concentration of RGO exists in the specimen. Indeed, with addition of RGO sheets, there is an increase in the stiffness, and,

subsequently, a decrease in displacement for a force of 10 mN. In comparison to neat epoxy, the modulus increases for 0.1, 0.5 and 1.0 wt.% EP/RGO nanocomposites by 17%, 28% and 31%, respectively.

Many recent studies have revealed for polymers and polymer nanocomposites that the moduli as determined by the nanoindentation technique, are greater than those reported by universal tensile machines tests. These ratios of the moduli measured to those reported by universal tensile machine tests are 1.64 for polycarbonate (PC), 1.70 for polystyrene (PS) (Tranchida et al. 2007) and 1.33 for epoxy (EP) (King et al. 2012), while this ratio reached  $\sim 1.4$  in the current study. This ratio is possibly attributed to the indentation pile-up plastic phenomenon of material around the contact area and the viscoelasticity of the polymer-based-nanocomposites that is not clarified by the modulus determined by the Oliver-Pharr method (Tranchida et al. 2006; Tranchida et al. 2007). However, the unexpected high value found for the elastic moduli can be interpreted noticing that a pile-up has occurred in the nanoindentation testing. Therefore, this value is greater than that measured through tensile tests. Testing below a depth equivalent to one-third of the indenter radius tip of the indenter is not reliable because the area function used to determine the modulus does not apply to these indentation depths.

The average tensile modulus from the nanoindentation test for the pure EP was 3.9 GPa when compared with 2.72 GPa (see Table 4-4) from the tensile machine test. Therefore, a ratio of 1.4 was found for our pure EP composites.

#### **4.4.4 Conductivities properties**

##### **4.4.4.1 Thermal conductivity**

The thermal conductivity ( $\kappa$ ) of EP composites is typically synthesised by introducing nano-fillers, such as pristine graphene, RGO and CNTs, with superior thermal transport in the host polymer. These materials have potential engineering applications where heat dissipation is an

issue in electronic devices. The thermal conductivity of RGO is experimentally reported at 3-61 W m<sup>-1</sup> k<sup>-1</sup> (Renteria et al. 2015).

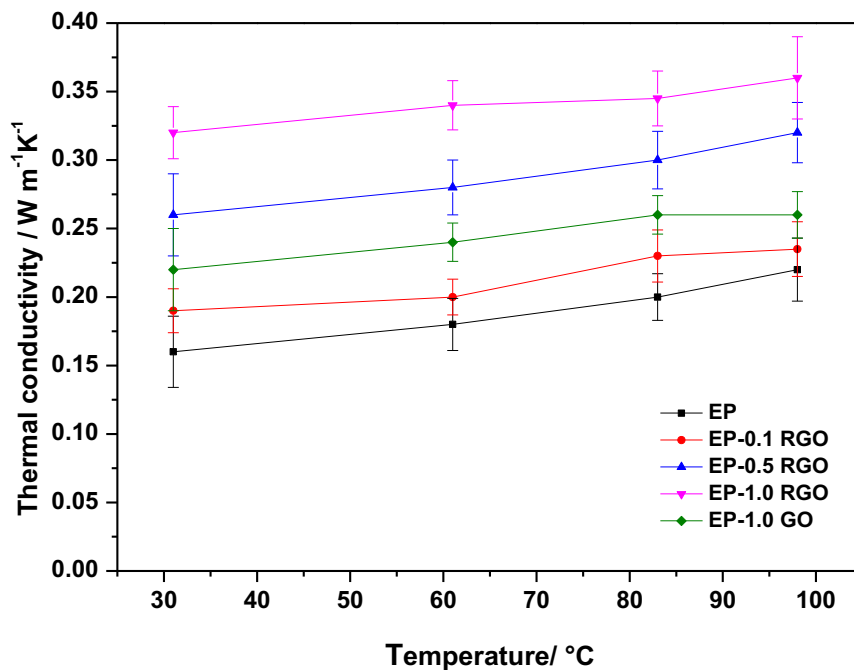


**Figure 4-10.** Plots of thermal conductivities vs temperatures (25–100°C) of neat EP and its nanocomposites.

As expected, in the glassy state region, the experimental results show that the  $\kappa$  behaviour of all specimens tend to increase dramatically with increasing RGO loading. This increase in thermal conductivity can be attributed to the large lateral size of RGO nano-sheet (an average lateral size of  $1.348 \pm 0.6 \mu\text{m}$  – AFM and TEM) that helps maximise the interface between nano-sheet and EP matrix, which assists the heat flow. As shown in Fig. 4-10, the  $\kappa$  behaviour of the nanocomposite shows an increase of up to 85% at low-loading content with the change in temperature, and the maximum value reached was  $0.36 \pm 0.025 \text{ W m}^{-1} \text{ K}^{-1}$  at EP-1.0 RGO and high temperature ( $\sim 100^\circ\text{C}$ ). At room temperature, the corresponding thermal conductivities of neat EP and EP-1.0 RGO nanocomposites are  $0.16 \pm 0.03 \text{ W m}^{-1} \text{ K}^{-1}$  and  $0.33 \pm 0.02 \text{ W m}^{-1} \text{ K}^{-1}$ , respectively. After taken the average value of three specimens test, these nanocomposites have shown relatively high thermal conductivities compared with the reported value of  $0.24 \text{ W m}^{-1}$

$^1\text{K}^{-1}$  of EP-1.0 RGO nanocomposite (Olowojoba et al. 2016), which is higher than the value measured of  $0.21 \text{ W m}^{-1} \text{ K}^{-1}$  for the EP-1.0 RGO nanocomposite by Chandrasekaran et al. (2013).

In contrast, EP-0.5 RGO exhibited a high in the  $\kappa$  value compared to EP-1.0 GO, as the former is shown to have fewer oxygen groups on its structures. The large reduction in thermal conductivity of EP-1.0 GO is ascribed to the considerably enhanced electron-phonon scattering induced by the OCFGs defects, so this coverage of oxygen introduces considerable structural deformations (Mu et al.2014).

#### **4.4.4.2 Electrical conductivity**

The electrical conductivity data were used to verify the formation of conductive pathways in the EP matrix. Prior to the current study, there had been no more reports on the increase of the DC electrical conductivity of the RGO-based EP composite. The electrical conductivity of RGO/EP composites as a function of the RGO weight fraction (0.1, 0.5 and 1.0 wt. %) at room temperature is shown in Fig. 4-11. The electrical conductivity of RGO nano-sheets is experimentally reported as  $243 \pm 12 \text{ S cm}^{-1}$  by (Kumar et al. 2015).

The volumetric electrical resistivity measurements were performed via the standard four-point probe technique in the case of the electrical resistivity  $< 10^{10} \Omega \text{ cm}$  to avoid a contact resistance error during measurement. The results show that the electrical conductivity ( $\sigma$ ) of the RGO-based EP composites greatly increased.

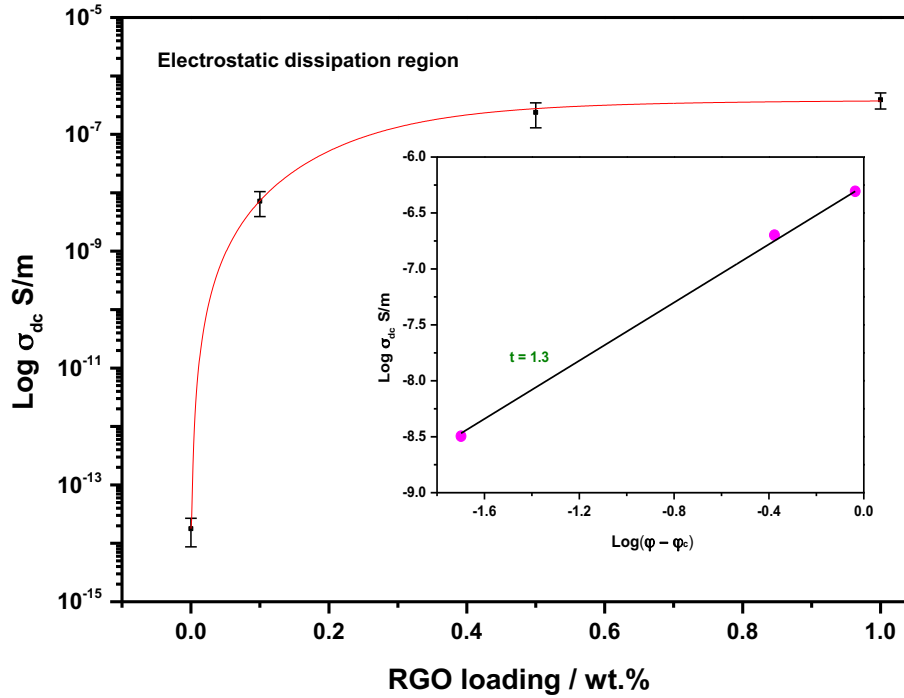


**Figure 4-11.** Electrical conductivity ( $\sigma_{dc}$ ) versus filler weight fraction ( $\phi$ ) for RGO/EP composites. Inset shows a log–log plot of  $\sigma_c$  versus  $(\phi - \phi_c)$ .

At a low-level content ( $< 0.08$  wt. %), RGO nano-sheets cannot establish a conductive network to create a continuous conductive path across the insulating matrix and therefore prevents the charge-carriers to move, and the resulting EP nanocomposites still show low conductivity ( $< 10^{-8} \text{ S m}^{-1}$ ). The insulator-semiconductor transition is more clearly shown in Fig. 4-11. The increase in conductivity as a function of RGO filling can be modelled by the scaling law between composite conductivity ( $\sigma_c$ ) and loading fraction ( $\phi$ ) above the percolation threshold ( $\phi_c$ ) (Zois et al. 1999; Wajid et al. 2012). The expression is represented as the following:

$$\sigma_c = \sigma_f (\phi - \phi_c)^t$$

where  $\sigma_f$  and  $t$  are the conductivities of RGO and the universal critical exponents, respectively. The exponent  $t$  is frequently related to the dimensionality of the filler loading, with usual values between 1 and 1.3 for the 2D distribution of fillers and between 1.6 and 2.0 for the 3D

distribution of fillers. The exponent is measured as about 1.3 in the current study.

With increased filling, a sharp increase in electrical conductivity was close in proximity to 0.08 wt. %, which is a critical weight content of RGO nano-sheets (percolation threshold,  $P_c$ ), and is characteristic for when the critical threshold transition occurs. At 0.1 wt. % loading, the nanocomposite results in an increase of five orders of magnitude ( $7.21 \times 10^{-9} \text{ S m}^{-1}$ ) in the bulk conductivity of the RGO/EP composite compared to the neat EP sample. When the network became continuous throughout the matrix, the conductivity increased to more than  $2.38 \times 10^{-7} \text{ S m}^{-1}$  at 0.5 wt. % of RGO. This significantly improved conductivity is mainly ascribed to the good interconnection of RGO filler with EP because of good dispersion via a speed mixing process. Thus, the interconnected RGO provides a more efficient network for free electron transfer across the matrix than an RGO below the percolation threshold.

Above 0.5 wt. %, the conductivity slightly improved with increased RGO concentration. At loading levels near 1.0 wt. %, the conductivity approaches  $5.92 \times 10^{-7} \text{ S m}^{-1}$ . These dc conductivity results were compared with the previous studies (Hsiao et al. 2013; Wajid et al. 2012), as shown in Table 4-5. This data can be ascribed to the effective restoring of the electrical properties of RGO via the rapid thermal reduction process besides the high quality of dispersion in the matrix.

At a given loading of 0.1 wt. % (the percolation threshold of this current study), the electrical conductivity of the nanocomposite is higher than those reported in previous reports (Liang et al. 2009 and Wajid et al. 2012). The electrical conductivity data also clearly show that the mixing process slightly reduced aggregation and clustering in the matrix that occurs at high-RGO concentrations. The loading level of the filler for creating the percolation threshold varies from a polymeric matrix to other matrices. For example, (Liang et al. 2009) records the lowest percolation threshold of 0.1 vol% for the solution-processable functionalised graphene loaded

EP composites compared to the percolation of 0.53 vol% for the pristine graphene/EP nanocomposite (Khanam et al. 2015).

For the graphene-based polyethylene nanocomposite, the percolation threshold was reached at loadings of 0.07 vol% (Pang et al. 2010). Park et al. (2014) determined the percolation threshold at loading  $\sim 0.25$  vol. % of RGO/polystyrene (PS) composites. Kim et al. (2010) reported a lower percolation threshold ( $P_c$ ) of  $< 0.5$  vol% for TRGO-based TPU composite whereas this  $P_c$  increased to  $> 2.7$  vol% in the case of filling with graphite. Also, adding GO to the EP resin leads to a slight increase in electrical conductivity because very little scale  $\pi$ -bonds may exist (Zong et al. 2016).

There are many factors that affect the effective electrical conductivity in thermoset EP such as free-electron mobility, large scale  $\pi$ -bonds (Feng et al. 2013) and ultra-high dispersion of RGO sheets in the EP-matrix and, thereby, confirm an increase in interfacial bonding between EP matrix and RGO. The poor dispersing of RGO in a polymer matrix only leads to a fragile conducting network, and the generated voids can easily interrupt the interconnection of the sheets, thus reducing the conductivity. Therefore, the conductivity slightly increased at high loading (1.0 wt. %). One of the extremely promising aspects of developing these types of composites is their potential for use in electronics applications such as electrostatic-sensitive devices (ESD) and EMF shielding devices because of their high electrical conductivity. Table 4-5 shows a comparison of results obtained in the current study to previous studies.

The volumetric electrical resistivity test of the rectangular samples was conducted with a two-probe method according to ASTM D4496 at 23°C. This method is appropriate for the sample that possesses an electrical resistivity  $> 10^{10}$   $\Omega$  cm. The electrical conductivity of GO-based EP composite at loading (1.0 wt. %) is recorded as  $1.6 \times 10^{-10}$  S  $m^{-1}$ . This is low conductivity because of disrupted (break)  $sp^2$  bonding networks of GO sheets. However, neat EP is an

insulating polymer with a low conductivity of  $\sim 10^{-14}$  S m<sup>-1</sup>.

**Table 4-5.** Different procedures for dispersing TRGO in EP resins and the thermal, electrical and mechanical properties of RGO/EP composites.

Reference	Filler	wt. %	Mechanical Properties		Electrical Conductivity/ S m <sup>-1</sup>	Thermal Conductivity /Wm <sup>-1</sup> k <sup>-1</sup>
			Tensile Modulus/ GPa	Tensile Strength/ MPa		
This Study	RGO/THF	0.1	2.82 (4%)	51.6 (16%)	$\sim 7.2 \times 10^{-9}$ (increased by 5 orders of magnitude)	0.19 (15.8%)
		0.5	3.23 (19%)	59 (31%)	$\sim 2.4 \times 10^{-7}$ (increased by 7 orders of magnitude)	0.27 (41%)
		1.0	3.56 (20%)	50 (12%)	$\sim 6 \times 10^{-7}$ (increased by 7 orders of magnitude)	0.33 (51.5%)
Zakaria <i>et al.</i> (2017)	GNP/free-solvent	1.0	1.65 (10%)	51.6 (11%)	-	0.27 (30%)
Olowojoba <i>et al.</i> (2016)	RGO/free-solvent	1.0	3.10 (6.4%)	41.0 (decreased by 37%)	-	0.24 (25%)
Liang <i>et al.</i> (2009)	RGO/acetone	1.0	-	-	$1 \times 10^{-9}$ (increased by 3 orders)	-
Tang <i>et al.</i> (2013)	RGO/ethanol	0.1	3.05 (6%)	55 (7.5%)	-	-
T.K <i>et al.</i> (2014)	RGO/acetone	0.5	2.65 (7.7%)	56 (7.2%)	-	-
Chandrasekaran <i>et al.</i> (2013)	GNP/ethyl acetate	1.0	3.0 (storage modulus)	-	$1 \times 10^{-6}$ (increased by 2 orders)	0.22 (6%)
Hsiao <i>et al.</i> (2013)	RGO/Acetone	1.0	-	-	$1 \times 10^{-8.5}$ (increased by 6 orders)	0.25 (20%)

\* The percentage of increase was calculated according to the neat EP composite.



## 4.5 Section Two- Vacuum oven

### 4.5.1 Production of EP nanocomposites reinforced by RGO (at low-temperature)

To investigate the efficiency of the vacuum-assisted thermal reduction method in enhancing the mechanical and thermal properties of the synthesised RGO/EP composites; GO, RGO-120, RGO-160 and RGO-180 nano-sheets were dispersed in EP resin using the solution mixing approach (see Table 4.6). Typically, the nano-sheets were initially dispersed in 100 ml of distilled water with the sonication-assist for 2 h and magnetic stirring for 24 h to achieve a homogeneous suspension, and the desired amount of EP resin was subsequently included in the suspension using magnetic stirring for 6 h at 600 rpm under a temperature of 45°C. Then, the mixtures were mixed by using a bath sonication for 30 min and high-speed shear mixer at 1600 rpm for 90 min to disperse the nano-sheets directly into EP. After most of the solvent was eliminated through gradual pouring and suction (Fig.S5 in Appendix), the mixtures were exposed to vacuum drying at 80°C for 4 h. Next, curing agents (MNA) and a catalyst (N, N-Dimethyl-benzylamine) were added to the above mixture with the help of magnetic stirring for 20 min. After degassing via a vacuum oven at 80°C for 30 min, the mixtures were poured onto silicone moulds and cured in an oven, from 80 to 120°C for 1 h, then to 150°C for 30 min, and next to 180°C for 3 h, followed by post curing at 200°C for 30 min.

**Table 4-6.** Different procedures for dispersing TRGO in EP resins and the thermal, electrical and mechanical properties of RGO/EP composites.

Sample	wt. %	Fillers / mg	EP / g	Curing agent / g	H <sub>2</sub> O/ ml
EP	0.0	0	20	18	100
EP/GO	0.5	190	20	18	100
EP/RGO-120	0.5	190	20	18	100
EP/RGO-160	0.5	190	20	18	100
EP/RGO-180	0.5	190	20	18	100

## 4.5.2 Characterisation

The characterisation techniques that were employed in this study have been detailed in the previous section.

## 4.6 Results and discussion

### 4.6.1 Spectroscopic measurements

#### 4.6.1.1 FT-IR

Fig. 4.12. shows the IR peaks of EP, EP/GO and EP/RGOs composite samples. A series of weak peaks located in the 521 and 664  $\text{cm}^{-1}$  regions correspond to out-plane-bending vibrations of the aromatic C–H band. Peak at 1014  $\text{cm}^{-1}$  corresponds to symmetrical aromatic C–O stretch. 1150  $\text{cm}^{-1}$  is related to asymmetrical aliphatic C–O stretch and epoxy C–O at 1260  $\text{cm}^{-1}$ . The sharp peaks at 793 and 1091  $\text{cm}^{-1}$  are related to the stretching C–O–C of oxirane groups and stretching C–O–C of ethers, respectively. In addition, the peaks at 1620 and 1608  $\text{cm}^{-1}$  is ascribed to the stretching vibration of the aromatic ring C=C and the peak at 1508  $\text{cm}^{-1}$  is related to C–C aromatic stretching vibration. Moreover, 2851 and 2967  $\text{cm}^{-1}$  are associated with symmetric and asymmetric vibrations of  $\text{CH}_2$ . All previous FT-IR spectrum peaks refers to the main spectrum bands for benzene ring in EP and emphasise the association of RGO aromatic planes with EP.

Also, after the curing process of EP and its nanocomposites, the intensity of the characteristic bands of the oxirane ring at 970 and 914  $\text{cm}^{-1}$  showed a large decrease when compared with uncured EP system.

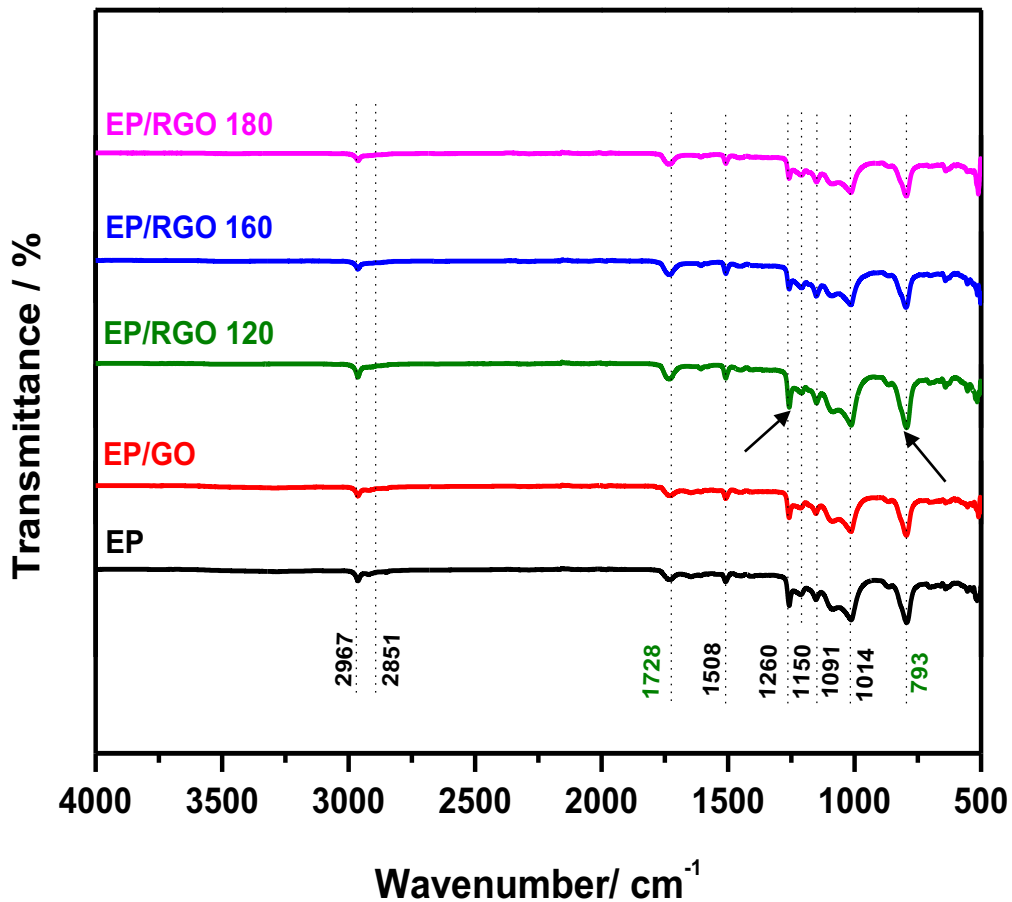


*Figure 4-12. FTIR spectra of pure EP and RGOs reinforced EP nanocomposites.*

A slight shift of C=C at 1620 to 1608  $\text{cm}^{-1}$  and C=O peaks from 1728 to 1733  $\text{cm}^{-1}$  in all nanocomposites samples. These shifting can be ascribed to the strong interaction between the epoxy matrix and RGO sheets. Moreover, by comparing the five curves of the cured EP and its nanocomposites, the IR spectra appears a low intensity in the case of RGO-160 and RGO-180 samples because of the inclusion of RGO in matrix, which did not exceed 0.5 wt. %. In addition, low content of OCFGs (high degree of reduction) compared to that of RGO-120, which showed high intensity peak at 793 and 1260  $\text{cm}^{-1}$ . Therefore, the FT-IR spectra showed that with increasing of the degree of reduction of OCFGs, the intensity peaks are decreased in EP nanocomposites.

### 4.6.1.2 SEM microscopy

Fig. 4-13 shows the SEM images of cryo-fracture surfaces of nanocomposites containing 0.5 wt. % reduction at different temperatures. The mechanical and physical properties of nanocomposites depend on the dispersion of filler agent into the matrix. Here, the dispersion of RGO in EP was analysed using SEM. The SEM samples were obtained by breaking the composites at the required place inside the liquid nitrogen to obtain a clean fracture surface.

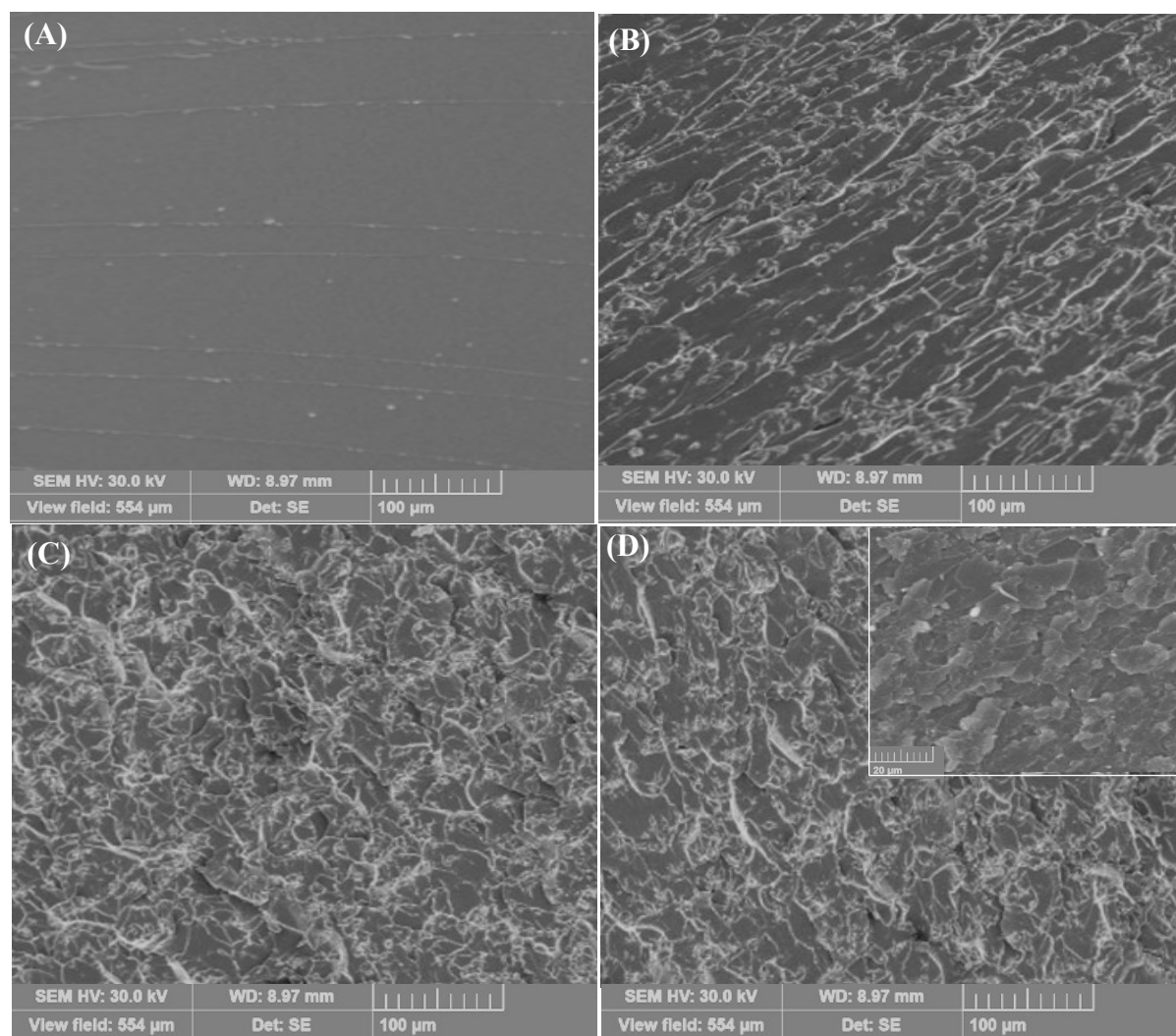


**Figure 4-13.** SEM images of cryo-fracture surfaces of (A) neat EP and its nanocomposites at 0.5 wt. % content of RGO at different reduction temperatures of (B) 120°C, (C) 160°C and (D) 180°C.

Fig. 4-13, the neat EP is a homogeneous polymer as expected, see Fig. 4-13(a). Note that the white lines in Fig. 4-13(a) are river lines caused by the brittle fracture of the polymer (Hull 1999), and for the purposes of considering the dispersion of the RGO, such features associated with fracture can be disregarded in Fig. 4-13. The images shown in Fig. 4-13 (b, c, d) indicate a good dispersion of RGO in the EP for the nanocomposites containing 0.5 wt.% of RGO, and significant agglomeration could not be detected even at high magnifications. Obviously, the fractured surfaces of the RGO/EP composites were rougher compared with that of neat EP sample. With the increase of temperatures for reduction process, the surface became rougher and bumpier, showing the improved toughness of the material, which might result in improving tensile properties and bending properties (Liu et al. 2012).

The RGO layers in EP can be identified via color contrast caused by the polarized light (Salom et al. 2018). However, it is an accurate and reliable technique to evaluate the RGO dispersion and distribution in polymer matrix. Fig. 4-13 shows SEM images of EP composite and its EP/RGO nanocomposites (RGO-120, RGO-160 and RGO-180) at different magnification powers. The white spots and streaks are the RGO sheets in matrix. In all cases, the RGO can be seen to be dispersed all over the surface. However, the RGO sheets is reasonably well dispersed in RGO-160 and RGO-180 samples better than RGO-120 sample. The wrinkled surface morphology of the RGO sheets is shown in Fig. 4-13(d). According to Shen et al. (2013), it is this morphology which plays an important role in enhancing mechanical interlocking and transferring load from the EP matrix to RGO sheets.

## 4.6.2 Thermal and thermomechanical properties

### 4.6.2.1 TGA

Fig. 4-14 shows the TGA/DTG curves of EP, EP/GO and EP/RGO nanocomposites under the flow of nitrogen at a heating rate of  $10^{\circ}\text{C min}^{-1}$ . Every samples repeated two times to produce reproducibility of analysis.  $T_{50\%}$  is typically determined by using DTG curves at the maximum peak.

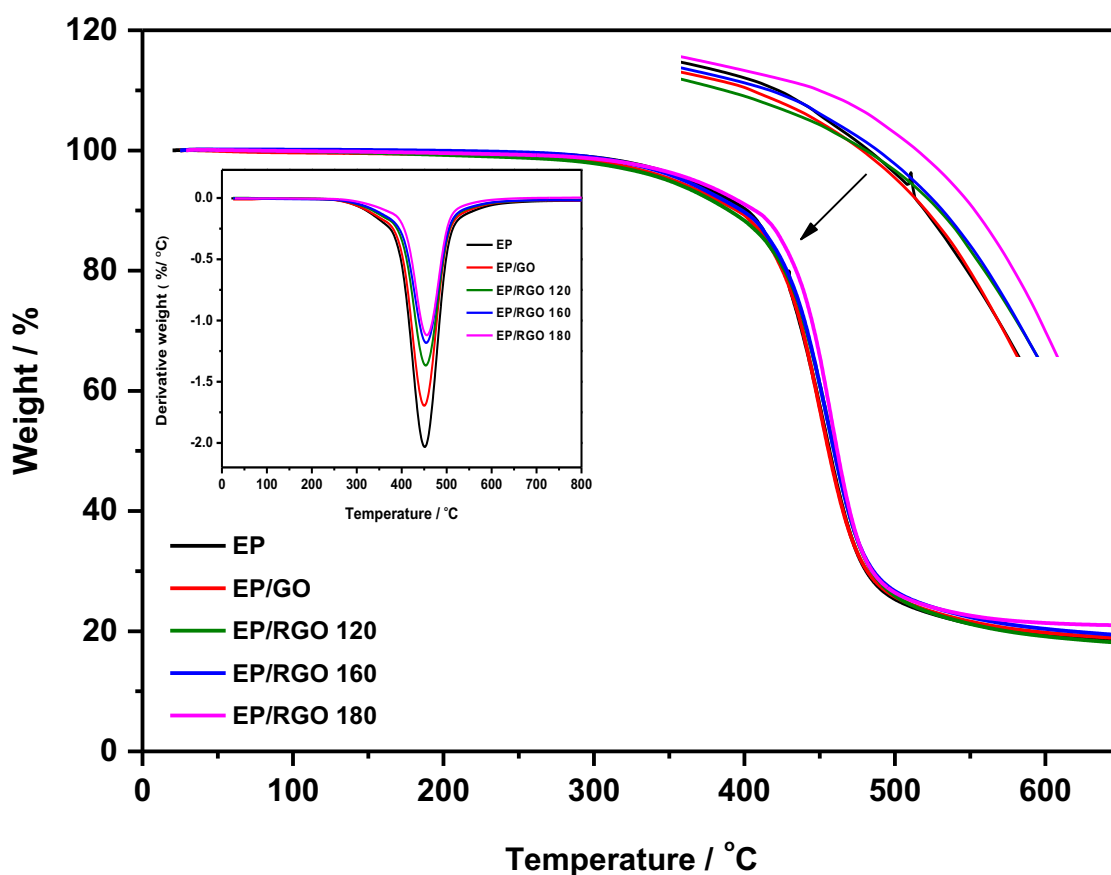


*Figure 4-14. TGA curves for pure EP and its nanocomposites*

In fig. 4-14, the decomposition temperature  $T_{5\%}$  (5% weight loss) of RGO/EP composites showed an increased trend with the higher of temperatures of reduction process and fixed the RGO loading at 0.5 wt.%. The RGO-160 and RGO-180 samples showed significant increase of  $21^{\circ}\text{C}$  and  $\sim 23^{\circ}\text{C}$ , respectively. In addition, the  $T_{50\%}$  (50% weight loss) of RGO/EP

nanocomposites also showed an increased trend with the increase of temperature of reduction, and RGO-120, RGO-160 and RGO-180 samples resulted in significant increase of 7°C, 12°C and 14°C, respectively, while the incensement of  $T_{50\%}$  for the GO loading did not appreciably affect the  $T_d$  value of EP composites.

The enhanced thermal stability of RGO/EP composites was mainly attributed to a better barrier effect of RGO which retarded the volatilization of polymer decomposition products due to a better dispersibility and interface between RGO and epoxy matrix (Visakh & Nazarenko 2015). The  $T_{5\%}$  of RGO/EP nanocomposites (0.5 wt.% RGO-180) was increased by ~23 °C compared to blank EP sample.

Table 4-7 shows the  $T_d$  temperature peaks of all samples and confers an indication of the development of the thermal performance versus the integration of GO and RGOs within the EP matrix.

**Table 4-7.** Summary of decomposition temperature ( $T_d$ ) for EP and its nanocomposites.

<b>Sample</b>	<b><math>T_d</math> / °C</b>	<b>Derv. Wt. (% /°C)</b>
<b>EP</b>	458±0.5	2.0
<b>EP/GO</b>	459±0.4	1.7
<b>EP/RGO-120</b>	465±0.3	1.4
<b>EP/RGO-160</b>	470±0.2	1.2
<b>EP/RGO-180</b>	472±0.3	1.1

#### 4.6.2.2 DSC

The  $T_g$  values of neat EP and its nanocomposites are shown in Fig. 4-15. The average of  $T_g$  was taken from three specimens test of each type. The  $T_g$  is typically calculated by using half-height technique in the transition region. The result showed that, that the  $T_g$  of neat EP is about  $131.5\pm 0.4^\circ\text{C}$ , whereas the  $T_g$  value of the EP-GO sample showed a slight increase when GO was added to the matrix at 0.5 wt. %. There were increases of approximately 6.5, 8 and  $12^\circ\text{C}$  in the  $T_g$  with the incorporation of 0.5 wt. % of RGO-120, RGO-160 and RGO-180, respectively. Results that are quite similar can be seen for  $T_g$  values, for all samples, using the DMA technique, as shown in Table 4-8. These results were confirmed by (Ahmed et al. 2018) where they ascribed the increased in  $T_g$  values to the considerable impact of the RGOs on the molecular chain mobility of polymer. Therefore, the existence of GO or RGO nano-sheets (as stiffer materials than EP matrix) could play a significant role in providing confinement on the polymer chains which could lead to increased  $T_g$  values. This result emphasises the concept of strong interfacial bonding that occurs between the EP or other polymer matrix from one side and the RGO nano-sheets from the other side (Xu et al. 2013; Ahmed et al. 2018; Sheng et al. 2015).



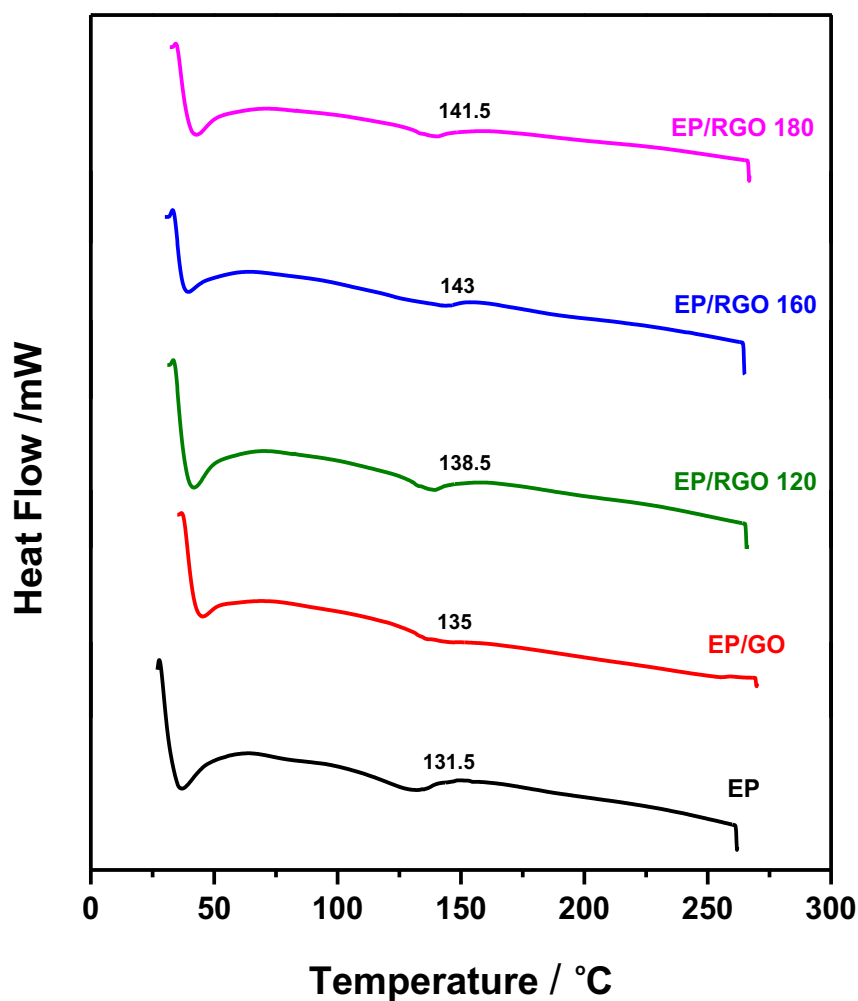


*Figure 4-15. The  $T_g$  values obtained by DSC for EP and its nanocomposites*

In contrast, the limited increase in  $T_g$  for the GO sample maybe attributed to the impeding of the EP curing reaction. This impediment could be associated with reactive moieties in EP–resin and the curing agent, which could be covered by GO, and because of the high surface area of the sample. Therefore, the optimised ratio between the EP–resin and hardener in the curing reaction was affected ( Galpaya et al. 2014).

It is significant to clarify that the large increase in  $T_g$ 's of EP/RGO nanocomposites (for RGO obtained at 120, 160, 180°C) by about 5%, 8.7% and 7.6% respectively, was because of the successful reduction by using the vacuum-assisted technique at low-temperature levels.

It is significant to clarify that the large increase in  $T_g$ 's of EP/RGO nanocomposites (RGO reduction at 120, 160, 180°C) by about 5%, 13% and 12% of RGO-120, RGO-160 and RGO - 180, respectively, was because of the successful reduction by using the vacuum-assisted technique at low-temperature levels.

#### 4.6.2.3 DMA

A dynamic mechanical analyser (RSA-G2, TA Instruments, New Castle, DE, USA) was used to evaluate the dynamic properties using rectangular specimens of size of  $40 \times 10 \times 2.0 \text{ mm}^3$  (L×W×T) in dimensions. For this purpose, dual cantilever clamp mode was used and a heating rate of  $3 \text{ }^\circ\text{C min}^{-1}$  from 20 to 200°C was applied. A constant frequency of 1 Hz was used, and data were collected every 10 s, with at least three specimens of each type tested. This high-performance instrument featuring a new forced convection oven for precise and accurate temperature control, with a force resolution of 0.00001 N, modulus precision of  $\pm 1\%$  and displacement resolution of 1 nm.

The storage modulus,  $E'$ , and the loss factor,  $\tan \delta$ , for the EP and its composites incorporated with nano-sheets of GO and RGOs at 0.5 wt. % are shown in Fig. 4.16 and summarized in Table 4-8. The addition of 0.5 wt. % GO has a slight effect on both  $E'$  and  $T_g$  in the nanocomposite, which increased the  $T_g$  by 3°C and the  $E'$  by 5.3% in the glassy state region compared to the values of the neat EP matrix. In contrast, the inclusion of only 0.5 wt. % of RGO into the EP matrix showed significant increases of  $E'$  in the glassy state region compared to that measured of the GO sample.

The  $E'$  of pure EP at 30°C is  $2.68 \pm 0.07 \text{ GPa}$  and that of nanocomposites containing RGOs (RGO-120, RGO-160 and RGO-180) were  $2.94 \pm 0.04$ ,  $3.26 \pm 0.05$  and  $3.74 \pm 0.04 \text{ GPa}$ , respectively. The moduli of EP/RGO nanocomposites slightly decreased at temperatures below and above the  $T_g$ . Hence, the  $E'$  at 30°C (as illustrated in Table 4.8) increased by 10%, 18%

and 29% compared to that of pure EP with the inclusion of RGO-120, RGO-160 and RGO-180, respectively. These values are ascribed to their improved dispersion and thereby allow for a strong interfacial bonding interaction with the EP matrix (as observed previously in the SEM micrographs in Fig. 4-13) to be obtained.

Monteserín et al. (2017) confirms that the  $E'$  values in the composites containing RGO nanosheets are largely affected by the interfacial bonding strength that arises between the matrix and nano-filler reinforcements. Also, as the temperature increases, the  $E'$  for the nanocomposite samples tend falls gradually, indicating energy dissipation which occurs when the samples start to undergo a state transition from glassy to rubbery.

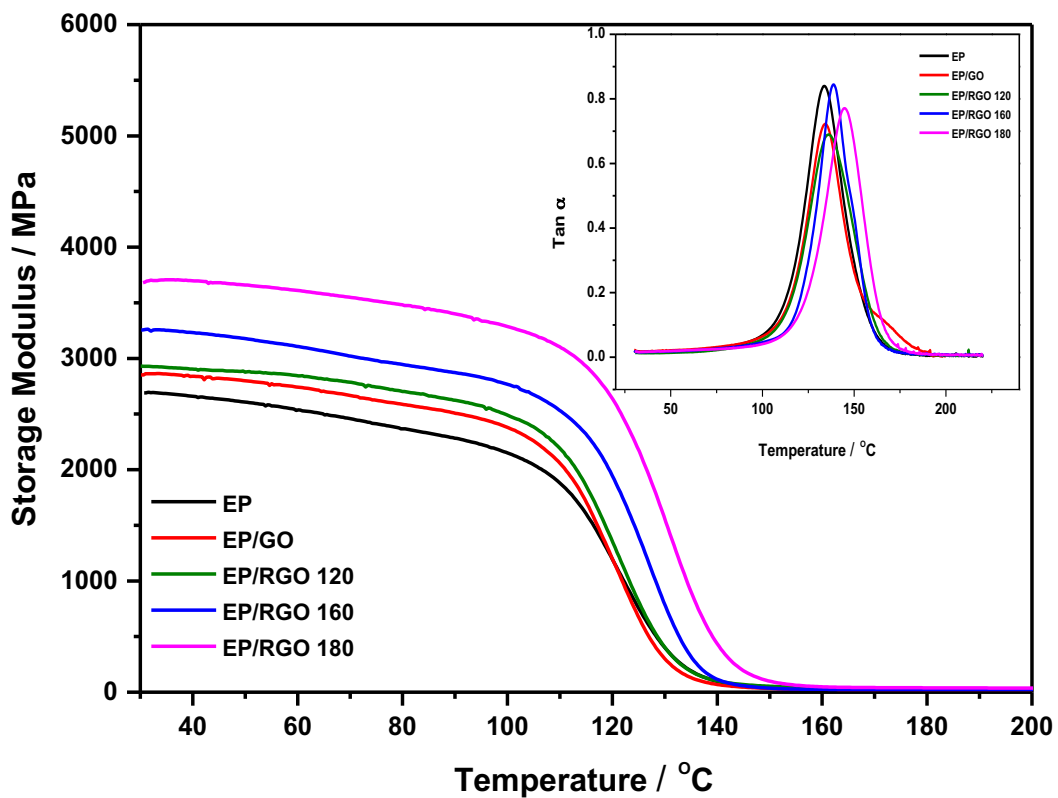


**Figure 4-16.** The storage modulus  $E'$  and loss factor  $\tan \delta$  of EP and its nanocomposites at 0.5 wt. % of GO and RGOs obtained at different temperatures.

Compared to the pure EP, the  $T_g$  is either changed slightly upwards (as noted in the case of

GO, 3°C) or increased by a maximum of 12°C (with RGO-180). Similar results, which include a large increase in  $E'$  and small increases in  $T_g$ , have also been reported by (T.K et al. 2014; Monteserín et al. 2017; Olowojoba et al. 2017).

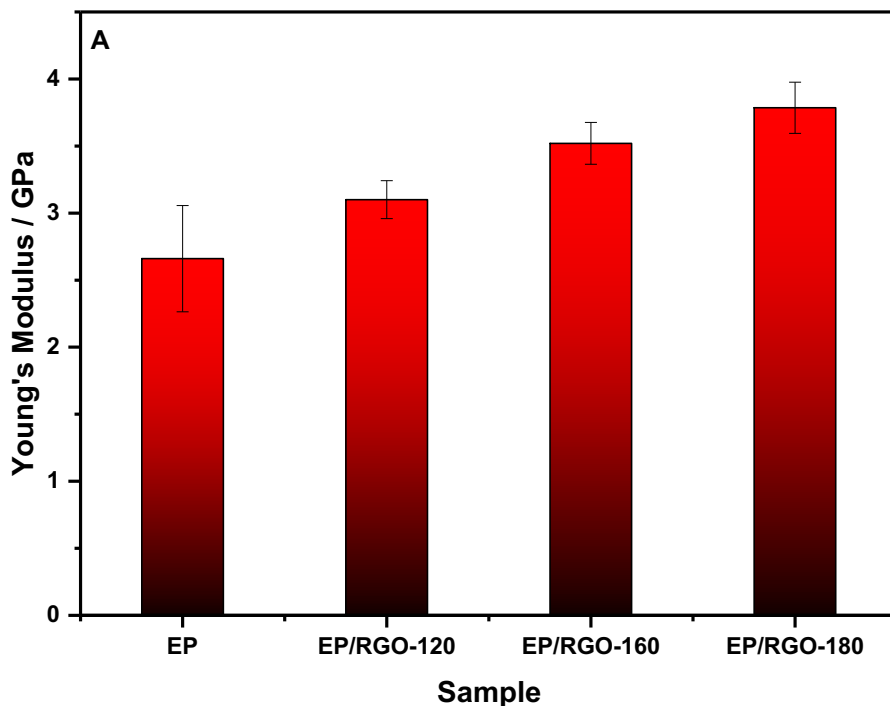
**Table 4-8.** DMA results for EP and its nanocomposites of GO and RGOs at a 0.5wt. % level.

Sample	$E'$ (at 30°C, GPa)	$T_g$ / °C
EP	2.68±0.07	133± 0.5
EP/GO	2.83±0.05	134±0.4
EP/RGO-120	2.94±0.04	136±0.3
EP/RGO-160	3.26±0.05	139±0.2
EP/RGO-180	3.74±0.04	145±0.3

The high  $T_g$  values upon the addition of nano-fillers are often ascribed to a higher degree of crosslinking and hindrance in molecular motion, indicating considerable changes in polymer chain dynamics (Ganguli et al. 2008). In addition, the surface geometry of nano-sheets could affect polymer mobility (Naebe et al. 2014). Hence, the nanoscale wrinkled nature and roughness of nano-sheets surface (i.e. GO and RGO) could restrict molecular motion and induce interfacial interactions with polymer chains through their mechanical interlocking. Moreover, the existence of carboxylic functional groups (–COOH) on the surface of GO and RGO could enhance the uniform dispersion within the resin matrix. As a result, it induces an interphase zone surrounding nano-sheets (Smith et al. 2002; Naebe et al. 2014). Therefore, higher  $T_g$  values in the EP nanocomposites reflect the ability of RGO sheets to the dynamic chain restriction in EP matrix, especially in RGO-180. The significant increase in the  $E'$  values could be ascribed to two main causes: the complete reduction of GO samples to attain the RGO forms and their good dispersion within the matrix, which can enhance the interfacial interactions for the nano-sheets with the polymer chains.

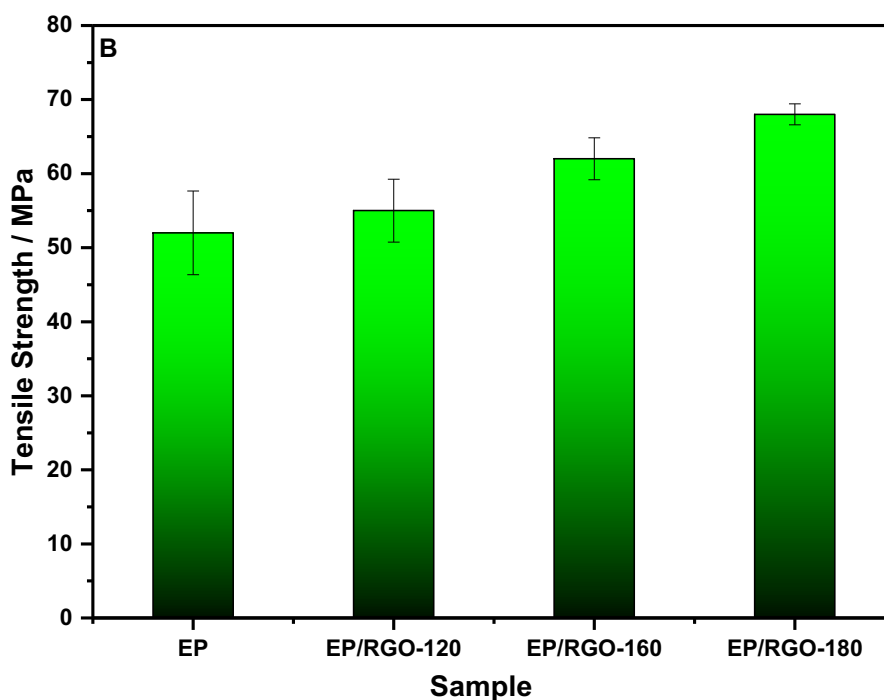
### 4.6.3 Mechanical properties

Fig. 4.17 (A) shows the static mechanical properties of the pure EP and its nanocomposites reinforced with GO and RGO nano-sheets. This test was performed under room temperature and the average value of each type were taken from 5-7 specimens. The results show there is a large increase in the tensile modulus values for nanocomposites, as observed in Table 4.9 and Fig. 4.17 (A), compared with pure EP. However, the increase in the tensile modulus values for the matrix reinforced with RGO indicates that the stiffness of material significantly improved the nanocomposites. For example, the modulus increased from about  $3.11 \pm 0.14$  GPa for RGO-120 sample to  $3.52 \pm 0.15$  GPa for RGO-160 sample content of 0.5 wt. %. The noteworthy increase in Young's modulus values achieved over the current study could be reflected by the nanocomposite synthesis approach selected, which plays an important role in obtaining better dispersion for RGO material with strong interfacial interactions between the individual RGO nano-sheets and EP matrix. The Young's modulus of the RGO-180 sample showed a maximal value of  $3.78 \pm 0.19$  GPa. This increase can be associated with the high degree of reduction for RGO material that is obtained via the vacuum reduction process, thereby enabling the material to partially restore their properties (i.e., stiffness).



**Figure 4-17 (A).** Plots of the Tensile modulus values for the pure EP and its nanocomposites at 0.5 wt. % of fillers.

The tensile strength values for pure EP and other nanocomposites are shown in Fig. 4-17 (B). There is a slight increase in ultimate strength values versus the increasing degree of reduction of GO (RGO-120 and RGO-160), which measured  $55.3 \pm 4.2$ ,  $62.2 \pm 2.8$  GPa, respectively. However, the RGO-180 sample noted a large increase in tensile strength value compared with pure EP. The tensile strength increased from about  $51.2 \pm 5.4$  MPa for the pure EP to  $68.8 \pm 1.4$  MPa for the composite inclusion with a RGO-180 content of 0.5 wt. %. Similarly, an increase in the elongation at break was found from  $2.71 \pm 0.3\%$  MPa for the EP to  $4.62 \pm 0.3\%$  MPa for RGO-180.



**Figure 4-17 (B):** Plots of the tensile strength for the pure EP and its nanocomposites at 0.5 wt.% of fillers.

Therefore, the result for the UTS of RGO nanocomposites relative to EP can be ascribed to RGO sheets into the matrix that was reduced by using the vacuum oven. Therefore, the increase tensile strength and elongation at break (see Table 4-9) of the RGO result could be because of the uniform dispersion of RGO sample onto the matrix and of efficient load-transfer between the polymer matrix and RGO nano-sheets within the matrix. As a result, this advance in the mechanical behaviour may be assigned through strong interactions introduced by the matrix onto the main structure for the RGO sample and thereby provides a good load transfer across the interphase. Generally, the level of dispersion, quality of interfacial bonding and the load transfer from the host polymer-chains into the nano-sheets are considered as major factors that affect the results of the mechanical properties that are attained in this work and are affirmed in academic research (Zaman et al. 2011; T.K et al. 2014). Table 4-9 lists the obtained values for modulus, UTS, elongation at a break and toughness for all samples.

*Table 4-9. Illustrates the static mechanical properties of nanocomposites.*

<b>Sample</b>	<b>No. of specimens Test</b>	<b>Young's modulus / GPa</b>	<b>UTS / MPa</b>	<b>Elongation at Break / %</b>	<b>Toughness MJ m<sup>-3</sup></b>
<b>EP</b>	7	2.66 ± 0.39	51.2 ± 5.4	2.71 ± 0.3	83.3 ± 12.3
<b>EP/RGO-120</b>	5	3.11 ± 0.14	55.3 ± 4.2	3.47 ± 0.5	102.5 ± 15.1
<b>EP/RGO-160</b>	7	3.52 ± 0.15	62.2 ± 2.8	4.06 ± 0.4	110.1 ± 9.9
<b>EP/RGO-180</b>	6	3.78 ± 0.19	68.8 ± 1.4	4.62 ± 0.3	124.5 ± 11.4



## 4.7 Conclusion

This research demonstrated a relatively simple and very efficient method for preparing EP–RGO nanocomposites with improving the dispersed at low loadings of RGO sheets as the reinforcing agent. EP composites reinforced with RGO nanosheets were prepared by the solution blending technique. RGO nano-sheets, which were derived from thermal reduction of GO nano-sheets, were characterized by FT-IR, XRD and Raman.

A morphological study showed that, because of the formation of chemical bonds, the RGO was dispersed well in the EP matrix. In the case of RGO generated by a tube furnace at high temperature of reduction, the tensile strength of the RGO-reinforced EP nanocomposite has significantly increase of  $(31 \pm 4.3) \%$  with an addition of 0.5% RGO concentration, when compared with neat EP. When the weight fraction of the nano-filler exceeded 0.5wt. % RGO concentration, the UTS of the nanocomposite decreased moderately, although the material tensile strength was still higher than for EP/GO nanocomposite. In the case of RGO obtained by the vacuum-oven method (at 180°C), the tensile strength and Young's modulus of EP nanocomposites were improved from  $58.6 \pm 2.8$  MPa to  $68.8 \pm 1.4$  MPa and  $3.23 \pm 0.16$  GPa to  $3.78 \pm 0.19$  GPa respectively and corresponding to  $(17.4 \pm 2.3) \%$  and  $(17 \pm 0.1) \%$ , respectively, compared with the EP nanocomposite filled with RGO obtained via the tube furnace technique. This increase of the mechanical properties can be attributed to the small size of RGO flakes produced at low-temperature reduction which have a significant effect on the mechanical properties (toughening and strengthening) of the EP nanocomposites.

Although most OCFGs can be removed after the successful reduction of GO, the holes and other defects are usually observed within the edges and main structure, especially at high-temperature zones. A lattice relaxation of RGO occurs because of out-gassing produced as a result of the residual carboxyl and partial hydroxyl groups, at temperatures less than 180°C.

Because of in-plane C=C cracking, many defects are generated while the residual hydroxyl and partial epoxide groups are removed, at temperatures less than 1400°C. As a result, the EP nanocomposites reinforced by RGO (obtained by the tube-furnace technique) showed lower Young's modulus and tensile strength compared with that RGO obtained at low temperature.

However, the moduli of nanocomposites that were measured by the nanoindentation technique are greater than that measured by universal tensile machines tests with a ratio of 1.4 of pure EP composite, and thus unexpected high value found for the elastic moduli can be interpreted noticing that a pile-up has occurred in the nanoindentation testing. Therefore, this value is greater than that measured through tensile tests. However, in the case of RGO obtained at high temperature reduction, the DMA results indicated an increase of up to 26.5% in the storage modulus for the EP composite filling with 0.5 wt. % RGO compared with the unfilled system. Whereas, the addition of 0.5 wt. % RGO obtained by the vacuum-assisted method (at 120, 160 and 180°C) enhanced the storage moduli from  $2.68 \pm 0.07$  GPa (EP) to  $2.94 \pm 0.04$  GPa (RGO-120),  $3.26 \pm 0.05$  GPa (RGO-160) and  $3.74 \pm 0.04$  GPa (RGO-180) respectively, corresponding to  $(9.7 \pm 0.7)$  %,  $(21.6 \pm 1.1)$  % and  $(39.5 \pm 1.5)$  % respectively, compared with the same of the neat EP composite.

This significant increase in the storage modulus is related to the the better dispersion as revealed by SEM imaging. In both methods, the TGA results confirmed the higher thermal stability of the resulting nanocomposite specimens, regardless of the amount of weight of the RGOs.

The thermal conductivity of EP was improved by up to 85%, reaching the maximum value of  $0.36 \pm 0.025$  W m<sup>-1</sup> K<sup>-1</sup> at 1.0 wt. % RGO. The same addition also significantly improved the electrical conductivity of EP ( $\sim 10^{-14}$  S m<sup>-1</sup>) by about seven orders of magnitude to  $5.92 \times 10^{-7}$  S m<sup>-1</sup>. Therefore, the novel improve of EP nanocomposites that fabricated in this study has

high mechanical strength, stability and good thermal and electrical conductivities, and they could find potential application in the fabrication of high-performance components for applications in electronic circuit boards and electrostatic-sensitive devices.

## **5 Chapter 5 Effect of RGO–SiO<sub>2</sub> nano-hybrids on the mechanical and electrical properties of epoxy**

## 5.1 Introduction

The development of high-performance RGO nanocomposites is still need to improve their properties because of a very low number of OCFGs in a polymeric matrix has significant effects on their composite properties. The RGO is inevitable in the polymer composites because of the weak interactions of individual sheets with the most of polymer matrixes or solvents and the  $\pi$ - $\pi$  stacking interactions between the layers.

For the above reasons, RGO material is commonly co-loaded with various inorganic parts, e.g. metal or non-metal oxide nanoparticles, to enhance a specific physical property or to improve the polymer composites with multiple functions to acquire multifunctional polymer nanocomposites, which can be attained through adding small concentrations of RGO.

In this study, an RGO-SiO<sub>2</sub> nano-hybrid was fabricated by a chemical reaction of the hydrolysis of TEOS with the existence of hydrophilic GO produced from Hummer's approach and subsequently incorporated with the matrix with different mixing times by using the high-shear mixer technique. The novelty of this study is to synthesize a highly efficient and simple methodology for the preparation of RGO-SiO<sub>2</sub> with high dispersion in polymer matrix. EP-nanocomposites were synthesised using organic solvent and then their mechanical, thermal and electrical properties at different loading content were investigated. SiO<sub>2</sub> nanoparticles embedded ultrathin RGO to improve the dispersion in the matrix, which acts as a stabiliser against the aggregation of individual sheets of RGO.

## 5.2 Experimental section

### 5.2.1 Materials

The raw materials that were employed for the synthesis of RGO-SiO<sub>2</sub> samples and subsequent preparing of nanocomposites are depicted in Table 5-1.

**Table 5-1.** Lists the typical material characteristics that are desired for use during this work and their manufacturer and direct supplier.

<i>Material</i>	<i>Characteristics</i>	<i>Manufacture /U.K</i>	<i>Supplier /U.K</i>
EPON 828	DGEBA with 185–192 g/eq, Medium viscosity: 100–160 poise at 25°C.	Delta Resins Ltd	Delta Resins Ltd
Epoxy embedding medium, hardener MNA	Oily liquid of $\geq 99\%$ purity	Sigma-Aldrich	Sigma-Aldrich
N,N-Dimethyl-benzylamine	Catalyst, purity $\geq 99\%$		
Tetraethyl orthosilicate (TEOS)	Liquid of $> 99.99\%$ purity		
Ammonia hydroxide solution	28% NH <sub>3</sub> in H <sub>2</sub> O		
Tetrahydrofuran (THF)	Liquid, purity $> 99.9\%$		
Absolute ethanol (EtOH)	Liquid of $> 99.8\%$ purity		

All the materials were employed as received, without additional purifications.

## **5.2.1 Synthesis of GO, RGO–SiO<sub>2</sub> nano-hybrids and their nanocomposites**

### **5.2.1.1 Synthesis of graphite oxide**

Graphite oxide was made using the modified Hummers method employed in Section 3.2.2.

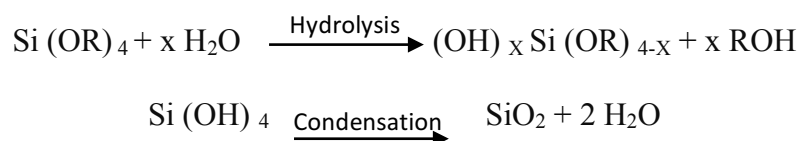
### **5.2.1.2 Synthesis of GO**

It was prepared according to the method of (Ming et al. 2013) using the ultrasonication technique. The resultant graphite oxide suspension obtained from Hummers' method was exfoliated to generate GO nano-sheets by sonication at room temperature for 1 h using an ultrasonic generator (37 kHz, 280 W, Fisher brand Elma, Germany) and separated by the

centrifugation technique for 30 min at 8000 rpm. This solution was then poured into metallic dishes and frozen in a freezer at -40°C for 48 h. Next, the frozen GO was dried in a freeze dryer (300 W, Bradley refrigeration. Edwards, UK) under a pressure around 10<sup>-1</sup> bar at -54°C for 96 h. A fluffy powder GO was then obtained from this process (7.2 g).

### 5.2.1.3 The preparation of RGO–SiO<sub>2</sub> composite

This section describes investigations on how GO with its abundance of OCFGs on the surface might be facilitated to covalently bond with SiO<sub>2</sub> via the sol–gel process before reduction to RGO–SiO<sub>2</sub> using a vacuum-assisted method. To this end, an RGO–SiO<sub>2</sub> nano-hybrid composite was fabricated with a ratio of 1:3 of GO and SiO<sub>2</sub>. The SiO<sub>2</sub> nanoparticles were deposited on the surface of GO through in situ hydrolysis and condensation reactions of TEOS and are written as follows:



An RGO–SiO<sub>2</sub> (GO: TEOS/ 1:3) composite was obtained by hydrolysis and condensation reactions for TEOS with the existence of GO nano-sheets during the formation of SiO<sub>2</sub>. The sol–gel process resulted in the formation of silica nanoparticles attached to the basal planes and edges with the partial thermal reduction of GO to obtain RGO–SiO<sub>2</sub>. This slight chemical reduction for GO can be ascribed to the existence of ammonium hydroxide as a reducing agent, during the sol–gel process.

A typical fabrication process consisted of 100 mg of GO powder prepared by the Hummers' method that was well dispersed into a 250 mL 3-neck round-bottom flask equipped with a condenser with N<sub>2</sub> inlet and containing 27 mL of distilled water and 180 mL of absolute ethanol (99%) as a reaction medium. The suspension was sonicated for 2 h at 37 kHz and room temperature after being stirred for 20 min. Thereafter, aqueous ammonia solution NH<sub>4</sub>OH

(28% - 7.4 mL) as a catalyst was added drop-wise, under magnetic stirring at 375 rpm and 40°C, and left for 24 h to obtain homogeneous dispersion of the mixture.

The pH of the solution was adjusted to a value of approximately 11. Under continuous stirring on a magnetic heat plate, a sol–gel reaction was initiated by adding 1.35 mL of TEOS (MW = 208.33 g mol<sup>-1</sup>) with a constant flow rate of 500  $\mu$ l min<sup>-1</sup> to the above solution with the aid of a control pipe. This reaction was performed at about 95°C for 8 h with constant stirring at 375 rpm. The resulting solution was separated by centrifugation at a speed of 9400 rpm for 30 min, followed by washing three times with an ethanol: water (1:1 volume) mixture (to also remove the free silica nanoparticles). The resultant sample was poured in metallic dishes and kept inside a freezer to be frozen at -40°C for 24 h. Then, the sample was dried in a freeze dryer (300 W, Bradley refrigeration. Edwards, UK) under a pressure around 10<sup>-1</sup> bar at -54°C for 132 h. A vacuum-assisted method was employed for *in situ* reduction of the sample at a temperature as low as 120°C. A fluffy powder RGO–SiO<sub>2</sub> material was obtained from this process. This produced 404 mg (actual value) of nano-hybrid material, which is almost identical to the theoretical value (A theoretical maximum value assumes 100% conversion of TEOS to silica 300 mg). The RGO–SiO<sub>2</sub> produced was used for further measurements.

#### **5.2.1.4 Preparation of RGO–SiO<sub>2</sub> /EP Composites**

All the EP nanocomposites were prepared via a solution mixing approach, and the setup for which is described in Fig. 5-1. The RGO–SiO<sub>2</sub> nano-hybrids were dispersed in different polar solvents (de-ionised water and THF) with ultrasonic treatment and a high-shear mixer (at 1200 rpm) for 2 h for each one. Subsequently, nano-hybrids were magnetically stirred for 72 h to obtain good homogeneity between the filler and solvent.



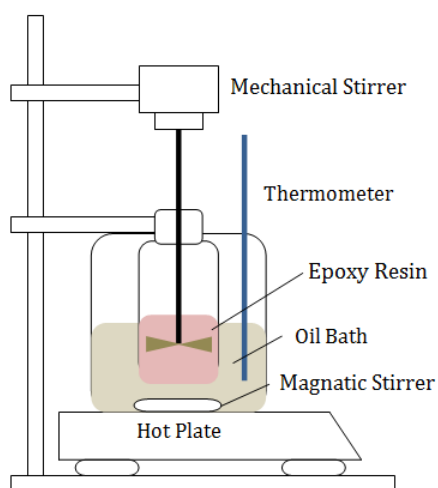


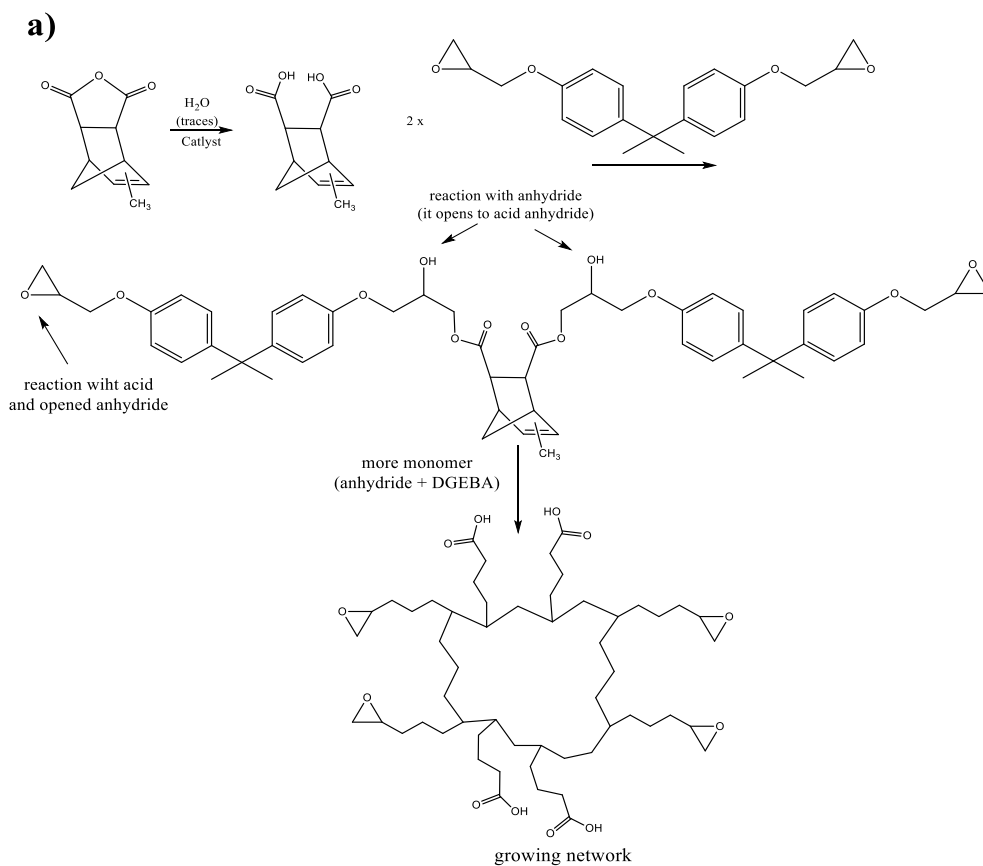
**Figure 5-1.** EP system mixing setup

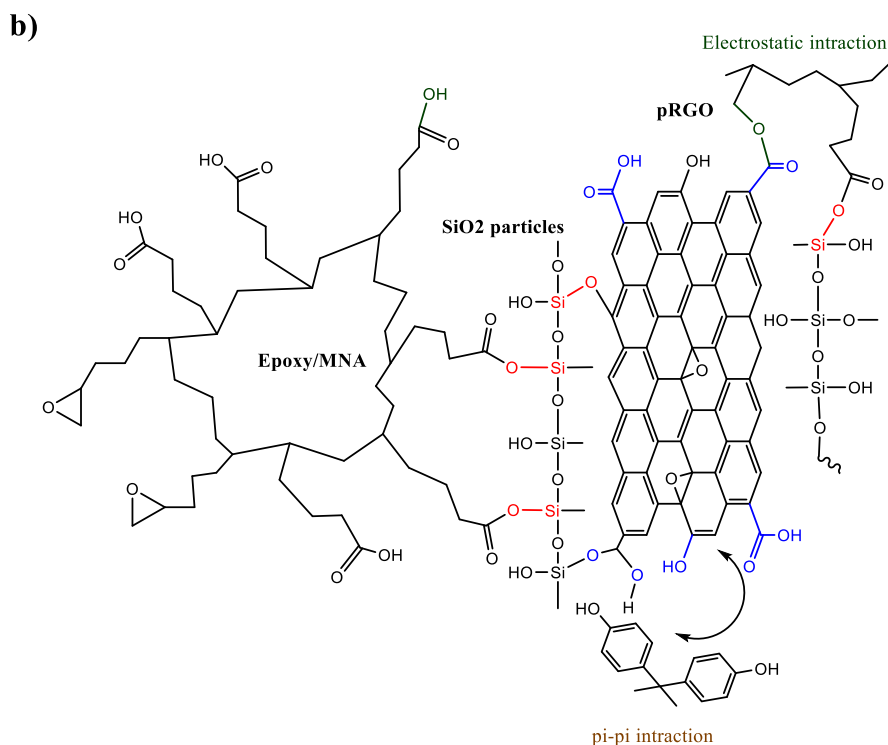
EP resin (20 g) was mixed with the desired amount of RGO–SiO<sub>2</sub> in a 500 mL beaker at room temperature. The ingredients were then mixed with a high-shear mixer for two different lengths of time (all samples for 90 min, except one sample for 30 min) at speeds 1600 rpm, after underwent to sonication for 20 min. The glass beaker containing the mixture was placed in a hot oil bath onto a magnetic stirring plate at 40°C and mechanically stirred for 20 min prior to gradually raising reaction temperature to 70°C. Then, the blend was magnetically stirred for 6 h after removal of the solvent by evaporation to obtain homogenous dispersion of the fillers, with the residual solvent separating from the EP/ RGO–SiO<sub>2</sub> phase.

Next, the mixture underwent vacuum drying at 80°C for 4 h and then the stoichiometric amount of hardener MNA (18 g) and N, N-Dimethylbenzenamine (0.2 g) were slowly added into the mixture. The mixture was then placed on a magnetic stir plate at 80°C for 20 min at 600 rpm.

After the degassing process in a vacuum oven at 80°C for 20 min to eliminate the remaining solvent, the final product was poured into a differently shaped preheated mould and pre-cured at 80 to 120°C for 1 h, then 150°C for 30 min, and finally to 180°C for 3 h at a temperature rate increase of 0.3°C min<sup>-1</sup> in an oven. Next, a post-cure step at 200°C for 30 min which was

followed by a ramp down in temperature of  $0.5^{\circ}\text{C min}^{-1}$  to  $24^{\circ}\text{C}$ . Neat EP composite specimen was also prepared using the same procedure.





**Scheme 5-1.** The proposed curing mechanism of EP in the presence of RGO sheets decorated with SiO<sub>2</sub> nanoparticles along with the curing agent methyl nadic anhydride in the presence of catalytic amount of accelerator *N, N*-Dimethylbenzylamine (a, b).

## 5.3 Characterisation

The characterisation techniques (AFM, FT-IR, Raman, XRD, XPS, SEM, TEM, TGA, DMA and Tensile test) that were employed in this study have been detailed in the previous section.

### 1. Dielectric spectroscopy

The sample surfaces (10 × 10 × 2 mm) were really smooth after using three different types of monocrystalline diamond suspensions for polishing using (Buehler, Germany) at 300 rpm for 2 min. each. The grain sizes began at 100 μm, went to 6 μm and ended with 1 μm. The samples were covered on two sides to accomplish great contact between the electrodes of the test apparatus. The silver coating was also used to eliminate air gap errors caused by small-scale measured sample surface unevenness.

Each test sample was then placed between the electrodes of the 16451B test fixture and associated with the Agilent impedance analyser 4184A at a test voltage of 500 mV. The real and imaginary components of the complex permittivity were calculated using the complex impedance as a function of frequency. The amount of polarisation and dielectric loss of material are calculated from the following equations (Suzuki et al. 2001):

$$C = \frac{\varepsilon' \varepsilon_0 A}{d}$$

$$\tan\delta = \frac{\varepsilon''}{\varepsilon'}$$

where  $C$  is the capacitance (Farad)  $\varepsilon'$  is the dielectric constant (real part) that measures the amount of polarisation,  $\varepsilon''$  is the dielectric loss (imaginary part) that is encountered through the polarisation processes,  $\varepsilon_0$  is the permittivity of free space  $\sim 8.8562 \times 10^{-12}$  F m<sup>-1</sup>,  $d$  is the sample thickness (2 mm) and  $A$  is the area of the sample (100 mm<sup>2</sup>).

## 5.4 Results and discussion

### 5.5 Section One-GO and RGO–SiO<sub>2</sub> hybrid

#### 5.5.1.1 SEM and TEM

The distinctive nanostructure of GO material has achieved successful covalent bonding with the SiO<sub>2</sub> nanoparticles via hydrolysis of TEOS, obtaining a GO–SiO<sub>2</sub> composite where subsequent reduction to RGO–SiO<sub>2</sub> occurs via the vacuum-assisted method at low temperature. The existence of these nanoparticles was confirmed by TEM and SEM images shown in Fig. 5-2 and Fig. 5-3, respectively.

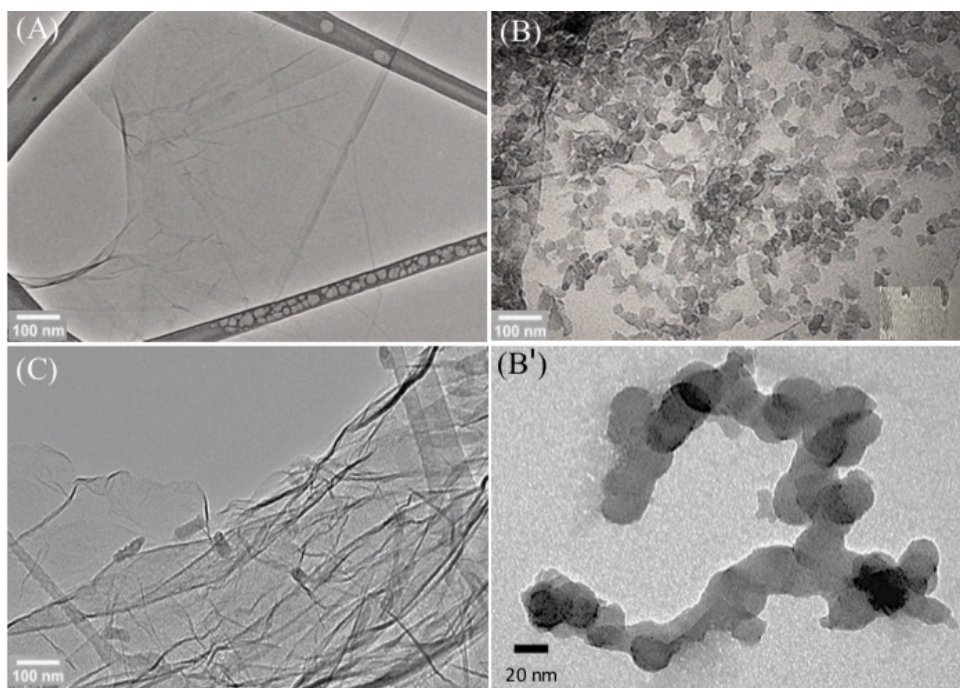


**Figure 5-2.** The TEM images of (A) GO, (B) RGO–SiO<sub>2</sub> nano-hybrids (C) RGO and (B') high magnification RGO–SiO<sub>2</sub> nano-hybrids.

As shown in Fig. 5-2 (A, C), the TEM images of the GO and RGO nano-sheets were transparent and had a lamellar structure. In contrast with the RGO, the GO nano-sheets had a very smooth surface, with a low level of waviness and folding which were identified at their bent edges. The spherical nano-sized SiO<sub>2</sub> particles (approximately 25 nm) were distributed on the RGO layers in Fig. 5-2 (B) and can be seen clearly with high magnification in Fig. 5-2 (B'). As shown in the TEM images, the RGO sheet was transparent and had a lamellar structure, whereas the graphite was very dark and opaque. The circular profile can be seen clearly, confirming the existence of SiO<sub>2</sub> nanoparticles, Fig. 5-2 (B'). Also, the formed SiO<sub>2</sub> nanoparticles were found to be attached strongly to the RGO surface after the thermal reduction process; therefore, we can conclude that the 2-D nanostructure of the RGO layers can give a facile model for the hydrolysis process of tetraethoxysilane. In addition, after the reaction process with TEOS, strong interconnection occurred between RGO and SiO<sub>2</sub> nanoparticles, which can be ascribed to the conversion of the C=O functional group on the RGO sheet to a Si–O–C band.

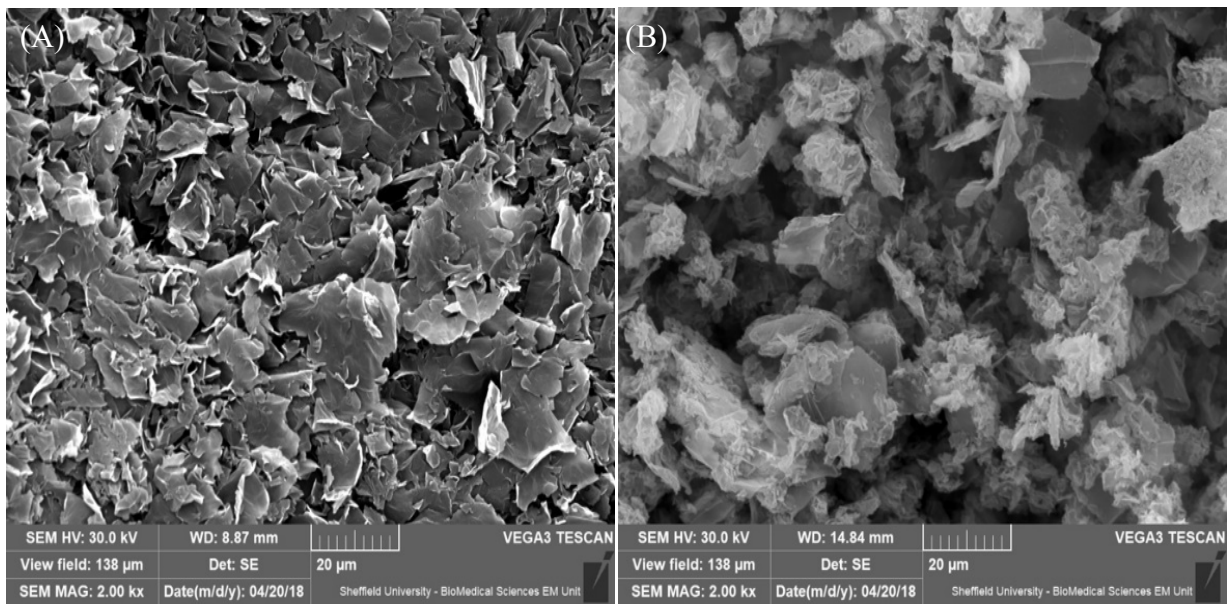


**Figure 5-3.** The SEM images of (A) GO and (B) RGO–SiO<sub>2</sub> nano-hybrids.

SEM magnified images of the samples detect rather conspicuous features around their microstructure and morphology. Fig. 5-3 (A) reveals the formation of bulky agglomerates of GO sheets stacked tightly with good uniformity extending to several micro-meters and layered structures at the edges. Meanwhile, for RGO–SiO<sub>2</sub> nano-hybrids (Fig. 5-3 (B)), the silica nanoparticles prevented the re-stacking of RGO sheets by acting as a spacer against the aggregation of individual RGO nano-sheets. Interestingly, some semi-rolled sheets can be seen clearly, indicating the flexibility of RGO–SiO<sub>2</sub> nano-hybrids, and we can also see many ultra-thin sheets that stand individually, as observed by (Kou & Gao 2011). The defects in the carbon-lattice, because of the residue of the epoxy reaction sites and other OCFGs after the in-situ hydrolysis process and reduction of GO into RGO, provided an explanation for such wrinkles.

These results are in close agreement with several characterisation techniques (XRD, FTIR, and XPS) that confirm the formation of silica nanoparticles regularly on the surface of RGO to obtain RGO–SiO<sub>2</sub> with a high degree of reduction as well as increase in d-spacing between the RGO sheets.

### 5.5.1.2 AFM

This technique confirmed the formation of a uniform covering of the silica layer on the planes and edges of the RGO surface with many protuberances (approximately 30 nm), as opposed to the smooth uncovered pristine GO, as illustrated in Fig. 5-4, which agrees with the SEM and TEM images. The AFM image shows the formation of silica nanoparticles on the RGO surface with good uniformity, extending to several micrometers.

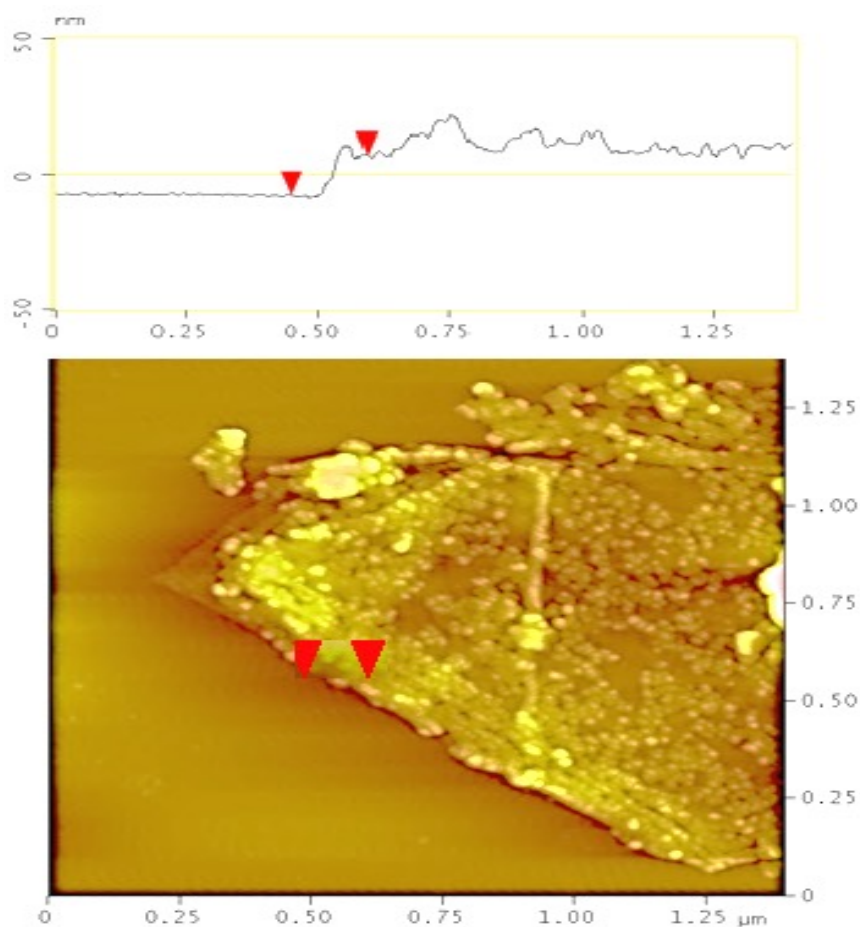


**Figure 5-4.** Representative AFM images of RGO-SiO<sub>2</sub> at high magnifications

However, it was also observed that there was an accumulation of silica nanoparticles on the edges of the RGO surface, which might be provides proof of occurrence bonding between RGO nanosheet and the silica nanoparticles. This is a result of the concentration of most of the oxygen functional groups on the edges of the RGO sheets on both sides.

### 5.5.1.3 FT-IR

To verify the introduction of SiO<sub>2</sub> nanoparticles on the RGO surface in the nano-hybrids composite, the GO, RGO, SiO<sub>2</sub> and RGO–SiO<sub>2</sub> nano-hybrids were investigated using FT-IR spectroscopy (Fig. 5-5).

The GO sample showed very broad absorption peaks between 3000–3700 cm<sup>-1</sup> and 1387 cm<sup>-1</sup> were assigned to O–H stretching modes from C–OH groups and in-plane (O–H) hydroxyl group deformation vibrations in the C–OH group respectively, which are much stronger in the GO sample than in the RGO sample. The peak located at 1721 cm<sup>-1</sup> corresponds to the stretching vibration of the carbonyl or carboxyl groups C=O bond, whereas the band at 1621 cm<sup>-1</sup> could be ascribed to the sp<sup>2</sup> hybridised C=C groups in the GO structure.

The abundance of negative OCFGs such as carbonyl, hydroxyl and carboxyl on the GO edges and basal planes act as anchoring sites that are covered by a thin layer of SiO<sub>2</sub> particles which hydrolyse from TEOS. After the reaction of GO nano-sheets with TEOS via the sol–gel process and the forming of the RGO–SiO<sub>2</sub> nano-hybrid, the characteristic bands relating to the silica were clearly identified, indicating that the silica intensively formed on the surface of the RGO. Which are strongly crosslinked with the RGO surfaces via Si–O bonds. Compared with the RGO, RGO–SiO<sub>2</sub> nano-hybrid composites show two major peaks observed at 1067–1074 cm<sup>-1</sup> and 796–801 cm<sup>-1</sup>. These peaks can be ascribed to the (Si–O–C/Si–O–Si) asymmetric stretching and bending vibration, respectively.



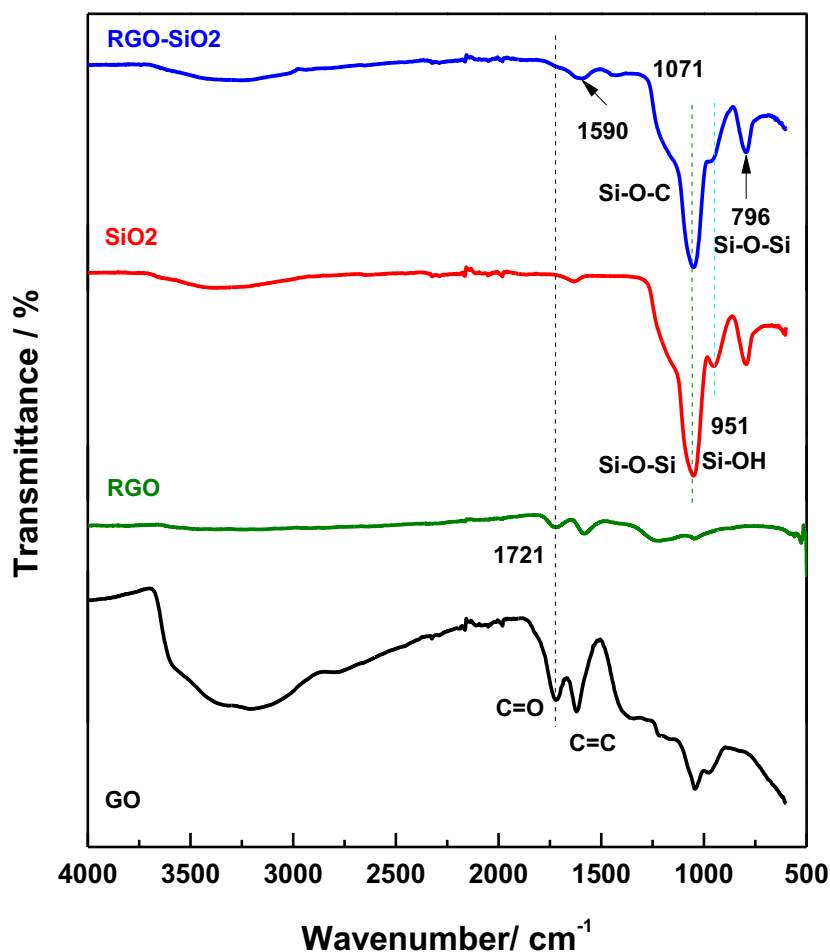


*Figure 5-5. The FT-IR spectra for the GO, RGO, SiO<sub>2</sub> and RGO–SiO<sub>2</sub> powders*

However, the peak related to Si–OH group located in SiO<sub>2</sub> (987–996 cm<sup>-1</sup>) nanoparticles disappeared after nano-hybrid formation, suggesting the dehydration of the sample.

Finally, the OCFG peaks in the RGO–SiO<sub>2</sub> composite spectra decreased dramatically or vanished after the thermal treatment process, demonstrating that most of these OCFGs were removed successfully and that the C=C vibration peak appeared at 1590 cm<sup>-1</sup> but was assigned at 1621 cm<sup>-1</sup> in the case of GO. This shift in position suggests that the pyrolysis process led up to the restoring of the basal nanostructure in the C sp<sup>2</sup> domains of GO (Huang et al. 2014).

### 5.5.1.4 XRD

XRD was used to study the effect of the SiO<sub>2</sub> nanoparticles on phase structure for the RGO surface in RGO–SiO<sub>2</sub> composite, as shown in Fig. 5-6. After the successful exfoliation of graphite oxide via the ultrasonication technique, the GO nano-sheets exhibited a highly reduced peak at  $2\theta = 11.6^\circ$  (corresponds to the (002) reflection plane and a d-spacing of  $\sim 0.83$  nm) which concurs with the work of Zhang and Choi (2012).

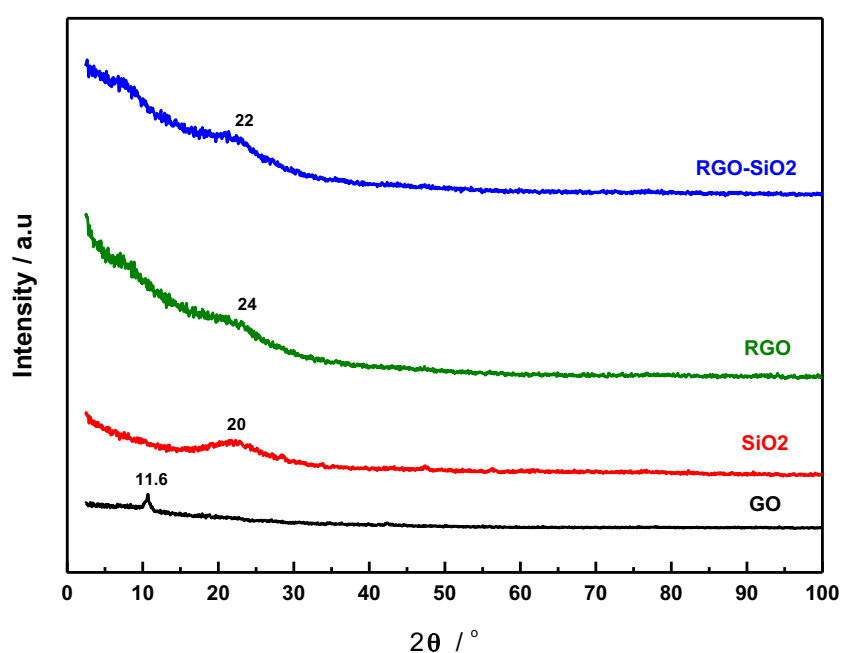


**Figure 5-6.** The XRD patterns for GO, RGO, SiO<sub>2</sub> and RGO–SiO<sub>2</sub>

The reduction of the GO (RGO), which is theoretically a mono-or-few layered structure, exhibits a very broad peak centred at  $24^\circ$  (corresponding to  $\sim 0.38$  nm) as shown in Fig. 5-6. This weakening or disappearance even, of RGO peaks can be ascribed to the randomly ordered graphitic layers with a corrugated structure that are destroyed via the exfoliation process (Kou & Gao 2011).

For SiO<sub>2</sub> the emergence of a broad peak around  $20^\circ$  was observed, which is assigned to the original SiO<sub>2</sub> nanoparticles. With regards to the RGO–SiO<sub>2</sub> sample, the broad peak that was

observed between the SiO<sub>2</sub> and RGO was shown for the RGO–SiO<sub>2</sub> nano-hybrid, indicating that the nano-hybrid consisted of SiO<sub>2</sub> nanoparticles and RGO nano-sheets. Furthermore, this very broad peak might be attributed to the formation of a silica layer on both sides of the RGO sheet, which prevents the re-stacking of the RGO and consequently causes it to stay in a random stacking state (Hsiao et al. 2013). The results show that the XRD technique is not sufficiently sensitive for characterising a single-layer of GO or RGO. However, the significant peak which originates from GO had disappeared at RGO–SiO<sub>2</sub> nano-hybrids due to the introduction of SiO<sub>2</sub> nanoparticles on its surface and because the peak that originates from RGO had shifted downwards because of the reduction of GO (pyrolysis) during the chemical/thermal reduction process. The d-spacing of nano-hybrid was calculated at 0.4 nm based on a Bragg's law calculation (Layek et al. 2014), which is a reduction of 52% compared to GO. This reduction is also because of the introduction of nano-silica particles on the RGO structure, which could have an advantageous effect on the dispersion behaviour (Ma et al. 2016).

### 5.5.1.5 XPS

XPS spectra were utilised to study the reduction of GO nano-sheets and their interaction with SiO<sub>2</sub> nanoparticles. Fig. 5-7 exhibits the survey spectra of SiO<sub>2</sub>, GO, RGO and RGO–SiO<sub>2</sub> (1:3). The surface of the Si nanoparticles is rich in oxygen (54.6 at. %), which is a result of the formation of a thick layer of silica, whereas RGO nano-sheets typically showed only C 1s and O 1s peaks with a C/O ratio of 3.1. This results suggest low levels of oxidation compared to an XPS survey of a GO sample that had a ratio of 2.28 (reported in Section 3.6.1.5). This reduction of O 1s peaks can be ascribed to the success of the thermal treatment process of the GO sample. The OCFGs were characterised by the deconvolution of the C1s and O1s spectra of RGO, and the peaks centred at 285, 286.6, 289.3 and 291.5 eV correspond to C–C, C=C, epoxy/ether (C–O–C), carbonyl (C=O) and carboxylate (O–C=O) groups, respectively, as observed in Fig. 5.8

for the RGO sample.

Introducing SiO<sub>2</sub> into the GO surface through the sol–gel process followed by heat treatment via the vacuum-assisted approach (at 120°C for 24 h) led to a decreased C/O ratio (to ~2.0), the presence of Si peaks, and a decrease in the OCFGs seen from the RGO C1s spectra, and these changes can be attributed to the presence of silica. XPS shows an increase in SiO<sub>2</sub> on the material, which would mask parts of surface reducing the opportunity for the scan to reveal the surface of the RGO. The analysis depth of XPS is a few nanometres, so covering the surface with SiO<sub>2</sub> will stop the analysis of the RGO surface as the nanoparticles dominate the spectrum.

In the case of RGO–SiO<sub>2</sub>, Fig. 5-8, shows the curve-fitting of the O1s and Si2p peaks at 531.5, 533.6 and 105.7 eV, which are demonstrative of the construction of a SiO<sub>2</sub> network, and that the prominent peaks at 531.5 and 104.4 eV (assigned to the Si–O–C bond) were proof of a significant formation of covalent bonding between the RGO and SiO<sub>2</sub>, agreeing with the FTIR results. (Liu et al. 2017) reported similar peaks to those in this current study when they fabricated a sandwich structure of RGO (0.5 wt. %) coated with mesoporous SiO<sub>2</sub> by using an autoclave at 180°C, for 12 h, and they claim that domains were highly increased for the graphene, thereby achieving lower defect levels for the RGO.

In addition, the O/Si atomic ratio is 1.73, which can be associated with the existence of the thick layer of SiO<sub>2</sub> and/or by the presence of oxygen introduced by the RGO phase. The total content of Si element in the RGO–SiO<sub>2</sub> nano-hybrids, as specified by the XPS tool (16.3 atomic %), corresponds to 29.09 wt. % Si, which is slightly lower than the estimated goal of synthesis (34.7 wt. %), as shown in Table 5-2. Thus, this reduction in Si (wt. %) could be ascribed to the accumulation of SiO<sub>2</sub> nanoparticles on the edges of RGO nano-sheets because of the existence of most of the functional groups on RGO edges that do not decompose at temperatures lower

than 200°C. Because the XPS tool is highly sensitive for surface analysis with a penetration depth of X-ray less than about 10 nm, it cannot detect multi-layers of silica that occur on the edges of RGO.

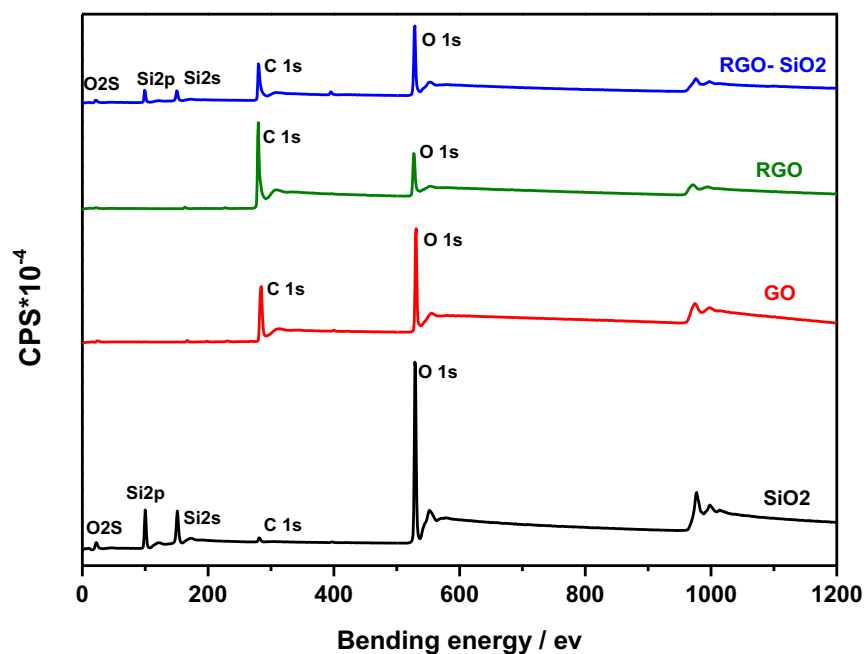


*Figure 5-7. Survey scan spectra of SiO<sub>2</sub>, GO, RGO and RGO-SiO<sub>2</sub>.*

*Table 5-2. Atomic ratio of RGO-SiO<sub>2</sub> corresponding to the calculated wt. %.*

Atomic	C	O	N	Si
Atomic Ratio (%)	53.20	28.20	2.30	16.30
Weight (%)	40.36	28.51	2.03	29.09

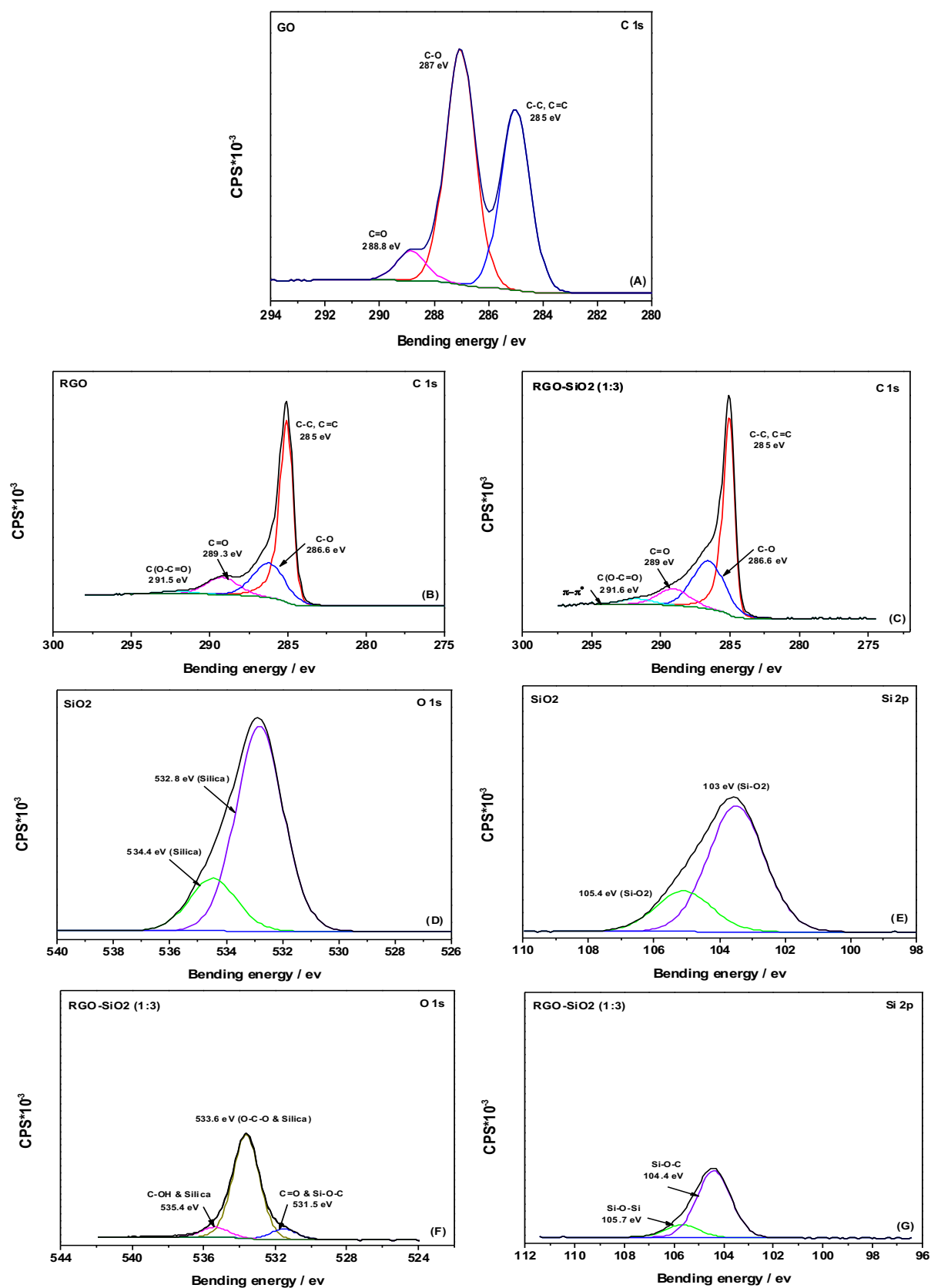


**Figure 5-8.** C 1s XPS spectra of GO (A), RGO (B) and RGO-SiO<sub>2</sub>, and O 1s for SiO<sub>2</sub> (D) and RGO-SiO<sub>2</sub> (F), and Si 2p for SiO<sub>2</sub> and RGO-SiO<sub>2</sub> (E, and G).

### 5.5.1.6 Raman spectroscopy

The XPS and XRD result can be further confirmed using Raman spectroscopy, as it is an effective tool of characterising small changes in the structural morphology that occur in carbon nanomaterials. Raman spectroscopy monitors the G peak ( $\sim 1587\text{ cm}^{-1}$ , which arises from the bond-stretching motion of C  $\text{sp}^2$  atoms in pairs,  $\text{E}_{2g}$  mode) and the D peak ( $\sim 1352.7\text{ cm}^{-1}$ , which corresponds to the  $\text{A}_{1g}$  breathing mode) (Hsiao et al. 2010).

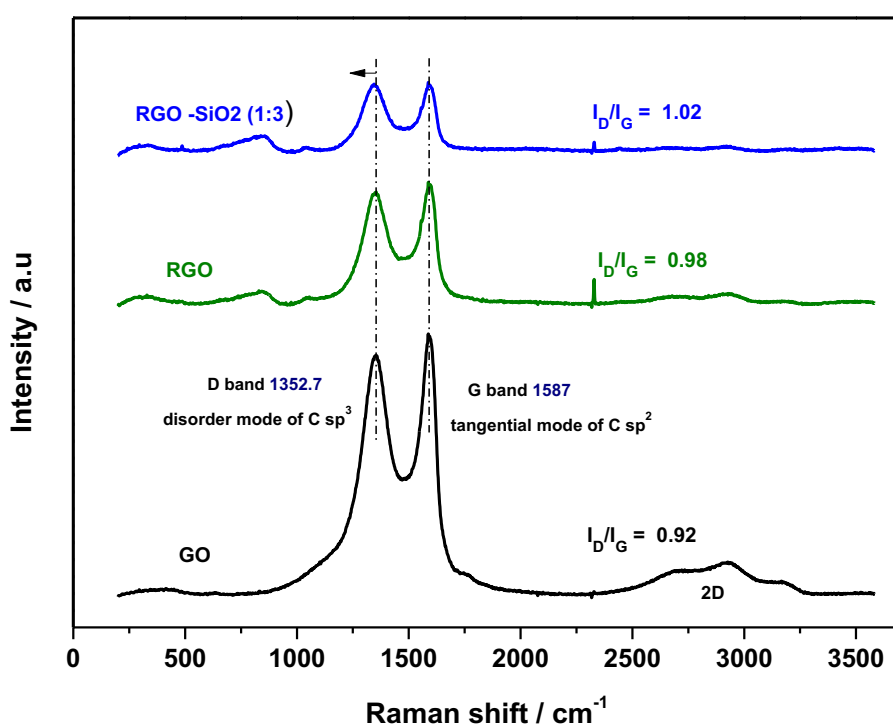


*Figure 5-9. The crystal structure of GO, RGO and RGO-SiO<sub>2</sub> by the Raman technique*

As shown in Fig. 5-9, RGO and RGO-SiO<sub>2</sub> show typical broad peaks of D and G mode because of the large number of defects on the  $\text{sp}^2$  carbon network that occur during the GO fabrication process, where C is broken into an aromatic  $\text{sp}^2$  domain and a nanoscale oxidised domain (Hsiao et al. 2013). In addition, the  $I_D/I_G$  intensity value of RGO and RGO-SiO<sub>2</sub> were 0.98 and 1.02, respectively, which are greater than that of the GO sample (0.92) and suggest an increase in the domain numbers of GO through the reduction process, hence decreasing the mean size

of the  $sp^2$  domains. This result is indicative of the formation of new graphitic domains that are very small in size compared to those in GO before being exposed to the reduction process. The RGO–SiO<sub>2</sub> possesses a higher  $I_D/I_G$  value than that of RGO, indicating a greater surface area of the three-dimensional network, providing more active sites for reaction and resulting in a more complete reduction (Huang et al. 2017). The D-band of the RGO–SiO<sub>2</sub> composite positively shifts from 1352.7 to 1349  $cm^{-1}$ . This result implies that a stronger interaction occurs between the RGO and SiO<sub>2</sub> nanoparticles.

### 5.5.1.7 TGA

TGA curves were used to determine the thermal stability for each powder sample. Fig. 5-10 shows the change in the mass as a function of temperature from 25 to 800°C for GO, RGO, SiO<sub>2</sub> and RGO–SiO<sub>2</sub>. In both thermograms of GO and RGO, there were three major weight loss steps, the first of which, at about 25–100°C, can be associated with the evaporation of adsorbed water. The second weight loss step, at about 100–245°C, of around 40% in the case of GO and just 15.0% in the case of RGO, is ascribed to the decomposition of OCFGs on the surface of GO or RGO to CO and CO<sub>2</sub>. The third step was a slight decrease further, at up to 800°C, which is a result of the thermal decomposition of the carbon structure. On the other hand, the RGO–SiO<sub>2</sub> sample showed a mass loss only in two steps; one of them, at about 25–100°C, due to the evaporation of adsorbed H<sub>2</sub>O, while the other, arose from the pyrolysis of the RGO structure, with 88.6 wt. % retained at up to 800°C.



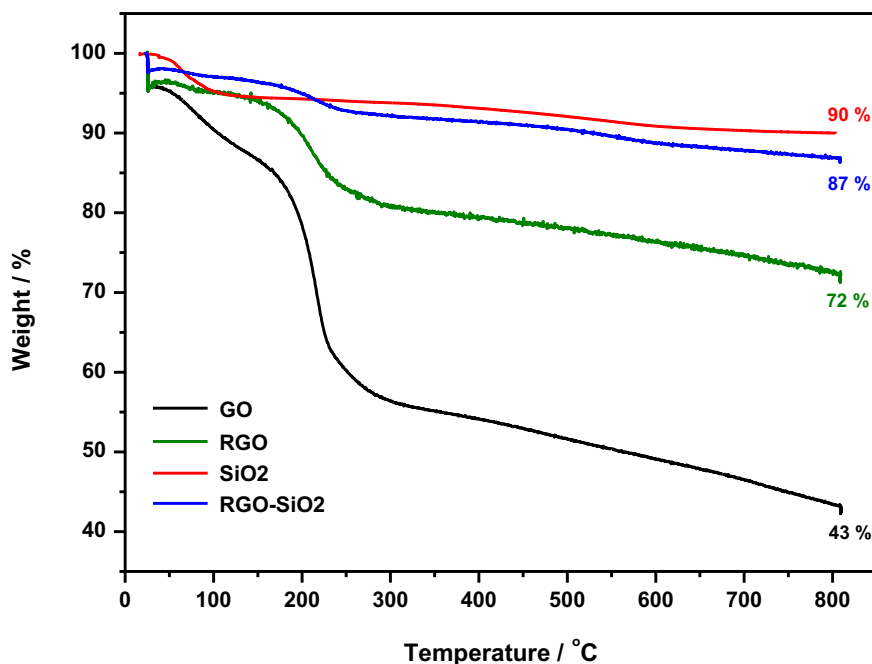


**Figure 5-10.** TGA curves of GO, RGO and RGO–SiO<sub>2</sub> nano-hybrid composite.

The RGO–SiO<sub>2</sub> composite sample showed a large reduction in mass loss with an increase of 15 wt. % over than that achieved by the RGO sample. The curve remained steady up to 800°C, indicating more overall thermal stability than the RGO sample (Huang et al. 2017). An introduction of SiO<sub>2</sub> nanoparticles onto the surfaces of RGO sheets resulted in slow decomposition rates with somewhat excess onset of mass loss related to the thermal-oxidative pyrolysis of carbonates. Thus, the composite tended to be more stable with inserting SiO<sub>2</sub> in the nano-hybrids. This result suggests that the formed SiO<sub>2</sub> nanoparticles on the surface of RGO can serve as a protective thin-layer that averts further thermal degradation of the carbon material. However, the SiO<sub>2</sub> curve showed high-level thermal stability, with virtually no clear weight loss unto 800°C (Hsiao et al. 2013).

## 5.6 Section Two-RGO–SiO<sub>2</sub> nanocomposites

### 5.6.1.1 SEM

The quality of the interfacial interactions and dispersion level between the RGO–SiO<sub>2</sub> nano-hybrids and the EP matrix were examined utilising the SEM technique for cryo-fracture surfaces of nanocomposites, as seen in Fig. 5-11. The neat EP composite exhibited smooth and clean rupture surfaces as a result of the brittle failure of the sample. In contrast, inserting the fillers into the EP matrix led to completely different morphologies of the fracture surfaces. The presence of a silica layer on the RGO structure to the roughness of the surface resulted in a river structure shape and bowl-like domes to be formed, which are shown in the magnified images in Fig. 5-11(C). The fracture surfaces were also found to be rougher when the fillers were of two-dimensional morphology, and the wrinkles were clearly notable, as shown in Fig. 5-11 (C) – (F). In contrast, the RGO–SiO<sub>2</sub> and SiO<sub>2</sub> nanoparticle samples showed a good uniform distribution within EP polymer, reflecting good compatibility between the filler from one side and the matrix from the other side, as shown in Fig. 5-11 (F). The existence of a silica layer in the system helped to overcome the strong  $\pi$ – $\pi$  interactions that occur among the individual RGO nano-sheets and improve the chemical bonding between RGO nano-sheets and EP polymer. Therefore, silica can act as a stabiliser against the aggregation formed between RGO sheets (SEM images in Chapter three, Section 3.4.1.3). The wavy sheets, with their wrinkled and nano-size roughness, resulted in strong mechanical-interlocking properties with the polymer and hence the strong interfacial adhesion between the fillers and the matrix can permit the stresses to be transmitted when the sample is exposed to externally applied forces (stress), limiting the sliding of interfaces.

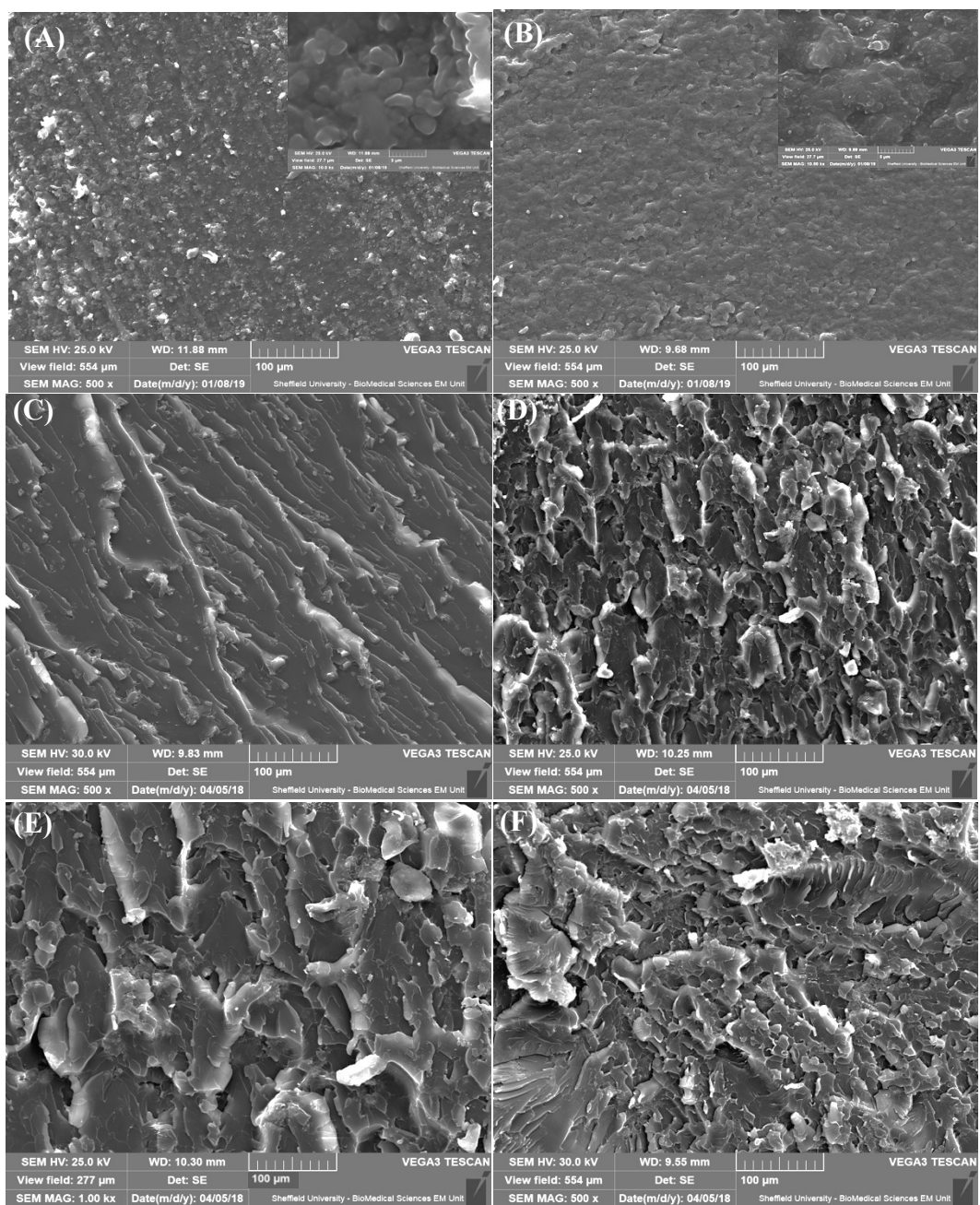


**Figure 5-11.** The SEM images of (A) a pure EP composite, and (B) EP nanocomposites containing 5.0 wt. % of silica, (C and D) 1.0 wt. % of RGO–SiO<sub>2</sub> nano-sheets using THF and distilled water for dispersion, respectively, and (E and F) 3.0 wt. % of RGO–SiO<sub>2</sub> nano-sheets at low and high times of dispersion respectively. The images are magnified 25 kV.

### 5.6.1.2 FT-IR

FT-IR was used to investigate the effect of the silica layer on the RGO surface to characterise the structure and the curing behaviour of EP nanocomposites. Fig. 5-12 shows the FT-IR analysis of neat EP and its EP nanocomposites.

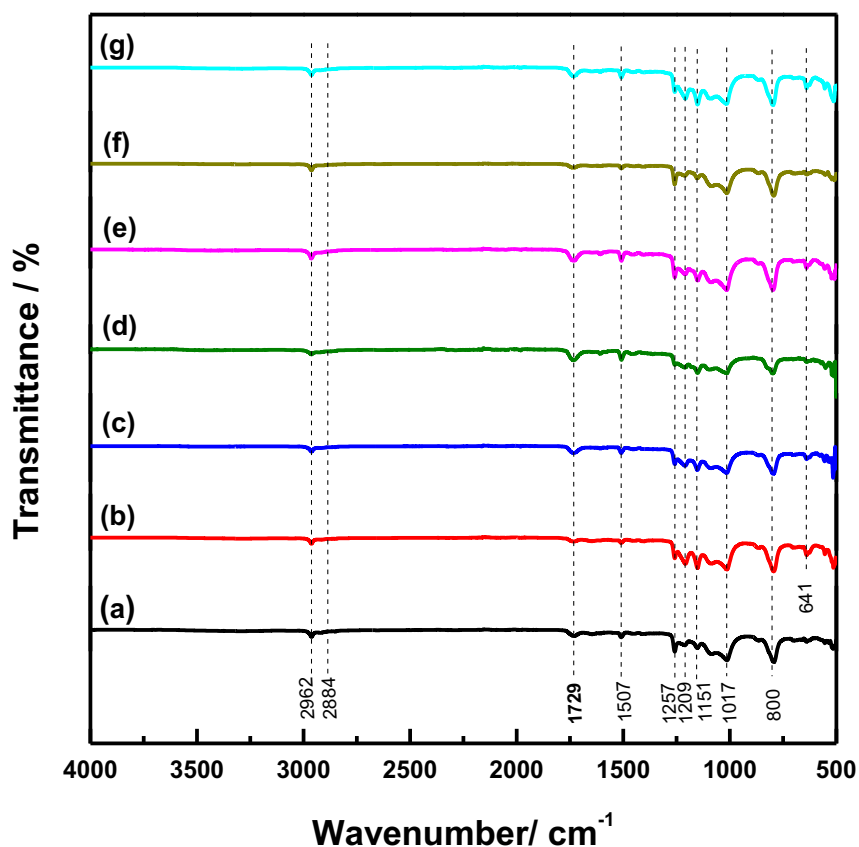


**Figure 5-12.** FT-IR spectra for (a) neat EP and its nanocomposites of RGO–SiO<sub>2</sub> (b, c) at 1 wt. % (H<sub>2</sub>O, THF), (d, e) at 3 wt. % (30, 90 min), and (f) at 5 wt. % and 5 wt. % of pure SiO<sub>2</sub>.

For all samples, FT-IR results showed an absence of symmetric and asymmetric stretching features of the epoxy group at 862 and 914 cm<sup>-1</sup>, respectively, confirming the formation of a three dimensional EP network (Nazir et al. 2011). The formation of SiO<sub>2</sub> layers was confirmed by the absorption peak for Si–O–Si asymmetric stretching at 1151 cm<sup>-1</sup>, as shown in Fig. 5-12. The adsorption peak at 641 cm<sup>-1</sup> was attributed to the Si–OH stretching band and because hydrogen (Si–OH) is associated with the electrically negative oxygen atom. Furthermore,

because (C=O) can serve as the electron donator, it is possible for the occurrence of hydrogen bonding ( $-\text{Si}-\text{O}\dots\text{H}\dots\text{O}=\text{C}-$ ) between these species (Zhang et al. 2008).

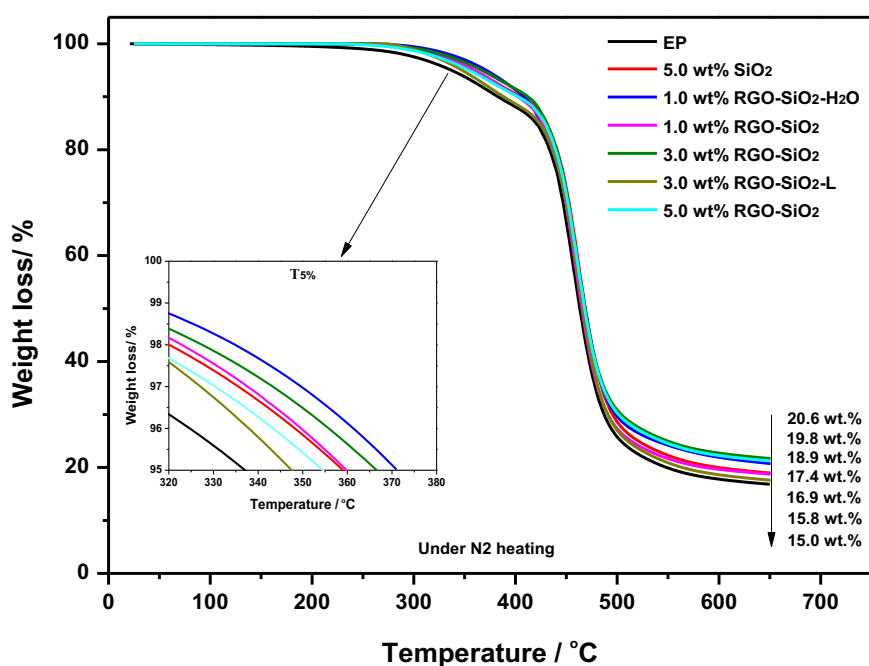
The complex feature of the nanocomposites and the existence of similar bonds in various series of formed composite materials are difficult to characterise between them via their FTIR spectra. Moreover, on comparing the curves of the cured EP and its nanocomposites, the FT-IR spectra showed somewhat similar peaks to that of the neat EP but with an attenuated intensity because of the incorporation of RGO-SiO<sub>2</sub>, which do not exceed 5.0 wt. %.

### **5.6.1.3 TGA**

Decorating SiO<sub>2</sub> NPs on the surfaces of RGO nano-sheets has been used widely in polymer matrices to enhance thermal stability. For instance, (Huang et al. 2014) found that the addition of RGO-SiO<sub>2</sub> into the EP matrix delays the onset temperature of decomposition, suggesting an increase in thermal stability. The researchers ascribed this increase to the existence of the SiO<sub>2</sub> layer that acts as a protective layer, preventing the polymer degradation. Additionally, the 2D structure for the RGO filler works to hinder oxygen diffusion within the nanocomposites and obstructs diffusion of volatiles materials. A comparable result has been reported by (Hsiao et al. 2013). In other studies, increased thermal stability has been reported for TiO<sub>2</sub>/RGO-based EP nanocomposites (Chen et al. 2013).

The results of the current study are consistent with other studies; as in this study, the incorporation of RGO-SiO<sub>2</sub> samples into the EP matrix enhanced the thermal stability of EP in the presence of both nitrogen gas and air, as illustrated in Fig. 5-13 and 5-14, respectively. In addition, the  $T_{5\%}$  values taken from these curves are exhibited in Table 5-3. From Fig. 5-13, the DTG thermograms showed that the values of  $T_d$  for the nanocomposites are greater than that for neat EP in both atmospheres by approximately 5°C, confirming that RGO-SiO<sub>2</sub> nano-hybrids enhance thermal stability. The enhanced thermal stability can be attributed to the reality

that RGO/metal or non-metal oxide can increase the cross-linking density of the EP (Zhou et al. 2009 and Huang et al. 2014), leading to higher thermal stabilities. The TGA curve (Fig. 5-13) shows that the  $T_{5\%}$  values for pure EP are approximately 338°C and 290°C in nitrogen and air, respectively. However,  $T_{5\%}$  values for the samples having 1.0 wt. % RGO–SiO<sub>2</sub> (THF) are around 360°C and 309°C in nitrogen and air, respectively. The addition of >1.0 wt. % RGO–SiO<sub>2</sub> decreased the thermal stability slightly because of the agglomeration of RGO during solution mixing at higher loadings (Alshammari et al. 2017).



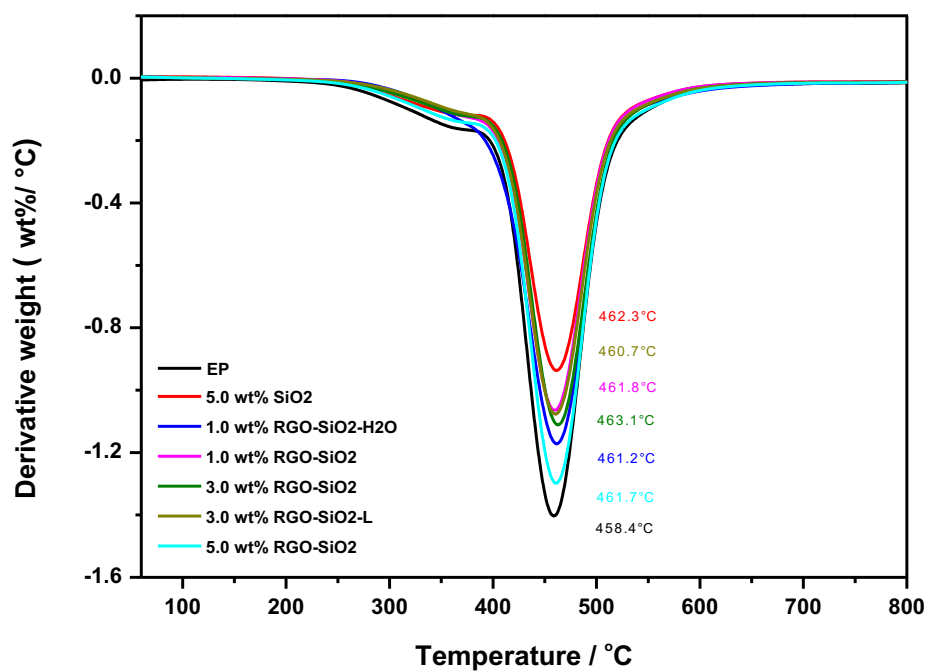


**Figure 5-13.** TGA/DTG thermograms for nanocomposites examined under  $N_2$  atmosphere.

Moreover, neat EP and its nanocomposites have lower  $T_{5\%}$  values when measured under air (Fig. 5-14) compared to those obtained under  $N_2$  atmosphere. In addition, the increment of the  $T_{5\%}$  values in nitrogen is higher than that in air when compared to pure EP. For example, with the addition of 5.0 wt. % of RGO-SiO<sub>2</sub>, the  $T_{5\%}$  values are greater than those of unfilled EP matrix by approximately 16°C and 6.0°C in nitrogen and air atmospheres, respectively, as shown in Table 5-3.

**Table 5-3.** Thermal degradation temperatures ( $T_{5\%}$ ) for EP-RGO-SiO<sub>2</sub> nanocomposites under nitrogen and air atmospheres.

Sample	mixing time/ min	wt. %	Solvent	N2 $T_{5\%}$ (°C)	Air $T_{5\%}$ (°C)
EP	90	0.0	THF	338	290
EP-RGO-SiO <sub>2</sub>	90	1.0	H <sub>2</sub> O	371	319
EP-RGO-SiO <sub>2</sub>	90	1.0	THF	360	309
EP-RGO-SiO <sub>2</sub>	30	3.0	THF	347	310
EP-RGO-SiO <sub>2</sub>	90	3.0	THF	366	316
EP-RGO-SiO <sub>2</sub>	90	5.0	THF	354	296
EP-SiO <sub>2</sub>	90	5.0	THF	359	318

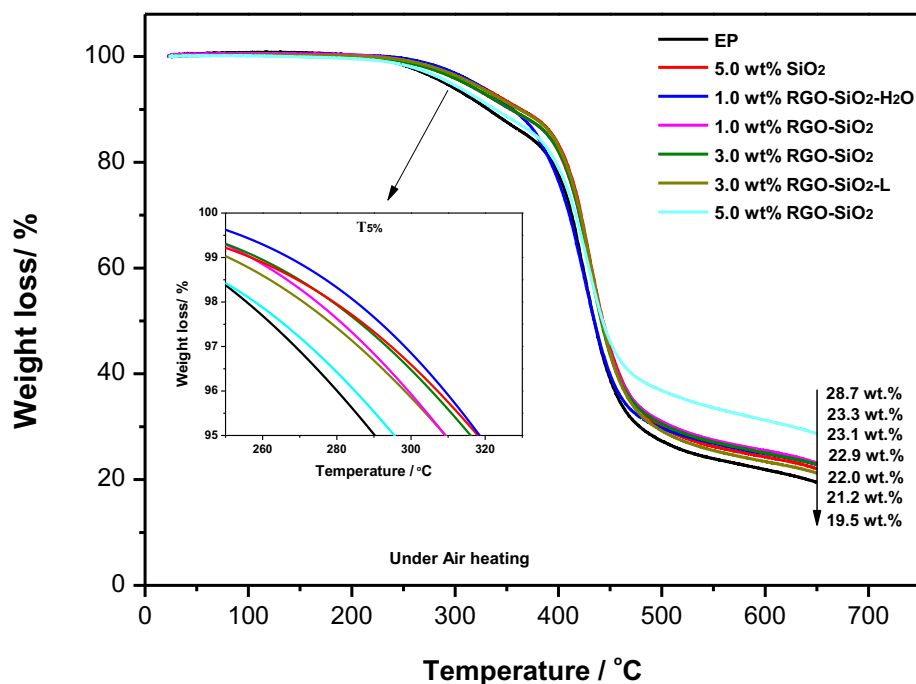


**Figure 5-14.** TGA thermograms of nanocomposites examined in air.

In addition, silica nanoparticles are strongly attached with an ultra-thin layer of RGO nano-sheets, through the sol-gel process of TEOS with the existence of GO, forming unique structures which efficiently disturb the agglomeration of RGO within the polymer.



Fig. 5-13 shows that the thermal stability is significantly influenced by the degree of dispersion and the RGO ratio in the system. For instance, the addition of 5.0 wt. % RGO–SiO<sub>2</sub> nano-hybrids into the matrix did not profoundly affect the thermal stability of the EP composite. This lack of change can be observed from the simple difference of residue of these samples at a temperature range between 650 and 700°C and the  $T_d$  value which does not exceed 3°C higher than pure EP (458.4°C). However, the addition of a decreased amount of content filler (i.e. 3.0 wt. % RGO–SiO<sub>2</sub> at long shear mixing time) led to the highest increase in decomposition temperature ( $T_d \sim 463^\circ\text{C}$ ) as well as the highest amount of residue ( $\sim 20.6$  wt. %) of the nanocomposites at a temperature range of 650–700°C.

When the shear mixer was used for a decreased amount of time for the 3.0 wt. % RGO–SiO<sub>2</sub> sample in the current study, the non-uniform dispersion of RGO–SiO<sub>2</sub> decreased the properties of the nanocomposite, and as a result, the sample exhibited a higher decomposition rate under heating of N<sub>2</sub> compared to the same samples after prolonged use of the shear mixer.

The  $T_d$  for the neat EP is near 458°C. However, for the EP loaded with SiO<sub>2</sub> nanoparticles, a  $T_d$  value of 462.3°C was obtained. As for nano-hybrids, the nanocomposites showed increased thermal stability of the EP resin by adding RGO–SiO<sub>2</sub> nano-hybrids and increasing the mixing time. This increase in thermal properties could be ascribed to the better distribution of nano-hybrids in the EP matrix and stronger interactions between the RGO–SiO<sub>2</sub> surface with the EP matrix.

#### **5.6.1.4 DMA**

Fig. 5-15 (a) shows curves of storage modulus ( $E'$ ) and (b)  $\tan \delta$  versus temperature for EP/RGO–SiO<sub>2</sub>-based nanocomposites at different loading. The average of  $T_g$  and modulus value were taken from three specimens test of each type. The result showed that in the glassy

state region, the modulus of EP at 30°C is  $2.31\pm 0.12$  GPa, whereas the modulus of the nanocomposite containing (5.0 wt. %) SiO<sub>2</sub> nanoparticles had increased to  $2.75\pm 0.09$  GPa. With the incorporation of RGO–SiO<sub>2</sub> nano-hybrids into the matrix in the presence of THF for 1.0, 3.0 (at low/high mixing), and 5.0 wt. %, the nanocomposite samples showed highly increased storage moduli of  $3.13\pm 0.03$ ,  $3.28\pm 0.04$ ,  $3.47\pm 0.03$  and  $3.70\pm 0.02$  GPa, respectively. However, with the use of deionised water as a solvent at low content, 1.0 wt. % of RGO–SiO<sub>2</sub>, the nanocomposites showed an increased E' with the value reaching  $3.96\pm 0.06$  GPa. This value described is the highest E' among all other samples. This increase can be ascribed to the compatible interactions between the fillers and matrix, suggesting uniform dispersion of filler in the matrix resulting in a high degree of cross linking.

Huang et al. (2014) fabricated RGO–SiO<sub>2</sub> nano-hybrids via the electrostatic assembly method for GO–SiO<sub>2</sub>, subsequently, by the thermal reduction process to improve the dispersion of RGO in the EP matrix. The EP nanocomposites that were filled with 30 wt. % of RGO–SiO<sub>2</sub> yielded a significantly increased storage modulus of 3.5 GPa as well as an increase in  $T_g$  by 14.3°C, compared to that of neat EP. This result was achieved in this current study at low levels of fillers and can be ascribed to the improved interfacial interaction between the matrix and fillers.

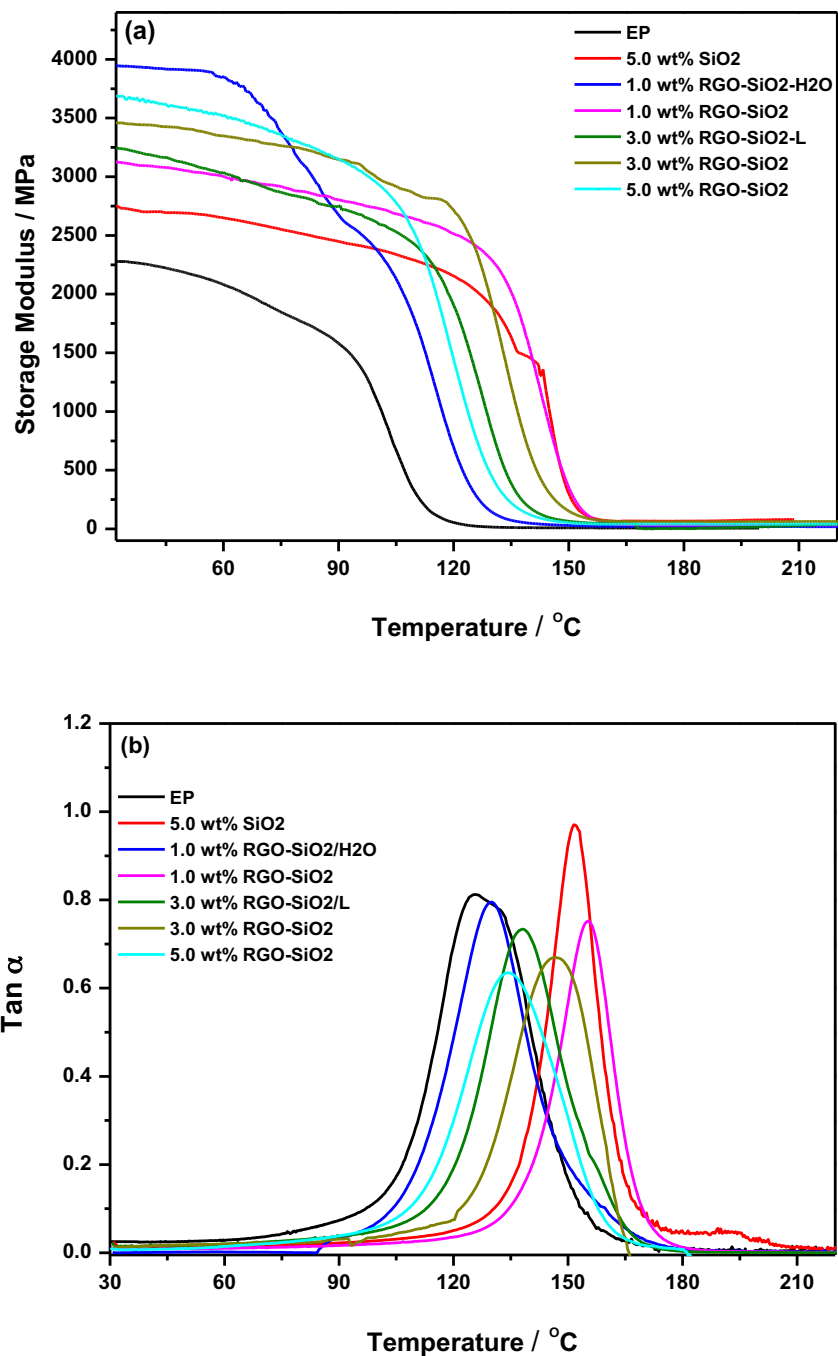


**Figure 5-15.** The DMA plots for EP and its nanocomposites: (a)  $E'$ ; and (b)  $\tan \delta$

The  $T_g$  is highly related to the local segmental motion in polymers and can be identified at the peak in the  $\tan \delta$  curve, as seen in Fig. 5.15 (b). The  $\tan \delta$  peak for 1.0 wt. % of RGO-SiO<sub>2</sub> nanocomposite that was prepared with H<sub>2</sub>O was observed at  $132 \pm 0.4^\circ\text{C}$ , and for the nanocomposite prepared with 100 mL of THF at the same content (1.0 wt. %), the  $T_g$  shifted to a higher temperature of  $155 \pm 0.5^\circ\text{C}$ . This shift may be because the stiffness of the RGO-

SiO<sub>2</sub> results in a constructed chain mobility of the EP matrix, thereby resulting in an increase in the value of  $T_g$ . Moreover, the high cross-linking density between molecules leads to the  $T_g$  values shifting towards the higher value of the nanocomposites. Fig. 5-15 (b) shows that the plots of the  $T_g$  values increased significantly at a low content (1.0 wt. %) of RGO–SiO<sub>2</sub> nanocomposites, reaching 155°C. The likely cause for this increase is that the EP adsorbed on the filler surface increased the cross-linking density, therefore leading to stronger covalent bonds between each other. However, as the loading of filler was increased by 3.0 (low/high mixing) and 5.0 wt. %, the  $T_g$  values of the nanocomposite decreased to 147±0.3, 138±0.4 and 134±0.4°C, respectively. This decrease in the values of  $T_g$  can be explained by the possibility that some solvent might be trapped in the system because of the higher surface area of RGO nano-sheets. As the content of fillers increases, the amount of trapped solvent also increases in the matrix, leading to a negative effect on the DMA results. The  $T_g$  value was increased by 21.2°C with the inclusion of 5.0 wt. % SiO<sub>2</sub>, compared with neat EP. When SiO<sub>2</sub> was incorporated into the EP matrix, the nanoparticles could anchor the EP chains through hydrogen bonding between the hydroxyl groups –OH in the matrix and silanol groups on the SiO<sub>2</sub> surface, and hence the mobility of the EP chains becomes disturbed.

Among all these increments, the 1.0 wt. % of RGO-SiO<sub>2</sub> with THF-based EP nanocomposites reached the highest  $T_g$  value of 155±0.5°C, which is greater than that of the neat EP sample by about 25°C. Increments in  $T_g$  of 4.3°C, 8°C and 17°C were observed for 5.0 wt. % of RGO–SiO<sub>2</sub> and 3.0 wt. % at a short/long time of dispersion for RGO–SiO<sub>2</sub> samples, respectively. This increase can be explained by the SiO<sub>2</sub>-decorated RGO surfaces not merely preventing the aggregation of RGO sheets, but also ameliorating RGO sheet compatibility and interfacial adhesion with the EP matrix, which limits the segmental motion of the EP chains.

However, 3.0 wt. % of RGO–SiO<sub>2</sub> nanocomposite prepared via the solution mixing technique at a lower time (30 min) in the shear mixer at 1600 rpm shows a lower  $T_g$  value of 138±0.4°C,

compared with  $147\pm 0.3^\circ\text{C}$  after 90 min at the same content. The reason for this increase is the synergistic effect process of both sonication and the shear mixer on the dispersion of RGO–SiO<sub>2</sub> in the matrix, thus leading to an increase in the cross-linking structure of the nanocomposites. In addition, (Hsiao et al. 2013) has interpreted the low peaks of the  $\tan \delta$  for polymer-based nanocomposites which reflects the good dispersion within the matrix, contributing to the stronger interfacial bonding that occurs between the fillers and host polymers. In the current study, the RGO–SiO<sub>2</sub> samples showed low peaks on the  $\tan \delta$  curves compared to those of silica-based nanocomposites. Comparing between the long and low time of dispersion of loading 3.0 wt. % RGO–SiO<sub>2</sub> nanocomposite, the long time for dispersion showed lower  $\tan \delta$  values with the less time. To epitomise the thermo-mechanical properties by DMA analysis, because of the strong van der Waals and  $\pi$ – $\pi$  stacking interactions on dispersed RGO nano-sheets, RGO tends to re-aggregate a liquid matrix with the passing of time.

Fig. 5-15 (a) and (b) show that SiO<sub>2</sub> nanoparticles decorated RGO nano-sheets, act as stabilisers against the aggregation of individual RGO sheets in the matrix because of their high tendency to aggregate. Moreover, the excellent properties of non-metal oxide nanoparticles and RGO can be combined, thereby obtaining some particular properties because of the synergistic effect between them. The results also show that the nanocomposite, after a long time of RGO–SiO<sub>2</sub> dispersion, showed a higher  $T_g$  and UTS (illustrated in the next section) than those with less time, although no significant difference in the Young's moduli is caused by the various dispersion levels. The  $T_g$  value decreased with an increasing load of RGO–SiO<sub>2</sub>. This relationship can be attributed to the trapping of some solvent in the system because of the large surface area of RGO nano-sheets increasing the amount of solvent in the system as the content of filler increases, leading to a decline in  $T_g$  values. Table 5-4 summarises the DMA results for EP and its nanocomposites at different loading of fillers.

**Table 5-4.** DMA results for EP and its nanocomposites at different loading of fillers.

Sample	Ratio	wt. %	Solvent	mixing time/ min	E' (at 30°C) / GPa	T <sub>g</sub> / °C
EP	-	0.0	THF	90	2.31±0.12	130±0.5
EP/SiO <sub>2</sub>	-	5.0	THF	90	2.75±0.09	151±0.5
EP/RGO-SiO <sub>2</sub>	1:3	1.0	H <sub>2</sub> O	90	3.96±0.06	132±0.4
EP/RGO-SiO <sub>2</sub>	1:3	1.0	THF	90	3.13±0.03	155±0.5
EP/RGO-SiO <sub>2</sub>	1:3	3.0	THF	30	3.28±0.04	138±0.4
EP/RGO-SiO <sub>2</sub>	1:3	3.0	THF	90	3.47±0.03	147±0.3
EP/RGO-SiO <sub>2</sub>	1:3	5.0	THF	90	3.70±0.02	134±0.4

## 5.7 Mechanical properties

The tensile results of EP and its nanocomposites are shown in Fig. 5-16, and the details of the results are listed in Table 5-5. This test was performed under room temperature and the average value of each type were taken from 5 specimens. For a pure EP composite, the averages of the Young's moduli (E<sub>Y</sub>) and tensile strength (σ<sub>s</sub>) are 2.68 ± 0.37 GPa and 56.5 ± 0.6.5 MPa, respectively. The addition of 5.0 wt. % from silica NPs results in a slightly enhanced elastic modulus and maximal strength of EP composites, reaching 2.75 ± 0.32 GPa and 78.1 ± 6.8 MPa, respectively.

This increase in σ<sub>s</sub> values is due to established strong interactions of hydrogen bonding; one interaction is between the oxygen atoms of the ether group present in the bisphenol A-type EP chain and the surface silanol (Si-OH) of the SiO<sub>2</sub> nanoparticles, and the other interaction is established between the oxygen atoms of the carboxylic or ester groups of methyl nadic anhydride and Si-OH of the SiO<sub>2</sub> nanoparticles.

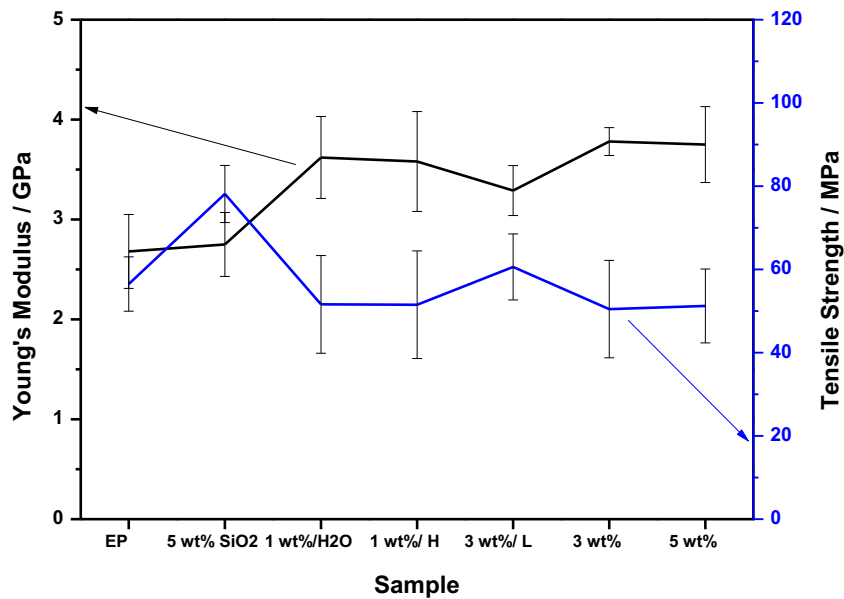


**Figure 5-16.** Plots of the elastic modulus for the pure EP and its nanocomposites at different concentrations of SiO<sub>2</sub> and RGO–SiO<sub>2</sub>.

The nanocomposites prepared at different low-loadings of RGO-SiO<sub>2</sub> (1.0, 3.0 and 5.0 wt. %), have achieved a favourable impact on the the young’s modulus of nanocomposites. Composites filled with RGO–SiO<sub>2</sub> hybrids with different concentrations, and the time employed for mixing (90 mins) and the solvent used, have showed quite different mechanical behaviour. For example, the composites incorporated with 1.0 wt. % RGO–SiO<sub>2</sub> (H<sub>2</sub>O) and RGO–SiO<sub>2</sub> (THF) attained good stiffness, and the enhancement for RGO–SiO<sub>2</sub> dispersed in H<sub>2</sub>O was much greater than that nanocomposite prepared in THF solvent, where the modulus greatly increased to  $3.62 \pm 0.41$  GPa. This result increased to approximately 2% and 35% higher than the composites that were incorporated with RGO–SiO<sub>2</sub> (THF) and neat EP, respectively. Whereas the tensile strength, elongation and toughness were lower by approximately of 23, 13 and 39% respectively. This drop in results could be attributed to accumulate most of SiO<sub>2</sub> nanoparticles on the edges of RGO surfaces that incorporated in the polymer matrix which may lead to the formation of micro-voids as soon as stress is increased.

**Table 5-5. Mechanical properties of EP, EP/GO and its nanocomposites.**

Sample	wt. %	Young's modulus / GPa	UTS / MPa	Elongation at Break / %	Toughness MJ m <sup>-3</sup>
EP	-	2.68 ± 0.37	56.5 ± 6.5	2.49 ± 0.56	87.1 ± 11.3
EP/SiO <sub>2</sub>	5.0	2.75 ± 0.32	78.1 ± 6.8	6.60 ± 2.65	207.0 ± 27.9
EP/RGO–SiO <sub>2</sub>	1.0 /H <sub>2</sub> O	3.62 ± 0.41	51.6 ± 11.7	3.23 ± 0.67	82.7 ± 22.8
EP/RGO–SiO <sub>2</sub>	1.0	3.58 ± 0.53	51.5 ± 12.9	3.45 ± 1.30	80.3 ± 43.3
EP/RGO–SiO <sub>2</sub>	3.0/L time	3.29 ± 0.25	60.6 ± 7.9	5.06 ± 0.99	127.8 ± 37.5
EP/RGO–SiO <sub>2</sub>	3.0	3.78 ± 0.14	50.5 ± 11.7	3.78 ± 0.54	73.2 ± 39.6
EP/RGO–SiO <sub>2</sub>	5.0	3.75 ± 0.38	51.2 ± 8.9	3.89 ± 1.19	93.7 ± 25.2

Moreover, composites containing 3.0 wt. % RGO–SiO<sub>2</sub> dispersed into the EP matrix for a long time of 90 min showed the most optimal E<sub>Y</sub> value among all other nanocomposites, which is an increase of 14.9 and 41% compared to composites filled with the same loading of RGO–SiO<sub>2</sub> at a shorter time of mixing (30 min) and neat EP, respectively. In addition, it has been observed that the tensile strength of EP was not influenced by the addition of RGO–SiO (3 wt. %) after mixing for a long period of time (90 min). At low time of mixing, the EP composite reinforcement by RGO–SiO<sub>2</sub> at a concentration of 3 wt. % showed the maximum value of both elongations at break and toughness by a percentage of 56.2 and 7.6%, respectively. At a shorter-time of shear mixing, the EP composite reinforcement by RGO–SiO<sub>2</sub> at concentration of 3 wt. % showed the optimal values of both elongations at break and toughness by percentages of 25 and 43%, respectively compared to that of 3 wt.% of RGO–SiO<sub>2</sub> after a duration of 90 min. Compared with the neat EP, the inclusion of 5.0 wt. % of RGO–SiO<sub>2</sub> improved the E<sub>Y</sub>, UTS, elongation at break and toughness by 40, 10.4, 56.2 and 7.6%, respectively. Due to the quite lack of the previous studies have concerning in using RGO/SiO<sub>2</sub> composite as a filler in epoxy matrix and measured their mechanical properties, it was compared these results with GO–SiO<sub>2</sub>



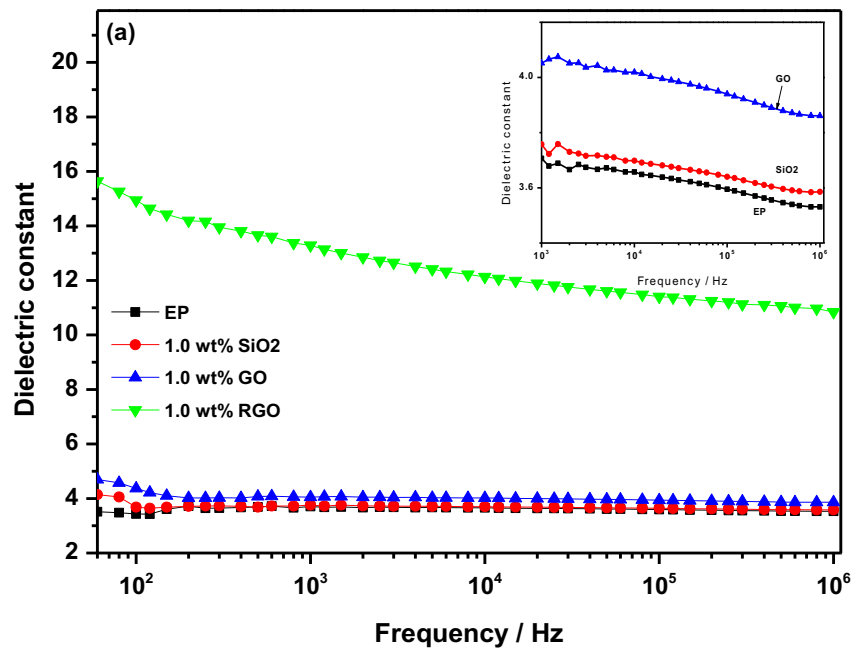
nanocomposites. Chen et al (2012) found that the addition of SiO<sub>2</sub>–GO hybrid leads to an effective enhancement of tensile modulus of EP composites at 5 wt. % loading a factor of 32%. The E<sub>Y</sub> that is obtained here by using RGO covered in the nano-sized SiO<sub>2</sub> particles even at low content is significantly improved than that using GO/SiO<sub>2</sub> composite by about 8%.

The notable increase in the E<sub>Y</sub> values found in this study could be referred to the nanocomposite synthesis route adopted and the existence of SiO<sub>2</sub> as a stabiliser against the aggregation of individual RGO, which results in a good quality of RGO–SiO<sub>2</sub> dispersion and strong interfacial interactions arising between the matrix and fillers.

On the other hand, this approach showed that the Young's modulus of nanocomposites samples at a longer time of mixing are higher than that EP composites reinforced by RGO only. For example, the Young's modulus of nanocomposites was noticeably improved by approximately of 4% compared to that EP system reinforced by RGO-180. Whereas the tensile strength, elongation and toughness were lower by approximately of 23, 13 and 39% respectively. This drop in results could be attributed to accumulate most of SiO<sub>2</sub> nanoparticles on the edges of RGO surfaces which may lead to the formation of micro-voids as soon as stress is increased.

## 5.8 Dielectric characteristics

The capability of dielectric mediums to store electrical energy is due to the polarisation process, whereby an external E-field induces the alignment and separation of electric charges, resulting in an increment in capacitance. The dielectric constant of neat EP and its nanocomposites loaded with different contents of RGO–SiO<sub>2</sub> composite as function of frequency at range ( $10^1$  –  $10^6$  Hz) was studied using Agilent impedance analyser 4184A, and the average result of three specimens of each nanocomposite are shown in Fig. 5-17.



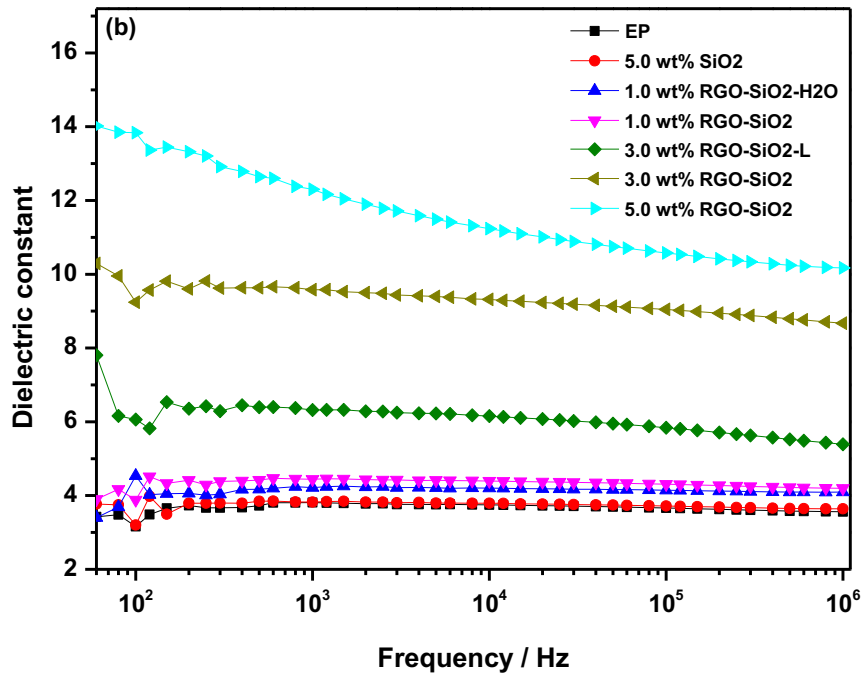


**Figure 5-17.** Dielectric constant ( $\epsilon'$ ): (a)  $\text{SiO}_2$ , GO and RGO /EP nanocomposite; (b) RGO– $\text{SiO}_2$ /EP nanocomposites

A slight increase in the dielectric constant has been achieved for EP resin reinforced by an insulating GO filler (of 13.5% at 1 kHz) when compared to the same content of 1.0 wt. % of  $\text{SiO}_2$  for the  $\text{SiO}_2$ /EP nanocomposite, as shown in Fig. 5-17 (a). However, for RGO nanocomposites, even at a low filling content of 1.0 wt. %, an intrinsic increase in dielectric constant can be detected, which attained 15 at 1 kHz. This great difference can be attributed to the significant low electrical conductivity of GO material.

Fig. 5-17 (b) illustrates the permittivity of neat EP and RGO– $\text{SiO}_2$ /EP composites as a function of the frequency. In the case of using filler 1.0 wt. % RGO– $\text{SiO}_2$ , the dielectric constant of the nanocomposites exhibits good frequency stability. Moreover, the dielectric constant grew significantly, as the weight fraction of nano-filler loading increased. This increase can be attributed to the figuration of an abundance of nano-capacitor structure, polymer matrix as nano-dielectric material and conductive filler as nanoelectrode, experiencing interfacial

polarisation (Arjmand et al. 2012). Huang et al. (2014) reported a significant increase in dielectric constant (77.23 at 2 wt. % content of filler) and a relatively low dielectric loss of RGO–SiO<sub>2</sub>/EP nanocomposites. Moreover, the ascending trend of the dielectric constant with filler loading might be explained by the presence of a great dipole moment of interfacial polarisation together with an abundance of nano-capacitor structures. Additionally, as the content of conductive fillers increases, a conducting pathway would be created from the cluster, which played a crucial role in enhancing the dielectric constant.

The results show that with an increased in the RGO ratio of the polymer matrix, the dielectric constant decreased significantly along with frequency. For instance, the dielectric permittivity of 1.0 wt. % RGO/EP and 5.0 wt. % RGO–SiO<sub>2</sub>/EP nanocomposites were 15.7 and 14.2 at 40 Hz, respectively, which decreased to about 11 and 10 at 1MHz, respectively. This is claimed to be occurring at high frequencies as a result of a large relaxation time of interfacial polarisation regarding the external electric field (Celozzi et al. 2008; Arjmand et al. 2012; Da Silva et al. 2014). In generally, at high frequencies, the electric field is too quick and the free electrons cannot be considered to accumulate near the interface, indicating that the dipole and space charge polarisation phenomena do not obey the alteration in the electrical field direction at high frequency.

As shown in Fig. 5-17 (b), at filler loadings of 1.0 and 3.0 (with 30 min mixing) and a frequency of 1 kHz, the RGO–SiO<sub>2</sub>/EP nanocomposites showed dielectric constants of 4.2 and 4.5, respectively. The dielectric constant for 3.0 wt. % RGO–SiO<sub>2</sub> dispersing in the matrix for a long time reached a high value of 9.7 at 1 KHz, which is about 3 times greater than that of EP ( $\epsilon=3.2$ ). This increase is due to the uniform dispersion of RGO–SiO<sub>2</sub> in the matrix because of the synergistic effect of the shear mixer and ultra-sonication. However, the RGO/EP nanocomposites (Fig. 5-17 (a)) exhibited a significant value of 13.8 at 1 KHz for the dielectric constant because of the higher conductivity of the RGO nano-sheets that supported the

composites with a large quantity of the charge mobility participating in the space charge polarisation for inducing a greater dielectric constant.

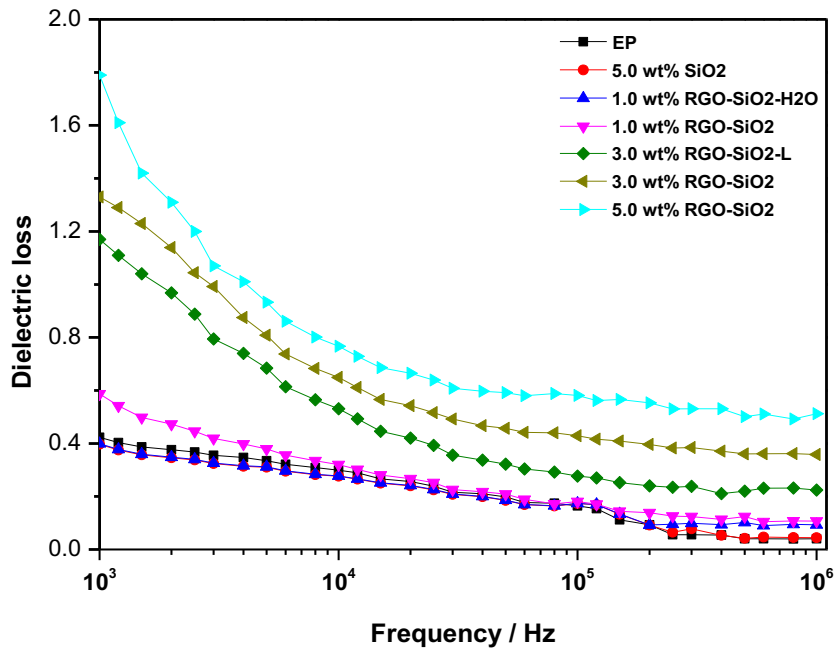


**Figure 5-18.** Dielectric loss ( $\epsilon''$ ) of RGO-SiO<sub>2</sub>/EP nanocomposites

Fig. 5-18 shows the dielectric loss as functions of the frequency of nanocomposite samples. The curves confirmed that the dielectric loss increased somewhat with a rise in filler content. Such slight increases in dielectric loss can be ascribed to the enhancement of polarisation loss and Ohmic loss because of the figuration of a conductive network, thereby dissipating more electrical energy (Da Silva et al. 2014). Meanwhile, the dielectric loss rises beyond the percolation threshold as a consequence of the excellent electrical conductivity of RGO nano-sheets and their ability to establish electrical paths through the host EP matrix (Huang et al. 2014).

The dielectric loss of EP composites inclusion by 1.0 wt. % of RGO-SiO<sub>2</sub> at 1 kHz is 0.6, whilst it recorded 1.2 for 3.0 wt. % at a low time of dispersing (30 min). However, the greatly

increased dielectric constant of the EP nanocomposite incorporated with 3.0 wt. % of RGO–SiO<sub>2</sub> (dispersing in the matrix for a long time of 90 min) shows a large dielectric loss of 1.83. This is certainly a consequence of figuration of the electric conductive network that formed at specific loading of the conductive nano-fillers (0.28 vol. %) and would lead to a great dielectric loss, thereby considerably increasing leakage current (Huang et al. 2014). The lower dielectric loss values,  $\leq 2$  of the nanocomposites, are ascribed to the uniform dispersion of RGO in the matrix (Jung 2008; Da Silva et al. 2014) as well as the oxide layer that covers the surface of RGO nano-sheets, which may avert forming of a conductive network by shrinking the free path of electric charges (Ohmic loss) (Da Silva et al. 2014).

## 5.9 Conclusion

The sol–gel method was employed to obtain the RGO–SiO<sub>2</sub> nano-hybrid with in situ hydrolysis of TEOS on GO nano-sheets. FT-IR, XRD and TGA data exhibit the structural differences between RGO–SiO<sub>2</sub> nano-hybrid and pristine GO, where the former reflected excellent thermal stability up to 900°C to GO sample. In addition, the SEM and TEM measurements proved successful chemical bonding of silica nanoparticles to the RGO surface.

The synergistic effects of the ultrasonication generator and high-shear mixer with mixing times of 20 min and 90 min, respectively, presented better results compared to those with the shorter-time of the high-shear mixer of 30 min, as confirmed by the results of DMA, tensile properties and images of SEM and TEM. A shorter-time of shear mixing led to a deterioration in the integrity of the RGO–SiO<sub>2</sub> nano-hybrids, which negatively affects the performance of the nanocomposites. Despite this deterioration, all the results for nanocomposites demonstrated a real increase in all of the tested properties compared with those seen in polymer reinforced by RGO nano-sheets only.

Presence of silica nanoparticles at the surface of RGO prevents restacking and agglomeration of nano-layers, resulting in high-quality dispersion of RGO throughout the polymeric matrix. The formation of a strong bond between the remaining OCFGs of RGO sheets after the reduction process and polar segments of epoxy chain results in a strong interface enhancing the final properties of the nanocomposites.

The dielectric constant is a function of frequency. As the frequency of alternating current increases, the value of dielectric constant of samples decreases because of polarization mechanisms never again having the ability to pursue the quickly changing field.

The dielectric properties of EP composites reinforced by RGO–SiO<sub>2</sub> after mixing by using ultrasonication and high shear mixer at long and short times showed that the nanocomposites after mixing a long time presented higher dielectric constant and dielectric loss than the same EP nanocomposites at a shorter time of dispersing. This increase in dielectric constant was ascribed to the abundance of a nano-capacitor structure because of the uniform dispersion of intrinsic conductivity of RGO in RGO–SiO<sub>2</sub>/EP nanocomposites, polymer matrix as nano-dielectric and conductive filler as nanoelectrode. Therefore, the uniform dispersion of RGO–SiO<sub>2</sub> nano-hybrids can provide the samples with additional free electric charges that participate in interfacial polarisation. In contrast, the decline of dielectric loss ( $\leq 2.0$ ) in the samples can be attributed to the existence of a silica layer that covered the surface of the RGO nano-sheet, resulting in direct contact between RGO sheets being avoided. Therefore, it can be alleged that the combination of excellent electrical conductivity for RGO as a core material with the existence of silica nanoparticles as an insulating layer on RGO surfaces yielded novel nanocomposites with excellent dielectric properties. Dielectric properties as a function of temperature and time still need to be studied to investigate this behaviour to a greater extent.



## 6 Chapter 6: General Discussion

The compatibility between graphene and organic polymers was not evident; thus, no homogeneous composites were created, which affected its potential use as a mechanical reinforcing agent due to the agglomeration of graphene. In contrast, the partially-oxygenated graphene makes up the RGO that comprises several functional groups, such as epoxy, carboxylic, and the presence of debris that has the ability to significantly change the van der Waals interactions; the organic polymers, as a result, have better compatibility (Wei et al. 2015).

Several routes of dispersing have been used in order to eradicate these issues while saving the original sp<sup>2</sup> structure and improving the dispersion of RGO in a polymer matrix. In this study, high shear mixing and ultrasonication techniques have been used simultaneously to mix the filler suspension with the polymer solution. Upon evaporating the solvent, polymer chains may reassemble, wrapping the nanofillers (Ahmed et al. 2018; Wei et al. 2015).

THF is commonly used as a dispersant for nanoparticles because it is soluble and interacts well with epoxy. In addition, THF evaporates easily due to its relatively low boiling point (66°C). THF was therefore chosen as solvent in the first experiment (system 1) with RGO-1400 sheets although the RGO sheets is less dispersing in THF than water. Therefore, to improve the dispersion of RGO sheets highly in matrix, it was decided to choose a distilled water as solvent instead of THF in the second experiment (system 2).

When the nanocomposites with RGO-120, RGO-160 and RGO-180 were made, it was difficult to remove the water because the RGO particles increased the chances for bumpy boiling during the evaporation in the rotavapor, and the results of the DSC and DMA test showed that the samples didn't appear to give the required improvement of the nanocomposites properties.

Therefore, it was necessary to increase the temperature to remove the water from the system or carry out the evaporation step under vacuum. Therefore, it was decided to keep the temperature as low as possible during evaporation in rotavapor and perform experiment under vacuum. Since the removal of water was an issue, it was decided to modify the curing process by maintaining the temperature at 80 to 120°C for 1 h, then increasing to 150°C and keeping it constant for 30 min, and then at 180°C for 3 h, followed by post curing at 200°C for 30 min) to obtain completely curing. This resulted in improving the thermal and mechanical properties. However, to date, a relatively limited number of studies have attempted to characterise and evaluate the thermal and electrical conductance and mechanical performance of EP composite incorporated with low-level contents of RGO nano-sheets and good dispersion. The novelty of this study was to synthesise relatively straightforward methods for preparation of RGO at low temperatures via the vacuum-oven method and high temperature by using tube furnace technique.

In this thesis, RGO nanosheets were successfully produced by relatively straightforward methods. These efficient methods utilised in this study were more ecologically friendly ways of producing RGO in contrast to any other approaches that require tedious chemical reactions and involve use of toxic solvents, hence high toxicity. In addition, RGO was synthesised via a tube furnace starting by GO material rather than graphite oxide that was used in previous studies to avoid a large number of defects were generated because of in-plane C=C cracking as a result of build-up of a large pressure between graphite oxide layers from CO and other gases and as a result can reduce suffering of sp<sup>2</sup> structure. This hypothesis was confirmed by Raman spectroscopy, where the intensity ratio  $I_D/I_G$  of RGO sample was decreased from 1.75 as reported in a previously reported study (Kurniasari et al. 2017) to 0.94 in our study. It is envisaged that this lower  $I_D/I_G$  ratio may be due to the sp<sup>2</sup> domains that are newly formed during reduction and are larger than those of RGO in previously reported studies. In addition,

$I_D/I_G$  ratio in RGO is higher than that of graphite because the  $sp^2$  domains which are newly formed during reduction and are smaller than those of graphite ( $I_D/I_G \sim 0.04$ ). Another possible reason is the increased fraction of RGO edges, which could also contribute to the increase in the  $I_D/I_G$  ratio (Fathy et al. 2016).

Although reaction times under vacuum are longer than those under thermal treatment at high temperature, this technique is still simpler and straightforward than the other methods reported in previous studies. At lower temperatures of 120°C, 160°C and 180°C, a vacuum-assisted method for thermal exfoliation and large quantity reduction of GO was reported. Just a few layered sheets with an average thickness of 0.62, 0.49 and 0.46 nm of RGO sheets were obtained, and their lateral size  $< 2 \mu\text{m}$  is comparable to that of conventional RGO generated at 1400°C at atmospheric pressure  $> 2 \mu\text{m}$ . The increased C/O atomic ratio in comparison to that of GO confirmed the thermal reduction occurring during the exfoliation process.

In order to probe the chemical structure, the XPS was used to analyse raw graphite, GO, and the series of RGO samples; the full-scan spectra, higher resolution C1s spectra, atomic percentage of oxygen, and fraction percentage of each oxygen functionality are studied. Initially, pristine graphite contains a small amount of oxygen, 1.61% (from the atmosphere or trapped in the Earth's crust) which yields a high carbon to oxygen (C/O) ratio of 61.2. After oxidation, a well-defined double peak with a small tail towards higher binding energy was found in the high resolution C1s spectrum, which is a signature of a considerable degree of oxidation. It is also demonstrated by a significant increase in oxygen contents to 30%. It is noted that the C peak in sample GO showed a clear shift towards higher binding energy, reflecting significant surface charging caused by the electrically insulating oxygen functional groups. Reduction at 120°C (fig. 3-12), the double peak is present but there is a small decrease in the oxygen-related peak. The fraction of the epoxide/hydroxyl groups drops from 43% to

approximately 25%. Based on the XRD analysis, the intensity of the GO peak is greatly reduced and a small broad peak corresponding to RGO-120 appears indicating that the GO has been partially reduced and converted to RGO. This suggests that the reduction of GO took place at a low temperature due to the removal of thermally unstable epoxy groups (Mungse et al. 2014). Upon 160°C, the fractional percentage of C-O/C-OH bonds was further reduced but not fully eliminated. According to the density functional theory calculations reported by Kim et al. (2009) and Gao et al. (2010), the hydroxyl group attached to the edge of the sheets and the lattice vacancies is more stable, which is evident by the peak attributed to C-O/C-OH groups still can be seen.

Upon further thermal reduction, several changes were observed. The intensity of the C1s gradually increases while the intensity of the O1s spectral peak drops with increasing reduction temperature, as shown in fig. 3-12(E) and fig. 3-6 (B). It is noted that the C-C bond is stable during the treatment, whereas the C bonded to oxygen-carrying functionalities decreases which results in an increase in the C-C (sp<sup>2</sup> and sp<sup>3</sup>) component contents. The oxygen content reaches the lowest value of 14 and 12.8% for sample RGO-180 and RGO-1400, respectively; at this point, the C-O/C-OH fractional content also decreases to its minimum value. This suggests that the C-OH bond is the major residual oxygen functional group which is the key metric to determine the level of reduction. Additionally, when the C-OH and C-O groups are removed, they break/cut off the RGO sheets into small pieces; consequently, the sheets will agglomerate to reduce the surface energy and re-stacking could occur. Ma et al. (2012) have reported similar observations: the large sheets (>2 μm) are almost absent after thermal treatment and that the size of the RGO is dependent on the thermal treatment temperature. It is worth noting that only C and O spectral peaks were observed in the spectra for all the samples, indicating that no other undesired compounds were formed due to the use of water as a reductant.

Raman spectroscopy offers further insights to the structural changes in RGO (fig. 3-9). The main features of the GO and its derivatives have D, G, and 2D peaks. The G peak at around 1580 -1600  $\text{cm}^{-1}$  is due to the bond stretching of  $\text{sp}^2$  carbons in rings and chains, while the D peak at approximately 1330-1380  $\text{cm}^{-1}$  originates from the breathing modes of the six-membered rings that are activated by defects (Lucchese et al. 2010). The change in the intensity ratio of D and G bands ( $I_D/I_G$ ) with temperature-dependent GO reduction is plotted in the inset of fig. 3-9. It shows a slight yet gradual increment of the  $I_D/I_G$  ratio with the increase in reduction temperature. In the early stage of reduction, the  $I_D/I_G$  ratio slightly increases which refers to the increase in edge of the sheets when  $\text{sp}^2$  domains are torn apart by the removal of the oxygen functionalities (Tuinstra & Koenig 1970). With further reduction, deoxygenation continues as demonstrated in XPS results, which might remove some of the carbons from the graphitic structure and leave pores and defects. Hence, it results in a deteriorated structure, giving an increase in the  $I_D/I_G$  ratio. However, one should be noted that a solid conclusion is tough to make in the interpretation of Raman spectra for GO and its derivatives. This is due to the manifold defects within the carbon lattice which makes almost no change in the Raman spectra as compared to the pristine graphene or single-layer or few-layer GO and RGO (Dimiey & Eigler 2016). The Raman spectra of all the samples are shown in the Figure 3-9.

The structural change in the GO flakes was first revealed by XRD analysis, as shown in Fig. 3-10. In raw graphite, an intense crystalline peak was found at  $2\theta = 26^\circ$  (lattice spacing of 0.35 nm), which corresponds to the (002) diffraction peak of graphite (Trucano et al. 1975). After oxidation, the peak shifts to a lower angle at  $2\theta = 11.6^\circ$  with a lattice spacing of 0.78 nm, indicating the success in oxidation. As reported earlier, an increase in interlayer spacing is mainly attributed to the intercalation with water and the presence of oxygen functionalities such as epoxide and hydroxyl groups which populate on the basal plane of the carbon sheet (Lerf et al. 1998; Krihnamoorthy et al. 2013). Notably, the sharp and distinct peak is attributed

to the preserved and ordered stacking along the c-axis. Upon thermal treatment at 120°C, the intensity of the distinct peak in GO reduces and the peak becomes broader due to the partial breakdown of the long-range order of the GO. Moreover, the peak position has significantly shifted towards a higher angle ( $2\theta = 14.2^\circ$ ) showing the decrease in the lattice spacing (0.62 nm). Meanwhile, a relatively weak and broad shoulder was observed at  $2\theta = 22.8^\circ$ , yielding an interlayer separation of 0.4 nm. This indicates that the reduction has taken place at 120°C. Upon a 160, 80 and 1400°C thermal reduction, the broad and diffuse peak becomes dominant. Disappear of GO peak can be denoting of the complete of GO reduction.

The surface morphology for RGO sheets that have produced from both techniques were analysed by TEM and AFM. A monolayer or a few-layer RGO could be achieved after dispersing (0.02 mg/ml) in deionized water, in which the thickness of a single layer was measured to be 0.73 nm, as observed by AFM (fig 3-2). Before testing, RGO samples were dispersed onto ethanol (0.1 mg/ml) by ultrasonication, and then deposited onto a Formvar carbon-coated copper mesh grids. TEM image of RGO-180 sample indicates the coexistence of GO (layered structure) and RGO (disordered structure). Meanwhile, the number of layers reduces to less than 6 (Fig. 3-7) showing the breakdown of the long-range-order stacking, which is consistent with XRD observation. In contrast, RGO-1400 sample show many wrinkles. The possible explanation is; when GO sheets are reduced, they become regionally hydrophobic due to the removal of the oxygen functionalities, as confirmed by XRD and XPS results. After dropping onto the substrate, the locally hydrophobic RGO sheets will tend to aggregate to reduce the free energy, leading to the formation of wrinkled and folded morphology. Moreover, the edge-to-edge attraction interactions due to the hydrogen bonding between the remaining oxygen functionality might result in the aggregation of RGO sheets. The SEM image of Fig. 3-3 (A) shows layered sheets of RGO randomly aggregated with wrinkled and folded surfaces. However, the TEM image of the RGO sheets (Fig. 3-3 (a)) shows

a number of thin layers of sheets stacked together, and the average length is found to be  $>2 \mu\text{m}$ , while it is  $< 2 \mu\text{m}$  of RGO-180. Kee et al. (2017) measured the length of RGO sheet using TEM where the average length reached about  $738.5 \pm 141.1 \text{ nm}$ . TEM images of GO and RGO, consistent with AFM images, indicate that the sheets exhibit homogeneity with an average lateral size of  $1.348 \pm 0.6 \mu\text{m}$  after scan in three random place on the surface of nanomaterials. Moreover, the TEM images of RGO and GO sheets show they are transparent compared with graphite with a lamellar structure.

The GO sample showed significant weight loss with an onset temperature at slightly  $>100^\circ\text{C}$ , which was attributed to the elimination of inter-lamellar water, followed by loss of oxygen from the GO sheets themselves at slightly higher temperatures. RGO at  $120^\circ\text{C}$  showed much higher thermal stability because of the more complete de-oxygenation and better graphitization with enhanced van der Waals forces between layers. With increasing the temperature of reduction ( $160, 180$  and  $1400^\circ\text{C}$ ), the TGA results showed increase in thermal stabilities.

A thermal reduction process of GO has been extensively studied by employing XPS, XRD, Raman, FT-IR, SEM and TEM at different temperatures. Four temperature zones,  $120^\circ\text{C}$ ,  $160^\circ\text{C}$ ,  $180^\circ\text{C}$  and  $1400^\circ\text{C}$  were used for the thermal reduction process. Partial exfoliation of crystals was observed inside a temperature range of  $120^\circ\text{C}$ , because of the drastic vaporization of intercalated  $\text{H}_2\text{O}$  molecules. Contraction of the interlayers for RGO is seen while the main carboxyl groups are removed within the temperature range of  $160^\circ\text{C}$ . A lattice relaxation of RGO occurs because of out-gassing produced as a result of the residual carboxyl and partial hydroxyl groups, within the temperature range of  $180^\circ\text{C}$ . Because of in-plane  $\text{C}=\text{C}$  cracking, many defects are generated while the residual hydroxyl and partial epoxide groups are removed, within the range of  $1400^\circ\text{C}$ . However, the degree of reduction at  $180^\circ\text{C}$  was found to be slightly lower than that produced in a tube furnace at  $1400^\circ\text{C}$  by nearly 9%, and it is

subsequently higher than the C/O ratio of GO material by about 53%. In addition, the reduction of GO is not mostly concerned with the elimination of all oxygenated-functional groups; rather, it is directly associated with the electrical conductivity (semiconducting, to be precise) and effective graphitization (Raman suggest that more  $sp^2$  domains are formed during the reduction of GO). Some products can recover their higher electrical conductivity more than the original graphene by determining the time and the optimal temperature of reduction.

The damaged and porous RGO samples provide the sites for polymerization or metal oxide decoration/doping. The results reveal that GO flakes remain in the early stage of the reduction process and that they are fully reduced after 160°C thermal treatment. With an increase in the reduction temperature, the resulting product, i.e., RGO-180 and RGO-1400, has a low oxygen content, small interlayer spacing, and crumbled and wrinkled structures. Its structure can be designed or tuned by controlling or modifying the parameters in the thermal reduction process to satisfy the requirements for various applications.

The electrical conductivity of RGO obtained via the vacuum method (at 180°C) is the highest ( $293 \pm 4.0 \text{ S cm}^{-1}$ ), and the results of XPS experiments indicate that substantial de-oxygenation, principally the removal of carbonyl species, which can help to improve the electrical conductivity. In addition, this electrical conductivity of RGO obtained via the vacuum method is higher than that of RGO obtained via a tube furnace by 32%, which indicates a restoration of  $sp^2$  structure.

Mechanical performance of the RGO/EP based nanocomposites prepared by solution mixing method was summarized in Tables (4-4 and 4-9). It is well known that a small amount of uniformly dispersed RGO based materials will increase polymer mechanical properties significantly. In the case of RGO obtained at high temperature (1400°C) and prepared their EP nanocomposites using a THF solvent (system 1), fig. (4-7(a) & (b)) showed that the tensile



properties were increased greatly with the addition of RGO. Higher loadings of RGO displayed increased tensile stiffness when compared to neat EP sample. Ultimate tensile strength showed maximum improvement about ~31% in composite with 0.5 wt. % of RGO. As expected, RGO was more efficient in reinforcing epoxy than GO: the efficiency of RGO in improving the modulus and strength was about 10-23% higher than that of GO. The remarkable results for RGO composites demonstrate the effectiveness of interfacial adhesion between the epoxy molecules and the RGO sheets. In particular, the drastic increase in strength can be attributed to the excellent load bearing capacity of well-dispersed RGO sheets, as well as the excellent load transfer from the matrix to the reinforcements.

In the case of RGO obtained by vacuum oven at low temperatures (at 120, 160 and 180°C), and prepared their EP nanocomposites at different curing cycle and using water as solvent (system 2), the tensile properties of EP nanocomposites increased with the increasing temperatures of reduction process, fig. (4-17(a) &(b)). For example, RGO-160 displayed increased Young's modulus and tensile strength by ~13 % and ~12%, respectively, when compared with RGO-120, and about ~32% and ~21.5%, respectively, when compared with EP composite sample ( $2.66 \pm 0.39$  GPa and  $51.2 \pm 5.4$  MPa). The noteworthy increase in Young's modulus values achieved over the current study could be reflected by the nanocomposite synthesis approach selected, which plays an important role in obtaining better dispersion for RGO material with strong interfacial interactions between the individual RGO nano-sheets and EP matrix. However, the Young's modulus of the RGO-180 sample showed a maximal value of  $3.78 \pm 0.19$  GPa. Similarly, an increase in the elongation at break was found from  $2.71 \pm 0.3\%$  MPa for the EP to  $4.62 \pm 0.3\%$  MPa for RGO-180. This increase can be associated with the high degree of reduction for RGO material that is obtained via the vacuum reduction process, thereby enabling the material to partially restore their properties (i.e., stiffness).

DMA provided information on storage modulus of RGO/EP nanocomposites that obtained from two different systems, which showed a trend of decreasing with the increase of test temperature due to the softening of polymer chains at high temperature. In addition, the storage modulus of RGO (0.5 wt.%) obtained by the help of the tube furnace method increased by ~26.5% up to the value of  $2.86 \pm 0.3\%$  GPa compared to neat EP sample (2.1 GPa). In the glassy region, the polymer chains and segments were “frozen”, and addition of RGO sheets into epoxy resin increased the storage modulus over the whole temperature range, this may due to RGO reinforcement and the better interfacial interactions between RGO and the matrix due to the improvement of the interfacial compatibility between the sheets and the EP matrix. Therefore, it can be concluded that RGO could enhance mechanical properties of EP/RGO composites, which improved dispersion and exfoliation properties of the nanosheets as well as strong interfacial bonding were beneficial for enhancing the load transfer from the matrix to the RGO sheets, significantly increasing the mechanical properties.

In the other system, the addition of 0.5 wt. % RGO obtained by the help of the vacuum-assisted method (at 120, 160 and 180°C) enhanced the storage modulus by about 8.8%, 17.8% and 28.4%, respectively, compared with the values of the neat EP composite. This significant increase in the storage modulus is related to the introduced strong interfacial interactions and the better dispersion, as revealed by SEM and TEM imaging.

The thermal stability of cured EP composites based on the temperatures of reduction process and the different content of RGO was analysed using loss factor (tan delta) and TGA for both systems. The glass transition temperature ( $T_g$ ) was recorded based on a maximum peak of loss factor curve. As shown in figure 4-6, the  $T_g$  value as-obtained from tan delta of the composites showed a clearly increase trend from 148°C (neat EP) to 158°C (~6.7%) with increase of RGO (0.5 wt.%). Other system that produced RGO sheets at low temperatures and different curing

schedule, showed slight improvement of  $T_g$  values for EP/ RGO composites reinforced by RGO-120, RGO-160 and RGO-180 by about 3%, 5% and 9%, respectively, compared to that of pure EP (133°C) (Fig. 4-16). The reason of increased  $T_g$  values was speculated that wrinkled morphology of RGO sheets with high specific surface constrain the segmental movement of polymer chains to a certain degree.

The decomposition temperature  $T_d$  value of RGO/EP composites showed an increased trend with the increase of RGO content, and 1.0 wt.% of RGO resulted in a significant increase of ~18°C compared to blank EP sample (fig. 4-3). In addition, the  $T_{50\%}$  (50% weight loss) of RGO/EP composites also showed an increased trend with the increase of RGO content, and 1.0 wt.% of RGO sheets resulted in a significant increase of 10°C, while the incensement of  $T_{50\%}$  for the GO loading did not appreciably affect the  $T_d$  value of epoxy composites. On the other system, in fig. 4-14, the decomposition temperature  $T_d$  value of RGO/EP composites showed an increased trend with the higher of temperatures of reduction process and fixed the RGO loading at 0.5 wt.%. The  $T_{5\%}$  of RGO-160 and RGO-180 samples showed significant increase of 21°C and ~23°C, respectively. In addition, the  $T_{50\%}$  (50% weight loss) of RGO/EP nanocomposites also showed an increased trend with the increase of temperature of reduction, and RGO-120, RGO-160 and RGO-180 samples resulted in significant increase of 7°C, 12°C and 14°C, respectively, while the incensement of  $T_{50\%}$  for the GO loading did not appreciably affect the  $T_d$  value of EP composites. The enhanced thermal stability of RGO/EP composites of both systems were mainly attributed to a better barrier effect of RGO which retarded the volatilization of polymer decomposition products due to a better dispersibility and interface between RGO and epoxy matrix (Visakh & Nazarenko 2015). Based on the above analysis, the mechanical and thermal properties of epoxy composites including tensile strength, young's modulus, storage modulus,  $T_g$ , decomposition temperature ( $T_d$ ) and TGA curves of various RGO/EP nanocomposite systems were studied. It can be concluded that the RGO/EP

nanocomposite with good balance among the outstanding mechanical and thermal properties at a low content of sheets ( $\leq 0.5$  wt. %) and thermal reduction process that not effect on the RGO structure, indicating the RGO sheets could improve the related performance of EP composites.

The mechanical and physical properties of nanocomposites depend on the dispersion of filler agent into the matrix. Here, the dispersion of RGO in EP was analysed using SEM. Samples for the SEM analysis were obtained by breaking the composites at the middles place inside the liquid nitrogen to obtain a clean fracture surface (system 1). Typical cross-sectional view SEM images of EP composites with different RGO loadings are shown in Fig. 4-1(a-e). All EP composites were prepared by a simple solution-casting procedure. It can be seen that EP composite sample showed a relatively homogeneous morphology in Fig. 4-1(a). Whereas, the fractured surfaces of the RGO/EP composites were rougher compared with that of neat EP sample. The RGO sheets of various loadings (0.1, 0.5 and 1.0 wt.%) were homogenously dispersed and embedded in EP matrix, as shown in Fig. 4-1(c-e), suggesting good compatibility between the RGO and polymer matrix. With the increase of RGO sheets, the surface became rougher and bumpier and more dimples appeared, showing the improved toughness of the material, which might result in improving tensile properties and bending properties (Liu et al. 2012).

On the other system, fig. 4-13, the neat EP is a homogeneous polymer as it was expected, see fig. 4-13(a). Note that the white lines in Fig. 4-13(a) are river lines caused by the brittle fracture of the polymer (Hull 1999), and for the purposes of considering the dispersion of the RGO, such features associated with fracture can be disregarded in Fig. 4-13. The images shown in Fig. 4-13 (b, c, d) indicate a good dispersion of RGO in the EP for the nanocomposites containing 0.5 wt.% of RGO, and significant agglomeration could not be detected even at high

magnifications. Obviously, the fractured surfaces of the RGO/EP composites were rougher compared with that of neat EP sample. With the increase of temperatures for reduction process, the surface became rougher and indicated the improved toughness of the material, which might result in improving tensile properties and bending properties (Liu et al. 2012).

The RGO layers in EP can be identified via colour contrast caused by using the polarized light (Salom et al. 2018). It is an accurate and reliable technique to evaluate the RGO dispersion and distribution in polymer matrix. Fig. 4-13 shows SEM images of EP composite and its EP/RGO nanocomposites (RGO-120, RGO-160 and RGO-180) at different magnification powers. The white spots and streaks are the RGO sheets in matrix. In all cases, the RGO can be seen to be dispersed all over the surface. However, the RGO sheets is reasonably well dispersed in RGO-160 and RGO-180 samples better than RGO-120 sample. The wrinkled surface morphology of the RGO sheets is shown in Fig. 4-13(d). According to Shen et al. (2013), it is this morphology which plays an important role in enhancing mechanical interlocking and transferring load from the EP matrix to RGO sheets.

According to the above mechanical and thermal properties of RGO/EP nanocomposites containing different content of 0.5 wt.% RGO sheets, it was further compared to the data of tensile strength, and  $T_g$  of various commercial DGEBA systems and the relative increments after embedding of RGO sheets into epoxy resin. In order to obtain the related values, the selected epoxy systems have the RGO content of 0.5 wt.%. The tensile strength and thermal properties were relatively lower compared with commercial epoxy systems, the increments of properties were much higher than those of commercial epoxy systems, indicating that RGO obtained by vacuum oven was much more effective than other RGO in enhancing mechanical and thermal properties of EP systems (see table 6-1). Furthermore, the mechanical and thermal properties of epoxy composites were closely related to the dispersibility, aspect ratio of GO

nanosheets, and testing conditions, etc. The RGO/EP systems had the comparable mechanical and thermal properties with that of commercial epoxy composites in previous studies, as summarized in Table 6-1.

**Table 6-1.** Comparison of increments in the modulus, tensile strength and  $T_g$ , among various commercial DGEBA composites containing 0.5 wt.% RGO nanosheets.

Ref.	Young's modulus/% (Matrix)	Tensile strength/% (Matrix)	$T_g/^\circ\text{C}$ (Matrix)
Sharmila et al. (2014)	8 (2.65)	56 (7.2)	6.5 (62.0)
Tang et al. (2013)	7.5 (2.93)	6 (52)	11(143)
T.K et al. (2014)	16 (2.40)	10.9 (48)	- 5 (103)
Current study	42 (2.66)	32 (51.2)	9 (133)

The elastic modulus was measured from a 16-cycle indentation test at 10 mN with a resolution of 50 nN for EP/RGO nanocomposites, fig. 4-9. Indeed, with addition of RGO sheets, there is an increase in the stiffness, and, subsequently, a decrease in displacement for a force of 10 mN. In comparison to neat epoxy, the modulus increases for 0.1, 0.5 and 1.0 wt.% EP/RGO nanocomposites by 17%, 28% and 31%, respectively. When the indenter (Berkovich probe) encounters a polymer–matrix–rich area or an RGO–rich area on the specimen, an error can be introduced into the data via this test approach. Therefore, as the RGO concentration increases, the error bars become larger because a larger concentration of RGO exists in the specimen. Many recent studies have revealed for polymers and polymer nanocomposites that the moduli as determined by the nanoindentation technique, are greater than those reported by universal tensile machines tests. These ratios of the moduli measured to those reported by universal tensile machine tests are 1.64 for polycarbonate (PC), 1.70 for polystyrene (PS) (Tranchida et al. 2007) and 1.33 for epoxy (EP) (King et al. 2014), while this ratio reached ~ 1.4 in the current study. This ratio is possibly attributed to the indentation pile-up plastic phenomenon of material around the contact area and the viscoelasticity of the polymer–based–nanocomposites that is not clarified by the modulus determined by the Oliver–Pharr method (Tranchida et al. 2006;

Tranchida et al. 2007). However, the unexpected high value found for the elastic moduli can be interpreted noticing that a pile-up has occurred in the nanoindentation testing. Therefore, this value is greater than that measured through tensile tests.

As discussed in chapter 4, the electrical conductivities as a function of RGO content with an average values of three specimens test are given in Fig. 4-11. GO/EP composites suffer from a very low electrical conductivity regardless of GO content due to the insulating nature of GO; however, upon reduction to RGO, the electrical conductivity was remarkably restored. Due to the uniform dispersion of monolayer RGO sheets in the EP matrix, the electrical conductivity jumped by almost five orders of magnitude when 0.1 wt.% RGO was added. A further increase in RGO content beyond 1.0 wt.% resulted in a rather saturated conductivity with a remarkable value above  $10^{-7} \text{ S m}^{-1}$  (an average value of three specimen) that is high enough for many practical applications including electrostatic discharge protection and thermal conductors. In the previous studies of EP/RGO nanocomposites, (Hsiao et al. 2013; Liang et al. 2009), reported an increased in dc conductivities at low loading (1.0 wt.%) by 6 and 3 orders of magnitude, respectively. This data can be ascribed to the effective restoring of the electrical properties of RGO via the rapid thermal reduction process besides the high quality of dispersion in the matrix. In addition, with the average value of three specimens test, these EP composites filling by (0.1, 0.5 and 1.0) of RGO have shown relatively high thermal conductivities compared with the reported value of  $0.24 \text{ W m}^{-1} \text{ K}^{-1}$  of EP-1.0 RGO nanocomposite (Olowojoba et al. 2016), which is higher than the value measured of  $0.21 \text{ W m}^{-1} \text{ K}^{-1}$  for the EP-1.0 RGO nanocomposite by Chandrasekaran et al. (2013). The thermal behaviour of these nanocomposites (Fig. 4-10) shown an increase of up to 85% at low-loading content with the change in temperature, and the maximum value reached was  $0.36 \text{ W m}^{-1} \text{ K}^{-1}$  at 1.0 wt.% of RGO at temperature ( $\sim 100^\circ\text{C}$ ).

As discussed in Chapter 5, the sol–gel method was employed to obtain the RGO–SiO<sub>2</sub> nano-hybrid with in situ hydrolysis of TEOS on GO nano-sheets. FT-IR, XRD and TGA data exhibit the structural differences between RGO–SiO<sub>2</sub> nano-hybrid and pristine RGO, where the former reflected excellent thermal stability up to 900°C to the RGO sample. In addition, the FTIR, SEM and TEM measurements proved successful of chemical bonding of silica nanoparticles to the RGO surface. After the reaction of GO nano-sheets with TEOS via the sol–gel process and the forming of the RGO–SiO<sub>2</sub> nano-hybrid, the characteristic bands relating to the silica were clearly identified, indicating that the silica intensively formed on the surface of the RGO (fig.5-5). Compared with the RGO, RGO–SiO<sub>2</sub> nano-hybrid composites show two major peaks observed at 1067–1074 cm<sup>-1</sup> and 796–801 cm<sup>-1</sup>. These peaks can be ascribed to the (Si–O–C/Si–O–Si) asymmetric stretching and bending vibration, respectively. Moreover, the intense bands at 1721 cm<sup>-1</sup> (C=O) disappeared but appeared at 1071 cm<sup>-1</sup> after the reaction with TEOS. This evidence strongly supports the idea that the carbonyl groups, C=O were converted to Si–O–C bands and strengthened the interconnection between the RGO nano-sheets and SiO<sub>2</sub> nanoparticles.

XRD was used to study the effect of the SiO<sub>2</sub> nanoparticles on phase structure for the RGO surface in RGO–SiO<sub>2</sub> composite, as shown in Fig. 5-6. With regards to the RGO–SiO<sub>2</sub> sample, the broad peak that was observed between the SiO<sub>2</sub> and RGO was shown for the RGO–SiO<sub>2</sub> nano-hybrid, indicating that the nano-hybrid consisted of SiO<sub>2</sub> nanoparticles and RGO nano-sheets. Furthermore, this very broad peak might be attributed to the formation of a silica layer on both sides of the RGO sheet, which prevents the re-stacking of the RGO (Hsiao et al. 2013). The d-spacing of nano-hybrid was calculated at 0.4 nm based on a Bragg's law calculation (Layek et al. 2014), which is a reduction of 52% compared to GO. This reduction is also because of the introduction of nano-silica particles on the RGO structure, which could have an advantageous effect on the dispersion behaviour (Ma et al. 2016).



XPS of RGO–SiO<sub>2</sub> sample shows the curve-fitting of the O1s and Si2p peaks at 531.5, 533.6 and 105.7 eV (fig. 5-8), which are demonstrative of the construction of a SiO<sub>2</sub> network, and that the prominent peaks at 531.5 and 104.4 eV (assigned to the Si–O–C bond) were proof of a significant formation of covalent bonding between the RGO and SiO<sub>2</sub>, agreeing with the FTIR results. Liu et al. (2017) reported similar peaks to those in this current study when they fabricated a sandwich structure of RGO (0.5 wt. %) coated with mesoporous SiO<sub>2</sub> by using an autoclave at 180°C, for 12 h, and they claim that domains were highly increased for the graphene, thereby achieving lower defect levels for the RGO.

The TGA analysis of RGO–SiO<sub>2</sub> composite sample showed a large reduction in mass loss with an increase of 15 wt. % over than that achieved by the RGO sample (fig.5-10). The curve remained steady up to 800°C, indicating more overall thermal stability than the RGO sample (Huang et al. 2017). An introduction of SiO<sub>2</sub> nanoparticles onto the surfaces of RGO sheets resulted in slow decomposition rates with somewhat excess onset of mass loss related to the thermal-oxidative pyrolysis of carbonates. Thus, the composite tended to be more stable with inserting SiO<sub>2</sub> in the nano-hybrids. This result suggests that the formed SiO<sub>2</sub> nanoparticles on the surface of RGO can serve as a protective thin-layer that averts further thermal degradation of the carbon material (Hsiao et al. 2013). However, the addition of RGO–SiO<sub>2</sub> into the EP matrix delays the onset temperature of decomposition, suggesting an increase in thermal stability. The researchers ascribed this increase to the existence of the SiO<sub>2</sub> layer that acts as a protective layer, preventing the polymer degradation. Additionally, the 2D structure for the RGO filler works to hinder oxygen diffusion within the nanocomposites and obstructs diffusion of volatiles materials. A comparable result has been reported by (Hsiao et al. 2013). Fig. 5-13 shows that the thermal stability is significantly influenced by the degree of dispersion and the RGO concentration in system. For instance, the addition of 5.0 wt. % RGO–SiO<sub>2</sub> nano- hybrids

into the matrix did not profoundly affect the thermal stability of the EP composite. This lack of change can be observed from the simple difference of residue of these samples at a temperature range between 650 and 700°C and the  $T_d$  value which does not exceed 3°C higher than pure EP (458.4°C). However, the addition of a decreased amount of content filler (i.e. 3.0 wt. % RGO–SiO<sub>2</sub> at long shear mixing time) led to the highest increase in decomposition temperature ( $T_d \sim 463^\circ\text{C}$ ) as well as the highest amount of residue ( $\sim 20.6$  wt. %) of the nanocomposites at a temperature range of 650–700°C. When the shear mixer was used for a decreased amount of time for the 3.0 wt. % RGO–SiO<sub>2</sub> sample in the current study, the non-uniform dispersion of RGO–SiO<sub>2</sub> decreased the properties of the nanocomposite, and as a result, the sample exhibited a higher decomposition rate under heating of N<sub>2</sub> compared to the same samples after prolonged use of the shear mixer.

AFM study of the RGO/SiO<sub>2</sub> hybrid (Fig. 5-4) clearly exhibited the formation of a uniform covering of the silica layer on the planes and edges of the RGO surface with many protuberances (approximately 30 nm), as opposed to the smooth uncovered pristine RGO, as illustrated in Fig. 5-4, which agrees with the SEM and TEM images. However, it was also observed that there was an accumulation of silica nanoparticles on the edges of the RGO surface. This is a result of the concentration of most of the OCFGs on the edges of the GO sheets on both sides. SEM and TEM studies were utilized to examine the morphologies of RGO-based silica nanoparticles. To compare with GO and RGO sheet, the SEM and TEM images of RGO/silica nanoparticles (shown in Fig. 5-2 and Fig. 5-3) reveal that the as-formed SiO<sub>2</sub> nanoparticles were homogeneously and uniformly deposited on the surface of the RGO nanosheets. However, Inserting the RGO/SiO<sub>2</sub> hybrid into the EP matrix led to completely different morphologies of the fracture surfaces. The presence of a silica layer on the RGO structure to the roughness of the surface resulted in a river structure shape and bowl-like domes to be formed, which are shown in the magnified images in Fig. 5-11(C). The fracture surfaces

were also found to be rougher when the fillers were of two-dimensional morphology, and the wrinkles were clearly notable, as shown in Fig. 5-11(c and f). Moreover, the RGO–SiO<sub>2</sub> and SiO<sub>2</sub> nanoparticle samples showed a good uniform distribution within EP polymer, reflecting good compatibility between the filler from one side and the matrix from the other side, as shown in Fig. 5-11(f). The existence of a silica layer in the system helped to overcome the strong  $\pi$ – $\pi$  interactions that occur among the individual RGO nano-sheets and improve the chemical bonding between RGO nano-sheets and EP polymer.

From DMA analysis, fig. 5-15(a) showed the storage modulus of EP at 30°C is 2.31 GPa, whereas the modulus of the nanocomposite containing (5.0 wt. %) SiO<sub>2</sub> nanoparticles had increased to 2.75 GPa. With the incorporation of RGO–SiO<sub>2</sub> nano-hybrids into the matrix in the presence of THF for 1.0, 3.0 (at low/high mixing), and 5.0 wt. %, the nanocomposite samples showed increased in storage moduli of 3.13, 3.28, 3.47 and 3.70 GPa, respectively. This increase can be ascribed to the compatible interactions between the fillers and matrix, suggesting uniform dispersion of filler in the matrix resulting in a high degree of cross linking. However, DMA shows that the plots of the  $T_g$  values increased significantly at a low content (1.0 wt. %) of RGO–SiO<sub>2</sub> nanocomposites, reaching 155°C (Fig. 5-15 (b)). The likely cause for this increase is that the EP adsorbed on the filler surface increased the cross-linking density, therefore leading to stronger covalent bonds between each other. However, as the loading of filler was increased by 3.0 (low/high mixing) and 5.0 wt. %, the  $T_g$  values of the nanocomposite decreased to 147, 138 and 134°C, respectively. This decrease in the values of  $T_g$  can be explained by the possibility that some solvent might be trapped in the system because of the higher surface area of RGO nano-sheets. As the content of fillers increases, the amount of trapped solvent also increases in the matrix, leading to a negative effect on the DMA results. The  $T_g$  value was increased by 21.2°C with the inclusion of 5.0 wt. % SiO<sub>2</sub>, compared with neat EP. When SiO<sub>2</sub> was incorporated into the EP matrix, the nanoparticles could anchor the

EP chains through hydrogen bonding between the hydroxyl groups –OH in the matrix and silanol groups on the SiO<sub>2</sub> surface, and hence the mobility of the EP chains becomes disturbed. Among all these increments, the 1.0 wt. % of RGO-SiO<sub>2</sub> with THF-based EP nanocomposites reached the highest  $T_g$  value of 155°C, which is greater than that of the neat EP sample by about 25°C. Increments in  $T_g$  of 4.3°C, 8°C and 17°C were observed for 5.0 wt. % of RGO–SiO<sub>2</sub> and 3.0 wt. % at a short/long time of dispersion for RGO–SiO<sub>2</sub> samples, respectively. This increase can be explained by the SiO<sub>2</sub>-decorated RGO surfaces not merely preventing the aggregation of RGO sheets, but also ameliorating RGO sheet compatibility and interfacial adhesion with the EP matrix, which limits the segmental motion of the EP chains.

The synergistic effects of the ultrasonication generator and high-shear mixer with mixing times of 20 min and 90 min, respectively, presented better results compared to the shorter-time of the high-shear mixer of 30 min, as confirmed by the results of tensile properties and images of SEM. The nanocomposites prepared at different low-loadings of RGO-SiO<sub>2</sub> (1.0, 3.0 and 5.0 wt. %), have achieved a favourable impact on the the young's modulus of nanocomposites. Composites filled with RGO–SiO<sub>2</sub> hybrids with different concentrations, and the time employed for mixing (90 mins) and the solvent used, have showed quite different mechanical behaviour. For example, the composites incorporated with 1.0 wt. % RGO–SiO<sub>2</sub> (H<sub>2</sub>O) and RGO–SiO<sub>2</sub> (THF) attained good stiffness, and the enhancement for RGO–SiO<sub>2</sub> dispersed in H<sub>2</sub>O was much greater than that nanocomposite prepared in THF solvent, where the modulus greatly increased to  $3.62 \pm 0.41$  GPa. This result increased to approximately 2% and 35% higher than the composites that were incorporated with RGO–SiO<sub>2</sub> (THF) and neat EP, respectively. Whereas the tensile strength, elongation and toughness were lower by approximately of 23, 13 and 39% respectively, compared with EP composite. This drop in results could be attributed to accumulate most of SiO<sub>2</sub> nanoparticles on the edges of RGO surfaces that incorporated in the polymer matrix which may lead to the formation of micro-

voids as soon as stress is increased. However, composites containing 3.0 wt. % RGO–SiO<sub>2</sub> dispersed into the EP matrix for a long time of 90 min showed the most optimal EY value among all other nanocomposites, which is an increase of 14.9 and 41% compared to composites filled with the same loading of RGO-SiO<sub>2</sub> at a shorter time of mixing (30 min) and neat EP, respectively. This increase can be attributed to a reduction in the average agglomerate size by a high percentage compared to that mixed at 1600 rpm after only half an hour. These results are useful to further understand the properties of thermally RGO materials, to help develop consistent methods to produce these materials and to give researchers further insight into the utilization of RGO/EP for more advanced applications. When the obtained results were compared with other existing scientific research regarding the Young's modulus of EP/RGO-SiO<sub>2</sub> nanocomposites (Ragosta et al. 2005; Zaman et al. 2012; Chen et al. 2012), the increase in the Young's modulus values found in this current work could be referred to the nanocomposite synthesis route adopted and the existence of SiO<sub>2</sub> as a stabiliser against the aggregation of individual RGO, which results in a good quality of RGO–SiO<sub>2</sub> dispersion and strong interfacial interactions arising between the matrix and fillers.

The dielectric constant of neat EP and its nanocomposites loaded with different contents of RGO–SiO<sub>2</sub> composite as function of frequency at range (101-106 Hz) was studied using Agilent impedance analyser 4184A, and the average result of three specimens of each nanocomposite are shown in Fig. 5-17. RGO nanocomposites, even at a low filling content of 1.0 wt. %, an intrinsic increase in dielectric constant can be detected, which attained 15 at 1 kHz (of 240%) when compared to the same content of GO for the GO/EP nanocomposite. This great difference can be attributed to the significant low electrical conductivity of GO material.

The dielectric constant of RGO–SiO<sub>2</sub>/EP shown a significantly improved with increasing the wt.% of RGO sheets in the polymer matrix (fig. 5-17). This increase can be attributed to the

figuration of an abundance of nano-capacitor structure, polymer matrix as nano-dielectric material and conductive filler as nanoelectrode, experiencing interfacial polarisation (Da Silva et al. 2014). Moreover, the ascending trend of the dielectric constant with filler loading might be explained by the presence of a great dipole momentum of interfacial polarisation together with an abundance of nano-capacitor structures. Additionally, as the content of conductive fillers increases, a conducting pathway would be created from the cluster, which played a crucial role in enhancing the dielectric constant. The results show that with an increased in the RGO ratio of the polymer matrix, the dielectric constant decreased significantly along with frequency. For instance, the dielectric permittivity of 1.0 wt. % RGO/EP and 5.0 wt. % RGO–SiO<sub>2</sub>/EP nanocomposites were 15.7 and 14.2 at 40 Hz, respectively, which decreased to about 11 and 10 at 1MHz, respectively. This is claimed to be occurring at high frequencies as a result of a large relaxation time of interfacial polarisation regarding the external electric field (Celozzi et al. 2008; Arjmand et al. 2012; Da Silva et al. 2014). In generally, at high frequencies, the electric field is too quick and the free electrons cannot be considered to accumulate near the interface, indicating that the dipole and space charge polarisation phenomena do not obey the alteration in the electrical field direction at high frequency. However, the lower dielectric loss values,  $\leq 2$  of the nanocomposites, are ascribed to the uniform dispersion of RGO in the matrix (Jung 2008; Da Silva et al. 2014) as well as the oxide layer that covers the surface of RGO nano-sheets, which may avert forming of a conductive network by shrinking the free path of electric charges (Ohmic loss) (Da Silva et al. 2014).

## 7 Chapter 7

### General conclusions and future work

#### 7.1 General conclusions

The compatibility between graphene and organic polymers was not evident; thus, no homogeneous composites were created. The RGO that comprises several functional groups, such as epoxy, carboxylic, and the presence of debris that has the ability to significantly change the van der Waals interactions; the organic polymers, as a result, have better compatibility.

In this thesis, RGO nanosheets were successfully produced by a facile and relatively straightforward method and utilizing the outcomes of AFM, XPS, XRD, Raman, FT-IR, SEM, TEM and TGA. The results confirm that the morphology of RGO has a prominent key role in determining the EP/RGO nanocomposites properties. The thickness of RGO is within 0.7-0.8 nm, doubling that of the pristine graphene due to the presence of prominent surface contaminants and organic adsorbates. At lower temperatures 120°C, 160°C and 180°C of RGO sheets showed d-spacing of 0.62, 0.49 and 0.46 nm. However, the degree of reduction at 180°C was found to be slightly lower nearly 9% than that RGO produced by tube furnace, and it is subsequently higher than the C/O ratio of GO material by about 53%. In addition, the electrical conductivity of RGO obtained via the vacuum method is higher than that of RGO obtained via a tube furnace by 32% ( $293 \pm 4 \text{ S cm}^{-1}$ ), which indicates a restoration of  $\text{sp}^2$  structure. The obtained RGO sheets were used as reinforcement in the EP matrix. The results indicate that the addition of a low amount of RGO was considered as part of a strategy to improve the mechanical properties of the EP nanocomposites. Furthermore, the DMA results indicated an increase of up to 26.5% ( $2.86 \pm 0.3\% \text{ GPa}$ ) in the storage modulus for the EP composite filling with 0.5 wt. % RGO compared with that of the unfilled system. In contrast, the addition of 0.5

wt. % RGO obtained by the help of the vacuum-assisted method enhanced the storage modulus by about 8.8%, 17.8% and 28.4%, respectively, compared with the values of the neat EP composite. This significant increase in the storage modulus is related to the introduced strong interfacial interactions and the better dispersion. The tensile properties of EP nanocomposites increased with the increasing temperatures of reduction process. The Young's modulus of the RGO-180 sample showed a maximal value of  $3.78 \pm 0.19$  GPa. Similarly, an increase in the elongation at break was found from  $2.71 \pm 0.3\%$  MPa for the EP to  $4.62 \pm 0.3\%$  MPa for RGO-180. The noticeably increase in Young's modulus values achieved over the current study could be reflected by the nanocomposite synthesis approach selected, which plays an important role in obtaining better dispersion for RGO material in EP matrix.

The thermal conductivity of EP was improved by up to 85%, reaching the maximum value of  $0.36 \text{ W m}^{-1} \text{ K}^{-1}$  at 1.0 wt. % RGO. The same addition also significantly improved the electrical conductivity of EP by about seven orders of magnitudes to  $5.92 \times 10^{-7}$ . Therefore, AFM showed an image of a single-layer of RGO with a thickness of about 0.8 nm and an average lateral size of about  $1.348 \mu\text{m}$ , via the complete dispersion of RGO in water with no aggregation. Compared to RGO-SiO<sub>2</sub> sheets showed dense coverage of silica nanoparticles on RGO surfaces with a thickness of around 50 nm. These results were consistent with TEM measurements.

The resultant RGO-SiO<sub>2</sub> nano-hybrids with different very low loading of 1.0, 3.0 and 5.0 wt. %, achieved a favourable impact on the performance of nanocomposites properties. The intrinsic conductivity of RGO sheets covered with a layer of SiO<sub>2</sub> results in novel nanocomposites with excellent dielectric properties (dielectric constant). For example, the Young's modulus of nanocomposites was noticeably increased by approximately of 4% compared to that EP system reinforced by RGO-180. Whereas the tensile strength, elongation



and toughness were lower by approximately of 23, 13 and 39% respectively. This drop in results could be attributed to accumulate most of SiO<sub>2</sub> nanoparticles on the edges of RGO surfaces that incorporated in the polymer matrix which may lead to the formation of microvoids as soon as stress is increased. These results are useful to further understand the properties of RGO materials, to help develop consistent methods to produce these materials and to give researchers further insight into the utilization of EP/RGO for more advanced applications.

## **7.2 Future work**

1. Much research and numerous studies conducted in this area have confirmed that in-situ polymerisation mixture has been selected as the best method to attain a uniform distribution of the nano-fillers in various host polymers compared to other pertinent mixing methods. More research will be performed using the in-situ polymerisation method to produce EP/RGO nanocomposites at very low filler loadings of the nanoparticles to explore its properties of these nanocomposites and compare them with the results that have been attained by the solution mixing process.
2. Different green approaches will be explored for reducing GO to RGO form such as using green tea, vitamins and natural reductants, as well as drawing conclusions about the degree of reduction of GO by environmentally friendly approaches and comparing them with the thermal reduction process that was applied in this current study.
3. The effect of mixing both GO and RGO with different ratios in the EP matrix on the thermal and electrical conductivities performance will be studied. In addition, future research will study various types of nano-sized fillers that can be blended with EP resin, such as CNTs, expandable graphite and nano-clay, and study different properties to

achieve a comprehensive vision for different nano-reinforcements to identify better nano-fillers for different properties of the nanocomposites.

4. Future research will investigate the influence of the alignment of RGO nano-sheets within the epoxy matrix by using a magnetic or electric field and study their resulting nanocomposites properties.

### 7.3 Conferences and papers

Name of Conference	Participation	Title of Presentation	Date
9th World Congress on Materials Science and Engineering, Rome, Italy	Poster presentation (Abstract published)	Studying the effect of reduced graphene oxide on the structure and properties of epoxy/RGO nanocomposites	14/6/2017

### 7.4 Papers in preparation

1. The effect of reduced GO on the mechanical, thermal and electrical properties of epoxy.
2. Synthesis, characterization and mechanical properties of EP composites reinforced by RGO sheets produced by using a vacuum-assisted method at low temperatures
3. Studying the extent effect of RGO–SiO<sub>2</sub> nano-hybrids on the mechanical and electrical properties of the epoxy matrix.

## 8 References

- Abdolhosseinzadeh, S., Asgharzadeh, H. and Seop Kim, H., (2015). Fast and fully-scalable synthesis of reduced graphene oxide. *Scientific Reports*, 5(1), 10160.
- Ahmad, A., Ab Aziz, S., Abbas, Z., Obaiys, S., Khamis, A., Hussain, I., and Zaid, M. (2018). Preparation of a Chemically Reduced Graphene Oxide Reinforced Epoxy Resin Polymer as a Composite for Electromagnetic Interference Shielding and Microwave-Absorbing Applications. *Polymers*, 10(11), 1180.
- Ajayan, P.M., Schadler, L.S., and Braun, P.V., (eds) (2003). *Nanocomposite Science and Technology*, WILEY-VCH Verlag GmbH Co, KGaA, Weinheim.
- Al-Haik, M. S., Garmestani, H., Li, D. S., Hussaini, M. Y., Sablin, S. S., Tannenbaum, R., and Dahmen, K. (2004). Mechanical properties of magnetically oriented epoxy. *Journal of Polymer Science Part B: Polymer Physics*, 42(9), pp.1586–1600.
- Al-nafiey, A. K. H. (2016). *Reduced graphene oxide-based nanocomposites : Synthesis characterization and applications*. (Doctoral dissertation, Villeneuve-d'Ascq), Universite lille 1 sciences et technologies, France, Dissertation.
- Al-Saleh, M. H., and Sundararaj, U. (2009). A review of vapor grown carbon nanofiber/polymer conductive composites. *Carbon*, 47(1), pp. 2–22.
- Aldosari, M.A., Othman, A.A, and Alsharaeh, E.H., (2013). Synthesis and Characterization of the in Situ Bulk Polymerization of PMMA Containing Graphene Sheets Using Microwave Irradiation. *Molecules*, 18(3), pp. 3152–3167.
- Alshammari, B.A., Wilkinson, A.N. and Almutairi, G., (2017). Electrical, Thermal, and Morphological Properties of Poly(ethylene terephthalate)-Graphite Nanoplatelets Nanocomposites. *International Journal of Polymer Science*, 2017, pp. 1-9.
- Altan, M., and Uysal, A. (2016). An Experimental Study on Mechanical Behavior of Nanographene/Epoxy Nanocomposites. *Advances in Polymer Technology*, 37(4), pp.1061–1066.
- Arjmand, M., Apperley, T., Okoniewski, M., & Sundararaj, U. (2012). Comparative study of electromagnetic interference shielding properties of injection molded versus compression molded multi-walled carbon nanotube/polystyrene composites. *Carbon*, 50(14), pp. 5126–5134.
- ASTM Standard D4496. (2013). *Standard test method for D-C resistance or conductance of moderately conductive materials*. West Conshohocken, PA: ASTM International (5p.).

- ASTM E1461–13. (2013). *Standard Test Method for Thermal Diffusivity by the Flash Method*, American Society for Testing and Materials, West Conshohocken, PA.
- ASTM Standard D257. (1999). *Standard method for DC resistance of conductance of insulating materials*. American Society of Testing Materials, Pennsylvania.
- ASTM Standards. (2006). D4065-06. *Standard practice for plastics: dynamic mechanical properties: determination and report of procedures*. Philadelphia, Pa.: ASTM Intl.
- Atif, R. and Inam, F., (2016). Modeling and Simulation of Graphene Based Polymer Nanocomposites: Advances in the Last Decade. *Graphene*, 5 (2). pp. 96-142.
- Bajpai, R., Roy, S., Kumar, P., Bajpai, P., Kulshrestha, N., Rafiee, J., Misra, D. S. (2011). Graphene Supported Platinum Nanoparticle Counter-Electrode for Enhanced Performance of Dye-Sensitized Solar Cells. *ACS Applied Materials & Interfaces*, 3(10), pp. 3884–3889.
- Balandin, A. A., Ghosh, S., Bao, W., Calizo, I., Teweldebrhan, D., Miao, F., and Lau, C. N. (2008). Superior Thermal Conductivity of Single-Layer Graphene. *Nano Letters*, 8(3), pp. 902–907.
- Bao, C., Guo, Y., Song, L., and Hu, Y. (2011). Poly(vinyl alcohol) nanocomposites based on graphene and graphite oxide: a comparative investigation of property and mechanism. *Journal of Materials Chemistry*, 21(36), pp. 13942-13950.
- Bashyam, R. and Zelenay, P. (2006). A class of non-precious metal composite catalysts for fuel cells. *Nature* 443, pp. 63–66.
- Beams, R., Gustavo Cançado, L., and Novotny, L. (2015). Raman characterization of defects and dopants in graphene. *Journal of Physics: Condensed Matter*, 27(8), 083002.
- Berger, M.A. and Mc Cullough, R.L. (1985). Characterization and Analysis of the Electrical Properties of a metal-filled polymer. *Composites Science and Technology*, 22, pp. 81-106.
- Bhattacharya, M. (2016). Polymer nanocomposites-A comparison between carbon nanotubes, graphene, and clay as nanofillers. *Materials*, 9(4), pp.1–35.
- Biron, M. (2007). *Thermoplastics and Thermoplastic Composites: Technical Information for Plastics Users*, 1st ed. Elsevier Ltd.
- Boehm, H.P., Clauss, A., Fischer, G., and Hofmann, U. (1962). Surface properties of extremely thin graphite lamellate, *Proceedings of the Fifth Conference on Carbon*, pp. 73-80.
- Boehm, H.P., Setton, R. and Stumpp, E. (1994). Nomenclature and terminology of graphite intercalation compounds (IUPAC Recommendations 1994). *Pure and Applied Chemistry*, 66(9), pp.1893–1901.
- Bolotin, K. I., Sikes, K. J., Jiang, Z., Klima, M., Fudenberg, G., Hone, J., Kim, P., Stormer, H.

- L. (2008). Ultrahigh electron mobility in suspended graphene. *Solid State Communications*, 146(9-10), 351–355.
- Bora, C., Bharali, P., Baglari, S., Dolui, S. K., and Konwar, B. K. (2013). Strong and conductive reduced graphene oxide/polyester resin composite films with improved mechanical strength, thermal stability and its antibacterial activity. *Composites Science and Technology*, 87, pp. 1–7.
- Botta, L.; Scaffaro, R.; Sutura, F.; Mistretta, M.C. (2018). Reprocessing of PLA/Graphene Nanoplatelets Nanocomposites. *Polymers*, 10(1), 18.
- Boyle, A. M., Martin, C. J., and Neuner, J. D. (2001). *Epoxy Resins*. Eds. Miracle D.B. and Donaldson S.L. ASM Handbook Composites (Materials Park: ASM International), 21, pp. 78-89.
- Brent, S.A. (2008). *Fundamentals of composites manufacturing: Materials, methods and applications* 2nd ed., Society of Manufacturing Engineers, MI, pp. 159-161.
- Buchsteiner, A., Lerf, A., and Pieper, J. (2006). Water dynamics in graphite oxide investigated with neutron scattering. *The Journal of Physical Chemistry B*, 110(45), pp. 22328–22338.
- Celozzi, S, Lovat, G., and Araneo, R. (2008). *Electromagnetic Shielding*. John Wiley & Sons, Hoboken, NJ.
- Chandrasekaran, S. (2014). *Development of nano-particle modified polymer matrices for improved fibre reinforced composites*. (Doctoral dissertation, Hamburg-Harburg), Technology University Hamburg, Dissertation.
- Chandrasekaran, S., Seidel, C., and Schulte, K. (2013). Preparation and characterization of graphite nano-platelet (GNP)/epoxy nano-composite: Mechanical, electrical and thermal properties. *European Polymer Journal*, 49(12), pp. 3878–3888.
- Chang, T. D., & Brittain, J. O. (1982). Studies of epoxy resin systems: Part D: Fracture toughness of an epoxy resin: A study of the effect of crosslinking and sub-T<sub>g</sub> aging. *Polymer Engineering and Science*, 22(18), pp.1228–1236.
- Chen, G.H., Wu, D.J., Weng, W.G., He, B., and Yan, W.L. (2001) Preparation of polystyrene-graphite conducting nanocomposite via intercalation polymerization. *Polymer International*, 50, pp. 980-985.
- Chen, H., Müller, M. B., Gilmore, K. J., Wallace, G. G., and Li, D. (2008). Mechanically Strong, Electrically Conductive, and Biocompatible Graphene Paper. *Advanced Materials*, 20(18), pp. 3557–3561.
- Chen, J., Kinloch, A. J., Sprenger, S., and Taylor, A. C. (2013b). The mechanical properties and toughening mechanisms of an epoxy polymer modified with polysiloxane-based core-

- shell particles. *Polymer*, 54(16), pp. 4276–4289.
- Chen, L., Chai, S., Liu, K., Ning, N., Gao, J., Liu, Q., Chen, F., and Fu, Q. (2012). Enhanced Epoxy/Silica Composites Mechanical Properties by Introducing Graphene Oxide to the Interface. *ACS Applied Materials & Interfaces*, 4(8), pp. 4398–4404.
- Chen, L., Zhou, Y., Tu, W., Li, Z., Bao, C., Dai, H., Yu, T., Liu, J., and Zou, Z. (2013). Enhanced photovoltaic performance of a dye-sensitized solar cell using graphene–TiO<sub>2</sub> photoanode prepared by a novel in situ simultaneous reduction-hydrolysis technique. *Nanoscale*, 5(8), pp. 3481–3485.
- Chen, W., Yan, L., and Bangal, P. R. (2010). Preparation of graphene by the rapid and mild thermal reduction of graphene oxide induced by microwaves. *Carbon*, 48(4), pp. 1146–1152.
- Chen, Y., Zhang, X., Zhang, D., Yu, P., & Ma, Y. (2011). High performance supercapacitors based on reduced graphene oxide in aqueous and ionic liquid electrolytes. *Carbon*, 49(2), pp.573–580.
- Chen, Z., Ren, W, Liu, B., Gao, L. (2010). Bulk growth of mono-to few -layer graphene on nickel particles by chemical vapor deposition. *IEEE methane. Carbon*, 48, 3543-50.
- Cho, J., Joshi, M. S., & Sun, C. T. (2006). Effect of inclusion size on mechanical properties of polymeric composites with micro and nano particles. *Composites Science and Technology*, 66(13), pp. 1941–1952.
- Chua, C. K., & Pumera, M. (2012). Reduction of graphene oxide with substituted borohydrides. *Journal of Materials Chemistry A*, 1(5), pp. 1892–1898.
- Chua, C. K., & Pumera, M. (2014). Chemical reduction of graphene oxide: a synthetic chemistry viewpoint. *Chem. Soc. Rev.*, 43(1), pp. 291–312.
- Chun, K.Y., Oh, Y., Rho, J., Ahn, J. H., Kim, Y.-J., Choi, H. R., and Baik, S. (2010). Highly conductive, printable and stretchable composite films of carbon nanotubes and silver. *Nature Nanotechnology*, 5(12), pp. 853–857.
- Chung, D. D. L. (2012). Carbon materials for structural self-sensing, electromagnetic shielding and thermal interfacing. *Carbon*, 50(9), pp.3342–3353.
- Cosmoiu, I., Apostol, D. A., Picu, C. R., Constantinescu, D. M., Sandu, M., & Sorohan, S. (2016). Influence of Filler Dispersion on the Mechanical Properties of Nanocomposites. *Materials Today: Proceedings*, 3(4), pp.953–958.
- Da Silva, A. B., Arjmand, M., Sundararaj, U., & Bretas, R. E. S. (2014). Novel composites of copper nanowire/PVDF with superior dielectric properties. *Polymer*, 55(1), 226–234.
- Dabrowska, A., Bellucci, S., Cataldo, A., Micciulla, F., & Huczko, A. (2014). Nanocomposites

- of epoxy resin with graphene nanoplates and exfoliated graphite: Synthesis and electrical properties. *Physica Status Solidi (B)*, 251(12), pp. 2599–2602.
- Dang, Z.M., Wang, L., Yin, Y., Zhang, Q., and Lei, Q.Q. (2007). Giant Dielectric Permittivities in Functionalized Carbon-Nanotube/ Electroactive-Polymer Nanocomposites. *Advanced Materials*, 19(6), pp. 852–857.
- Dang, Z.M., Yuan, J.K., Zha, J.W., Zhou, T., Li, S.T., and Hu, G.H. (2012). Fundamentals, processes and applications of high-permittivity polymer–matrix composites. *Progress in Materials Science*, 57(4), pp. 660–723.
- Das, T. K., and Prusty, S. (2013). Graphene-Based Polymer Composites and Their Applications. *Polymer-Plastics Technology and Engineering*, 52(4), pp. 319–331.
- Dimiev, A. M. and Eigler, S. (2016). *Characterization techniques. In Graphene oxide: fundamentals and applications* 85, John Wiley & Sons, Ltd.
- Ding, H., Zhang, S., Chen, J.-T., Hu, X.-P., Du, Z.-F., Qiu, Y.-X., & Zhao, D.-L. (2015). Reduction of graphene oxide at room temperature with vitamin C for RGO–TiO<sub>2</sub> photoanodes in dye-sensitized solar cell. *Thin Solid Films*, 584, pp. 29–36.
- Ding, J. H., Peng, W. J., Luo, T. and Hai, B. Y. (2017). Study on the curing reaction kinetics of a novel epoxy system. *RSC Adv.* 7, pp. 6981–6987.
- Dubois, S. M.M., Zanolli, Z., Declerck, X., and Charlier, J.C. (2009). Electronic properties and quantum transport in Graphene-based nanostructures. *The European Physical Journal B*, 72(1), pp. 1–24.
- Durmus, Z., Durmus, A., and Kavas, H. (2014). Synthesis and characterization of structural and magnetic properties of graphene/hard ferrite nanocomposites as microwave-absorbing material. *Journal of Materials Science*, 50(3), pp.1201–1213.
- Dutta, S., Ray, C., Sarkar, S., Pradhan, M., Negishi, Y., & Pal, T. (2013). Silver Nanoparticle Decorated Reduced Graphene Oxide (rGO) Nanosheet: A Platform for SERS Based Low-Level Detection of Uranyl Ion. *ACS Applied Materials & Interfaces*, 5(17), pp. 8724–8732.
- Eda, G. and Chhowalla, M., (2010). Chemically derived graphene oxide: Towards large-area thin-film electronics and optoelectronics. *Advanced Materials*, 22(22), pp.2392–2415.
- Eda, G., Mattevi, C., Yamaguchi, H., Kim, H., & Chhowalla, M. (2009). Insulator to Semimetal Transition in Graphene Oxide. *The Journal of Physical Chemistry C*, 113(35), pp. 15768–15771.
- Edwards, R. S., and Coleman, K. S. (2013). Graphene synthesis: relationship to applications. *Nanoscale*, 5(1), pp. 38–51.

- El-Khodary, S. A., El-Enany, G. M., El-Okr, M., & Ibrahim, M. (2014). Preparation and Characterization of Microwave Reduced Graphite Oxide for High-Performance Supercapacitors. *Electrochimica Acta*, *150*, pp. 269–278.
- Ellis B. (1993) Introduction to the chemistry, synthesis, manufacture and characterization of epoxy resins. Chemistry and Technology of Epoxy Resins. *Springer, Dordrecht*, pp 1-36.
- Fathy, M., Gomaa, A., Taher, F. A., El-Fass, M. M., and Kashyout, A. E.-H. B. (2016). Optimizing the preparation parameters of GO and rGO for large-scale production. *Journal of Materials Science*, *51*(12), pp. 5664–5675.
- Feng, H., Cheng, R., Zhao, X., Duan, X., & Li, J. (2013b). A low-temperature method to produce highly reduced graphene oxide. *Nature Communications*, *4*(1), pp 1537-1539.
- Feng, H., Li, Y., & Li, J. (2012). Strong reduced graphene oxide–polymer composites: hydrogels and wires. *RSC Advances*, *2*(17), pp. 6988-6993.
- Feng, H., Wang, X., & Wu, D. (2013a). Fabrication of spirocyclic phosphazene epoxy-based nanocomposites with graphene via exfoliation of graphite platelets and thermal curing for enhancement of mechanical and conductive properties. *Industrial & Engineering Chemistry Research*, *52*(30), pp. 10160–10171.
- Ferrari, A. C., (2007). Raman spectroscopy of graphene and graphite: Disorder, electron-phonon coupling, doping and nonadiabatic effects. *Solid State Communications*, *143*(1–2), pp.47–57.
- Galpaya, D., Wang, M., George, G., Motta, N., Waclawik, E., & Yan, C. (2014). Preparation of graphene oxide/epoxy nanocomposites with significantly improved mechanical properties. *Journal of Applied Physics*, *116*(5), 053518.
- Galpaya, D., Wang, M., Liu, M., Motta, N., Waclawik, E., & Yan, C. (2012). Recent Advances in Fabrication and Characterization of Graphene-Polymer Nanocomposites. *Graphene*, *01*(02), pp. 30–49.
- Galusek, D. and Galusková, D. (2015). Alumina Matrix Composites with Non-Oxide Nanoparticle Addition and Enhanced Functionalities. *Nanomaterials*, *5*(1), pp.115–143.
- Ganguli, S., Roy, A.K. & Anderson, D.P., (2008). Improved thermal conductivity for chemically functionalized exfoliated graphite/epoxy composites. *Carbon*, *46*(5), pp.806–817.
- Gao, X., Jang, J., & Nagase, S. (2010). Hydrazine and Thermal Reduction of Graphene Oxide: Reaction Mechanisms, Product Structures, and Reaction Design. *The Journal of Physical Chemistry C*, *114*(2), pp.832–842.
- Gay, D., (2014). *Composite materials: Design and Applications*, 3rd ed., CRC Press. Boca



Raton, FL, USA.

- Garg, A. C., & Mai, Y.-W. (1988). Failure mechanisms in toughened epoxy resins—A review. *Composites Science and Technology*, 31(3), pp.179–223.
- Geim, A. K, and Novoselov, K. S. ( 2007). The rise of graphene. *Nature Materials*, 6(3), pp.183–191.
- Geim, A.K. and Kim, P., (2008). Carbon Wonderland. *Scientific American*, 298(4), pp.90–97.
- Georgakilas, V., Otyepka, M., Bourlinos, A. B., Chandra, V., Kim, N., Kemp, K. C., Hobza, P., Kim, K. S. (2012). Functionalization of Graphene: Covalent and Non-Covalent Approaches, Derivatives and Applications. *Chemical Reviews*, 112(11), pp. 6156–6214.
- Ghorbani, M., Abdizadeh, H., and Golobostanfard, M. R. (2015). Reduction of graphene oxide via modified hydrothermal method. *Procedia Materials Science* 11, pp 326-330.
- Gómez-Navarro, C., Meyer, J. C., Sundaram, R. S., Chuvilin, A., Kurasch, S., Burghard, M., Kurasch, S., and Kaiser, U. (2010). Atomic Structure of Reduced Graphene Oxide. *Nano Letters*, 10(4), pp. 1144–1148.
- Gong, L., Kinloch, I. A., Young, R. J., Riaz, I., Jalil, R., & Novoselov, K. S. (2010). Interfacial Stress Transfer in a Graphene Monolayer Nanocomposite. *Advanced Materials*, 22(24), pp. 2694–2697.
- Gong, L., Young, R. J., Kinloch, I. A., Riaz, I., Jalil, R., & Novoselov, K. S. (2012). Optimizing the Reinforcement of Polymer-Based Nanocomposites by Graphene. *ACS Nano*, 6(3), pp. 2086–2095.
- Greco, A., Timo, A. & Maffezzoli, A., (2012). Development and characterization of amorphous thermoplastic matrix graphene nanocomposites. *Materials*, 5(10), pp.1972–1985.
- Grillet, A. C., Galy, J., Gérard, J.-F., & Pascault, J.-P. (1991). Mechanical and viscoelastic properties of epoxy networks cured with aromatic diamines. *Polymer*, 32(10), pp.1885–1891.
- Gu, H., Guo, J., Wei, H., Yan, X., Ding, D., Zhang, X., He, Q., Tadakamalla, S., Wang, X., Ho, T. C., Wei, S., and Guo, Z. (2015). Transparent anhydride-cured epoxy nanocomposites reinforced with polyaniline stabilized nanosilica. *Journal of Materials Chemistry C*, 3(31), pp. 8152–8165.
- Guo, H.-L., Wang, X.-F., Qian, Q.-Y., Wang, F.-B., and Xia, X.-H. (2009). A Green Approach to the Synthesis of Graphene Nanosheets. *ACS Nano*, 3(9), pp. 2653–2659.
- Guo, S., and Dong, S. (2011). Graphene nanosheet: synthesis, molecular engineering, thin film, hybrids, and energy and analytical applications. *Chemical Society Reviews*, 40(5), pp.

2644-2672.

- Hass, J., de Heer, W. A., & Conrad, E. H. (2008). The growth and morphology of epitaxial multilayer graphene. *Journal of Physics: Condensed Matter*, 20(32), 323202.
- Hayes, W. I., Joseph, P., Mughal, M. Z., and Papakonstantinou, P. (2014). Production of reduced graphene oxide via hydrothermal reduction in an aqueous sulphuric acid suspension and its electrochemical behaviour. *Journal of Solid State Electrochemistry*, 19(2), pp. 361–380.
- Hsiao, M. -C., Liao, S. -H., Yen, M. -Y., Teng, C.-C., Lee, S.-H., Pu, N. W., Wang, C. A., Sung, Y., Ger, M.D., Ma, C.C., and Hsiao, M.-H. (2010). Preparation and properties of a graphene reinforced nanocomposite conducting plate. *Journal of Materials Chemistry*, 20(39), 8496.
- Hsiao, M.-C., Ma, C.-C. M., Chiang, J.-C., Ho, K.-K., Chou, T.-Y., Xie, X., Tsai, C.-H., Chang, L.-H, and Hsieh, C.-K. (2013). Thermally conductive and electrically insulating epoxy nanocomposites with thermally reduced graphene oxide–silica hybrid nanosheets. *Nanoscale*, 5(13), pp. 5863-5871.
- Hsu, C.-H., Hsu, M.-H., Chang, K.-C., Lai, M.-C., Liu, P.-J., Chuang, T.-L., Yeh, J.-M., Liu, W.-R. (2014). Physical study of room-temperature-cured epoxy/thermally reduced graphene oxides with various contents of oxygen-containing groups. *Polymer International*, 63(10), pp. 1765–1770.
- Hsu, K.-C., & Chen, D.-H. (2014). Green synthesis and synergistic catalytic effect of Ag/reduced graphene oxide nanocomposite. *Nanoscale Research Letters*, 9(1), 484.
- Hu, K., Kulkarni, D. D., Choi, I., and Tsukruk, V. V. (2014). Graphene-polymer nanocomposites for structural and functional applications. *Progress in Polymer Science*, 39(11), pp. 1934-1972.
- Huang, D., Li, X., Wang, S., He, G., Jiang, W., Hu, J., Wang, Y., Hu, N., Zhang, Y., and Yang, Z. (2017). Three-dimensional chemically reduced graphene oxide templated by silica spheres for ammonia sensing. *Sensors and Actuators B: Chemical*, 252, pp. 956–964.
- Huang, H.-H., De Silva, K. K. H., Kumara, G. R. A., and Yoshimura, M. (2018). Structural Evolution of Hydrothermally Derived Reduced Graphene Oxide. *Scientific Reports*, 8(1), 6849.
- Huang, L., Zhu, P., Li, G., (Daniel) Lu, D., Sun, R., and Wong, C. (2014). Core–shell SiO<sub>2</sub>@RGO hybrids for epoxy composites with low percolation threshold and enhanced thermo-mechanical properties. *Journal of Materials. Chemistry. A*, 2(43), pp. 18246–18255.

- Huang, X., Zhou, X., Wu, S., Wei, Y., Qi, X., Zhang, J., Boey, F., and Zhang, H. (2010). Reduced graphene oxide-templated photochemical synthesis and in situ assembly of Au nanodots to orderly patterned Au nanodot chains. *Small*, 6(4), pp. 513–516.
- Huang, Y., and Paul, D. R. (2007). Effect of molecular weight and temperature on physical aging of thin glassy poly(2,6-dimethyl-1,4-phenylene oxide) films. *Journal of Polymer Science Part B: Polymer Physics*, 45 (12), pp. 1390-1398.
- Huh, S. H. (2011). *Thermal reduction of graphene oxide. Physics and Applications of Graphene-Experiments*; Mikhailov, S., Ed.; Intech, pp. 73-90.
- Hull & Clyne, T.W., 1996. *In An introduction to composites materials* 2nd ed., Cambridge University Press.
- Hull D. (1999). *Fractography: observing, measuring, and interpreting fracture surface topography*. Cambridge University Press, Cambridge, U.K., pp. 91-150.
- ISO 527-1. (2012). *Plastics - Determination of tensile properties - Part 1: General principles*. International Organization for Standardization- ISO, Geneva.
- ISO 527-2. (2012). *Plastics -Determination of tensile properties - Part 2: Test conditions for moulding and extrusion plastics*. International Organization for Standardization- ISO, Geneva.
- Ji, Z., Shen, X., Zhu, G., Zhou, H., and Yuan, A. (2012). Reduced graphene oxide/nickel nanocomposites: facile synthesis, magnetic and catalytic properties. *Journal of Materials Chemistry*, 22(8), 3471.
- Jia, W., Tchoudakov, R., Narkis, M., and Siegmann, A. (2005). Performance of expanded graphite and expanded milled-graphite fillers in thermosetting resins. *Polymer Composites*, 26(4), pp. 526–533.
- Joung, D., Singh, V., Park, S., Schulte, A., Seal, S., and Khondaker, S. I. (2011). Anchoring Ceria Nanoparticles on Reduced Graphene Oxide and Their Electronic Transport Properties. *The Journal of Physical Chemistry C*, 115(50), pp. 24494–24500.
- Ju, H.-M., Huh, S. H., Choi, S.-H., and Lee, H.-L. (2010). Structures of thermally and chemically reduced graphene. *Materials Letters*, 64(3), pp. 357–360.
- Jung, I., Vaupel, M., Pelton, M., Piner, R., Dikin, D. A., Stankovich, S., An, J., and Ruoff, R. S. (2008). Characterization of Thermally Reduced Graphene Oxide by Imaging Ellipsometry. *The Journal of Physical Chemistry C*, 112(23), pp. 8499–8506.
- Karimzadeh, R., and Arandian, A. (2015). Unusual nonlinear absorption response of graphene oxide in the presence of a reduction process. *Laser Physics Letters*, 12(2), 025401.
- Ke, Y.C., Stroeve, P. (2005). *Polymer-Layered Silicate and Silica Nanocomposites*. Elsevier

B.V., Amsterdam, the Netherlands.

- Kee, S., Munusamy, Y., Ong, K., and Lai, K. (2017). Effect of Preparation Methods on the Tensile, Morphology and Solar Energy Conversion Efficiency of RGO/PMMA Nanocomposites. *Polymers*, 9(12), 230.
- Khan, M., Tahir, M. N., Adil, S. F., Khan, H. U., Siddiqui, M. R. H., Al-warthan Abdulrahman A., and Tremel, W. (2015). Graphene based metal and metal oxide nanocomposites: synthesis, properties and their applications. *Journal of Materials Chemistry A*, 3(37), pp. 18753–18808.
- Khanam, P. N.; Ponnamma, D.; AL-Madeed, M. A. (2015). *Electrical Properties of Graphene Polymer Nanocomposites*. In *Graphene-Based Polymer Nanocomposites in Electronics*; Sadasivuni K. K., Ponnamma, D., Kim, J., Thomas, S., Eds.; Springer International Publishing: Switzerland, pp 25–47.
- Kim, B. C., Park, S. W., & Lee, D. G. (2008). Fracture toughness of the nano-particle reinforced epoxy composite. *Composite Structures*, 86(1-3), pp. 69–77.
- Kim, H., Abdala, A. A., and Macosko, C.W. (2010). Graphene/Polymer Nanocomposites. *Macromolecules*, 43(16), pp. 6515–6530.
- Kim, H., Miura, Y., and Macosko, C. W. (2010). Graphene/Polyurethane Nanocomposites for Improved Gas Barrier and Electrical Conductivity. *Chemistry of Materials*, 22(11), pp.3441–3450.
- Kim, H., Seo, D.-H., Kim, S.-W., Kim, J., and Kang, K. (2011). Highly reversible Co<sub>3</sub>O<sub>4</sub>/graphene hybrid anode for lithium rechargeable batteries. *Carbon*, 49(1), pp. 326–332.
- Kimiagar, S., Rashidi, N., & Ghadim, E. E. (2015). Investigation of the effects of temperature and time on reduction of graphene oxide by microwave hydrothermal reactor. *Bulletin of Materials Science*, 38(7), pp.1699–1704.
- Kim, M. C., Hwang, G. S., and Ruoff, R. S. (2009). Epoxide reduction with hydrazine on graphene: A first principles study. *The Journal of Chemical Physics*, 131(6), 064704.
- King, J. A., Klimek, D. R., Miskioglu, I., & Odegard, G. M. (2012). Mechanical properties of graphene nanoplatelet/epoxy composites. *Journal of Composite Materials*, 49(6), pp. 659–668.
- Kochetov, R., Andritsch, T., Morshuis, P. H. F., & Smit, J. J. (2012). Anomalous behaviour of the dielectric spectroscopy response of nanocomposites. *IEEE Transactions on Dielectrics and Electrical Insulation*, 19(1), pp. 107–117.
- Konios, D., Stylianakis, M. M., Stratakis, E., & Kymakis, E. (2014). Dispersion behaviour of

- graphene oxide and reduced graphene oxide. *Journal of Colloid and Interface Science*, 430, pp. 108–112.
- Kotchey, G. P., Allen, B. L., Vedala, H., Yanamala, N., Kapralov, A. A., Tyurina, Y. Y., Klein-Seetharaman, J., Kagan, V.E., and Star, A. (2011). The Enzymatic Oxidation of Graphene Oxide. *ACS Nano*, 5(3), pp. 2098–2108.
- Kou, L. and Gao, C. (2011). Making silica nanoparticle-covered graphene oxide nanohybrids as general building blocks for large-area superhydrophilic coatings. *Nanoscale*, 3(2), pp.519–528.
- Krishnamoorthy, K., Veerapandian, M., Mohan, R., & Kim, S.-J. (2012). Investigation of Raman and photoluminescence studies of reduced graphene oxide sheets. *Applied Physics A*, 106(3), pp.501–506.
- Krishnamoorthy, K., Veerapandian, M., Yun, K. and Kim, S. -J. (2013). The chemical and structural analysis of graphene oxide with different degrees of oxidation. *Carbon* 53, pp. 38–49.
- Kuan, C.-F., Kuan, H.-C., Ma, C.-C. M., & Chen, C.-H. (2008). Mechanical and electrical properties of multi-wall carbon nanotube/poly(lactic acid) composites. *Journal of Physics and Chemistry of Solids*, 69(5-6), 1395–1398.
- Kudin, K. N., Ozbas, B., Schniepp, H. C., Prud'homme, R. K., Aksay, I. A., and Car, R. (2008). Raman Spectra of Graphite Oxide and Functionalized Graphene Sheets. *Nano Letters*, 8(1), pp. 36–41.
- Kumar, P., Singh, A.K., Hussain, S., Hui, K.N., Hui, K.S., Eom, J., Jung, J. and Singh, J. (2013). Graphene: Synthesis, Properties and Application in Transparent Electronic Devices. *Reviews in Advanced Sciences and Engineering*, 2(4), pp.1–21.
- Kumar, P., Shahzad, F., Yu, S., Hong, S. M., Kim, Y.-H., & Koo, C. M. (2015). Large-area reduced graphene oxide thin film with excellent thermal conductivity and electromagnetic interference shielding effectiveness. *Carbon*, pp. 94, 494–500.
- Kurniasari, Maulana, A., Nugraheni, A. Y., Jayanti, D. N., Mustofa, S., Baqiya, M. A., and Darminto. (2017). Defect and Magnetic Properties of Reduced Graphene Oxide Prepared from Old Coconut Shell. *IOP Conference Series: Materials Science and Engineering*, 196, 012021.
- Layek, R. K., Das, A. K., Park, M. U., Kim, N. H., and Lee, J. H. (2014). Layer-structured graphene oxide/polyvinyl alcohol nanocomposites: dramatic enhancement of hydrogen gas barrier properties. *Journal of Materials Chemistry A*, 2(31), 12158.
- Lee, H. C., Liu, W.-W., Chai, S.-P., Mohamed, A. R., Aziz, A., Khe, C.-S., Hidayah, N. M. S.,

- and Hashim, U. (2017). Review of the synthesis, transfer, characterization and growth mechanisms of single and multilayer graphene. *RSC Advances*, 7(26), pp.15644–15693.
- Lee, K. G., Wi, R., Imran, M., Park, T. J., Lee, J., Lee, S. Y., and Kim, D. H. (2010). Functionalization Effects of Single-Walled Carbon Nanotubes as Templates for the Synthesis of Silica Nanorods and Study of Growing Mechanism of Silica. *ACS Nano*, 4(7), pp. 3933–3942.
- Lemme, M.C. (2010). Current Status of Graphene Transistors. *Solid State Phenomena, Vols (156-158)*, pp.499-509.
- Lepoittevin, B., Pantoustier, N., Devalckenaere, M., Alexandre, M., Calberg, C., Jérôme, R., Henrist, C., Rulmont, A., and Dubois, P. (2003). Polymer/layered silicate nanocomposites by combined intercalative polymerization and melt intercalation: a masterbatch process. *Polymer*, 44(7), pp. 2033-2040.
- Lerf, A., He, H., Forster, M. and Klinowski, J. (1998). Structure of Graphite Oxide Revisited. *Journal of Physical Chemistry B*, 102(23), pp.4477–4482.
- Li, D., Müller, M. B., Gilje, S., Kaner, R. B., and Wallace, G. G. (2008). Processable aqueous dispersions of graphene nanosheets. *Nature nanotechnology*, 3, pp.101–105.
- Li, X., Magnuson, C. W., Venugopal, A., An, J., Suk, J. W., Han, B., Borysiak, M., Cai, W., Velamakanni, A., Zhu, Y., Fu, L., Voelkl, E., Colombo, L., and Ruoff, R. S. (2010). Graphene films with large domain Size by a two-step chemical vapor deposition process. *Nano Letters*, 10(11), 4328–4334.
- Li, Z. L., Young, R. J., Wilson, N. R., Kinloch, I. A., Vallés, C., Li, Z. (2016). Effect of the orientation of graphene-based nanoplatelets upon the Young's modulus of nanocomposites. *Composites Science and Technology*, 123, pp. 125-133.
- Liang, J., Wang, Y., Huang, Y., Ma, Y., Liu, Z., Cai, J., Zhang, C., Gao, H., and Chen, Y. (2009). Electromagnetic interference shielding of graphene/epoxy composites. *Carbon*, 47(3), 922–925.
- Lin, W., Zhang, R. and Wong, C. P. (2010). Modeling of Thermal Conductivity of Graphite Nanosheet Composites. *Journal of Electronic Materials*, 39(3), pp.268-272.
- Lin, Z., Karthik, P. S., Hada, M., Nishikawa, T., and Hayashi, Y. (2017). Simple Technique of Exfoliation and Dispersion of Multilayer Graphene from Natural Graphite by Ozone-Assisted Sonication. *Nanomaterials*, 7(125), pp.1-10.
- Liu, L., Ryu, S., Tomasik, M. R., Stolyarova, E., Jung, N., Hybertsen, M. S., Steigerwald, M. L., Brus, L. E., and Flynn, G. W. (2008). Graphene Oxidation: Thickness-Dependent Etching and Strong Chemical Doping. *Nano Letters*, 8(7), pp.1965–1970.

- Liu, Q., Zhou, X., Fan, X., Zhu, C., Yao, X., and Liu, Z. (2012). Mechanical and Thermal Properties of Epoxy Resin Nanocomposites Reinforced with Graphene Oxide. *Polymer-Plastics Technology and Engineering*, 51(3), pp.251–256.
- Liu, Y., Wu, H., & Chen, G. (2014). Enhanced mechanical properties of nanocomposites at low graphene content based on: *In situ* ball milling. *Polymer Composites*, 37(4), pp. 1190–1197.
- Liu, Z., Zhang, H., Song, S., and Zhang, Y. (2017). Improving thermal conductivity of styrene-butadiene rubber composites by incorporating mesoporous silica@solvothermal reduced graphene oxide hybrid nano-sheets with low graphene content. *Composites Science and Technology*, 150, pp.174–180.
- Lu, S-R., Jiang, Y-M., Wei, C. (2009). Preparation and characterization of EP/SiO<sub>2</sub> hybrid materials containing PEG flexible chain. *Journal of Materials Science*, 44, pp. 4047–4055
- Lucchese, M. M., Stavale, F., Ferreira, E. H. M., Vilani, C., Moutinho, M. V. O., Capaz, R. B., Achete, C. A., and Jorio, A. (2010). Quantifying ion-induced defects and Raman relaxation length in graphene. *Carbon*, 48(5), pp. 1592–1597.
- Ma, C., Chen, Z., Fang, M., and Lu, H. (2012). Controlled synthesis of graphene sheets with tunable sizes by hydrothermal cutting. *Journal of Nanoparticle Research*, 14(8), 996.
- Ma, Y., Di, H., Yu, Z., Liang, L., Lv, L., Pan, Y., Zhang, Y., and Yin, D. (2016). Fabrication of silica-decorated graphene oxide nanohybrids and the properties of composite epoxy coatings research. *Applied Surface Science*, 360, pp. 936–945.
- Majcher, A., Wiejak, J., Przybylski, J., Chudoba, T., and Wojnarowicz, J. (2013). A Novel Reactor for Microwave Hydrothermal Scale-up Nanopowder Synthesis. *International Journal of Chemical Reactor Engineering*, 11(1), pp. 1–8.
- Malucelli, G. (2017). Graphene-based Polymer Nanocomposites: Recent Advances and Still Open Challenges. *Current Graphene Science*, 1(1). pp. 16-25.
- Maphundu, N.M. (2017). *Investigating the percolation threshold of carbon/epoxy nanocomposites using dielectric spectroscopy*. 25th Southern African Universities Power Engineering Conference (SAUPEC 2017), pp. 660–665.
- Marcano, D. C., Kosynkin, D. V., Berlin, J. M., Sinitskii, A., Sun, Z., Slesarev, A., Alemany, L. B., Lu, W., and Tour, J. M. (2010). Improved Synthesis of Graphene Oxide. *ACS Nano*, 4(8), pp. 4806–4814.
- Mattevi, C., Eda, G., Agnoli, S., Miller, S., Mkhoyan, K. A., Celik, O., Mastrogiovanni, D., Granozzi, G., Garfunkel, E., and Chhowalla, M. (2009). Evolution of Electrical,

- Chemical, and Structural Properties of Transparent and Conducting Chemically Derived Graphene Thin Films. *Advanced Functional Materials*, 19(16), pp. 2577–2583.
- Mazumdar, S. K. (2002). *Composites manufacturing: materials, product, and process engineering*. Boca Raton, Florida: CRC Press LLC.
- McAllister, M. J., Li, J.-L., Adamson, D. H., Schniepp, H. C., Abdala, A. A., Liu, J., Herrera-Alonso, M., Milius, D. L., Car, R., Prud'homme, R. K., and Aksay, I. A. (2007). Single Sheet Functionalized Graphene by Oxidation and Thermal Expansion of Graphite. *Chemistry of Materials*, 19(18), pp. 4396–4404.
- McCullough, R. L. (1985). Generalized combining rules for predicting transport properties of composite materials. *Composites Science and Technology*, 22(1), pp.3–21.
- Menard, K. P., & Menard, N. R. (2015). Dynamic Mechanical Analysis in the Analysis of Polymers and Rubbers. *Encyclopedia of Polymer Science and Technology*, pp.1–33.
- Menard, K.P. (2008). *Dynamic mechanical analysis: a practical introduction*. Boca Raton, FL.: CRC Press. 208 p.
- Meng, Q., Wu, H., Zhao, Z., Araby, S., Lu, S., and Ma, J. (2017). Free-standing, flexible, electrically conductive epoxy/graphene composite films. *Composites Part A: Applied Science and Manufacturing*, 92, pp. 42–50.
- Ming, R., Zhang, P., He, X., Feng, J., Ding, Y., Chang, F., and Wang, C. (2013). Humidity-dependant compression properties of graphene oxide foams prepared by freeze-drying technique. *Micro & Nano Letters*, 8(2), pp. 66–67.
- Mittal, G., Dhand, V., Rhee, K. Y., Park, S.-J., and Lee, W. R. (2015). A review on carbon nanotubes and graphene as fillers in reinforced polymer nanocomposites. *Journal of Industrial and Engineering Chemistry*, 21, pp. 11–25.
- Mkhoyan, K. A., Contryman, A. W., Silcox, J., Stewart, D. A., Eda, G., Mattevi, C., Miller, S., and Chhowalla, M. (2009). Atomic and Electronic Structure of Graphene-Oxide. *Nano Letters*, 9(3), pp. 1058–1063.
- Móczó, J., and Pukánszky, B. (2008). Polymer micro and nanocomposites: Structure, interactions, properties. *Journal of Industrial and Engineering Chemistry*, 14(5), pp. 535–563.
- Mohan, V. B., Brown, R., Jayaraman, K., and Bhattacharyya, D. (2015). Characterisation of reduced graphene oxide: Effects of reduction variables on electrical conductivity. *Materials Science and Engineering: B*, 193, pp. 49–60.
- Mohanty, N., Nagaraja, A., Armesto, J., and Berry, V. (2010). High-Throughput, ultrafast synthesis of solution- dispersed graphene via a facile hydride chemistry. *Small*, 6(2),



pp.226–231.

- Monteserín, C., Blanco, M., Aranzabe, E., Aranzabe, A., Laza, J. M., Larrañaga-Varga, A., & Vilas, J. L. (2017). Effects of Graphene Oxide and Chemically-Reduced Graphene Oxide on the Dynamic Mechanical Properties of Epoxy Amine Composites. *Polymers*, 9(12), 449.
- Monti, M., Rallini, M., Puglia, D., Peponi, L., Torre, L., & Kenny, J. M. (2013). Morphology and electrical properties of graphene–epoxy nanocomposites obtained by different solvent assisted processing methods. *Composites Part A: Applied Science and Manufacturing*, 46, pp. 166–172.
- Moon, I. K., Lee, J., Ruoff, R. S., and Lee, H. (2010). Reduced graphene oxide by chemical graphitization. *Nature Communications*, 1(6), pp.1–6.
- Moore, W.R. (1963). *An Introduction to Polymer Chemistry*, University of London Press Ltd., London.
- Mozetič, M., Ostrikov, K., Ruzic, D.N., Curreli, D., Cvelbar, U., Vesel, A., Primc, G., Leisch, M., Jousten, K., Malyshev, O.B., Hendricks, J.H., Kövér, L., Tagliaferro, A., Conde, O., Silvestre, A.J., Giapintzakis, J., Buljan, M., Radić, N., Dražić, G., Bernstorff, S., Biederman, H., Kylián, O., Hanuš, J., Milošević, S., Galtayries, A., Dietrich, P., Unger, W., Lehocky, M., Sedlarik, V., Stana-Kleinschek, K., Drmota-Petrič, A., Pireaux, J.J., Rogers, J.W., and Anderle, M. (2014) Recent advances in vacuum sciences and applications. *Journal of Physics D: Applied Physics*, 47(15), 153001.
- Mu, X., Wu, X., Zhang, T., Go, D. B., & Luo, T. (2014). Thermal Transport in Graphene Oxide - From Ballistic Extreme to Amorphous Limit. *Scientific Reports*, 4(1), pp. 1-9.
- Mukhopadhyay, P, and Gupta. R. K., (2013). *Graphite, graphene, and their polymer nanocomposites*, Boca Raton: Fla, CRC Press.
- Mungse, H.P., Sharma, O.P., Sugimura, H. & Khatri, O.P. (2014). Hydrothermal deoxygenation of graphene oxide in sub- and supercritical water. *RSC Advances* 4(43), pp. 22589–22595.
- Muszynski, R., Seger, B. and Kamat, P. V. (2008). Decorating graphene sheets with gold nanoparticles. *The Journal of Physical Chemistry C*, 112(14), pp.5263–5266.
- Muzyka, R., Drewniak, S., Pustelny, T., Chrubasik, M., & Gryglewicz, G. (2018). Characterization of Graphite Oxide and Reduced Graphene Oxide Obtained from Different Graphite Precursors and Oxidized by Different Methods Using Raman Spectroscopy. *Materials*, 11(7), 1050.
- Naebe, M., Wang, J., Amini, A., Khayyam, H., Hameed, N., Li, L. H., Chen, Y., and Fox, B.

- (2014). Mechanical Property and Structure of Covalent Functionalised Graphene/Epoxy Nanocomposites. *Scientific Reports*, 4(1), pp. 1-7.
- Nan, C.-W., Shen, Y., and Ma, J. (2010). Physical Properties of Composites Near Percolation. *Annual Review of Materials Research*, 40(1), pp.131–151.
- Narkis, M., Lidor, G., Vaxman, A., Zuri, L. (1998). Novel electrically conductive injection moldable thermoplastic composites for ESD applications. Conference Proceedings at Antec '98: Plastics on My Mind, Vols I-III: Vol I; Processing, Vol II; Special Areas, Vol III; Materials. 44, pp.1375-80.
- Nazir, T., Afzal, A., Siddiqi, H. M., Saeed, S., & Dumon, M. (2011). The influence of temperature and interface strength on the microstructure and performance of sol–gel silica–epoxy nanocomposites. *Polymer Bulletin*, 67(8), pp. 1539–1551
- Nguyen, K. T., Li, D., Borah, P., Ma, X., Liu, Z., Zhu, L., Gruner, G., Xiong, Q., and Zhao, Y. (2013). Photoinduced Charge Transfer within Polyaniline-Encapsulated Quantum Dots Decorated on Graphene. *ACS Applied Materials & Interfaces*, 5(16), pp. 8105–8110.
- Ni, Z., Wang, Y., Yu, T., and Shen, Z. (2008). Raman spectroscopy and imaging of graphene. *Nano Research*, 1(4), pp. 273–291.
- Nikolic, G., Zlatkovic, S., Cakic, M., Cakic, S., Lacnjevac, C., & Rajic, Z. (2010). Fast Fourier Transform IR Characterization of Epoxy GY Systems Crosslinked with Aliphatic and Cycloaliphatic EH Polyamine Adducts. *Sensors*, 10(1), 684–696.
- Novoselov, K. S. (2004). Electric Field Effect in Atomically Thin Carbon Films. *Science*, 306(5696), pp. 666–669.
- Ojha, K., Anjaneyulu, O. and Ganguli, A. K. (2014). Graphene-based hybrid materials: Synthetic approaches and properties. *Current Science*, 107(3), pp.397–418.
- Olevsky, E., Aleksandrova, E., Ilyina, A., Dudina, D., Novoselov, A., Pelve, K., & Grigoryev, E. (2013). Outside mainstream electronic databases: Review of studies conducted in the USSR and post-soviet countries on electric current-assisted consolidation of powder materials. *Materials*, 6(10), pp. 4375–4440.
- Olowojoba, G. B., Eslava, S., Gutierrez, E. S., Kinloch, A. J., Mattevi, C., Rocha, V. G., & Taylor, A. C. (2016). In situ thermally reduced graphene oxide/epoxy composites: thermal and mechanical properties. *Applied Nanoscience*, 6(7), pp. 1015–1022.
- Olowojoba, G. B., Kopsidas, S., Eslava, S., Gutierrez, E. S., Kinloch, A. J., Mattevi, C., Rocha, V. G., and Taylor, A. C. (2017). A facile way to produce epoxy nanocomposites having excellent thermal conductivity with low contents of reduced graphene oxide. *Journal of Materials Science*, 52(12), pp. 7323–7344.

- Ott, H.W. (2009). *Electromagnetic Compatibility Engineering*, John Wiley and Sons Inc., Hoboken, New Jersey.
- Pan, L., Ban, J., Lu, S., Chen, G., Yang, J., Luo, Q., Wu, L., and Yu, J. (2015). Improving thermal and mechanical properties of epoxy composites by using functionalized graphene. *RSC Advances*, 5(74), pp. 60596–60607.
- Pang, H., Chen, T., Zhang, G., Zeng, B., and Li, Z.-M. (2010). An electrically conducting polymer/graphene composite with a very low percolation threshold. *Materials Letters*, 64(20), pp. 2226–2229.
- Paredes, J. I., Villar-Rodil, S., Martínez-Alonso, A., and Tascón, J. M. D. (2008). Graphene Oxide Dispersions in Organic Solvents. *Langmuir*, 24(19), 10560–10564.
- Park, M., Park, J., and Jeong, U. (2014). Design of conductive composite elastomers for stretchable electronics. *Nano Today*, 9(2), 244–260.
- Park, S., An, J., Jung, I., Piner, R. D., An, S. J., Li, X., Velamakanni, A., and Ruoff, R. S. (2009). Colloidal Suspensions of Highly Reduced Graphene Oxide in a Wide Variety of Organic Solvents. *Nano Letters*, 9(4), pp. 1593–1597.
- Park, S., An, J., Potts, J. R., Velamakanni, A., Murali, S., & Ruoff, R. S. (2011). Hydrazine-reduction of graphite- and graphene oxide. *Carbon*, 49(9), pp. 3019–3023.
- Park, W., Hu, J., Jauregui, L. A., Ruan, X., & Chen, Y. P. (2014). Electrical and thermal conductivities of reduced graphene oxide/polystyrene composites. *Applied Physics Letters*, 104(11), pp. 113101-4.
- Pearson, R. A., & Yee, A. F. (1989). Toughening mechanisms in elastomer-modified epoxies. *Journal of Materials Science*, 24(7), 2571–2580.
- Pei, S. and Cheng, H.-M. (2012). The reduction of graphene oxide. *Carbon*, 50(9), pp.3210–3228.
- Peng, J.-P., Zhang, H., Tang, L.-C., Jia, Y., and Zhang, Z. (2013). Dielectric Properties of Carbon Nanotubes/Epoxy Composites. *Journal of Nanoscience and Nanotechnology*, 13(2), pp. 964–969.
- Peponi, L., Puglia, D., Torre, L., Valentini, L., and Kenny, J. M. (2014). Processing of nanostructured polymers and advanced polymeric based nanocomposites. *Materials Science and Engineering: R: Reports*, 85(1), pp. 1–46.
- Pettes, M.T., Jo, I., Yao, Z. and Shi, L. (2011). Influence of Polymeric Residue on the Thermal Conductivity of Suspended Bilayer Graphene. *Nano Letters*, 11(3), pp. 1195-1200.
- Pimenta M, Dresselhaus G, Dresselhaus M, Cancado L, Jorio A, Saito R., (2007). Studying

- disorder in graphite-based system by Raman spectroscopy. *Physical Chemistry Chemical Physics*; 9(11), 1276-1291.
- Pizzutto, C. E., Suave, J., Bertholdi, J., Pezzin, S. H., Coelho, L. A. F., and Amico, S. C. (2011). Study of epoxy/CNT nanocomposites prepared via dispersion in the hardener. *Materials Research*, 14(2), pp. 256–263.
- Plimpton, S. (1995). Fast Parallel Algorithms for Short-Range Molecular Dynamics. *Journal of Computational Physics*, 117(1), pp. 1–19.
- Potts, J. R., Dreyer, D. R., Bielawski, C. W., and Ruoff, R. S. (2011). Graphene-based polymer nanocomposites. *Polymer*, 52(1), pp.5–25.
- Prolongo, S. G., Moriche, R., Jiménez-Suárez, A., Sánchez, M., and Ureña, A. (2014). Epoxy Adhesives Modified with Graphene for Thermal Interface Materials. *The Journal of Adhesion*, 90(10), pp. 835–847.
- Pullicino, E., Zou, W., Gresil, M., and Soutis, C. (2016). The Effect of Shear Mixing Speed and Time on the Mechanical Properties of GNP/Epoxy Composites. *Applied Composite Materials*, 24(2), pp. 301–311.
- Pu, X., Zhang, H.-B., Li, X., Gui, C., & Yu, Z.-Z. (2014). Thermally conductive and electrically insulating epoxy nanocomposites with silica-coated graphene. *RSC Adv.*, 4(29), pp. 15297–15303.
- Qi, B., Lu, S. R., Xiao, X. E., Pan, L. L., Tan, F. Z., and Yu, J. H. (2014). Enhanced thermal and mechanical properties of epoxy composites by mixing thermotropic liquid crystalline epoxy grafted graphene oxide. *Express Polymer Letters*, 8(7), pp. 467–479.
- Qian, R., Yu, J., Wu, C., Zhai, X., and Jiang, P. (2013). Alumina-coated graphene sheet hybrids for electrically insulating polymer composites with high thermal conductivity. *RSC Advances*, 3(38), pp.17373-17379.
- Rafiee, M. A., Rafiee, J., Wang, Z., Song, H., Yu, Z. and Koratkar, N. (2009). Enhanced Mechanical Properties of Nanocomposites at Low Graphene Content. *ACS Nano*, 3(12), pp. 3884 –3890.
- Ragosta, G., Abbate, M., Scarinzi, G., Mascia, L. (2005). Epoxy-silica particulate nanocomposites: Chemical interactions, reinforcement and fracture toughness. *Polymer*, 46(23), pp.10506–10516.
- Rahman, R. (2013) The Role of Graphene in Enhancing the Stiffness of Polymeric Material: A Molecular Modeling Approach. *Journal of Applied Physics*, 113(24), 243503.
- Ramanathan, T.; Abdala, A. A.; Stankovich, S.; Dikin, D. A.; Herrera-Alonso, M.; Piner, R. D.; Adamson, D. H.; Schniepp, H. C.; Chen, X.; Ruoff, R. S.; Nguyen, S. T.; Aksay, I.

- A.; Prud'Homme, R. K.; Brinson, L. C. (2008). Functionalized graphene sheets for polymer nanocomposites. *Nature Nanotechnology*, 3(6), pp.327–331.
- Rathnayake, R. M. N. M., Wijayasinghe, H. W. M. A. C., Pitawala, H. M. T. G. A., Yoshimura, M., & Huang, H.-H. (2017). Synthesis of graphene oxide and reduced graphene oxide by needle platy natural vein graphite. *Applied Surface Science*, 393, pp. 309–315.
- Rehab, A. and Salahuddin, N., (2005). Nanocomposite materials based on polyurethane intercalated into montmorillonite clay. *Materials Science and Engineering A*, 399(1–2), pp.368–376.
- Reina, A., Jia, X., Ho, J., Nezich, D., Son, H., Bulovic, V., Dresselhaus, M. S., Kong, J. (2009). Large Area, Few-Layer Graphene Films on Arbitrary Substrates by Chemical Vapor Deposition. *Nano Letters*, 9(1), pp. 30–35.
- Renteria, J. D., Ramirez, S., Malekpour, H., Alonso, B., Centeno, A., Zurutuza, A., Cocemasov, A. I., Nika, D. L., and Balandin, A. A. (2015). Strongly Anisotropic Thermal Conductivity of Free-Standing Reduced Graphene Oxide Films Annealed at High Temperature. *Advanced Functional Materials*, 25(29), pp. 4664–4672.
- Romão, B. M. V., Diniz, M. F., Azevedo, M. F. P., Lourenço, V. L., Pardini, L. C., Dutra, R. C. L., & Burel, F. (2006). Characterization of the curing agents used in epoxy resins with TG/FT-IR technique. *Polímeros: Ciência e Tecnologia*, 16, pp.94–98.
- Rommozzi, E., Zannotti, M., Giovannetti, R., D'Amato, C., Ferraro, S., Minicucci, M., Gunnella, R., and Di Cicco, A. (2018). Reduced Graphene Oxide/TiO<sub>2</sub> Nanocomposite: From Synthesis to Characterization for Efficient Visible Light Photocatalytic Applications. *Catalysts*, 8(12), 598.
- Rountree, K. S., Shah, S. A., Sweeney, C. B., Irin, F., Green, M. J. (2016). Graphene reflux: Improving the yield of liquid-exfoliated nano-sheets through repeated separation techniques. *Nanotechnology*, 27(50), pp.1–6.
- Salom, C., Prolongo, M. G., Toribio, A., Martínez-Martínez, A. J., de Cárcer, I. A., and Prolongo, S. G. (2018). Mechanical properties and adhesive behavior of epoxy-graphene nanocomposites. *International Journal of Adhesion and Adhesives*, 84, pp.119–125.
- Schniepp, H. C., Li, J.-L., McAllister, M. J., Sai, H., Herrera-Alonso, M., Adamson, D. H., Prud'homme, R. K., Car, R., Saville, D. A., and Aksay, I. A. (2006). Functionalized Single Graphene Sheets Derived from Splitting Graphite Oxide. *The Journal of Physical Chemistry B*, 110(17), pp. 8535–8539.
- Shahil, K.M.F. and Balandin, A.A. (2012). Graphene-multilayer graphene nanocomposites as highly efficient thermal interface materials. *Nano Letters*, 12(2), pp.861–867.

- Shelimov, K. B., Esenaliev, R. O., Rinzler, A. G., Huffman, C. B., and Smalley, R. E. (1998). Purification of single-wall carbon nanotubes by ultrasonically assisted filtration. *Chemical Physics Letters*, 282(5-6), pp. 429–434.
- Shen, L., Zhang, L., Wang, K., Miao, L., Lan, Q., Jiang, K., Lu, H., Li, M., Li, Y., Shen, B., and Zheng, W. (2018). Analysis of oxidation degree of graphite oxide and chemical structure of corresponding reduced graphite oxide by selecting different-sized original graphite. *RSC Advances*, 8(31), pp. 17209–17217.
- Shen, X.-J., Pei, X.-Q., Fu, S.-Y., and Friedrich, K. (2013). Significantly modified tribological performance of epoxy nanocomposites at very low graphene oxide content. *Polymer*, 54(3), pp. 1234–1242.
- Shen, Y., Jing, T., Ren, W., Zhang, J., Jiang, Z.-G., Yu, Z.-Z., and Dasari, A. (2012). Chemical and thermal reduction of graphene oxide and its electrically conductive polylactic acid nanocomposites. *Composites Science and Technology*, 72(12), pp. 1430–1435.
- Sheng, X., Xie, D., Cai, W., Zhang, X., Zhong, L., and Zhang, H. (2015). In situ thermal reduction of graphene nano-sheets based poly(methyl methacrylate) nanocomposites with effective reinforcements. *Industrial and Engineering Chemistry Research*, 54(2), pp.649–658.
- Shevchenko, V. G., Polschikov, S. V., Nedorezova, P. M., Klyamkina, A. N., Shchegolikhin, A. N., Aladyshv, A. M., & Muradyan, V. E. (2012). In situ polymerized poly(propylene)/graphene nanoplatelets nanocomposites: Dielectric and microwave properties. *Polymer*, 53(23), pp. 5330–5335.
- Silvestre, J., Silvestre, N., and de Brito, J. (2016). Polymer nanocomposites for structural applications: Recent trends and new perspectives. *Mechanics of Advanced Materials and Structures*, 23(11), pp. 1263–1277.
- Singh, S. C., Zeng, H., Guo, C., Cai, W. (2012). *Nanomaterials: Processing and Characterization with Lasers*, Weinheim, Germany: WILEY-VCH Verlag GmbH & Co.; 2012.
- Singh, V., Joung, D., Zhai, L., Das, S., Khondaker, S. I., and Seal, S. (2011). Graphene based materials: Past, present and future. *Progress in Materials Science*, 56(8), pp. 1178–1271.
- Singha, S., and Thomas, M. J. (2008). Reduction of Permittivity in Epoxy Nanocomposites at Low Nano-filler Loadings. *Annual Report Conference on Electrical Insulation and Dielectric Phenomena, Quebec, QC, 2008*, pp.726–729.
- Smith, G. D., Bedrov, D., Li, L., & Bytner, O. (2002). A molecular dynamics simulation study of the viscoelastic properties of polymer nanocomposites. *The Journal of Chemical*

- Physics*, 117(20), pp. 9478–9489.
- Soltani, T. S., and Lee, B.-K. (2017). A benign ultrasonic route to reduced graphene oxide from pristine graphite. *Journal of Colloid and Interface Science*, 486, pp. 337–343.
- Some, S., Kim, Y., Yoon, Y., Yoo, H., Lee, S., Park, Y., and Lee, H. (2013). High-Quality Reduced Graphene Oxide by a Dual-Function Chemical Reduction and Healing Process. *Scientific Reports*, 3(1). pp.1-5.
- Son, J. Y., Shin, Y.-H., Kim, H., and Jang, H. M. (2010). NiO Resistive Random Access Memory Nanocapacitor Array on Graphene. *ACS Nano*, 4(5), pp. 2655–2658.
- Stankovich, S., Dikin, D. A., Dommett, G. H. B., Kohlhaas, K. M., Zimney, E. J., Stach, E. A., Piner, R. D., Nguyen, S. T., and Ruoff, R. S. (2006). Graphene-based composite materials. *Nature*, 442(7100), pp.282–286.
- Stankovich, S., Dikin, D. A., Piner, R. D., Kohlhaas, A. K., Kleinhammes, A., Jia, Y., Wu, Y., Nguyen, S. T., Ruoff, R. S. (2007). Synthesis of graphene-based nano-sheets via chemical reduction of exfoliated graphite oxide. *Carbon*, 45(7), pp.1558–1565.
- Stobinski, L., Lesiak, B., Malolepszy, A., Mazurkiewicz, M., Mierzwa, B., Zemek, J., Jiricek, P., and Bieloshapka, I. (2014). Graphene oxide and reduced graphene oxide studied by the XRD, TEM and electron spectroscopy methods. *Journal of Electron Spectroscopy and Related Phenomena*, 195, pp. 145–154.
- Strumpler, R., and Glatz-Reichenbach, J. (1999). Conducting Polymer Composites. *Journal of Electroceramics*, 3(4), pp.329–346.
- Suzuki, K., Yamazaki, A., Yokoi, K. (2001). Non-linearity evaluation method of four-terminal-pair (4TP) LCR meter, *Conference Proceedings, 2001 NCSL International Workshop and Symposium*, p.6.
- Syurik, J., Alyabyeva, N., Alekseev, A., and Ageev, O.A. (2014). AFM-Based Model of Percolation in Graphene-Based Polymer Nanocomposites. *Composites Science and Technology*, 95, pp.38–43.
- Szabó, T., Berkesi, O., Forgó, P., Josepovits, K., Sanakis, Y., Petridis, D., and Dékány, I. (2006). Evolution of Surface Functional Groups in a Series of Progressively Oxidized Graphite Oxides Evolution of Surface Functional Groups in a Series of Progressively Oxidized Graphite Oxides. *Chemistry of Materials*, 18(11), pp.2740–2749.
- T.K., B. S., Nair, A. B., Abraham, B. T., Beegum, P. M. S., and Thachil, E. T. (2014). Microwave exfoliated reduced graphene oxide epoxy nanocomposites for high performance applications. *Polymer*, 55(16), pp. 3614–3627.
- Tanaka, T., Kozako, M., Fuse, N., and Ohki, Y. (2005). Proposal of a multi-core model for

- polymer nanocomposite dielectrics. *IEEE Transactions on Dielectrics and Electrical Insulation*, 12(4), pp. 669–681.
- Tang, H., Ehlert, G. J., Lin, Y., and Sodano, H. A. (2011). Highly Efficient Synthesis of Graphene Nanocomposites. *Nano Letters*, 12(1), pp. 84–90.
- Tang, L.-C., Zhang, H., Sprenger, S., Ye L., Zhang Z. (2012). Fracture mechanisms of epoxy-based ternary composites filled with rigid-soft particles. *Composites Science and Technology*, 72, pp. 558–565.
- Tang, L.-C., Wan, Y.-J., Yan, D., Pei, Y.-B., Zhao, L., Li, Y.-B., Wu, L.B., Jiang, J.-X., and Lai, G.-Q. (2013). The effect of graphene dispersion on the mechanical properties of graphene/epoxy composites. *Carbon*, 60, pp.16–27.
- Tang, L.-C., Wang, X., Gong, L.-X., Peng, K., Zhao, L., Chen, Q., Wu, L.-B., Jiang, J.-X., and Lai, G.-Q. (2014). Creep and recovery of polystyrene composites filled with graphene additives. *Composites Science and Technology*, 91, pp. 63–70.
- Thomas, H. R., Day, S. P., Woodruff, W. E., Valles, C.; Young, R. J., Kinloch, I. A., Morley, G. W., Hanna, J. V., Wilson, N. R. and Rourke, J. P. (2013). Deoxygenation of Graphene Oxide: Reduction or Cleaning? *Chem. Mater*, 25(18), pp. 3580–3588.
- Tortello, M., Colonna, S., Bernal, M., Gomez, J., Pavese, M., Novara, C., Giorgis, F., Maggio, M, Guerra, G., Saracco, G., Gonnelli, R. S., and Fina, A. (2016). Effect of thermal annealing on the heat transfer properties of reduced graphite oxide flakes: A nanoscale characterization via scanning thermal microscopy. *Carbon*, 109, pp. 390-401.
- Tran, M.-H., and Jeong, H. K. (2015). Effective reduction of graphene oxide for energy storage devices. *New Physics: Sae Mulli*, 65(3), pp. 240-244.
- Tranchida, D., Piccarolo, S., Loos, J., and Alexeev, A. (2006). Accurately evaluating Young’s modulus of polymers through nanoindentations: A phenomenological correction factor to the Oliver and Pharr procedure. *Applied Physics Letters*, 89(17), pp.171905-3.
- Tranchida, D., Piccarolo, S., Loos, J., and Alexeev, A. (2007). Mechanical Characterization of Polymers on a Nanometer Scale through Nanoindentation. A Study on Pile-up and Viscoelasticity. *Macromolecules*, 40(4), 1259–1267.
- Trucano, P. & Chen, R. (1975). Structure of graphite by neutron diffraction. *Nature* 258(5531), pp.136–137.
- Tschope, K., Beckert, F., Beckert, M., and Mülhaupt, R. (2014). Thermally reduced graphite oxide and mechanochemically functionalized graphene as functional fillers for epoxy nanocomposites. *Macromolecular Materials and Engineering*, 300(2), pp.140–152.



- Tse, W.-K., Qiao, Z., Yao, Y., MacDonald, A. H., and Niu, Q. (2011). Quantum anomalous Hall effect in single-layer and bilayer graphene. *Physical review. B, Condensed matter* 83(15), pp.1–9.
- Tuinstra, F. and Koenig, J. L. (1970). Raman spectrum of graphite. *The Journal of Chemical Physics*, 53, pp.1126–1130.
- Van Lier, G., Van Alsenoy, C., Van Doren, V., and Geerlings, P. (2000). Ab initio study of the elastic properties of single-walled carbon nanotubes and graphene. *Chemical Physics Letters*, 326(1-2), pp.181–185.
- Vidano, R. P., Fischbach, D. B., Willis, L. J., and Loehr, T. M. (1981). Observation of Raman band shifting with excitation wavelength for carbons and graphites. *Solid State Communications*, 39(2), pp.341–344.
- Visakh, P. M., & Nazarenko, O. B. (2015). Thermal Degradation of Polymer Blends, *Composites and Nanocomposites. Engineering Materials*, pp. 1–16.
- Wajid, A. S., Ahmed, H. S. T., Das, S., Irin, F., Jankowski, A. F., and Green, M. J. (2013). High-performance pristine graphene/epoxy composites with enhanced mechanical and electrical properties. *Macromolecular Materials and Engineering*, 298(3), pp. 339–347.
- Wallace, R. (1947). The Band Theory of Graphite. *American Physical Society*, 71, pp.622–634.
- Wan, Y.-J., Yang, W.-H., Yu, S.-H., Sun, R., Wong, C.-P., & Liao, W.-H. (2016). Covalent polymer functionalization of graphene for improved dielectric properties and thermal stability of epoxy composites. *Composites Science and Technology*, 122, pp. 27–35.
- Wang, C., Zhang, Q., Wu, Q.-H., Ng, T.-W., Wong, T., Ren, J., Shi, Z., Lee, C-S, Lee, S.-T., and Zhang, W. (2012). Facile synthesis of laminate-structured graphene sheet–Fe<sub>3</sub>O<sub>4</sub> nanocomposites with superior high reversible specific capacity and cyclic stability for lithium-ion batteries. *RSC Advances*, 2(28), pp.10680-10688.
- Wang, H., Robinson, J. T., Li, X., and Dai, H. (2009). Solvothermal reduction of chemically exfoliated graphene sheets. *Journal of the American Chemical Society*, 131(29), pp. 9910–9911.
- Wang, R., Zhuo, D., Weng, Z., Wu, L., Cheng, X., Zhou, Y., Wang, J., and Xuan, B. (2015). A novel nanosilica/graphene oxide hybrid and its flame retarding epoxy resin with simultaneously improved mechanical, thermal conductivity, and dielectric properties. *Journal of Materials Chemistry A*, 3(18), pp. 9826–9836.
- Wang, X., Naderikalali, E., Wang, D.-Y. (2016). Two-Dimensional inorganic nanocomposites: A solution to flame retardant polymers. *Nano Advances*, 1(1), pp. 1-16.

- Wang, Z., Wei, P., Qian, Y., and Liu, J. (2014). The synthesis of a novel graphene-based inorganic–organic hybrid flame retardant and its application in epoxy resin. *Composites Part B: Engineering*, 60, pp. 341–349.
- Wei, H., Zhang, Y., Zhang, H., and Jiang, Z. (2015). Research on performance and preparation of graphene/epoxy high dielectric permittivity polymer composites. *High Performance Polymers*, 27(8), pp.911–917.
- Wei, J., Vo, T., and Inam, F. (2015). Epoxy/graphene nanocomposites-processing and properties: a review. *RSC Advances*, 5(90), pp. 73510–73524.
- Wu, N., She, X., Yang, D., Wu, X., Su, F., & Chen, Y. (2012). Synthesis of network reduced graphene oxide in polystyrene matrix by a two-step reduction method for superior conductivity of the composite. *Journal of Materials Chemistry*, 22(33), 17254.
- Xie, F., Qi, S. H., Wu, D. (2016). A facile strategy for the reduction of graphene oxide and its effect on thermal conductivity of epoxy based composites. *Express Polymer Letters*, 10(6), pp.470–478.
- Xie, S.H., Liu, Y.Y. and Li, J.Y. (2008) Comparison of the Effective Conductivity between Composites Reinforced by Graphene Nanosheets and Carbon Nanotubes. *Applied Physics Letters*, 92(24), 243121.
- Xu, C., Gao, J., Xiu, H., Li, X., Zhang, J., Luo, F., Zhang, Q., Chen, F., and Fu, Q. (2013). Can in situ thermal reduction be a green and efficient way in the fabrication of electrically conductive polymer/reduced graphene oxide nanocomposites. *Composites Part A: Applied Science and Manufacturing*, 53(A), pp.24–33.
- Xu, C., Wang, X. and Zhu, J., (2008). Graphene - Metal Particle Nanocomposites Graphene - Metal Particle Nanocomposites. *The Journal of Physical Chemistry*, 112(50), pp.19841–19845.
- Yang, H., Li, F., Shan, C., Han, D., Zhang, Q., Niu, L., and Ivaska, A. (2009). Covalent functionalization of chemically converted graphene sheets via silane and its reinforcement. *Journal of Materials Chemistry*, 19(26), 4632.
- Yang, S., Lozano, K., Lomeli, A., Foltz, H. D., and Jones, R. (2005). Electromagnetic interference shielding effectiveness of carbon nanofiber/LCP composites. *Composites Part A: Applied Science and Manufacturing*, 36(5), pp.691–697.
- Yang, T., Liu, L., Liu, J., Chen, M.-L., and Wang, J.-H. (2012). Cyanobacterium metallothionein decorated graphene oxide nanosheets for highly selective adsorption of ultra-trace cadmium. *Journal of Materials Chemistry*, 22(41), pp. 21909-21916.
- Yasmin, A., Luo, J.-J., & Daniel, I. M. (2006). Processing of expanded graphite reinforced

- polymer nanocomposites. *Composites Science and Technology*, 66(9), pp. 1182–1189.
- Yin, G., Zheng, Z., Wang, H., Du, Q., and Zhang, H. (2013). Preparation of graphene oxide coated polystyrene microspheres by Pickering emulsion polymerization. *Journal of Colloid and Interface Science*, 394, pp.192–198.
- Yin, P. T., Shah, S., Chhowalla, M., and Lee, K.-B. (2015). Design, Synthesis, and Characterization of Graphene–Nanoparticle Hybrid Materials for Bioapplications. *Chemical Reviews*, 115(7), pp.2483–2531.
- Young & Lovell, P.A. (1990). *Introduction to polymers* 2nd ed., USA: CRC Press.
- Young, R. J., Liu, M., Kinloch, I. A., Li, S., Zhao, X., Vallés, C., & Papageorgiou, D. G. (2017). The mechanics of reinforcement of polymers by graphene nanoplatelets. *Composites Science and Technology*, 154, pp. 110–116.
- Yousefi, N., Lin, X., Shen, X., Jia, J. J., Dada, O. J., and Kim, J. K. (2013). Electrical properties of self-aligned in-situ reduced graphene oxide/epoxy nanocomposites. *Proceedings 19th International Conference on Composite Materials (ICCM19), Montreal*, pp. 8019-8025.
- Yousefi, N., Lin, X., Shen, X., Jia, J., Kim, J. K. (2014). Exceptional Dielectric Properties of Self-aligned in Situ Reduced Graphene Oxide/epoxy Nanocomposites. *ECCM16-16<sup>th</sup> European conference on composite materials, Seville, Spain*, 22–26.
- Zahed, B., and Hosseini-Monfared, H. (2015). A comparative study of silver-graphene oxide nanocomposites as a recyclable catalyst for the aerobic oxidation of benzyl alcohol: Support effect. *Applied Surface Science*, 328, pp.536–547.
- Zakaria, M. R., Abdul Kudus, M. H., Md. Akil, H., & Mohd Thirmizir, M. Z. (2017). Comparative study of graphene nanoparticle and multiwall carbon nanotube filled epoxy nanocomposites based on mechanical, thermal and dielectric properties. *Composites Part B: Engineering*, 119, pp.57–66.
- Zallen, R. (1985). Models of amorphous solids. *Journal of Nano-Crystalline Solids*. 75,(1-3), PP. 3-14.
- Zaman, I., Kuan, H.-C., Dai, J., Kawashima, N., Michelmore, A., Sovi, A., Dong, S., Luong, L., and Ma, J. (2012). From carbon nanotubes and silicate layers to graphene platelets for polymer nanocomposites. *Nanoscale*, 4(15), 4578.
- Zhai, D., Li, B., Du, H., Gao, G., Gan, L., He, Y., Yang, Q., and Kang, F. (2012). The preparation of graphene decorated with manganese dioxide nanoparticles by electrostatic adsorption for use in supercapacitors. *Carbon*, 50(14), pp. 5034–5043.
- Zhang, H.-B., Wang, J.-W., Yan, Q., Zheng, W.-G., Chen, C., and Yu, Z.-Z. (2011). Vacuum-assisted synthesis of graphene from thermal exfoliation and reduction of graphite oxide.

*Journal of Materials Chemistry*, 21(14), 5392.

- Zhang, W., Dehghani-Sani, A. A., and Blackburn, R. S. (2008). IR study on hydrogen bonding in epoxy resin–silica nanocomposites. *Progress in Natural Science*, 18(7), pp. 801–805.
- Zhang, W.L. and Choi, H. J. (2012). Silica-graphene oxide hybrid composite particles and their electroresponsive characteristics. *Langmuir*, 28(17), pp.7055–7062.
- Zhang, X.-J., Wang, G.-S., Cao, W.-Q., Wei, Y.-Z., Cao, M.-S., & Guo, L. (2014). Fabrication of multi-functional PVDF/RGO composites via a simple thermal reduction process and their enhanced electromagnetic wave absorption and dielectric properties. *RSC Advances*, 4(38), pp. 19594–19601.
- Zhang, Y., Small, J. P., Pontius, W. V., and Kim, P. (2004). Fabrication and Electric Field Dependent Transport Measurements of Mesoscopic Graphite Devices. *Applied Physics Letters*, 86(7), 073104.
- Zhang, Z., Zhang, W., Li, D., Sun, Y., Wang, Z., Hou, C., Chen, L., Cao, Y., and Liu, Y. (2015). Mechanical and anticorrosive properties of graphene/epoxy resin composites coating prepared by in-situ method. *International Journal of Molecular Sciences*, 16(1), pp.2239–2251.
- Zhao, X., Zhang, Q., Chen, D., and Lu, P. (2010). Enhanced mechanical properties of graphene-based polyvinyl alcohol composites. *Macromolecules*, 43(5), pp.2357–2363.
- Zhou, H., Qiu, C., Liu, Z., Yang, H., Hu, L., Liu, J., Yang, H., Gu, C., and Sun, L. (2010). Thickness-Dependent Morphologies of Gold on N -Layer Graphenes. *Journal of the American Chemical Society*, 132(3), pp.944–946.
- Zhou, M., Cai, T., Pu, F., Chen, H., Wang, Z., Zhang, H., and Guan, S. (2013). Graphene/carbon-coated si nanoparticle hybrids as high-performance anode materials for li-ion batteries. *ACS Applied Materials and Interfaces*, 5(8), pp.3449–3455.
- Zhou, X., Huang, X., Qi, X., Wu, S., Xue, C., Boey, F. Y. C., Yan, Q., Chen, P., and Zhang, H. (2009). In Situ Synthesis of Metal Nanoparticles on Single-Layer Graphene Oxide and Reduced Graphene Oxide Surfaces. *The Journal of Physical Chemistry*, 113(25), pp.10842–10846.
- Zhu, G., Liu, Y., Xu, Z., Jiang, T., Zhang, C., Li, X., and Qi, G. (2010). Flexible magnetic nanoparticles-reduced graphene oxide composite membranes formed by self-assembly in solution. *ChemPhysChem*, 11(11), pp.2432–2437.
- Zhu, J., Ji, X., Yin, M., Guo, S., and Shen, J. (2017). Poly (vinylidene fluoride) based percolative dielectrics with tunable coating of polydopamine on carbon nanotubes: Toward high permittivity and low dielectric loss. *Composites Science and Technology*,

144, pp. 79–88.

- Zhu, Y., Murali, S., Stoller, M. D., Ganesh, K. J., Cai, W., Ferreira, P. J., Pirkle, A., Wallace, R. M., Cyhosh, K. A., Thommes, M., Su, D., Stach, E. A., and Ruoff, R. S. (2011). Carbon-Based Supercapacitors Produced by Activation of Graphene. *Science (New York, N.Y.)*, 332(6037), pp.1537–1541.
- Zhuo, Q., Ma, Y., Gao, J., Zhang, P., Xia, Y., Tian, Y., Zhong, J., and Sun, X. (2013). Facile synthesis of graphene/metal nanoparticle composites via self-catalysis reduction at room temperature. *Inorganic Chemistry*, 52(6), pp.3141–3147.
- Zois, H., Apekis, L. and Omastova, M. (1999). Electrical properties and percolation phenomena in carbon black filled polymer composites. In: *Proceedings - International Symposium on Electrets, 10th International Symposium on Electrets (ISE 10)*, 7, pp.529–532.
- Zong, P. S., Fu, J. F., Chen, L. Y., Yin, J. T., Dong, x., Yuan, S., Shi, L. Y., and Deng, W. (2016). Effect of aminopropylisobutyl polyhedral oligomeric silsesquioxane functionalized graphene. *RSC Advances*, 6(13), pp.10498–10506.

## 9 Appendix

**Table S1:** Assignment of the main FT-IR bands for the materials used in this study with their references

Wavenumber / $\text{cm}^{-1}$	Assignment	Reference
4000–400	Graphene, no peaks for graphene structure	Dissanayake <i>et al.</i> 2014
	<b>GO</b>	
3500	O–H, Stretching vibration of hydroxyl groups from C–OH group or water molecule	Aldosari <i>et al.</i> 2013; Ming <i>et al.</i> 2013
1735–1725	C=O, Carbonyl and carboxylic acid groups (RGO/GO)	Aldosari <i>et al.</i> 2013
1622	C=C, Unoxidized graphitic domain	Sharmila <i>et al.</i> 2014; Aldosari <i>et al.</i> 2013
1575–1560	RGO, aromatic ring	Stankovich <i>et al.</i> 2006
1465–1340	C–H bending vibration	Ming <i>et al.</i> 2013
1280–1050	C–O, Stretching vibration of (–C–O–C) groups	Ming <i>et al.</i> 2013
1380–1365	O–H deformations in C–OH group	Țucureanu <i>et al.</i> 2016
	<b>EP</b>	
3100–2800	CH $\text{sp}^2$ from aromatic ring	Chhabra <i>et al.</i> 2012; Ming <i>et al.</i> 2013
2967	Asymmetrical C–H stretch of –CH <sub>3</sub> group	Cecen <i>et al.</i> 2006; Chen <i>et al.</i> 2010
2851	Aromatic ring stretch	Cecen <i>et al.</i> 2006; Chen <i>et al.</i> 2010
1737	C=O, Carbonyl and carboxylic acid groups	María <i>et al.</i> 2012
1508	Aromatic ring stretch	Cecen <i>et al.</i> 2006
1260–1108	Ar–O–C asymmetrical bond	Cecen <i>et al.</i> 2006
1044	Ar–O–C symmetrical bond	Cecen <i>et al.</i> 2006
791	C–O–C ethers stretching	Cecen <i>et al.</i> 2006

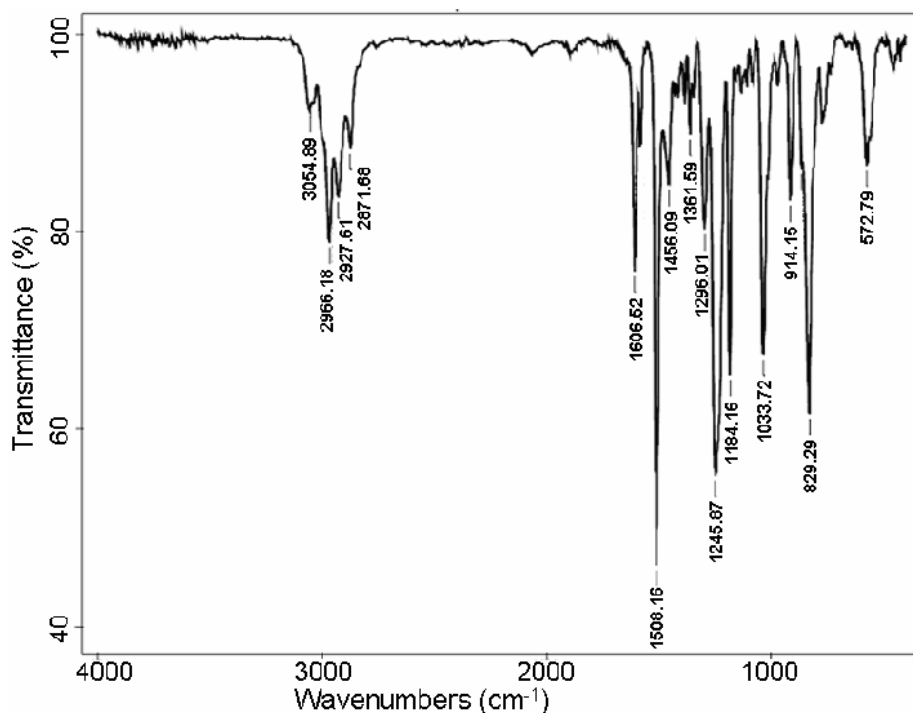


**Figure S1.** FT-IR spectrum of uncured epoxy-resin (Parimal et al. 2008).

**Table S2.** Summary of FT-IR spectra of EP nanocomposites Section 4.3.1.1. Peaks at:

i.	3054.89 cm <sup>-1</sup> corresponds to symmetrical & asymmetrical C–H stretch in aromatics.
ii.	2966.18 cm <sup>-1</sup> corresponds to asymmetrical C–H stretch of –CH <sub>3</sub> group.
iii.	2927.61 cm <sup>-1</sup> corresponds to asymmetrical C–H stretch of –CH <sub>2</sub> group.
iv.	2871.68 cm <sup>-1</sup> corresponds to symmetrical C–H stretch of –CH <sub>3</sub> group.
v.	1606.52 cm <sup>-1</sup> , 1581.44 cm <sup>-1</sup> , 1508.16 cm <sup>-1</sup> and 1456.09 cm <sup>-1</sup> correspond to C–C stretching vibration in aromatic.
vi.	1296.01 cm <sup>-1</sup> corresponds to asymmetrical –CH <sub>2</sub> deformation.
vii.	1245.87 cm <sup>-1</sup> corresponds to asymmetrical aromatic C–O stretch.
viii.	1184.16 cm <sup>-1</sup> corresponds to asymmetrical aliphatic C–O stretch.
X	1033.72 cm <sup>-1</sup> corresponds to symmetrical aromatic C–O stretch.
Xi	970.08 cm <sup>-1</sup> , 914.15 cm <sup>-1</sup> (characteristic peak) and 862.03 cm <sup>-1</sup> correspond to epoxide ring vibrations.
Xii	829.29 cm <sup>-1</sup> corresponds to –CH out of plane deformation in aromatic.

**Table S3:** Assignment of the Raman spectra bands for the materials used in this study with their references

Raman shift / $\text{cm}^{-1}$	Assignment (collected with 532 nm excitation)	Reference
<b>Graphite</b>		
1574	G-band related to $E_{2g}$ phonons by C $sp^2$ and caused by in-phase vibrational mode of the graphite lattice. This band is highly sensitive to the layer thickness. As the number of graphene layers increases the G-band position shifts to a lower wavenumber.	Liu <i>et al.</i> 2016; Krishnamoorthy <i>et al.</i> 2013; Ma <i>et al.</i> 2013
1347	D-band, disorder mode of C $sp^3$ (bond angle/length disorder, and other reasons). This band is associated with the ring breathing mode k point photons of $A_{1g}$ , symmetry. The intensity is directly proportional to the quality in the sample.	Liu <i>et al.</i> 2016; Krishnamoorthy <i>et al.</i> 2013; Ma <i>et al.</i> 2013
2700	2D-band is the result of the production of a two-photon lattice vibrational process with opposite momentum. This band is also associated with the number of layers.	Eda & Chhowalla 2010
<b>GO/RGO</b>		
1587	G-band and up-shifting in accordance with the oxidation process (GO)	Krishnamoorthy <i>et al.</i> 2013
1359	D-band and up-shifting in accordance with the formation of disorder mode of C $sp^2$ and defects (GO)	Krishnamoorthy <i>et al.</i> 2013
1358	D-band of RGOs caused by defects formation after the reduction process was performed	Chen <i>et al.</i> 2010
Very weak 2700	2D-band is the result of the production of a two-photon lattice vibrational process with opposite momentum. This band is also associated with the number of layers.	Eda & Chhowalla 2010



**Table S4:** Comparison of RGO properties between two different thermal reduction process at different temperatures.

Property at 0.5 wt. % of RGO sheet	GO	thermal reduction process at different temperatures			
		120°C	160°C	180°C	1400°C
		via vacuum oven process			Tube furnace
C/O ratio / %	2.28	3.43	5.42	5.93	6.61
Glass Transition Temp. $T_g$ / °C	134	136	139	145	158.3
Thermal stability $T_d$ / °C	451	453	455	457	462
Dispersion along matrix	excellent	very good	good	good	Excellent
d-spacing / nm	0.84	0.73	0.49	0.46	0.39
Young's modulus / GPa	2.83± 0.49	3.24 ± 0.49	3.48 ± 0.20	3.65 ± 0.40	3.23 ± 0.16
Tensile strength / MPa	66.4± 6.7	55.8 ± 5.2	57.7 ± 5.1	65.2 ± 9.7	58.6 ± 2.8
Storage modulus / GPa	2.83	2.94	3.26	3.74	2.86
Electrical conductivity / $S m^{-1}$	insulator	-	-	-	$2.38 \times 10^{-7}$

\* weight of the RGO powder after the thermal reduction process.

**Table S5:** Comparison of the resulting properties of EP/RGO–SiO<sub>2</sub> nanocomposites from the current study with previous studies at low contents.

Approach	wt. %	solvent	E' / %	T <sub>g</sub> (°C) Increased by	Reference
<b>EP/RGO–SiO<sub>2</sub></b>					
pyrolyzing GO–SiO <sub>2</sub> at 700°C for 1 h in an argon atmosphere / solution mixing	1.0	acetone	23.4	3.3	(Hsiao <i>et al.</i> 2013)
electrostatic self-assembly of GO–SiO <sub>2</sub> /solution mixing	30	solvent-free	27.2	14.3	(Huang, Zhu, Li, Lu, <i>et al.</i> 2014a)
GO–SiO <sub>2</sub> was reduced by hydrolysis of TEOS at 95°C with the presence of ammonia solution and GO (sol–gel process) / solution mixing	2	THF	37.5	21.2	current study
<b>EP/SiO<sub>2</sub></b>					
SiO <sub>2</sub> nanoparticles /solution mixing	30	solvent-free	18.7	15	(Huang, Zhu, Li, Lu, <i>et al.</i> 2014a)
SiO <sub>2</sub> nanoparticles /solution mixing	10	ethanol	9.8	12	(L. Chen <i>et al.</i> 2012a)
hydrolysis of TEOS /solution mixing	5	THF	16.1	4.6	current study

*All data were compared to neat EP.*

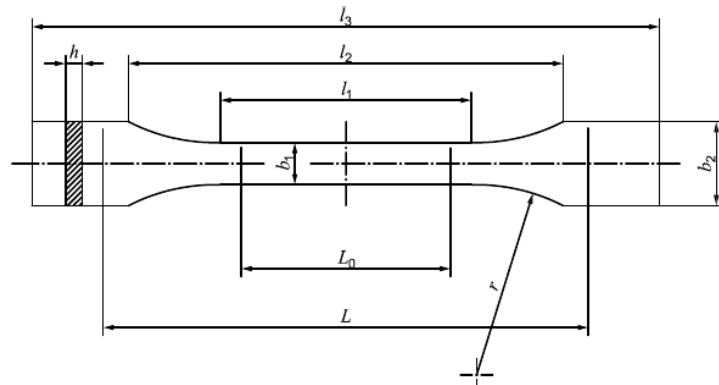


**Figure S2-** Type of test specimens according to ISO 527-2 (in the upper) and obtained samples in the current work (in the bottom)

**Table S6:** Specific dimensions of test specimens according to ISO 527-2.

Dimensions in millimetres

	Specimen type/1BA	ISO 527/2
$l_3$	Total length/Overall	$\geq 75$
$l_1$	Distance between the start of shoulders	$30.0 \pm 0.5$
$l_2$	Distance between the end of shoulders	$58 \pm 2$
$r$	Radius	$\geq 30$
$b_2$	Width at clamp end	$10.0 \pm 0.5$
$b_1$	Width at the middle	$5.0 \pm 0.5$
$L_o$	Gauge length	$25.0 \pm 0.5$
$L$	Original distance between clamps	$l_2^{+2}_0$
$h$	Thickness	$\geq 2$

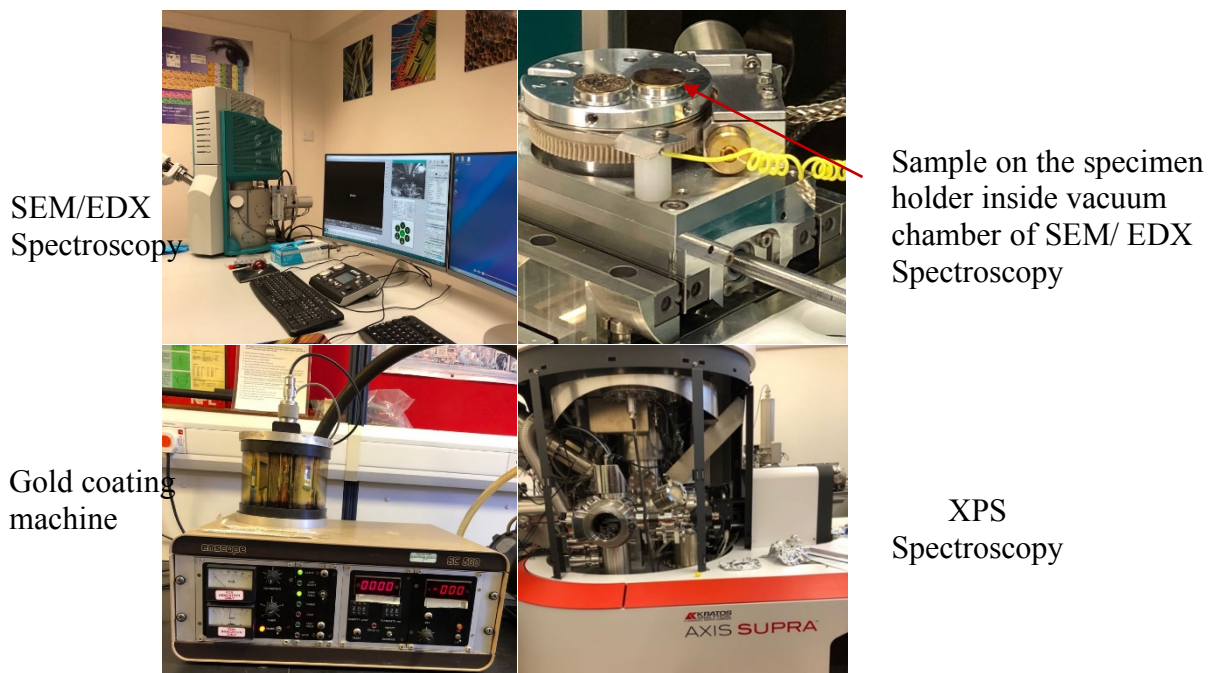


*Figure S3. Some of the tools that have been used for samples characterizations.*

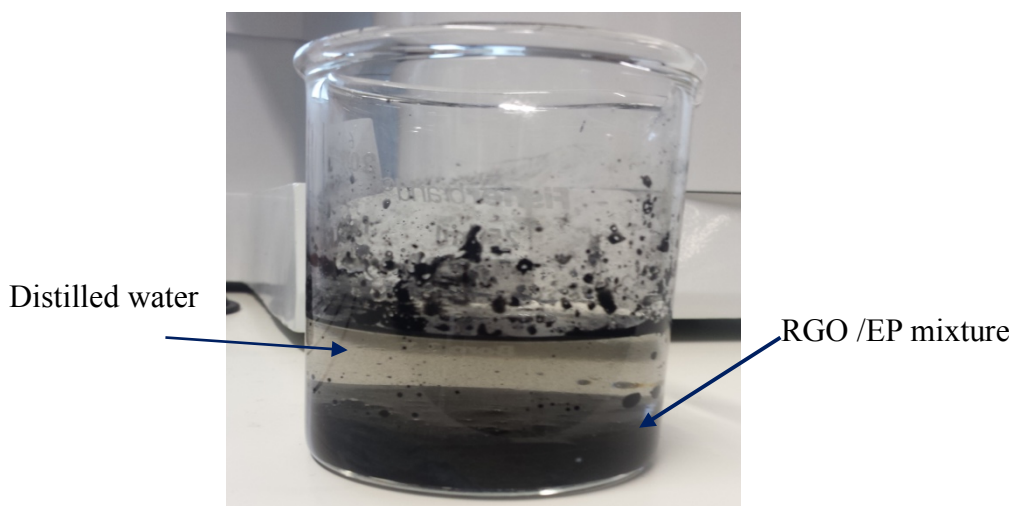


*Figure S4. Photograph of RGO/EP mixture after separated from solvent.*

